UNIVERSITY OF Southampton

University of Southampton Research Repository
ePrints Soton

Copyright © and Moral Rights for this thesis are retained by the author and/or other copyright owners. A copy can be downloaded for personal non-commercial research or study, without prior permission or charge. This thesis cannot be reproduced or quoted extensively from without first obtaining permission in writing from the copyright holder/s. The content must not be changed in any way or sold commercially in any format or medium without the formal permission of the copyright holders.

When referring to this work, full bibliographic details including the author, title, awarding institution and date of the thesis must be given e.g.

AUTHOR (year of submission) "Full thesis title", University of Southampton, name of the University School or Department, PhD Thesis, pagination

http://eprints.soton.ac.uk

University of Southampton

A dissertation submitted in partial fulfillment of the requirements for the degree of Doctor of Philosophy

---

Numerical Simulation of Nonlinear Wave-body Problem Based on Desingularized Rankine Source and Mixed Euler-Lagrange Method

---

Author:
Aichun Feng

Supervisor:
Dr. Zhimin Chen
Professor Jing Tang Xing

June 18, 2014

Abstract

Rankine source method coupled with Mixed Euler-Lagrange(MEL) algorithm is developed to investigate wave-body problems. Under Euler specification a boundary-value problem is solved by placing fundamental singularities outside the computational domain and satisfying the boundary conditions at prescribed control points. At every time step, Lagrangian frame is applied to update the control points position during regridding process.

A space increment method for source points distribution incorporating horizontal free surface source arrangement and vertical desingularized distance is developed and this method connects free surface panel to body panel size. By reducing the number of source points, this method significantly increases the computational efficiency.

A single node scheme is implemented to treat intersection points. This scheme regards intersection points only as body panel ending points. The first source points on the free surface are placed away from the intersection points and generated wave is started from these source points rather than intersection points. During regridding process, body panel number keeps constant and panel size varies to match the variation of wetted body surface.

In the process of repanelling the free surface, panels slide horizontally due to the variation of wetted body surface pushing them back and forth. After their horizontal positions are fixed, the source points follow the wave elevation and are located on the updated wave surface in the vertical direction. A least square based smoothing technique is developed to eliminate the "sawtooth" phenomenon occurred in the free surface updating for two-dimensional fully nonlinear problem.

Both two- and three-dimensional forced body oscillatory motion problems are studied and extensive comparisons show a good agreement with published results. The methods developed are proved to be accurate, efficient and robust for wave-body problems.

Contents

List of Figures viii

List of Tables xvi

Nomenclature xviii

Declaration of Authorship xxiv

Acknowledgements xxv

1 Introduction 1

1.1 Motivation and Background 1

1.2 Literature review of Free surface Green function method 4

1.2.1 Linear problem 4

1.2.2 Nonlinear wave-body problem 5

1.3 Literature review of Rankine source method 7

1.3.1 Source points distribution 8

1.3.2 Body/free-surface intersection points 10

1.4 Literature review of mixed Euler-Lagrange algorithm 11

1.4.1 Numerical procedure 11

1.4.2 Instability and smoothing 12

1.5 Overview 12

1.5.1 Novel contributions 13

1.5.2 Objectives 15

1.5.3 Layout of the thesis 15

2 Problem formulation and solution techniques 17

2.1 Coordination systems and problem sketch 17

2.2 Eulerian specification of the flow field 17

2.2.1 Governing equation and boundary conditions 18

2.2.2 Forced oscillatory body motions 20

2.2.3 Pressure and force exerted on body surface 21

2.2.4 Boundary integral formulation 22

2.3 Lagrangian specification of the flow field 29

2.3.1 Body surface force 30

2.3.2 Free surface boundary conditions 31

2.4 Time-stepping 32

2.4.1 Initial condition 32

2.4.2 Time-stepping for free surface conditions 32

2.4.3 Flowchart of formulation and solution techniques 34

2.5 Chapter summary 35

3 Numerical algorithm for two-dimensional wave-body problems 37

3.1 Discretization of free surface and body surface 37

3.2 Calculation for induced influence coefficient 39

3.3 Body surface and free surface re-gridding 42

3.3.1 Wetted body surface re-panellization 42

3.3.2 Free surface regridding 43

3.4 Wave-body intersection points 44

3.5 Instability and smoothing 46

3.5.1 Model function 46

3.5.2 Least square optimisation 47

3.6 Numerical process 48

3.7 Nondimensionalization 48

3.8 Chapter summary 51

4 Two-dimensional linear numerical simulation for forced body oscillation motion 53

4.1 Selection of body surface panel number 55

4.2 Numerical simulation for forced body oscillation motion 57

4.2.1 Free surface source points distribution 58

4.2.2 Numerical results for forced body oscillation motion 59

4.2.3 Source strength decaying 62

4.3 Error analysis 63

4.4 Concluding remarks 75

5 Two-dimensional nonlinear body boundary problem simulation for forced body oscillation motion 76

5.1 Intersection points treatment 77

5.2 Free surface source point distribution 79

5.2.1 Source point distribution pattern 80

5.2.2 Source points number selection 80

5.2.3 Source strength decaying 83

5.3 Numerical results for large body motion amplitude 88

5.3.1 Numerical results for circular cylinder with large motion amplitude 88

5.3.2 Numerical results for wedge with large motion amplitude 96

5.4 Concluding remarks 100

6 Two-dimensional fully nonlinear problem simulation for forced body oscillation motion 102

6.1 Overview 102

6.2 Numerical simulation setup 104

6.2.1 Numerical model 104

6.2.2 Free surface source point distribution 106

6.2.3 Source strength decaying 107

6.3 Numerical instability and smoothing 108

6.4 Numerical results for large body motion amplitude 109

6.4.1 Numerical results for circular cylinder with large motion amplitude 110

6.4.2 Numerical results for wedge with large motion amplitude 118

6.5 Concluding remarks 121

7 Numerical algorithm for three-dimensional wave-body problems 122

7.1 Discretisation of free surface and body surface . . . 125

7.2 Calculation for induced influence coefficient . . . 126

7.3 Space increment source point distribution . . . 127

7.3.1 Free surface inner domain distribution . . . 128

7.3.2 Matching interval separation and vertical desingularized distance distribution . . . 129

7.4 Intersection points treatment and source strength decaying . . . 132

7.5 Chapter summary . . . 133

8 Three-dimensional numerical simulation for forced body oscillation motion 135

8.1 Introduction . . . 136

8.2 Numerical results for linear problem . . . 137

8.3 Numerical results for nonlinear body boundary problem . . . 143

8.4 Computational effort comparison . . . 151

8.5 Concluding remarks . . . 151

9 Conclusions and recommendations for future work 154

9.1 Conclusions . . . 154

9.2 Recommendations for future work . . . 158

Appendix 160

A Three-dimensional influence coefficient calculation 160

A.1 Transformation from three-dimensional element to two-dimensional quadrilateral element . . . 160

A.2 Construction of the fundamental potential for one side of the quadrilateral element . . . 164

A.3 Summary of velocity components and fundamental potential . . . 168

A.4 Formulation for influence coefficients . . . 170

Bibliography **171**

List of Figures

1.1 Source points arrangement of even distribution method for three-dimensional problem. 9

2.1 Coordinate definition and problem sketch. 18

2.2 Definition of body motions in six degrees of freedom. 21

2.3 Profile of fluid domain, (A): P is within the fluid domain, (B): P is on the surface of fluid domain. (C): P is outside the fluid domain. 23

2.4 Profile of exterior and interior fluid domain. 26

2.5 General flowchart of formulation and solution techniques for the two-dimensional and three-dimensional problems. 35

3.1 Two-dimensional wave-body numerical model schematic. 38

3.2 Line integral model. 40

3.3 Wetted body surface varying at different time steps. 43

3.4 Free surface regridding at different time steps. 44

3.5 Points arrangement for wave-body intersection. 45

3.6 Flowchart of numerical process. 49

4.1 Flowchart of numerical process for two-dimensional linear problem. 54

4.2 Comparisons of analytical solution (4.1) and numerical results for different panel numbers N_b. 56

4.3 The variation of error coefficient C_e with different panel numbers N_b(or N_b^2). 57

4.4 Comparison of heave added mass coefficient A_{33} between Zhang (2007) numerical results, Vugts (1968) experimental data and current method prediction for a circular cylinder in oscillatory heave motion with amplitude $a = 0.1T$. 60

4.5 Comparison of heave damping coefficient B_{33} between Zhang (2007) numerical results, Vugts (1968) experimental data and current method prediction for a circular cylinder in oscillatory heave motion with amplitude $a = 0.1T$. 61

4.6 Comparison of sway added mass coefficient A_{22} between Zhang (2007) numerical results, Vugts (1968) experimental data and current method prediction for a circular cylinder in oscillatory sway motion with amplitude $a = 0.1T$. 62

4.7 Comparison of sway damping coefficient B_{22} between Zhang (2007) numerical results, Vugts (1968) experimental data and current method prediction for a circular cylinder in oscillatory sway motion with amplitude $a = 0.1T$. 63

4.8 Comparison of heave added mass coefficient A_{33} between Zhang (2007) numerical results, Vugts (1968) experimental data and current method prediction for a box in oscillatory heave motion with amplitude $a = 0.1T$. . . . 64

4.9 Comparison of heave damping coefficient B_{33} between Zhang (2007) numerical results, Vugts (1968) experimental data and current method prediction for a box in oscillatory heave motion with amplitude $a = 0.1T$. 65

4.10 Comparison of sway added mass coefficient A_{22} between Zhang (2007) numerical results, Vugts (1968) experimental data and current method prediction for a box in oscillatory sway motion with amplitude $a = 0.1T$. . . . 66

4.11 Comparison of sway damping coefficient B_{22} between Zhang (2007) numerical results, Vugts (1968) experimental data and current method prediction for a box in oscillatory sway motion with amplitude $a = 0.1T$. 67

4.12 Comparison of heave added mass coefficient A_{33} between Vugts (1968) experimental data and current method prediction for a wedge in oscillatory heave motion with amplitude $a = 0.1T$. 68

4.13 Comparison of heave damping coefficient B_{33} between Vugts (1968) experimental data and current method prediction for a wedge in oscillatory heave motion with amplitude $a = 0.1T$. 69

4.14 Comparison of sway added mass coefficient A_{22} between Vugts (1968) experimental data and current method prediction for a wedge in oscillatory sway motion with amplitude $a = 0.1T$. 70

4.15 Comparison of sway damping coefficient B_{22} between Vugts (1968) experimental data and current method prediction for a wedge in oscillatory sway motion with amplitude $a = 0.1T$. 71

4.16 Predicted pressure distributions P_b at different times around circular cylinder in oscillatory heave motion with amplitude $a = 0.1T$ and frequency $\omega^2 R/g = 1.0$. 72

4.17 Time records for vertical force $F(t)$ of circular cylinder in oscillatory heave motion with amplitude $a = 0.1T$ and frequency $\omega^2 R/g = 1.0$. 73

4.18 Time records for wave elevation $\eta(t)$ of circular cylinder in oscillatory heave motion with amplitude $a = 0.1T$ and frequency $\omega^2 R/g = 1.0$. 73

4.19 Source strength for the first 20 source point distribution for a circular cylinder in oscillatory heave motion with amplitude $a = 0.1T$ and frequency $\omega^2 R/g = 1.0$. 74

4.20 Source strength for the first 20 source point distribution for a circular cylinder in oscillatory sway motion with amplitude $a = 0.1T$ and frequency $\omega^2 R/g = 1.0$. 74

5.1 Flowchart of numerical process for two-dimensional nonlinear body boundary condition problem. 78

5.2 Profile of sources, nodes and intersection points at different time steps. . . 79

5.3 Comparisons for added mass coefficient between Vugts experiment data and current methods with different free surface node points N_f when $a = 0.1T$. 82

5.4 Comparisons for damping coefficient between Vugts experiment data and current methods with different free surface node points N_f when $a = 0.1T$. 83

5.5 Comparison of sway added mass coefficient A_{22} between Zhang (2007) numerical results, Vugts (1968) numerical results, Vugts (1968) experimental data and current method prediction for a circular cylinder in oscillatory sway motion with amplitude $a = 0.1T$. 84

5.6 Comparison of sway added mass coefficient B_{22} between Zhang (2007) numerical results, Vugts (1968) numerical results, Vugts (1968) experimental data and current method prediction for a circular cylinder in oscillatory sway motion with amplitude $a = 0.1T$. 85

5.7 Comparisons for node points distribution in inner domain between current method and Zhang and Beck (2006, 2007) method. 86

5.8 Source strength for the first 20 source point distribution for a circular cylinder in oscillatory heave motion with amplitude $a = 0.1T$ and frequency $\omega^2 R/g = 1.0$. 86

5.9 Source strength for the first 20 source point distribution for a circular cylinder in oscillatory sway motion with amplitude $a = 0.1T$ and frequency $\omega^2 R/g = 1.0$. 87

5.10 Comparisons of heave added mass coefficient A_{33} between Lee (1968) numerical results, Yamashita (1977) experimental data and current method prediction for a circular cylinder in oscillatory heave motion with amplitude $a = 0.2T$. 90

5.11 Comparisons of heave damping coefficient B_{33} between Lee (1968) numerical results, Yamashita (1977) experimental data and current method prediction for a circular cylinder in oscillatory heave motion with amplitude $a = 0.2T$. 91

5.12 Comparisons of first order force $F1(\omega)$ between Zhang and Beck (2007) numerical results, Kent (2005) numerical results, Tasai and Koterayama (1976) experimental data and current method predictions for a circular cylinder in oscillatory heave motion with amplitude $a = 0.2T$. 92

5.13 Comparisons of first order force $F1(\omega)$ between Zhang and Beck (2007) numerical results, Potash (1971) numerical results, Parissis (1966) numerical results, Yamashita (1977) experimental data and current method predictions for a circular cylinder in oscillatory heave motion with amplitude $a = 0.2T$. 93

5.14 Predicted wave elevation time records at various amplitudes of heave oscillatory motion when $\omega^2 B/2g = 1.0$. 94

5.15 Predicted vertical force time records at various amplitudes of heave oscillatory motion when $\omega^2 B/2g = 1.0$. 94

5.16 Predicted pressure distributions P_b at different times around circular cylinder in oscillatory heave motion with amplitude $a = 0.2T$ and frequency $\omega^2 R/g = 1.0$. 95

5.17 Comparison of heave added mass coefficient A_{33} Between Tasai and Koterayama (1976) numerical results, Tasai and Koterayama (1976) experimental data and current method prediction for a wedge of the beam-to-draught ratio $B/T = 2\sqrt{3}/3$ experiencing an oscillatory heave motion of amplitude $a = 0.2T$. 97

5.18 Comparison of heave damping coefficientB_{33} between Tasai and Koterayama (1976) numerical results, Tasai and Koterayama (1976) experimental data and current method prediction for a wedge of the beam-to-draught ratio $B/T = 2\sqrt{3}/3$ experiencing an oscillatory heave motion of amplitude $a = 0.2T$. 98

5.19 Predicted pressure distributions P_b at different times around wedge in oscillatory heave motion with amplitude $a = 0.2T$ and frequency $\omega^2 R/g = 1.0$. 99

6.1 Flowchart of numerical process for two-dimensional fully nonlinear problem. 105

6.2 Numerical model of node (source) points distribution for fully nonlinear problem. 106

6.3 Source strength for the first 20 source point distribution for a circular cylinder in oscillatory heave motion with amplitude $a = 0.4T$ and frequency $\omega^2 B/2g = 0.5$. 108

6.4 Numerical divergence of the wave profile at different time steps. 109

6.5 The frequency and amplitude that results can be obtained for an oscillatory heave motion before and after smoothing. 110

6.6 Comparison of heave added mass coefficient A_{33} between nonlinear body boundary condition method, linear numerical results, Yamashita (1977) experimental data, and current method prediction for a circular cylinder experiencing an oscillatory heave motion of amplitude $a = 0.4T$. 111

6.7 Comparison of heave damping coefficient B_{33} between nonlinear body boundary condition method, linear numerical results, Yamashita (1977) experimental data, and current method prediction for a circular cylinder experiencing an oscillatory heave motion of amplitude $a = 0.4T$. 112

6.8 Comparison of first order harmonic force $F^1(\omega)$ between Tasai and Koterayama (1976) linear numerical results, Tasai and Koterayama (1976) experimental data, and current method prediction for a circular cylinder experiencing an oscillatory heave motion of amplitude $a = 0.4T$. 113

6.9 Comparison of second order harmonic force $F^2(\omega)$ between Zhang and Beck (2007) numerical results, Yamashita (1977) experimental data, and current method prediction for a circular cylinder experiencing an oscillatory heave motion of amplitude $a = 0.4T$. 114

6.10 Comparison of third order harmonic force $F^3(\omega)$ between Yamashita (1977) numerical results, Yamashita (1977) experimental data, and current method prediction for a circular cylinder experiencing an oscillatory heave motion of amplitude $a = 0.4T$. 115

6.11 Time series of wave elevation $\eta(t)$ for circular cylinder in oscillatory heave motion with amplitude $a = 0.4T$ and frequency $\omega^2 B/g = 0.5$. 116

6.12 Time series of inertia component force $F^1(t)$ for circular cylinder in oscillatory heave motion with amplitude $a = 0.4T$ and frequency $\omega^2 B/2g = 0.5$. 116

6.13 Time series of quadratic component force $F^2(t)$ for circular cylinder in oscillatory heave motion with amplitude $a = 0.4T$ and frequency $\omega^2 B/2g = 0.5$. 117

6.14 Comparison of second order harmonic force $F^2(\omega)$ between Yamashita (1977) experimental data and current method prediction for a wedge experiencing an oscillatory heave motion of amplitude $a = 0.4T$. 119

6.15 Comparison of third order harmonic force $F^3(\omega)$ between Yamashita (1977) experimental data and current method prediction for a wedge experiencing an oscillatory heave motion of amplitude $a = 0.4T$. 120

7.1 Flowchart of numerical process for three-dimensional linear problem. 123

7.2 Flowchart of numerical process for three-dimensional nonlinear body boundary condition problem. 124

7.3 Three-dimensional wave-body numerical model sketch. 126

7.4 Profile of free surface domains distribution. 130

7.5 Source strength for the first 20 source point distribution when $\omega^2 R/g = 1.0$ and amplitude $a/R = 0.1$. 133

8.1 Comparison of added mass coefficient A_{33} between Hulme's analytical results, other numerical results and current method prediction. 138

8.2 Comparison of damping coefficient B_{33} between Hulme's analytical results, other numerical results and current method prediction. 139

8.3 Comparison of the time dependent nondimensional vertical force experienced by the sphere at oscillatory frequency $\omega^2 R/g = 0.6$ determined from the proposed method and the expression of Hulme (1982). 140

8.4 Comparison of the time dependent nondimensional vertical force experienced by the sphere at oscillatory frequency $\omega^2 R/g = 0.8$ determined from the proposed method and the expression of Hulme (1982). 140

8.5 Comparison of the time dependent nondimensional vertical force experienced by the sphere at oscillatory frequency $\omega^2 R/g = 1.0$ determined from the proposed method, the expression of Hulme (1982) and the formulation of Lin and Yue (1990); this is the only frequency for which Lin and Yue (1990) comparison can be made. 141

8.6 Comparison of the time dependent nondimensional vertical force experienced by the sphere at oscillatory frequency $\omega^2 R/g = 1.2$ determined from the proposed method and the expression of Hulme (1982). 141

8.7 Comparison of the time dependent nondimensional vertical force experienced by the sphere at oscillatory frequency $\omega^2 R/g = 1.4$ determined from the proposed method and the expression of Hulme (1982). 142

8.8 Comparison of the time dependent nondimensional vertical force experienced by the sphere at oscillatory frequency $\omega^2 R/g = 1.6$ determined from the proposed method and the expression of Hulme (1982). 142

8.9 Comparisons of time records for nondimensional inertial force $F^1(t)$ with oscillatory frequency $\omega^2 R/g = 1.0$ and amplitude $a/R = 0.2$ between the proposed method and Zhang and Beck (2008) method. 144

8.10 Time records for nondimensional inertial force $F^1(t)(--*--)$ and corresponding nondimensional wetted surface area $S_w(t)(----)$ with oscillatory frequency $\omega^2 R/g = 1.0$ and amplitude $a/R = 0.5$. 144

8.11 Nonlinear force peak amplitudes and trough amplitudes for both linear and nonlinear problems with oscillatory amplitude a increasing for frequency $\omega^2 R/g = 1.0$. 145

8.12 Comparisons of time records for quadratic force $F^2(t)$ when oscillatory amplitude $a/R = 0.2$ and $a/R = 0.5$ with frequency $\omega^2 R/g = 1.0$. 146

8.13 Comparisons of added mass coefficient A_{33} with increasing oscillatory amplitude a for frequency $\omega^2 R/g = 1.0$. 147

8.14 Comparisons of damping coefficient B_{33} with increasing oscillatory amplitude a for frequency $\omega^2 R/g = 1.0$. 148

8.15 Comparisons of $F^1(\omega)$ with increasing oscillatory amplitude a for frequency $\omega^2 R/g = 1.0$. 149

8.16 Comparisons of $F^2(\omega)$ with increasing oscillatory amplitude a for frequency $\omega^2 R/g = 1.0$. 150

A.1 Profile of corner points and vectors for a body panel in global coordinate system 162

A.2 Profile of plane quadrilateral element and field point P in local coordinate system 165

A.3 Discretization of integral over quadrilateral element into four sides 167

List of Tables

1.1 Estimation of order of force for different force types. 3

1.2 Summary of numerical techniques applied in earlier investigations based on Rankine source and MEL method. 14

3.1 Model functions $f(x)$. 46

4.1 The values of separation factors α_j in the inner domain for linear problem. 58

5.1 The values of separation factors α_j in the inner domain for nonlinear body boundary problem. 81

5.2 Comparisons of frequency components of circular cylinder in heave motion when amplitude $a = 0.2T$. 89

6.1 Selected collection of investigations applying smoothing techniques to suppress saw tooth instability. 104

6.2 Comparison of added mass A_{33} and damping coefficient B_{33} between experimental data (Yamashita, 1977) and numerical data varying with α_1 and α_2 for a cylinder in oscillatory heave motion with amplitude $a = 0.4T$, frequency $\omega^2 B/2g = 1.0$. Symbol $\bigotimes$ indicates numerical divergence with no data derived. 107

6.3 The values of separation factors α_j for fully nonlinear problem. 107

7.1 Error coefficient C_e of the analytical results of Hulme (1982) and the proposed distribution method with respect to the different number of source points when amplitude $a/R = 0.1$ and $\omega^2 R/g = 1.0$. 129

7.2 Error coefficient C_e of the analytical results of Hulme (1982) and the proposed distribution method with respect to different $\alpha_j (j = 1, ..., 4)$ when amplitude $a/R = 0.1$ and frequency $\omega^2 R/g = 0.9$. 131

7.3 Error coefficient C_e of the analytical results of Hulme (1982) and the proposed distribution method with respect to different $\beta_j (j = 1, ..., 4)$ when amplitude $a/R = 0.1$ and frequency $\omega^2 R/g = 1.6$. 132

7.4 Error coefficient C_e of the analytical results of Hulme (1982) and the proposed distribution method with respect to different α_1 for the first source point in region 1 when amplitude $a/R = 0.1$ and frequency $\omega^2 R/g = 0.8$. . 132

Nomenclature

General Rules:

- Symbols are generally defined where they appear in the text for the first time.
- Vectors are presented in bold symbols
- Same symbols with different subscripts indicate different variables
- Symbols used in Appendix A are exclude here and defined in Appendix A

Coordinate systems:

Earth-fixed frame coordinate system	$O - XYZ$
Body-fixed frame coordinate system	$O' - X'Y'Z'$
Local element coordinate system	$o - xyz$

Abbreviations:

MEL	Mixed Euler-Lagrange

Subscript:

Subscript	**Description**
i	Variable number
j	Variable number

Roman Symbols:

Scalar	**Description**
a	Body motion amplitude
a_{22}	Nondimensional added mass coefficient for sway motion
a_{33}	Nondimensional added mass coefficient for heave motion
A	Floating body sectional area
A_{22}	Added mass coefficient for sway motion
A_{33}	Added mass coefficient for heave motion
$A_{N_{f+b}N_{f+b}}$	Influence coefficient matrices
B	Body breadth
b_{22}	Nondimensional damping coefficient for sway motion
b_{33}	Nondimensional damping coefficient for heave motion
B_{22}	Damping coefficient for sway motion
B_{33}	Damping coefficient for heave motion
C_e	Error coefficient
D	Distance of neighbouring node points on free surface
D_d	Desingularized distance
$D_{x_{in}}$	Distance of neighbouring node points in inner domain
$D_{x_{out}}$	Distance of neighbouring node points in outer domain
$f(x)$	Model function
$f^0(\omega)$	Zero order Fourier component of time record force
$f^1(\omega)$	First order Fourier component of time record force
$f^2(\omega)$	Second order Fourier component of time record force
$f^3(\omega)$	Third order Fourier component of time record force
$F^0(\omega)$	Nondimensional frequency dependent second order steady force
$F^1(\omega)$	Nondimensional frequency dependent first order force
$F^2(\omega)$	Nondimensional frequency dependent second order harmonic force
$F^3(\omega)$	Nondimensional frequency dependent third order force
$f^1(t)$	Time dependent inertia force
$f^2(t)$	Time dependent quadratic force
$F^1(t)$	Nondimensional time dependent inertia force
$F^2(t)$	Nondimensional time dependent quadratic force
g	Gravitational acceleration

G	Rankine source potential
L	Body characteristic length
L_b	Body panel size
m	Mass
N	Unknown boundary element number
N_b	Body panel number
N_f	Free surface panel number
O	Centre of earth-fixed coordinate system
O'	Centre of body-fixed coordinate system
P	Field point
P_b	Field point position on body surface
P_f	Field point position on free surface
P_{fx}	Field point position on free surface in X axis direction
P_{fy}	Field point position on free surface in Y axis direction
P_{fz}	Field point position on free surface in Z axis direction
p_b	Pressure on body surface
Q	Source point
r	Distance between field point and source point
R	Cylinder radius
S	Total surface bounding fluid domain
S_b	Wetted body surface
S_f	Free surface
S_0	Bottom surface
S_∞	Enclosing surface at infinity
S_ϵ	Small ball surface
t	Time
T	Body draught
T_0	Wave period
u	Fluid velocity in X axis direction
v	Fluid velocity in Y axis direction
w	Fluid velocity in Z axis direction
v_{bn}	Normal velocity of body surface
v_{fz}	Free surface moving velocity in Z axis direction

$x(t)$	Fluid particle displacement history in X axis direction
$y(t)$	Fluid particle displacement history in Y axis direction
$z(t)$	Fluid particle displacement history in Z axis direction

Vector	**Description**
$\mathbf{e}_1$	Unit vector in X axis direction
$\mathbf{e}_2$	Unit vector in Y axis direction
$\mathbf{e}_3$	Unit vector in Z axis direction
$\mathbf{F}_b$	Force on body surface
$\mathbf{n}$	Flow domain surface unit normal vector
$\mathbf{n}_b$	Body surface unit normal vector
$\mathbf{n}_{fz}$	Free surface unit normal vector
$\mathbf{n}^+$	Exterior domain surface unit normal vector
$\mathbf{n}^-$	Interior domain surface unit normal vector
$\mathbf{s}$	Body displacement
$\mathbf{t}_b$	Body surface panel unit tangent vector
$\overline{\mathbf{t}}_b$	Conjugate-vector of $\mathbf{t}_b$
$\mathbf{U}$	Body translational velocity
$\mathbf{v}$	Fluid velocity
$\mathbf{v}_b$	Body oscillating velocity
$\mathbf{V}_b$	Source point moving velocity on body surface
$\mathbf{V}_f$	Source point moving velocity on free surface
$\mathbf{X}$	Field point position

Greek Symbols:

Symbol	**Description**
α	Least square optimisation coefficient
α_0	Least square optimisation coefficient
α_j	Separation factor
β	Least square optimisation coefficient
β_0	Least square optimisation coefficient
β_j	Separation factor

γ	Least square optimisation coefficient
γ_0	Least square optimisation coefficient
ϵ	Small ball radius
η	Free surface elevation
θ	Polar angle
λ	Wave length
μ	Fluid dynamic viscosity
ρ	Fluid density
σ	Source strength
σ^b	Source strength on body surface
σ^f	Source strength on free surface
τ^+	Exterior fluid domain
τ^-	Interior fluid domain
ϕ	Velocity potential
ϕ_a	Analytical form of velocity potential on circular cylinder
ϕ_n	Numerical solution of velocity potential on circular cylinder
ϕ_b	Velocity potential on body surface
ϕ_f	Velocity potential on free surface
ϕ^+	Velocity potential on the surface of exterior domain
ϕ^-	Velocity potential on the surface of interior domain
φ	Azimuth angle
ψ	Angular variation
ω	Frequency
Ω	Fluid domain
Ω_ϵ	Small ball domain
∞	Infinity domain
Δ	Laplace operator
Δt	Time interval

Declaration of Authorship

I, Aichun Feng declare that the thesis entitled "Numerical Simulation of Nonlinear Wave-body Problem Based on Desingularized Rankine Source and Mixed Euler-Lagrange Method" and the work presented in the thesis are both my own, and have been generated by me as the result of my own original research. I confirm that:

- this work was done wholly or mainly while in candidature for a research degree at this University;
- where any part of this thesis has previously been submitted for a degree or any other qualification at this University or any other institution, this has been clearly stated;
- where I have consulted the published work of others, this is always clearly attributed;
- where I have quoted from the work of others, the source is always given. With the exception of such quotations, this thesis is entirely my own work;
- I have acknowledged all main sources of help;
- where the thesis is based on work done by myself jointly with others, I have made clear exactly what was done by others and what I have contributed myself;
- none of this work has been published before submission,

Signed:

Date:

Acknowledgements

This is my opportunity to express my gratitude to all the people who helped me.

First I would like to acknowledge Dr. Zhimin Chen and Professor Jingtang Xing. Without their supervision and guidance, this thesis could never have been possible.

I would like to thank Processor W.G.Price. His knowledge, vision and experience help me quite a lot, especially regarding the thesis writing.

I am very much thankful for Professor Grant E. Hearn from University of Southampton and Professor Longbin Tao from University of Newcastle. They kindly served as my examiners for the Phd Viva and their suggestions and comments largely improve this thesis.

I would take this opportunity to express my gratitude to Xingshu Zhang who resides in America. My work largely follows his research. Though we never met, he always details his work and give me many useful advices by emails.

Special thanks go to Thomas Lloyd. He read through this thesis and kindly provided some proof reading. All the people in FSI group deserve big thanks. Bjorn Windon, Mirjam Furth, Aparna Subaiah-Varma. It is you who makes our office such a pleasant place to work and I will cherish the friendship with you forever.

I dedicate my thesis to my family. Their unconditional love allowed me to get through many difficulties in the last three years.

At last I would give a special gratitude to my girlfriend Juan for her care, encourage and love during these years. I hope everything goes well for her thesis.

Chapter 1

Introduction

1.1 Motivation and Background

In naval architecture and ocean engineering, a common fluid motion problem is the interaction of free surface waves and floating bodies. When a body experiences large fluid motion, the hydrodynamic effects resulting from body surface movement and free surface variation dominate the assessment of performance, safety and survivability.

Nonlinear wave-body response plays a major role in the design of ship and offshore floating bodies. Second-order quantities become an important factor in the design of FPSO, Spar, Semi-submersible platforms or shuttle tankers. One of the important issues in the design of these vessels is the second-order slow drift motion. This nonlinear response is especially serious for large water line area floating bodies like FPSO and shuttle tankers. The slow drift response can cause large amplitude motions of these floating structures and induce large mooring lines/riser tension. Therefore it is also related to the design of a dynamic positioning system and/or mooring lines/risers. As a result the nonlinear response has a significant effect on the hydrodynamic performance of these coupled structures.

For TLP platform without moored facility, nonlinear order wave loads can cause resonant axial deflection and transient structural deflections of the tendons. The first phenomenon is known as "springing" and the second is called "ringing" in engineering practice. These responses not only cause total breakdown of these platforms, even in

moderate storms, but also can hamper daily operations and lead to whole structure fatigue.

Accurate prediction of nonlinear hydrodynamic response for floating body is doubtless important. Viscous and incompressible flow are governed by Navier-Stokes equations and can be solved respectively by finite volume method and finite element method with Computational Fluid Dynamics (CFD) techniques. But the computational time of CFD is enormous and the numerical simulation can only be executed on supercomputing facility. Thus this technique is not suitable for preliminary engineering design.

Fortunately, viscous effects can be ignored due to their lower order of magnitude compared to inertial force and gravitational forces when floating body characteristic dimensions are large (Newman, 1977). Suppose the problem under consideration can be characterised by a physical length L, velocity U, fluid density ρ, gravity acceleration g and fluid dynamic viscosity μ. The estimation for orders of magnitude for three different forces are summarised in Table 1.1. The viscosity μ for water is $10^{-3}m^2/s$ approximately. For a typical ship or offshore structure with characteristic length of $100m$, the viscous force is trivial compared to the other two and can be neglected in the mathematical model of the problem under consideration. Therefore the present investigation aims to examine wave-body problems under potential flow assumption instead of Navier-Stokes equations.

With the use of the Laplace equation, the velocity potential can be expressed as an integral of sources distributed on body surface and flow boundary surfaces, and is discretised by boundary integral equation method (or panel method) to reduce computational cost. Following the work of Korvin-Kroukovsky and Jacobs (1957), strip theory has been widely used in wave-body interaction simulations. This theory has been extensively developed (Ogilvie and Tuck, 1969; Salvesen et al., 1970; Vugts, 1971; Newman, 1979; Bishop and Price, 1979) and provides initial engineering accuracy for ship structure design. The basic assumption in strip theory involves dividing the wetted hull surface into a finite number of strips. Hence, two-dimensional hydrodynamics coefficients can be computed for each strip and then summed over the length of the hull to yield three-dimensional coefficients.

Strip theory is a form of short wave theory. For long waves, a slender-body theory was first utilised in airship design (Munk, 1924) and later applied in hydrodynamics (Ursell, 1962; Newman, 1964; Newman and Tuck, 1964; Faltinsen, 1972) by dividing the flow field

Table 1.1: Estimation of order of force for different force types.

Type of force	Order of Magnitude
Inertial	$\rho U^2 L^2$
Gravitational	$\rho g L^3$
Viscous	$\mu U L$

into inner and outer regions and Green's theorem is used to match the intersection line. In an attempt to bridge these two theories, a unified theory (Newman, 1979; Newman and Sclavounos, 1980; Sclavounos, 1985) was developed to eliminate the limitation on frequency and applied generally for all frequencies in typical practices.

The development of three-dimensional methods was highly motivated by offshore activities in the North Sea, which requires accurate determination of hydrodynamic forces exerted on large offshore structures being designed. The pioneering work of three-dimensional panel method using singular sources distribution was conducted firstly by Hess and Smith (1964) in aerodynamics and then extensively developed by many researchers in hydrodynamics involving free surface (Davis, 1971; Faltinsen, 1974; Garrison, 1978; Hulme, 1982; Lin and Yue, 1990; Zhang and Beck, 2008). The three-dimensional Hess-Smith method approximates the body surface as a set of plane quadrilateral source panels. The calculation of the panel surface integral requires transformation from plane panel into flat panel under the local reference frame. Source strength is assumed to be constant on every single panel and can be determined by applying body boundary conditions. This method has become the most well known numerical tool and commercial softwares like WAMIT (Wamit, 2013) and SESAM (DNV, 2013) are already available for practical applications.

In order to use so called panel method, Green theorem needs to be applied to transfer the integral region from the fluid domain onto the fluid boundary surface. In wave-body problems involving a free surface, the boundary source is either in the sense of Rankine source (simple Green function source) or free surface source (free surface Green function source). If the free surface source is applied, the free surface boundary conditions are satisfied and the boundary integral is formulated as a singular wave integral on the body surface only. However, the evaluation of this singular integral requires high computational effort even under the linear assumption and becomes extremely complicated for nonlinear

problems.

1.2 Literature review of Free surface Green function method

1.2.1 Linear problem

For a floating body forced to oscillate with a small amplitude (amplitude-to-draught ratio $a/T \leq 0.1$), the resulting wave-body problem may be presented as a linear problem. Therefore the linear velocity potential can be expressed as a free surface Green function, with sources distributed on mean wetted surface of the floating body. The computation of this problem mainly lies in the evaluation of the free surface Green function. The classical expression for the singular integral of a free surface Green function is in the form of a semi-infinite integral involving a Bessel function and a Cauchy integral singularity. Derivations of free surface Green functions date back to the 1940s (Haskind, 1944; Dean, 1948) and were further developed in the 1950s (Ursell, 1950; John, 1950; Haskind, 1952; Thorne, 1953; Haskind, 1954; Havelock, 1955). A broader formulation for Green function and associated integral equation was discussed by Wehausen and Laitone (1960). The numerical evaluation for the singular integral is troublesome.

For two-dimensional deep water problem, dynamic pressure and wave elevation were calculated for a circular cylinder (Porter, 1960) and then for a ship-like section (Paulling and Porter, 1962) in heaving motions. Hydrodynamic coefficients with respect to a body in heaving, swaying and rolling motions were computed numerically by Frank (1967) and measured experimentally by Vugts (1968) with respect to different amplitude motions. Generally, predictions from heave and sway motions show a fairly good agreement with measured data except for rolling motion which bears a small disagreement due to viscous effects. In the context of finite water depth, the relationship between the added mass coefficient and damping coefficient was examined by Yu and Ursell (1961) and the hydrodynamic coefficients were first calculated by Kim (1969). Later the limitations of numerical simulation for these two coefficients were found in low and high frequency domains (Bai, 1977)

The evaluation of three-dimensional singular boundary integral always involves integration domain division and complex series expansions in different domains. Newman (1990, 1992) and Lin and Yue (1990) divided its integration domain or frequency domain into a number of regions and then employed ascending series, asymptotic expansion and polynomial expansions to approximate the singular wave integral of Green function. Similarly, Beck and Liapis (1987) divided the integration domain into three regions but applied series expansion, asymptotic expansion and Filon quadrature to the three regions respectively. Apart from three regions (Beck and Liapis, 1987), a method with one more region applied with Bessel function expansion was developed by King (1987).

Excited by a time-dependent body motion, the wave-body response is well defined in time domain. The solution of this problem requires the introduction of step-response function and convolution integral over all previous times as well as a time-dependent Green function which differs from frequency Green function with an explicit expression of time t in the form of exponent (Finkelstein, 1957; Cummins, 1962; Ursell, 1964; Noblesse, 1981; Yeung, 1982; Beck and Liapis, 1987). Alternatively the time domain problem can be evaluated directly by applying Fourier transform to the frequency domain solution without much extra effort. However this method is only applicable for linear cases but really limited to nonlinear problems (Beck and Reed, 2000).

1.2.2 Nonlinear wave-body problem

For a floating body forced to oscillate with a large amplitude (amplitude-to-draught ratio $a/T \geq 0.2$), nonlinear effects dominate wave-body response and therefore the assumption of linearisation is no longer suitable. Generally, this nonlinear problem can be formulated by the perturbation expansion method, expanding its governing equations into a power series with respect to a small dimensionless quantity ε (Wehausen and Laitone, 1960). The series give rise to a sequence of free surface and body surface boundary condition equations ordered according to the powers of ε. Hence the nonlinear solution of this problem can be computed iteratively from the first towards higher order response.

Second order solutions are suitable to evaluate slowly-varying hydrodynamic excitation responsible for large excursions of bodies constrained by weak restoring forces, and are also appropriate to describe rapidly varying hydrodynamic pressure force which contributes to the fatigue of offshore structures.

The computation of second order problem is substantially more complex compared to its linear counterpart because of the infinite extent of the non-homogeneity of the free-surface condition and the approximate knowledge of the linear solution (Sclavounos, 1988). Unlike the linear problem, the Sommerfeld radiation condition is not suitable as energy transfer across the vertical cylindrical radiation surface connecting free surface and sea bed. Second order response results are obtained under some assumptions for radiation conditions without proof (Chakrabarti, 1978; Molin, 1979; Faltinsen and Loken, 1979; Rahman, 1984; Eatock Taylor and Hung, 1987), but some of these results are either controversial or fail in some range of frequencies.

The second order velocity potential can be decomposed into free and forced terms which satisfy, respectively, homogeneous and inhomogeneous free surface boundary conditions. Molin (1979) presented an expression for the second order force in terms of the assisting potential and related first order parameters. This is known as Molin method requiring the vanishing of a far-field integral, which is essentially a weak radiation condition compensated by the asymptotic behaviour of the second order velocity potentials. This method has been extended widely to handle the second order problem (Faltinsen and Loken, 1979; Molin and Marion, 1986; Eatock Taylor et al., 1989; Matsui et al., 1992).

Alternatively, the second order velocity potential can be explicitly expressed in a boundary integral of double-frequency free surface Green function. This method is similar to that for the linear problem with the exception of a forcing term involving produces of first-order velocity potential, which is a slowly converging integral over the entire free surface. Therefore an effective evaluation for this integral is vital for this method (Newman, 1967; Kim and Yue, 1989, 1990). Since the second order velocity potential can be obtained explicitly, complete second order solutions such as pressures, velocities and surface elevations are readily available in addition to integrated forces and moments.

Although great efforts have been paid to address nonlinear wave-body intersection, the problem remains far from being well solved. A non-physical phenomenon, called irregular frequencies, arises in free surface Green function boundary integral formulations. At the irregular frequencies, the solution of the integral equation either disappears or non-unique solutions. The discretisation of the boundary integral equation generates ill-conditioned linear system on the body boundary and leads to appreciable errors. The existence of irregular frequencies is due to the selection of the specific boundary-integral

equation. The irregular frequency phenomenon was firstly observed by John (1950) and their effects in application were clarified in two-dimensional problem for the predicting of added mass and damping coefficients of ship sections (Frank, 1967). Subsequent numerical studies confirmed the presence of the irregular-frequency error in two-dimensional and three-dimensional problems, both in connection with the source distribution and free surface Green function. The strengths of the distributed sources satisfy a Fredholm integral equation of the second kind, which has an unique solution except at the irregular frequencies where the Fredholm determinant vanishes. Thus this leads to the failure of uniqueness and occurrence of irregular frequency phenomenon. Several numerical methods are readily available to eliminate the irregular frequencies, like Modified integral-equation method (Lee and Sclavounos, 1989; Liapis, 1993; Lee et al., 1996; Lee and Newman, 2005), modified Green function method (Ogilvie and Shin, 1978), and extended boundary condition method (Kleinman, 1982; Lee and Sclavounos, 1989) or moving the irregular frequencies to higher frequency which is out of the practically important range (Teng and Li, 1996).

1.3 Literature review of Rankine source method

Parallel to the free surface Green function method, Rankine source method or simple Green function used in this thesis has also been extensively developed in solving wave-body interaction problems. This method provides a great advantage in handling nonlinear wave-body interaction problems. It is superior not only from a computational point of view but it also simplifies the analysis of nonlinear effects from free surface and body surface boundaries. In addition, this method is free from irregular frequency effects and quite compatible to various boundary conditions. Instead of complicated singular wave integrals, it takes Rankine source ($\ln r$ for two-dimensional problem and $1/r$ for three-dimensional problem) as the integral kernel distributed along free surface as well as body surface.

Due to the difficulty to evaluate free surface Green function, the idea of Rankine source method was originated by Yeung (1973). Early stage research for Rankine source method was coupled with free surface Green function to satisfy the infinite radiation condition. That is, the free surface was divided into inner and outer ranges (Bai and Yeung, 1974; Nestegard and Sclavounos, 1984; Andersen and He, 1985). A simple Green

function is applied in the inner range, while free surface Green function is used for the outer range. A matching boundary condition on the common boundary of two regions is required. This matching technique actually reflected key concerns about the inherent limitations of Rankine source method:

1. Radiation condition: waves propagate from the oscillating body and tend to disappear at infinity;

2. Open-boundary condition: free surface is truncated into a finite domain and no significant reflection is produced from the truncated boundary.

1.3.1 Source points distribution

A Rankine source method without using free surface Green function was successfully developed by Dawson (1977), for steady flow describing a vehicle advancing at a uniform speed, to use simple Green function for meeting radiation and open-boundary conditions. The velocity potential in a boundary integral equation of Rankine sources distributed on free surface is solved by the use of a special four-point upstream finite-difference operator in a near-field range of free surface boundary. In the far-field range of free surface grid, two-point finite-difference operators were used to dampen the waves. This method usually under-predicts wavelength due to the artificially introduced damping. An improved method was developed to overcome this shortcoming by using quadratic splines for deriving another finite-difference operator (Nakos and Sclavounos, 1990; Schultz et al., 1990).

A compromise in the Rankine source method is formulated by covering enough free surface range, beyond which the free surface is truncated. To avoid wave reflection, a damping layer is introduced near the end-wall of the wave tank in a numerical wave tank experiment (Tanizawa, 1996; Koo and Kim, 2004, 2007; Guerber et al., 2010), but this gives rise to artificially induced numerical errors. Its availability for different problems is limited as the necessary damping coefficients need to be evaluated from case to case.

A simple but very efficient model divides the free surface into inner and outer domains. A fixed number of source points is evenly distributed in the inner range whereas in the outer domain, the distance between neighbouring source points increases exponentially

to allow a large free surface range to be covered (Lee, 1992). Lee (1992) introduces a contamination coefficient, which is defined to compare discrepancy between predicted wave and standard wave, to choose the number of source points in inner domain. 30 source points cause the least errors and therefore this value is selected in inner domain. His numerical test also indicts the error goes up by increasing source density if there is more than 30 points per wave length in this domain. Figure 1.1 shows source points distribution for three-dimensional problem of this method.

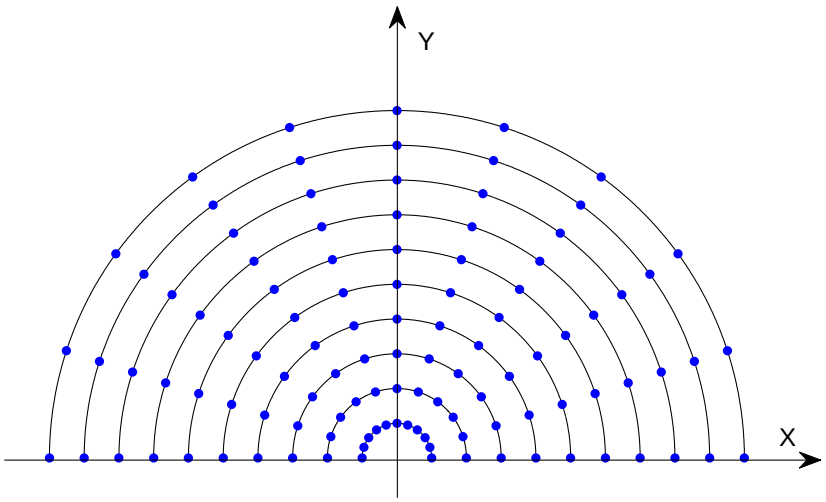

Figure 1.1: Source points arrangement of even distribution method for three-dimensional problem.

Due to the periodic characteristic of a wave, the numerical computation can be completed before the surface wave reaches the truncated boundary. This produces a postponement of the wave refection from the truncation boundary and satisfactory results can be obtained (Cao et al., 1990, 1991a; Beck, 1994; Bai et al., 1994; Beck et al., 1994; Scorpio, 1997; Finn, 2003; Lee, 2003; Zhang and Beck, 2006, 2007; Bandyk, 2009; Zhang et al., 2010). Apart from this even source points distributed method, no other distribution scheme has been developed so far.

The desingularized technology, allocating source points away from the computational fluid boundary, avoids the integral of singularity on free surface and therefore largely simplifies numerical computation. The desingularized distance needs careful investigation to avoid numerical divergence and keep accuracy. Early practice of this method succeeded

in locating sources outside the boundary integral domain without detailed comparison for different desingularization distances (Webster, 1975; Jensen et al., 1986; Schultz and Hong, 1989). Associated with the inner and outer domain source distribution method, Cao et al. (1990, 1991a,b) proposed a source desingularized distance scheme where distance is determined by the horizontal length of the local grid size. The selection for other source distribution parameters was optimised by convergence tests. This source distribution formulation with respect to desingularization distance was extensively quoted for various wave-body intersection problems (Beck, 1994; Beck et al., 1994; Scorpio, 1997; Finn, 2003; Lee, 2003; Zhang et al., 2007; Zhang and Beck, 2008; Bandyk, 2009).

1.3.2 Body/free-surface intersection points

The singularity originating from such intersection points is the result of the confluence of body and free surface boundary conditions. It has a global influence on wave-body interaction and can lead to numerical difficulties or even divergence if not properly treated (Kang, 1988; Tsai and Yue, 1996). Vinje and Brevig (1981) applied only body boundary rather than a free surface boundary condition at the intersection points; their positions together with the velocity potential at the intersection points are obtained by extrapolation. The results produced from this approach were not satisfactory. To derive acceptable computational results from this method, Greenhow et al. (1982) and Sun (2007) found that it is necessary to use experimental measurements to decide the intersection points in the process of their computation. Lee (1992) and Liu et al. (2001) developed a double-node technique which assumed that both body and free surface boundary conditions are satisfied at the intersection points. Similarly, Beck (1994) considered the intersection points as free surface control points and thus free surface boundary conditions are satisfied at the intersection points whereas the body boundary condition is satisfied on the top panels covering the intersection points. Then a desingularized source is placed vertically above each of the intersection points. Beck (1994) also discussed placing of a desingularized control point inside the body, regarding the intersection points as free surface control points. Each of these approaches has merits but, as in all numerical simulations differing degrees of difficulty.

1.4 Literature review of mixed Euler-Lagrange algorithm

The motivation for adopting Rankine source method is due to simple numerical computation with flexible consideration of various fluid boundary conditions, with the ultimate objective of solving fully nonlinear wave-body interaction problems. Fortunately this purpose can be achieved based on the development of a mixed Euler-Lagrange (MEL) algorithm.

1.4.1 Numerical procedure

Two different specifications are introduced to specify flow motions: Eulerian specification and Lagrangian specification. The fluid flow is measured with the moving fluids under the first specification while the second one identifies fluid motion in terms of an individual particle.

This method was first developed as a time-stepping scheme to solve a two-dimensional nonlinear water wave problem (Longuet-Higgins and Cokelet, 1976, 1978) and then subsequently extended to three-dimensional nonlinear water wave and wave-body interaction problems (Cao et al., 1990, 1991a; Schultz et al., 1990; Xue et al., 2001; Liu et al., 2001; Grilli et al., 2001; Zhang and Beck, 2008).

The procedure of MEL iteration requires two major tasks at each time step:

Step 1: Linear field equation is solved under Euler specification to derive wave elevation and free surface velocity potential. This mainly involves evaluation of boundary integration influence coefficients. The most computational effort is to solve a large algebraic system constructed by these influence coefficients.

Step 2: The nonlinear boundary conditions are applied to update control point position and velocity potential by Adams-Bashforth time iteration process, among which control point is tracked as individual particle under Lagrange frame.

1.4.2 Instability and smoothing

Under a Lagrange frame, the updated positions of fluid particles may lay alternately above or below a smooth curve. The discrepancy rapidly increases and leads to the divergence of the numerical simulation. This problem was encountered when a mixed Euler-Lagrange method was first applied and named as a sawtooth instability (Longuet-Higgins and Cokelet, 1976, 1978). It was observed that such instability is different from those associated with discrete time advancing of the free surface (Tsai and Yue, 1996). The instability rate of growth is independent of the number of time iteration steps and is not influenced by rounding errors. The reason for this instability is still not completely clear. Dommermuth and Yue (1987) contributes this sawtooth instability to fluid points concentration in high flow gradients. Moore (1983) claims that the cause of the instability is the resonant interaction between the numerically derived discrete wave pattern and the physically continuous wave profile.

To overcome this problem, a 5 point Chebyshev polynomial method is widely applied to free surface profile and velocity potential during time-stepping integration procedure (Longuet-Higgins and Cokelet, 1976, 1978; Ferrant, 1997; Koo and Kim, 2004, 2007; Zhang et al., 2006; Sun and Faltinsen, 2006, 2007). A similar method but with more points and high order polynomials techniques was derived and found to be more selective than lower-order technique (Dold, 1992). However, the node points on the free surface might become either too close to each other or too far away from each other, which may still cause numerical instabilities (Sun, 2007). These further require free surface regridding techniques like cubic spline approximation, but the regridding introduces more numerical errors and computational effort. Lin et al. (1984) utilised a relatively economic smoothing operator technique, which identifies the divergence occurring in the numerical process, but the research is still very limited.

1.5 Overview

A variety of numerical technologies based on either free surface Green function or simple Green function are available for wave-body interaction simulation. A free surface Green function involves singular integral as well as perturbation expansion. The accuracy

and efficiency of high order wave-body response depend on low order numerical predictions and proper radiation boundary conditions applied. The calculation for nonlinear response is still very challenging and time consuming.

The Rankine source method advances the simulation of the nonlinear problems but has not been comprehensively developed. In view of the literature review, the most challenging techniques for Rankine source method can be summarised as:

(1) Source points distribution on free surface

The free surface boundary condition is applied at isolated source points and therefore accuracy and efficiency of numerical results lie in the distributed patten and density of source points and the truncation of free surface.

(2) Body and free surface intersection points treatment

Both body and free surface boundary conditions are satisfied at the intersection theoretically, both intersection points have a global influence on the wave-body problem. The generated wave is initially stated from the intersection point. Different from other control points these points require special treatment.

(3) Sawtooth smoothing for fully nonlinear problem

The sawtooth instability previously observed during free surface profile updating, disturbs the free surface profile and leads to numerical divergence. A smoothing algorithm has to be applied to suppress the instability and enhance the simulation.

A summary of these techniques applied in earlier investigations based on Rankine source and MEL method are presented in Table 1.2. However no smoothing algorithms were applied in these sources as no fully nonlinear boundary conditions problem was addressed in these publications.

1.5.1 Novel contributions

In the Rankine source method, the continuous free surface profile is replaced by isolated source point and free surface conditions are applied on these source points. The

Table 1.2: Summary of numerical techniques applied in earlier investigations based on Rankine source and MEL method.

Author(s)/(year)	Source point	Intersection point	Smoothing
Beck(1994)	Even	Double point treatment	None
Cao/Beck/Schultz (1990, 1991a, 1991b,1993,1994)	Even	Single point treatment	None None
Lee(1992,2003)	Even	Single point treatment	None
Bandyk(2009, 2011)	Even	None	None
Zhang/Beck (2006, 2007,2008,2012)	Even	None	None
"Even" stands for even source points distribution.			
"None" means lack of such techniques applied.			

source point distribution pattern and density is crucial for numerical accuracy and efficiency.

The source strength decreases from the first source point outwards to the far field so that the importance of the source points decays correspondingly from the first to the last point on the free surface. The widely applied even increment distribution method essentially ignores the characteristics of source strength. In view of this, a space increasing source distribution method is developed to comply with the characteristics of source strength. This distribution method largely reduces the number of sources on the free surface and therefore the computational effort is significantly reduced whereas the numerical accuracy is kept.

To comply with this new source distribution method, a single point treatment is adapted for the intersection points. In this treatment, the intersection points are taken as a body panel ending points and only the body boundary condition is satisfied at these points. The first source point is shifted away from the intersection point and therefore the generated wave starts from this first source point.

Sawtooth instability disturbs the free surface profile and fails the numerical process for a fully nonlinear problem. A least square based smoothing method is newly implemented to suppress sawtooth phenomenon in the mixed Euler-Lagrange formulation for two-dimensional fully nonlinear body oscillatory motion.

By implementing these novel techniques, a more economic and robust numerical tool based on the Rankine source method and MEL algorithm are developed to simulate two-dimensional and three-dimensional linear and nonlinear wave-body interactions.

1.5.2 Objectives

This thesis aims to further develop new numerical algorithms to overcome the technique challenges based on desingularized Rankine Source and Mixed Euler-Lagrange Method. A reliable and robust numerical tool is constructed to model two-dimensional and three-dimensional floating structures oscillating around free-surface with the purpose to predict motion responses accurately and efficiently for a wave-body problem, which can aid evaluation of hydrodynamic characteristics for ship and offshore structure designs in engineering practice.

To achieve this, the following preliminary objectives are outlined as:

- to develop a more economic and robust numerical technology based on a panel method
- to assess the hydrodynamic reactive loads based on a combined Rankine source and MEL method
- to develop an efficient and stable Fortran 90 code to execute the computing process

1.5.3 Layout of the thesis

Following the background statement and literature review in Chapter 1, the following part comprises theoretical and numerical studies of wave-body problem based on Rankine source method and mixed Euler Lagrange algorithm. The wave-body problem is confined to forced body oscillatory motion within a free surface in this thesis.

After introducing mathematical model based on potential flow and boundary element formulation, the following context is divided into two-dimensional and three-dimensional wave-body problems and structured from numerical algorithms to numerical prediction. The numerical tests start from linear simulation and then advance to nonlinear problems.

Chapter 2 covers the mathematical formulation for this wave-body problem. The flow field is presented in a boundary integral form derived from governing equation and boundary conditions under Eulerian and Lagrangian specifications.

Chapter 3 is devoted to numerical algorithms of two-dimensional linear and nonlinear problems. The continuous boundary integral is discretised where source points are distributed in isolation above free surface and body surface is approximated by a set of panels. Key numerical techniques including influence coefficient calculation, Lagrangian point tracking, intersection points treatment and saw tooth smoothing are presented sequentially.

Chapter 4 illustrates extensive results produced from a linear numerical simulation for a two-dimensional forced body oscillatory motion. Various body shapes including circular cylinder, box and wedge are tested when they experience small amplitude heave motion and sway motion. The predicted results are compared with available experimental and numerical data to validate the accuracy and efficiency of the proposed numerical techniques.

Chapter 5 presents the numerical test for a nonlinear body boundary problem. A circular cylinder and wedge experiencing large heave motion are adopted as numerical models. First order and higher order responses are obtained and verified by comparing with published data.

Chapter 6 further investigates the least square based smoothing algorithm applied within the fully nonlinear problem and compares numerical predictions from linear method, nonlinear boundary condition method and fully nonlinear method for a circular cylinder with very large forced heave motion.

Chapter 7 describes the numerical techniques unique for a three-dimensional problems. The mathematical formulation for the influence coefficient is attached in Appendix A.

Chapter 8 shows linear wave-body numerical results predicted from proposed methods for a sphere with heave motion and then nonlinear body boundary condition problem. Numerical predictions are compared with analytical results or other numerical results to show the accuracy and efficiency of the adopted new techniques.

Chapter 9 outlines the achievement and contribution in this thesis and offers recommendations for further work.

Chapter 2

Problem formulation and solution techniques

2.1 Coordination systems and problem sketch

Two coordinate systems are used throughout this work. They are an Earth-fixed frame $O-XYZ$ and a body-fixed frame $O'-X'Y'Z'$. The Earth frame is a Cartesian inertial coordinate system and used as global reference frame. In the Earth-fixed frame, the Z-axis points upwards and the $X-Y$ plane coincides with the calm water surface. For the body-fixed frame, the definition of the X', Y', Z'-axes are similar to X, Y, Z-axes. The centre O' is placed at the centre of floating body, and moves with this body.

The fluid domain, Ω, is bounded by the free surface, S_f, body surface, S_b, bottom surface, S_0 and the enclosing surface at infinity, S_∞. A rigid body initially floats on the free surface with mass centre located on calm water surface. Surface waves are generated by the floating body undergoing forced oscillatory motion. Figure 2.1 illustrates the coordinates definition and problem sketch.

2.2 Eulerian specification of the flow field

The Eulerian specification of the flow field is a way of looking at fluid motion that focuses on specific locations in the space through which the fluid flows as time passes

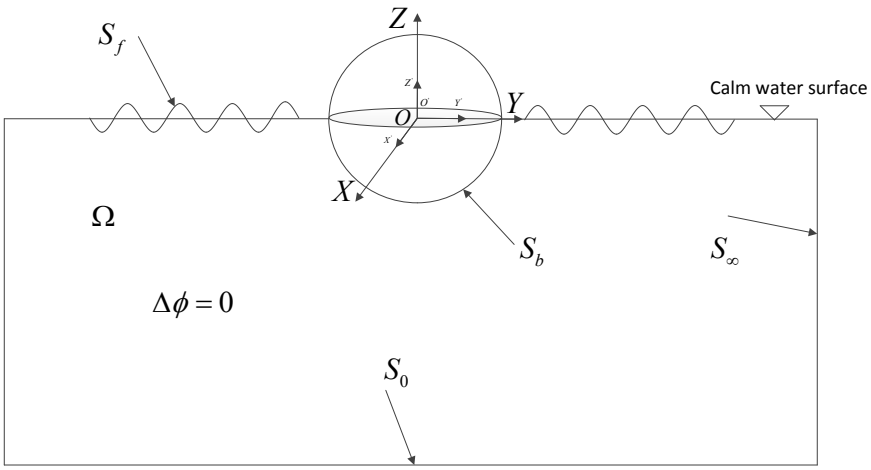

Figure 2.1: Coordinate definition and problem sketch.

(Lamb, 1993). It gives the history of what goes on at a particular point (x, y, z) in the flow field. Within a potential flow framework, the fluid is assumed inviscid and incompressible with irrotational flow and therefore a velocity potential ϕ exists. The fluid velocity $\mathbf{v}$ has 3 components u, v, w and under Eulerian specification, they are express as:

$$u = \frac{\partial \phi}{\partial x},$$

$$v = \frac{\partial \phi}{\partial y},$$

$$w = \frac{\partial \phi}{\partial z}.$$

2.2.1 Governing equation and boundary conditions

By assuming the fluid is incompressible, the continuity equation is satisfied everywhere in the fluid domain, governing equation for the boundary value problem in the Eulerian

specification is subject to Laplace equation:

$$\frac{\partial^2\phi}{\partial x^2}+\frac{\partial^2\phi}{\partial y^2}+\frac{\partial^2\phi}{\partial z^2}=0 \qquad \text{in fluid domain } \Omega. \tag{2.1}$$

No fluid can flow through the rigid body surface. Expressed in terms of the velocity potential, this impermeability condition becomes:

$$\frac{\partial\phi}{\partial\mathbf{n}_b}=\mathbf{v}_b\cdot\mathbf{n}_b \qquad \text{on body surface } S_b, \tag{2.2}$$

where $\mathbf{v}_b$ denotes the given velocity of the body surface oscillation and $\mathbf{n}_b$ is the unit body normal vector pointing into the fluid.

The kinematic free surface boundary condition requires that a free surface particle always remains in the free surface, that is,

$$\frac{D}{Dt}(\eta-z)=0 \qquad \text{on free surface } S_f, \tag{2.3}$$

or

$$\frac{\partial\eta}{\partial t}+\frac{\partial\phi}{\partial x}\frac{\partial\eta}{\partial x}+\frac{\partial\phi}{\partial y}\frac{\partial\eta}{\partial y}-\frac{\partial\phi}{\partial z}=0 \qquad \text{on free surface } S_f, \tag{2.4}$$

where $\eta=\eta(x,y,t)$ is the free surface elevation at time t. The dynamic boundary condition is derived from Bernoulli's equation as:

$$\frac{\partial\phi}{\partial t}+\frac{1}{2}|\nabla\phi|^2+g\eta=0 \qquad \text{on free surface } S_f, \tag{2.5}$$

where g is gravitational acceleration.

For a linear wave-body intersection problem, $\partial\eta/\partial t$, $\partial\eta/\partial x$, $\partial\eta/\partial y$, $\partial\phi/\partial x$, $\partial\phi/\partial y$ and $\partial\phi/\partial z$ are infinitesimal and therefore $\frac{\partial\phi}{\partial x}\frac{\partial\eta}{\partial x}$, $\frac{\partial\phi}{\partial y}\frac{\partial\eta}{\partial y}$ and $|\nabla\phi|^2$ are higher order terms. By linearisation, kinematic and dynamic free surface boundary conditions are reduced to:

$$\frac{\partial\eta}{\partial t}-\frac{\partial\phi}{\partial z}=0 \qquad \text{on free surface } S_f. \tag{2.6}$$

and

$$\frac{\partial\phi}{\partial t}+g\eta=0 \qquad \text{on free surface } S_f, \tag{2.7}$$

For an infinite deep water problem, the disturbance on the bottom surface is ignored and this reduces the boundary condition to:

$$\frac{\partial \phi}{\partial z} \to 0 \qquad \text{on } S_0. \tag{2.8}$$

The boundary condition applied on the far field boundary requires that the disturbance vanishes at infinity such that:

$$\nabla \phi \to 0 \qquad \text{on } S_\infty. \tag{2.9}$$

2.2.2 Forced oscillatory body motions

When a floating body undergoes oscillatory motion in the fluid domain, it can experience six degrees of freedom; the three translational motions parallel to X,Y,Z axes are defined as surge, sway and heave respectively, and three rotational motions about the same axes as roll, pitch and yaw respectively. Figure 2.2 presents the definition of body motions in six degrees of freedom. Symbols $\mathbf{e}_1$, $\mathbf{e}_2$ and $\mathbf{e}_3$ denote unit vectors with direction along the X, Y and Z axes respectively.

In this thesis, only sway and heave motions are considered. The body experiences forced harmonic oscillations of amplitude a and frequency ω, such that its displacement of this motion $\mathbf{s}$ is expressed as:

$$\mathbf{s}(t) = \begin{cases} \mathbf{0} & \text{if } t < 0 \\ \mathbf{e}_i a \sin(\omega t) & \text{if } t \geq 0 \end{cases}$$

while the velocity $\mathbf{v_b}(\mathbf{t})$ in the form of:

$$\mathbf{v}_b(t) = \begin{cases} \mathbf{0} & \text{if } t < 0 \\ \mathbf{e}_i a\omega \cos(\omega t) & \text{if } t \geq 0 \end{cases}$$

where the index $i = 2$ and 3 specify sway and heave motions.

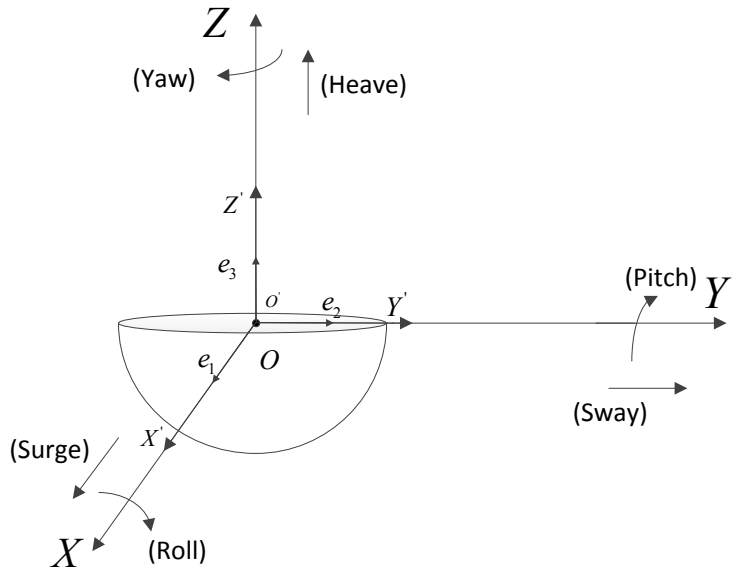

Figure 2.2: Definition of body motions in six degrees of freedom.

2.2.3 Pressure and force exerted on body surface

Once the velocity potential ϕ on the body surface is determined, the dynamic pressure $p_b(t)$ at any point can be evaluated from Bernoulli's equation as:

$$\frac{p_b(t)}{\rho} = -\frac{\partial \phi}{\partial t} - \frac{1}{2}|\nabla \phi|^2 \qquad \text{on body surface } S_b. \tag{2.10}$$

Alternatively Equation 2.10 can be rewritten as:

$$\frac{p_b(t)}{\rho} = -\frac{D\phi}{Dt} - (\frac{1}{2}|\nabla \phi|^2 - \mathbf{V}_b \cdot \nabla \phi) \qquad \text{on body surface } S_b, \tag{2.11}$$

by using the total derivative

$$\frac{D\phi}{Dt} = (\frac{\partial}{\partial t} + \mathbf{V}_b \cdot \nabla)\phi,$$

which is the time derivative of velocity potential ϕ following the point on S_b moving with velocity $\mathbf{V}_b$. The time record of force $\mathbf{F}_b(t)$ can be calculated by integrating the pressure over the whole body surface S_b,

$$\mathbf{F}_b(t) = \int_{S_b} p_b(t)\mathbf{n}_b \cdot \mathbf{ds}. \tag{2.12}$$

2.2.4 Boundary integral formulation

The velocity potential ϕ at any point in the fluid domain Ω can be decomposed into velocity potentials of Rankine source points distributed on the boundary of fluid domain based on boundary integral method. For field point P and source point Q, the Rankine source potential is expressed as:

$$G(P,Q) = \begin{cases} \ln r_{PQ} & \text{for two-dimensional case} \\ -\dfrac{1}{r_{PQ}} & \text{for three-dimensional case,} \end{cases}$$

where $r_{PQ} = |P - Q|$ is the distance between field point P and source point Q.

If field point P is located within the fluid domain Ω as shown in Figure 2.3, (A), the Rankine source potential $G(P,Q)$ satisfies Laplace Equation 2.1 in the fluid domain Ω except at the point $P = 0$. In order to circumvented this difficulty, a small ball Ω_ϵ of radius $\epsilon > 0$ is taken and its centre is located at the field point P. It follows from the infinite deep water condition Equation 2.8 and the decay condition on the far field boundary condition Equation 2.9 that the Green's identity,

$$\int_{S_b \cup S_f \cup S_\epsilon} (\phi \frac{\partial G}{\partial \mathbf{n}} - G\frac{\partial \phi}{\partial \mathbf{n}})ds = \int_{\Omega \setminus \Omega_\epsilon} (\phi \Delta G - G\Delta\phi)d\Omega \tag{2.13}$$

holds true for the body boundary S_b, the free-surface boundary S_f and the sphere S_ϵ of the ball Ω_ϵ. Here $\mathbf{n}$ is the unit normal vector pointing out the fluid domain Ω. The harmonic function property of G and ϕ on the domain $\Omega \setminus \Omega_\epsilon$ implies that the right-hand side of Equation 2.13 is zero, while the singularity property of the Rankine source at the field point P yields

$$\lim_{\epsilon \to 0} \int_{S_\epsilon} (\phi \frac{\partial G}{\partial \mathbf{n}} - G\frac{\partial \phi}{\partial \mathbf{n}})ds \;=\; \phi(P,t) \lim_{\epsilon \to 0} \int_{S_\epsilon} \frac{\partial G}{\partial \mathbf{n}} ds$$

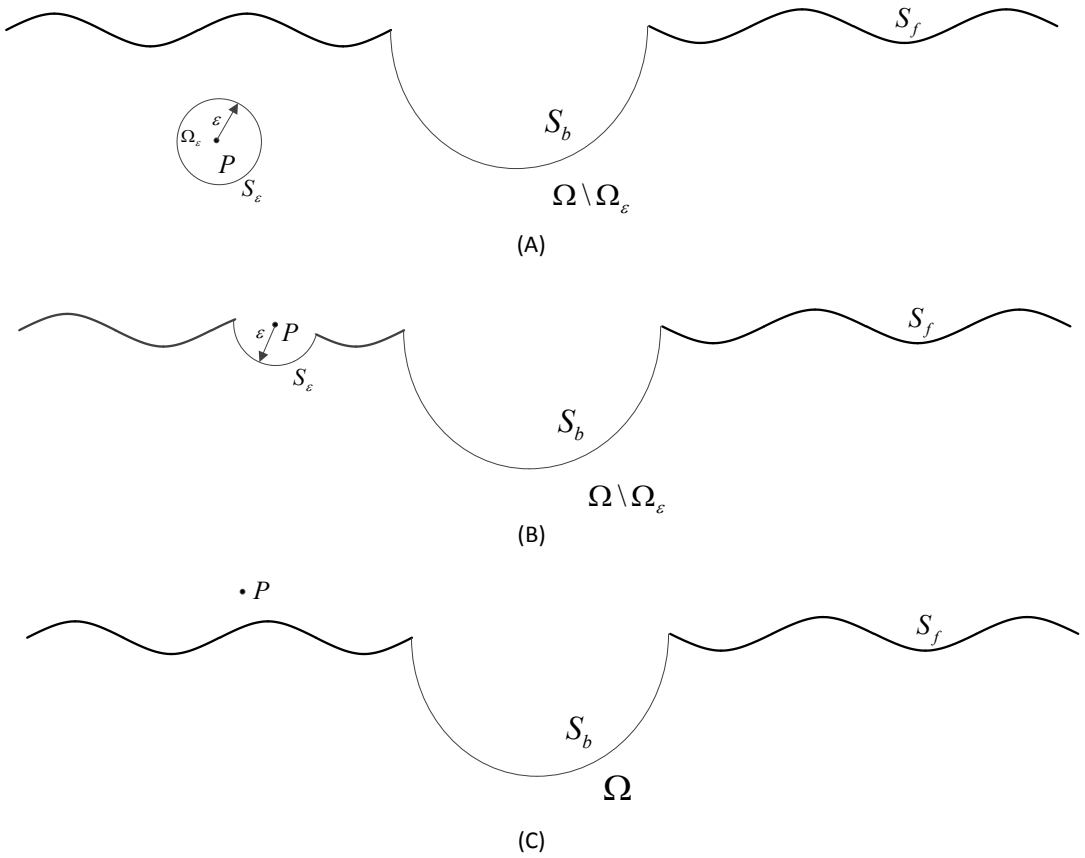

Figure 2.3: Profile of fluid domain, (A): P is within the fluid domain, (B): P is on the surface of fluid domain. (C): P is outside the fluid domain.

where the implied limits satisfy,

$$\begin{cases} \phi(P,t) \lim\limits_{\epsilon \to 0} \int_{r_{PQ}=\epsilon} \dfrac{ds_Q}{r_{PG}} = 2\pi\phi(P,t) & \text{for two-dimensional case,} \\ \phi(P,t) \lim\limits_{\epsilon \to 0} \int_{r_{PQ}=\epsilon} \dfrac{ds_Q}{r_{PG}^2} = 4\pi\phi(P,t) & \text{for three-dimensional case} \end{cases}$$

for source located off-body in fluid domain and hence Equation 2.13, for source points

located off-body in fluid domain, assumes the form:

$$0 = \int_{S_b \cup S_f} (\phi \frac{\partial G}{\partial \mathbf{n}} - G \frac{\partial \phi}{\partial \mathbf{n}}) ds + \begin{cases} 2\pi\phi(P,t) & \text{for two-dimensional case,} \\ 4\pi\phi(P,t) & \text{for three-dimensional case.} \end{cases} \tag{2.14}$$

If field point P is located on the surface of the fluid domain as shown in Figure 2.3, (B), a small half ball Ω_ϵ of radius $\epsilon > 0$ is taken and its centre is located at the field point P. Similar to the formula deduction of Equation 2.14, Equation 2.13 now has the form:

$$0 = \int_{S_b \cup S_f} (\phi \frac{\partial G}{\partial \mathbf{n}} - G \frac{\partial \phi}{\partial \mathbf{n}}) ds + \begin{cases} \pi\phi(P,t) & \text{for two-dimensional case,} \\ 2\pi\phi(P,t) & \text{for three-dimensional case.} \end{cases} \tag{2.15}$$

If field point P is located outside the fluid domain as shown in Figure 2.3, (C), the Rankine source potential $G(P,G)$ satisfies Laplace Equation 2.1 in the whole fluid domain Ω and therefore Green's identity is valid in the form:

$$\int_{S_b \cup S_f} (\phi \frac{\partial G}{\partial \mathbf{n}} - G \frac{\partial \phi}{\partial \mathbf{n}}) ds = \int_{\Omega} (\phi \Delta G - G \Delta \phi) dV, \tag{2.16}$$

and so Equation 2.16 reduces to:

$$0 = \int_{S_b \cup S_f} (\phi \frac{\partial G}{\partial \mathbf{n}} - G \frac{\partial \phi}{\partial \mathbf{n}}) ds + \begin{cases} 0 & \text{for two-dimensional case,} \\ 0 & \text{for three-dimensional case.} \end{cases} \tag{2.17}$$

This thesis aims to solve the boundary integral equation only for the case of field point P on the boundary surface $S_b \cup S_f$ and hence only Equation 2.15 is applied in the following thesis. The velocity potential ϕ can be formulated in the following boundary integral form:

$$\phi(P,t) = \frac{1}{\pi} \int_{S_f \cup S_b} [\ln r_{PQ} \frac{\partial \phi(Q,t)}{\partial \mathbf{n}} - \phi(Q,t) \frac{\partial}{\partial \mathbf{n}} (\ln r_{PQ})] ds, \quad P \in S_b \cup S_f, \tag{2.18}$$

for the two-dimensional case, and

$$\phi(P,t) = \frac{1}{2\pi} \int_{S_f \cup S_b} [\frac{1}{r_{PQ}} \frac{\partial \phi(Q,t)}{\partial \mathbf{n}} - \phi(Q,t) \frac{\partial}{\partial \mathbf{n}} (\frac{1}{r_{PQ}})] ds, \quad P \in S_b \cup S_f \tag{2.19}$$

for the three-dimensional case.

The velocity potential ϕ can be determined from either Equation 2.18 or Equation 2.19. Within these equations $\ln r_{PQ}$ and $\frac{\partial \ln(r_{PQ})}{\partial n}$ or $\frac{1}{r_{PQ}}$ and $\frac{\partial(1/r_{PQ})}{\partial n}$ are interpreted as the source and dipole of strengths $\frac{\partial \phi(Q,t)}{\partial n}$ and $\phi(Q,t)$ for the case of two-dimensional and three-dimensional fluid domains respectively. Some researchers such as Cao et al. (1991a) and Cao (1991) have named this method as the "Direct method".

Alternatively, the velocity potential ϕ can be decided only by source $\ln r_{PQ}$ or $\frac{1}{r_{PQ}}$ and some researchers such as Cao (1991) and Cao et al. (1991a) have named this method as "Indirect method". The indirect method has some advantages in terms of computational complexity and time consumption compared to its counterpart the "Direct method". Hence, the "Indirect method" is applied in the present work. The author considers the advantage to be its ability to examine fluid velocity or free surface profile at non wetted surface points.

In order to derive the expression of velocity potential ϕ for "Indirect method", a body with body surface S is introduced into a fluid domain. The exterior and interior fluid domains for this body are designed as τ^+ and τ^- respectively. The exterior and interior unit normal vectors are presented by $\mathbf{n}^+$ and $\mathbf{n}^-$. The directions of $\mathbf{n}^+$ and $\mathbf{n}^-$ are opposite. The profile of exterior and interior fluid domain is shown in Figure 2.4. The velocity potential ϕ^+ on the surface of exterior domain can be expressed as:

$$\phi^+ = \frac{1}{\pi}\int_S [G\frac{\partial \phi^+}{\partial \mathbf{n}^+} - \phi^+\frac{\partial G}{\partial \mathbf{n}^+}]ds, \quad P \in S, \tag{2.20}$$

for the two-dimensional case, and

$$\phi^+ = \frac{1}{2\pi}\int_S [G\frac{\partial \phi^+}{\partial \mathbf{n}^+} - \phi^+\frac{\partial G}{\partial \mathbf{n}^+}]ds, \quad P \in S \tag{2.21}$$

for the three-dimensional case.

Similarly, the velocity potential ϕ^- on the surface of interior domain can be expressed as:

$$\phi^- = \frac{1}{\pi}\int_S [G\frac{\partial \phi^-}{\partial \mathbf{n}^-} - \phi^+\frac{\partial G}{\partial \mathbf{n}^-}]ds, \quad P \in S, \tag{2.22}$$

for the two-dimensional case, and

$$\phi^- = \frac{1}{2\pi}\int_S [G\frac{\partial \phi^-}{\partial \mathbf{n}^-} - \phi^+\frac{\partial G}{\partial \mathbf{n}^-}]ds, \;\; P \in S \tag{2.23}$$

for the three-dimensional case.

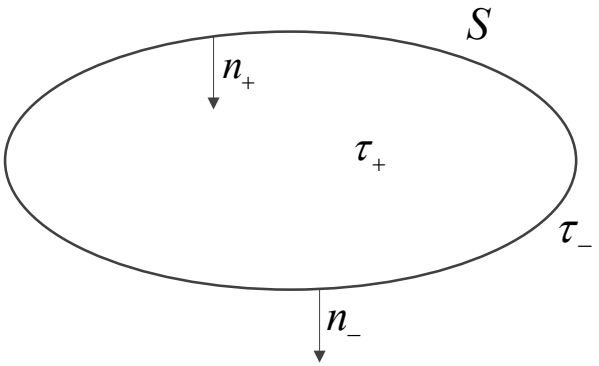

Figure 2.4: Profile of exterior and interior fluid domain.

By combining Equations 2.20 and 2.22, Equations2.21 and 2.23 together and with respect to $\mathbf{n}^+ = -\mathbf{n}^-$, the boundary integral equations become:

$$\phi^+ + \phi^- = \frac{1}{\pi}\int_S G(\frac{\partial \phi^+}{\partial \mathbf{n}^+} - \frac{\partial \phi^-}{\partial \mathbf{n}^+})ds, \;\; P \in S, \tag{2.24}$$

for the two-dimensional case, and

$$\phi^+ + \phi^- = \frac{1}{2\pi}\int_S G(\frac{\partial \phi^+}{\partial \mathbf{n}^+} - \frac{\partial \phi^-}{\partial \mathbf{n}^+})ds, \;\; P \in S \tag{2.25}$$

for the three-dimensional case.

Both ϕ^+ and ϕ^- on the same body surface S, so $\phi^+ = \phi^-$. Equations 2.24 and 2.25 now has the following format:

$$\phi^+ = \frac{1}{2\pi}\int_S G(\frac{\partial \phi^+}{\partial \mathbf{n}^+} - \frac{\partial \phi^-}{\partial \mathbf{n}^+})ds, \;\; P \in S, \tag{2.26}$$

for the two-dimensional case, and

$$\phi^+ = \frac{1}{4\pi}\int_S G(\frac{\partial\phi^+}{\partial\mathbf{n}^+} - \frac{\partial\phi^-}{\partial\mathbf{n}^+})ds, \quad P \in S \tag{2.27}$$

for the three-dimensional case.

Let source strength $\sigma = \frac{1}{2\pi}(\frac{\partial\phi^+}{\partial\mathbf{n}^+} - \frac{\partial\phi^-}{\partial\mathbf{n}^+})$ for the two-dimensional case and $\sigma = \frac{1}{4\pi}(\frac{\partial\phi^+}{\partial\mathbf{n}^+} - \frac{\partial\phi^-}{\partial\mathbf{n}^+})$ for the three-dimensional case, the previous two Equations 2.26 and 2.27 have convenient format:

$$\phi^+ = \int_S \sigma G ds, \quad P \in S, \tag{2.28}$$

for the two-dimensional case, and

$$\phi^+ = \int_S \sigma G ds, \quad P \in S \tag{2.29}$$

for the three-dimensional case.

By omitting the superscript + and replacing S with $S_f \cup S_b$, the velocity potential $\phi(P,t)$ can be expressed by a single singularity format as:

$$\phi(P,t) = \int_{S_f \cup S_b} \sigma(Q,t) \ln r_{PQ} ds, \quad P \in S_f \cup S_b, \tag{2.30}$$

for the two-dimensional case, and

$$\phi(P,t) = \int_{S_f \cup S_b} \sigma(Q,t) \frac{1}{r_{PQ}} ds, \quad P \in S_f \cup S_b \tag{2.31}$$

for the three-dimensional case.

For the velocity potential on body surface $\phi_{S_b}(P,t)$, the boundary integral equation based on "Indirect method" has the format as:

$$\phi_{S_b}(P,t) = \int_{S_f \cup S_b} \sigma(Q,t) \ln r_{PQ} ds, \quad P \in S_b \tag{2.32}$$

for the two-dimensional case, and

$$\phi_{S_b}(P,t) = \int_{S_f \cup S_b} \sigma(Q,t) \frac{1}{r_{PQ}} ds, \quad P \in S_b \tag{2.33}$$

for the three-dimensional case.

In order to apply the body boundary condition Equation 2.2, another boundary integral equation for body surface can be easily obtained. That is,

$$\frac{\partial \phi_{S_b}(P,t)}{\partial \mathbf{n}_b} = \int_{S_f \cup S_b} \sigma(Q,t) \frac{\partial \ln r_{PQ}}{\partial \mathbf{n}_b} ds, \quad P \in S_b \tag{2.34}$$

for the two-dimensional case, and

$$\frac{\partial \phi_{S_b}(P,t)}{\partial \mathbf{n}_b} = \int_{S_f \cup S_b} \sigma(Q,t) \frac{\partial}{\partial \mathbf{n}_b} \frac{1}{r_{PQ}} ds, \quad P \in S_b \tag{2.35}$$

for the three-dimensional case,

Similarly the velocity potential on free surface $\phi_{S_f}(P,t)$ has the format as:

$$\phi_{S_f}(P,t) = \int_{S_f \cup S_b} \sigma(Q,t) \ln r_{PQ} ds, \quad P \in S_f, \tag{2.36}$$

for the two-dimensional case, and

$$\phi_{S_f}(P,t) = \int_{S_f \cup S_b} \sigma(Q,t) \frac{1}{r_{PQ}} ds, \quad P \in S_f \tag{2.37}$$

for the three-dimensional case.

For the purpose of free surface updating using the free surface boundary condition Equations 2.4 and 2.5, the boundary integral equation for the free surface is formulated as:

$$\frac{\partial \phi_{S_f}(P,t)}{\partial z} = \int_{S_f \cup S_b} \sigma(Q,t) \frac{\partial \ln r_{PQ}}{\partial z} ds, \quad P \in S_f \tag{2.38}$$

for the two-dimensional case, and

$$\frac{\partial \phi_{S_f}(P,t)}{\partial z} = \int_{S_f \cup S_b} \sigma(Q,t) \frac{\partial}{\partial z} \frac{1}{r_{PQ}} ds, \quad P \in S_f \tag{2.39}$$

for the three-dimensional case.

The determination of source strength σ requires the solution of boundary integral

equations involving both free surface and body surface:

$$\phi_{S_f}(P,t) = \int_{S_f \cup S_b} \sigma(Q,t) \ln r_{PQ} ds$$

$$\frac{\partial \phi_{S_b}(P,t)}{\partial \mathbf{n}_b} = \int_{S_f \cup S_b} \sigma(Q,t) \frac{\partial \ln r_{PQ}}{\partial \mathbf{n}_b} ds \tag{2.40}$$

for the two-dimensional case, and

$$\phi_{S_f}(P,t) = \int_{S_f \cup S_b} \sigma(Q,t) \frac{1}{r_{PQ}} ds$$

$$\frac{\partial \phi_{S_b}(P,t)}{\partial \mathbf{n}_b} = \int_{S_f \cup S_b} \sigma(Q,t) \frac{\partial}{\partial \mathbf{n}_b} \frac{1}{r_{PQ}} ds \tag{2.41}$$

for the three-dimensional case.

The body surface condition $\frac{\partial \phi_{S_b}(P,t)}{\partial \mathbf{n}_b}$ on the left side of Equations 2.40 and 2.41 is body normal velocity v_{bn} and it is prescribed for forced oscillatory motion in Section 2.2.2.

With the known free surface condition $\phi_{S_f}(P,t)$ and body surface condition v_{bn} on the left side of Equations 2.40 and 2.41, the source strength σ on $S_f \cup S_b$ is determined by solving these Equations using Gaussian elimination algorithm.

Once the source strength σ on $S_f \cup S_b$ is readily available, the velocity potential ϕ_b can be evaluated by Equation 2.32 or 2.33 for the two-dimensional or three dimensional case. Following this, the excited body surface force can be calculated by Bernoulli's equation and this will be discussed in Section 2.3.1.

The left side $\frac{\partial \phi_{S_f}(P,t)}{\partial z}$ of Equations 2.38 and 2.39 is actually the vertical velocity $v_{fz} = \frac{\partial \phi_{S_f}(P,t)}{\partial z}$ of the free surface. v_{fz} requires evaluation by these two equations at every time step. It is applied in the free surface updating and this will be discussed in Section 2.4.2.

2.3 Lagrangian specification of the flow field

Lagrangian specification of the flow field is a way of looking at fluid motion by following an individual fluid particle as it moves through space and time in the fluid domain

(Lamb, 1993). It gives the motion history of a single particle in the fluid domain. For a fluid particle with displacement history of $x(t)$, $y(t)$ and $z(t)$ in X,Y and Z axis respectively, the fluid particle velocity $\mathbf{v}(u, v, w)$ in this specification is formulated by the derivative of displacement with respect to time t:

$$u = \frac{\partial x(t)}{\partial t},$$

$$v = \frac{\partial y(t)}{\partial t},$$

$$w = \frac{\partial z(t)}{\partial t}.$$

2.3.1 Body surface force

For moving body surface, the dynamic pressure $p_b(t)$ for any point P_b with velocity $\mathbf{V}_b$ on the body surface is evaluated by Bernoulli's equation in the format of time derivatives:

$$\frac{p_b(P_b,t)}{\rho} = -\frac{d\phi_{S_b}(P_b,t)}{dt} - (\frac{1}{2}|\nabla\phi_{S_b}(P_b,t)|^2 - \mathbf{V}_b(P_b,t)\cdot\nabla\phi_{S_b}(P_b,t)). \tag{2.42}$$

Upon noting that $\nabla\phi_{S_b}(P_b,t) = \mathbf{V}_b(P_b,t)$ it follows that:

$$\frac{p_b(P_b,t)}{\rho} = -\frac{d\phi_{S_b}(P_b,t)}{dt} + \frac{1}{2}|\mathbf{V}_b(P_b,t)|^2, \tag{2.43}$$

where the total derivative $\frac{d\phi_{S_b}(P_b,t)}{dt}$ is approximated in a backward difference scheme

$$\frac{d\phi_{S_b}(P_b(t),t)}{dt} = \frac{\phi_{S_b}(P_b(t),t) - \phi_{S_b}(P_b(t-\Delta t),t-\Delta t)}{\Delta t}, \tag{2.44}$$

for time interval Δt. Here $\mathbf{V}_b$ is computed in the Lagrangian specification:

$$\mathbf{V}_b(P_b(t),t) = \frac{P_b(t) - P_b(t-\Delta t)}{\Delta t}, \tag{2.45}$$

that is, change in position of point over time interval Δt gives new velocity.

This requires updating positions of point P_b at consecutive steps. Utilising Equations

2.44 and 2.45 then Equation 2.43 can be rewritten in an algebraic format:

$$\frac{p_b(P_b(t),t)}{\rho} = -(\frac{\phi_{S_b}(P_b(t),t) - \phi_{S_b}(P_b(t-\Delta t),t-\Delta t)}{\Delta t}) + \frac{1}{2}(\frac{P_b(t) - P_b(t-\Delta t)}{\Delta t})^2. \tag{2.46}$$

and inertial force $f^1(t)$ and quadratic force $f^2(t)$ can be obtained by integrating the first part and second part of $p_b(P_b,t)$ respectively over the whole body surface:

$$f^1(t) = \int_{S_b} -(\frac{\phi_{S_b}(P_b(t),t) - \phi_{S_b}(P_b(t-\Delta t),t-\Delta t)}{\Delta t})\rho n_b ds \tag{2.47}$$

$$f^2(t) = \frac{1}{2}\int_{S_b} (\frac{P_b(t) - P_b(t-\Delta t)}{\Delta t})^2 \rho n_b ds \tag{2.48}$$

2.3.2 Free surface boundary conditions

Similarly the kinematic surface boundary condition (2.4) can be reformulated in the time derivative form following the motion of any point P_f on free surface with velocity $\mathbf{V}_f(P_f,t)$:

$$\frac{d\eta}{dt} = (\mathbf{V}_f(P_f,t) - \nabla\phi_{S_f}(P_f,t)) \cdot \nabla\eta + \frac{\partial\phi_{S_f}(P_f,t)}{\partial z}, \tag{2.49}$$

while the dynamic boundary condition becomes:

$$\frac{d\phi_{S_f}(P_f,t)}{dt} = \mathbf{V}_f(P_f,t) \cdot \nabla\phi_{S_f}(P_f,t) - \frac{1}{2}|\nabla\phi_{S_f}(P_f,t)|^2 - g\eta, \tag{2.50}$$

where the total derivative is now expressed as:

$$\frac{d}{dt} = \frac{\partial}{\partial t} + \mathbf{V}_f(P_f,t) \cdot \nabla(P_f,t).$$

The point P_f moves exactly following the fluid particle on the free surface and therefore:

$$\mathbf{V}_f(P_f,t) = \nabla\phi_{S_f}(P_f,t). \tag{2.51}$$

Therefore the free surface boundary condition of (2.49) is reduced to:

$$\frac{d\eta}{dt} = \frac{\partial\phi_{S_f}(P_f,t)}{\partial z}, \tag{2.52}$$

and

$$\frac{d\phi_{S_f}(P_f,t)}{dt} = -g\eta + \frac{1}{2}|\mathbf{V}_f(P_f,t)|^2, \tag{2.53}$$

and $\mathbf{V}_f(P_f,t)$ can be computed under Lagrangian specification

$$\mathbf{V}_f(P_f,t) = \frac{P_f(t) - P_f(t-\Delta t)}{\Delta t}, \tag{2.54}$$

which corresponds to Equation 2.45 and requires updating positions of point P_f at consecutive steps $t - \Delta t$ and t.

2.4 Time-stepping

2.4.1 Initial condition

The free surface is still and coincides with the calm water surface at initial time $t = 0$, therefore the wave elevation $\eta(0)$, free surface velocity $\mathbf{V}_f(0)$ and velocity potential $\phi_{S_f}(0)$ at this instant can be stated as:

$$\eta(0) = 0, \tag{2.55a}$$

$$\phi_{S_f}(0) = 0, \tag{2.55b}$$

and

$$v_{fz}(0) = 0. \tag{2.55c}$$

These initial conditions and Equation 2.5 imply that

$$\frac{\partial\phi_{S_f}(t)}{\partial t} = 0. \tag{2.56}$$

As for body conditions, the initial boundary conditions are decided by forced oscillatory body motion conditions described in Section 2.2.2.

2.4.2 Time-stepping for free surface conditions

Both explicit and implicit linear techniques are available for free surface time-stepping. The 3rd-order Adams-Bashforth scheme (Butcher, 2008) is applied in this work. Accord-

ing to free surface boundary conditions 2.53 and 2.54, the free surface condition under Lagrangian specification can be formulated in a more convenient format at $t = 0$ as:

$$\eta(0) = v_{fz}(P_f, t)\Delta t, \tag{2.57}$$

$$\phi_{S_f}(0) = (-g\eta(0) + \frac{1}{2}|\mathbf{V}_f(P_f, 0)|^2)\Delta t, \tag{2.58}$$

and in a 2nd-order Adams-Bashforth scheme at $0 + \Delta t$,

$$\eta(\Delta t) = \eta(0) + \frac{\Delta t}{2}(3(v_{fz}(P_f, \Delta t) - v_{fz}(P_f, 0)), \tag{2.59}$$

$$\phi_{S_f}(\Delta t) = \phi_{S_f}(0) - g\frac{\Delta t}{2}(3\eta(\Delta t) - \eta(0)) + \frac{\Delta t}{2}|\mathbf{V}_f(P_f, \Delta t)|^2 \tag{2.60}$$

and for 3rd-order Adams-Bashforth scheme at $t + \Delta t$

$$\eta(t + \Delta t) = \eta(t) + \frac{\Delta t}{12}(23v_{fz}(P_f, t) - 16v_{fz}(P_f, t - \Delta t) + 5v_{fz}(P_f, t - 2\Delta t)) \tag{2.61}$$

$$\phi_{S_f}(t+\Delta t) = \phi_{S_f}(t)+\frac{\Delta t}{12}(-23g\eta(t)+16g\eta(t-\Delta t)-5g\eta(t-2\Delta t))+\frac{1}{2}\Delta t|\mathbf{V}_f(P_f, t+\Delta t)|^2. \tag{2.62}$$

In the numerical scheme of study, the free surface updating procedure adopts a 3rd-order Adams-Bashforth scheme from $t = t + \Delta t$ since enough data is available for time marching from this time step.

For linear problem, the free surface boundary condition is satisfied on the calm water surface and the free surface profile is coincided with calm water surface. Therefore,

$$|\mathbf{V}_f(P_f, t)| = 0. \tag{2.63}$$

For nonlinear body boundary problem, the position of intersection point changes due to wetted body surface varies. The free surface profile is still coincided with calm water surface. The motion of free surface source point is caused by intersection points moving in X direction for the two-dimensional case and $X - Y$ plane for the three-dimensional case. Therefore,

$$|\mathbf{V}_f(P_f, t)| = \frac{P_{fx}(t) - P_{fx}(t - \Delta t)}{\Delta t}, \tag{2.64}$$

for the two-dimensional case, and

$$|\mathbf{V}_f(P_f,t)| = \sqrt{(\frac{P_{fx}(t)-P_{fx}(t-\Delta t)}{\Delta t})^2+(\frac{P_{fy}(t)-P_{fy}(t-\Delta t)}{\Delta t})^2} \tag{2.65}$$

for the three-dimensional case. $P_{fx}(t)$, $P_{fx}(t-\Delta t))$ and $P_{fy}(t)$, $P_{fy}(t-\Delta t))$ are the updating positions of point P_f at consecutive steps t and $t-\Delta t$ in X and Y direction respectively.

For fully nonlinear problem, the point P_f moves with free surface profile at every time step and the evaluation for $\mathbf{V}_f(P_f,t)$ also requires the information for the updating positions of point P_f at consecutive steps in Z direction. Therefore,

$$|\mathbf{V}_f(P_f,t)| = \sqrt{(\frac{P_{fx}(t)-P_{fx}(t-\Delta t)}{\Delta t})^2+(\frac{P_{fz}(t)-P_{fz}(t-\Delta t)}{\Delta t})^2} \tag{2.66}$$

for the two-dimensional case, and

$$|\mathbf{V}_f(P_f,t)| = \sqrt{(\frac{P_{fx}(t)-P_{fx}(t-\Delta t)}{\Delta t})^2+(\frac{P_{fy}(t)-P_{fy}(t-\Delta t)}{\Delta t})^2+(\frac{P_{fz}(t)-P_{fz}(t-\Delta t)}{\Delta t})^2} \tag{2.67}$$

for the three-dimensional case.

2.4.3 Flowchart of formulation and solution techniques

The mathematical solution for both two-dimensional and three-dimensional wave-body problems have the same process within Euler and Lagrange frame. The solution starts from initial boundary conditions as shown in Section 2.4.1. Then the source strength σ can be available by solving Equations 2.40 or 2.41. Velocity potential ϕ_{S_b} can be evaluated by Equation 2.32 or 2.33 and then used for pressure and excited force calculation.

The free surface vertical velocity v_{fz} can be computed by Equation 2.38 or 2.39 and then applied for free surface updating by 3rd-order Adams-Bashforth scheme under the Lagrange frame. The free surface velocity potential ϕ_{S_f} can be obtained by the free surface updating by using Equations 2.57 to 2.62. Body surface velocity is prescribed at every time step. Free surface velocity potential and body surface normal velocity is known for next time step simulation. This process is repeated until the end of the simulation.

Figure 2.5 shows the general flowchart of formulation and solution techniques for the two-dimensional and three-dimensional problems regardless of different boundary conditions. More specific flowchart for linear problem, nonlinear body boundary problem and fully nonlinear problem will be shown in corresponding chapters.

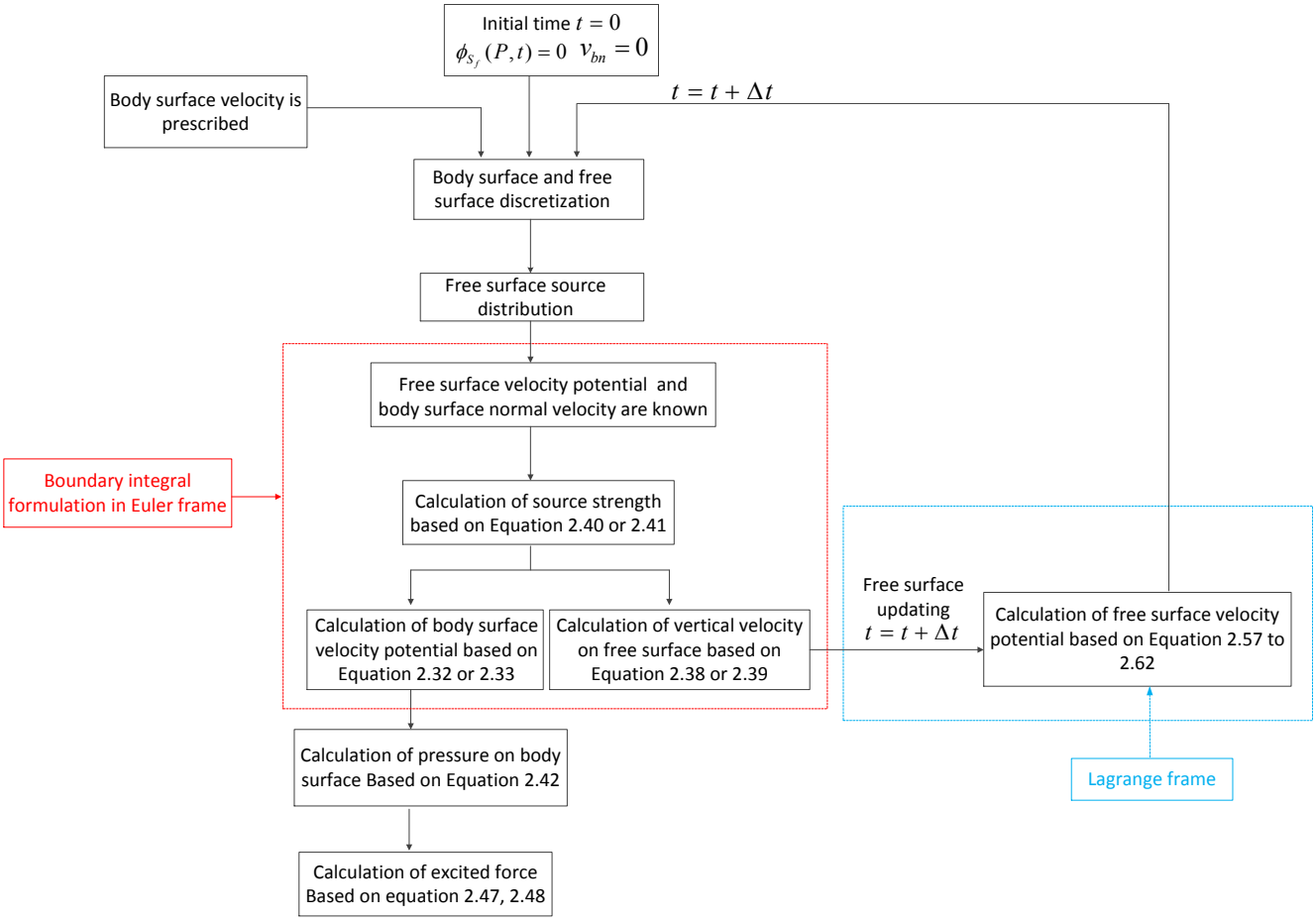

Figure 2.5: General flowchart of formulation and solution techniques for the two-dimensional and three-dimensional problems.

2.5 Chapter summary

This chapter outlined the main theoretical framework of boundary integral model under Eulerian and Lagrangian specifications for two-dimensional and three-dimensional

wave-body problems. The Rankine source method based boundary integral formats are derived from Laplace equation and boundary conditions. High order Adams-Bashforth time-stepping scheme is applied for free surface time marching process.

The next chapter will address numerical techniques applied to solve boundary integral model within the context of Rankine source and mixed Euler-Lagrange algorithm. These numerical techniques mainly include body surface and free surface discretization and regridding, free surface node and source point distribution, induced influence coefficient calculation, intersection points treatment and free surface smoothing.

Chapter 3

Numerical algorithm for two-dimensional wave-body problems

In this chapter, numerical techniques involving two-dimensional wave-body problems are discussed in detail. These numerical methods aim to overcome the difficulties which are introduced by applying the simple Green function and Mixed Euler-Lagrange(MEL) algorithm.

3.1 Discretization of free surface and body surface

Before the application of boundary integral formulation, the continuous fluid domain surface should be discretised into a set of source points on free surface and panels on body surface as shown in Figure 2.5. For linear problem, this step is executed only once but for nonlinear problems it is repeated at every time step to locate the position of source points and control points.

A two-dimensional arbitrary body floating on a free surface with forced oscillatory motion is considered. The continuous calm water surface is replaced by node points in isolation and N_f source points $Q_i(i = 1, ..., N_f)$ with source strength $\sigma_i^f(Q_i, t)(i = 1, ..., N_b)$ are placed vertically above each node point. The body surface S_b is divided evenly into N_b

panels with source points $Q_j(j = 1, ..., N_b)$ of constant strength $\sigma_j^f(Q_j, b)(j = 1, ..., N_b)$ along each panel. Figure 3.1 shows the numerical model sketch for this problem. This discretisation for both free surface S_f and body surface S_b implies that instead of solving Equation 2.40, a free surface time iteration is applied to the following desingularized formulations

$$\phi_{S_f}(P_f, t) = \sum_{i=1}^{N_f} \sigma_i^f(Q_i, t) \ln r_{P_f Q_i} + \sum_{j=1}^{N_b} \sigma_j^b(Q_j, t) \int_{S_{b,j}} \ln r_{P_f Q_j} ds, \tag{3.1a}$$

and

$$\frac{\partial \phi_{S_b}(P_b, t)}{\partial n_b} = \sum_{i=1}^{N_f} \sigma_i^f(Q_i, t) \frac{\partial \ln r_{P_b Q_i}}{\partial n_b} + \sum_{j=1}^{N_b} \sigma_j^b(Q_j, t) \int_{S_{b,j}} \frac{\partial \ln r_{P_b Q_j}}{\partial n_b} ds. \tag{3.1b}$$

Similarly Equations 2.32 and 2.38 can be formulated as:

$$\phi_{S_b}(P_b, t) = \sum_{i=1}^{N_f} \sigma_i^f(Q_i, t) \ln r_{P_b Q_i} + \sum_{j=1}^{N_b} \sigma_j^b(Q_j, t) \int_{S_{b,j}} \ln r_{P_b Q_j} ds, \tag{3.2a}$$

$$\frac{\partial \phi_{S_f}(P_f, t)}{\partial z} = \sum_{i=1}^{N_f} \sigma_i^f(Q_i, t) \frac{\partial \ln r_{P_f Q_i}}{\partial z} + \sum_{j=1}^{N_b} \sigma_j^b(Q_j, t) \int_{S_{b,j}} \frac{\partial \ln r_{P_b Q_j}}{\partial z} ds. \tag{3.2b}$$

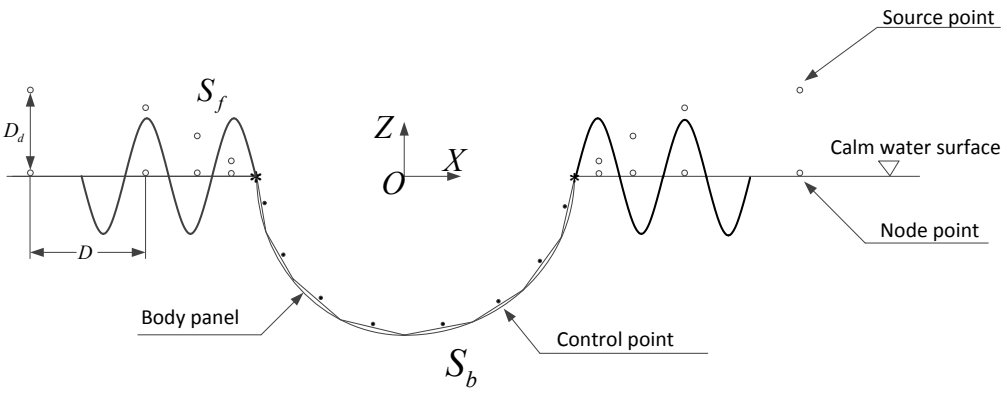

Figure 3.1: Two-dimensional wave-body numerical model schematic.

The desingularized distance D_d is the distance between a node point and correspond-

ing source point on the free surface. There is an optimum desingularization distance and Cao et al. (1991a) determined the desingularized distance D_d as the square root of the local mesh size as:

$$D_d = \sqrt{D} \tag{3.3}$$

where D is the distance between two neighbouring node points. This formulation is applied for two-dimensional numerical simulation in this work.

3.2 Calculation for induced influence coefficient

By replacing $\partial\phi_{S_b}(P_b,t)/\partial n_b$ and $\partial\phi_{S_f}(P_f,t)/\partial z$ with $v_{bn}(P_b,t)$ and $v_{fz}(P_f,t)$ respectively in the left sides of Equation 3.1b and Equation 3.2b, these two equations can be formulated in the following convenience format as:

$$\begin{bmatrix} A_{N_fN_f} & A_{N_fN_b} \\ A_{N_bN_f} & A_{N_bN_b} \end{bmatrix} \begin{bmatrix} \sigma^f \\ \sigma^b \end{bmatrix} = \begin{bmatrix} \phi_{S_f} \\ v_{bn} \end{bmatrix}, \tag{3.4}$$

and

$$\begin{bmatrix} C_{N_fN_f} & C_{N_fN_b} \\ C_{N_bN_f} & C_{N_bN_b} \end{bmatrix} \begin{bmatrix} \sigma^f \\ \sigma^b \end{bmatrix} = \begin{bmatrix} v_{fz} \\ \phi_{S_b} \end{bmatrix}, \tag{3.5}$$

where A_{ij} and C_{ij} are influence coefficients blocks and they require calculations respectively. The coefficients $A_{N_fN_f}$ and $C_{N_fN_f}$ reflect the influence of the free surface source points on free surface node points:

$$A_{N_fN_f} = \mathrm{Re}\{\ln r_{P_fQ_f}\}, \tag{3.6}$$

and

$$C_{N_fN_f} = \mathrm{Re}\{\frac{1}{r_{P_fQ_f}}\mathbf{n}_f\}, \tag{3.7}$$

where $\mathbf{n_f}$ is the unit normal vector on the free surface, while

$A_{N_bN_f}$ and $C_{N_bN_f}$ reflect the influence of free surface source points on the body panels control points:

$$A_{N_bN_f} = \mathrm{Re}\{\frac{1}{r_{P_bQ_f}}\mathbf{n}_b\}, \tag{3.8}$$

and

$$C_{N_b N_f} = \mathrm{Re}\{\ln r_{P_b Q_f}\}. \tag{3.9}$$

$A_{N_f N_b}$ and $C_{N_f N_b}$ reflect the influence of body panel source on free surface source points. Considering an isolated source point $P_f(x_{f,i}, z_{f,i})$ and a single body panel with two end points $Q_{b,j}(x_{b,j}, z_{b,j})$ and $Q_{b,j+1}(x_{b,j+1}, z_{b,j+1})$, this line integral model is shown in Figure 3.2. The length of the body panel $L_{b,j}$ is expressed as:

$$L_{b,j} = |Q_{b,j+1} - Q_{b,j}| = \sqrt{(x_{b,j+1} - x_{b,j})^2 + (z_{b,j+1} - z_{b,j})^2} \tag{3.10}$$

and unit normal vector $\mathbf{n}_{b,j}$ and tangent vector $\mathbf{t}_{b,j}$ of this panel can be formulated as:

$$\mathbf{n}_{b,j} = (-\frac{z_{b,j+1} - z_{b,j}}{L_{b,j}}, \frac{x_{b,j+1} - x_{b,j}}{L_{b,j}}), \tag{3.11}$$

and

$$\mathbf{t}_{b,j} = (\frac{x_{b,j+1} - x_{b,j}}{L_{b,j}}, \frac{z_{b,j+1} - z_{b,j}}{L_{b,j}}). \tag{3.12}$$

Then $\overline{\mathbf{t}}_{\mathbf{b,j}}$ is defined as:

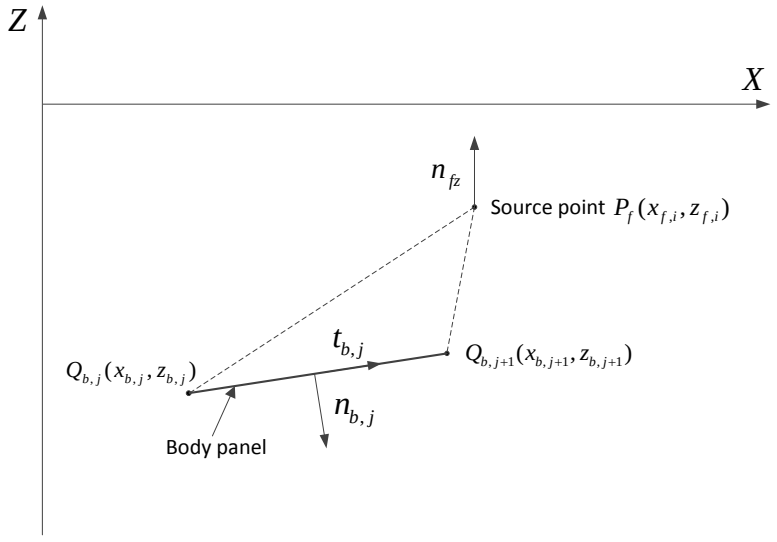

Figure 3.2: Line integral model.

$$\bar{\mathbf{t}}_{\mathbf{b,j}} = (\frac{x_{b,j+1} - x_{b,j}}{L_{b,j}}, -\frac{z_{b,j+1} - z_{b,j}}{L_{b,j}}), \tag{3.13}$$

and the unit normal vector on free surface $\mathbf{n_{fz}}$ is presented as:

$$\mathbf{n_{fz}} = (0, 1). \tag{3.14}$$

These results in the influence coefficients $A_{N_f N_b}$ and $C_{N_f N_b}$ being written as:

$$\begin{aligned}
A_{N_f N_b} &= \int_{S_{b,j}} \ln r_{P_f Q_j} ds \\
&= \mathrm{Re}\{\int_{S_{b,j}} \ln(P_{f,i} - Q_{b,j} - st_{b,j}) ds\} \\
&= \mathrm{Re}\{\ln(P_{f,i} - Q_{b,j} - st_{b,j}) s|_0^{L_{b,j}}\} - \mathrm{Re}\{\int_0^{L_{b,j}} \frac{-st_{b,j}}{P_{f,i} - Q_{b,j} - st_{b.j}} ds\} \\
&= \mathrm{Re}\{L_{b,j} \ln(P_{f,i} - Q_{b,j+1})\} - \mathrm{Re}\{\int_0^{L_{b,j}} (1 - \frac{P_{f,i} - Q_{b,j}}{P_{f,i} - Q_{b,j+1}}) ds\} \\
&= -L_{b,j} + \mathrm{Re}\{(P_{f,i} - Q_{b,j+1}) \bar{\mathbf{t}}_{\mathbf{b,j}} \ln(P_{f,i} - Q_{b,j+1}) + \bar{\mathbf{t}}_{\mathbf{b,j}} (P_{f,i} - Q_{b,j}) ln(P_{f,i} - Q_{b,j})\} \\
&= -L_{b,j} + \mathrm{Re}\{r_{P_{f,i} Q_{b,j+1}} \bar{\mathbf{t}}_{\mathbf{b,j}} \ln r_{P_{f,i} Q_{b,j+1}} + r_{P_{f,i} Q_{b,j}} \bar{\mathbf{t}}_{\mathbf{b,j}} \ln r_{P_{f,i} Q_{b,j}}\}
\end{aligned} \tag{3.15}$$

and

$$\begin{aligned}
C_{N_f N_b} &= \frac{\partial \int_{S_{b,j}} \ln r_{P_f Q_j} \, ds}{\partial z} \\
&= \mathrm{Re}\{\mathbf{n_{fz}} \frac{d \int_{S_{b,j}} \ln |P_{f,i} - Q_{b,j}| ds}{ds}\} \\
&= \mathrm{Re}\{\mathbf{n_{fz}} \int_0^l \frac{ds}{P_{f,i} - Q_{b,j} - st_{b,j}}\} \\
&= \mathrm{Re}\{-\mathbf{n_{fz}} (\bar{\mathbf{t}}_{\mathbf{b,j}}) \ln \frac{P_{f,i} - Q_{b,j+1}}{P_{f,i} - Q_{b,j}}\}.
\end{aligned} \tag{3.16}$$

$A_{N_b N_b}$ and $C_{N_b N_b}$ reflect the influence of body panel source on body control points. The evaluation of $A_{N_b N_b}$ and $C_{N_b N_b}$ follows a procedure similar to $C_{N_f N_b}$ and $A_{N_f N_b}$ respectively.

The computational cost mainly lies in the storage of these coefficients and their solutions via Equations 3.4 and 3.5. This introduces a computational cost of $O(N^{2\sim3})$ (Xue et al., 2001; Yan and Liu, 2011), where $N = N_b + N_f$ is the number of boundary element

and therefore the numerical efficiency depends on the number of body panel N_b and source points N_f. A Gaussian elimination algorithm will be applied as a solver for these linear algebra equation systems.

3.3 Body surface and free surface re-gridding

Due to the application of nonlinear free surface and body boundary conditions, it is necessary to regrid the body surface and free surface in both horizontal and vertical directions during time step.

3.3.1 Wetted body surface re-panellization

Linear wave-body mathematical models are suitable only for small amplitude oscillations as they assume the absence of body surface movement. If the amplitude is not small, the wetted body surface changes significantly over the course of body motion at different time steps and therefore nonlinear effects due to wetted body surface area varying have significant impact on the wave-body response. Considering a vertically oscillating circular cylinder with radius R around free surface, the wetted body surface S_b^t at time t becomes $S_b^{t+\Delta t}$ after one time step Δt. Figure 3.3 presents the wetted body surface varying at different time steps.

For this forced heave motion with prescribed velocity $v_b(t)$ and displacement $s(t)$, the angular position $\theta(t)$ can be expressed as:

$$\theta(t) = \arccos \frac{s(t)}{R} \qquad (0 \leq \theta \leq \pi), \tag{3.17}$$

and starting from the intersection point on the right, the coordinate of the end point $S_b^i(x^i(t), z^i(t))$ for the right part of the body panel can be formulated as:

$$x^i(t) = R \sin(\theta(t)(1 + \frac{2-2i}{N_b})) \qquad (0 \leq \theta \leq \pi), \tag{3.18}$$

and

$$z^i(t) = -R \cos(\theta(t)(1 + \frac{2-2i}{N_b})) - S_d^3(t) \qquad (0 \leq \theta \leq \pi). \tag{3.19}$$

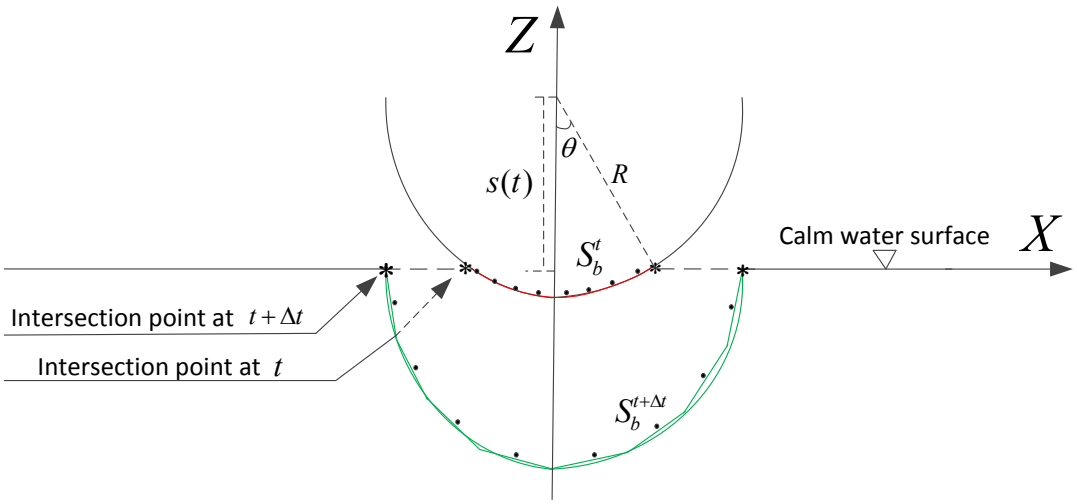

Figure 3.3: Wetted body surface varying at different time steps.

The left part is gridded in a similar manner as right. The body panel sizes are evenly distributed during the body surface regridding process, the body panel number N_b remains constant with the dimension of the influence coefficient matrix also remaining unchanged while each panel size L_b adjusts to accommodate the wetted body surface varying. For three-dimensional wetted body, the regriding principle is same as two-dimensional case and therefore the process is not presented here.

3.3.2 Free surface regridding

In the process of repanelling the free surface panels slide horizontally due to the variation of wetted body surface pushing them back and forth. After their horizontal positions are fixed based on Equation 3.18, the source points follow the wave elevation and are located on the updated wave surface profile in the vertical direction. It should be noted that the wave elevation is tracked in the Lagrange frame. This regridding approach keeps a smooth panel covering of the free surface profile and therefore reduces the numerical

inaccuracy. Meanwhile the smoothness of the intersection panels is guaranteed by the connection of panel sizes. Figure 3.4 illustrates the free surface regridding at different time steps.

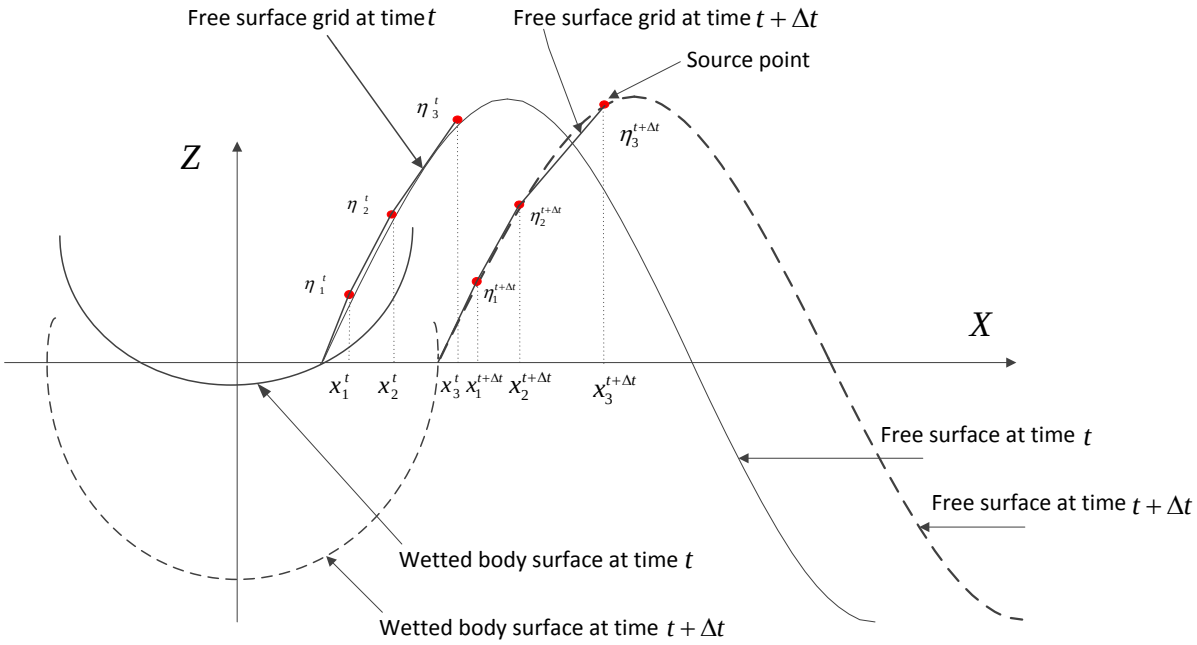

Figure 3.4: Free surface regridding at different time steps.

3.4 Wave-body intersection points

The intersection point defines the intersection between the wetted body surface and free surface. These points move in a horizontal direction within the body-fixed frame $O'-X'Y'Z'$ during body motion because of the absence of shear force applied to the body surface in a potential flow theory. The exact position of intersection points defines the wetted body surface variation. By applying different boundary conditions, these points can be treated as double nodes where both body boundary and free surface boundary are satisfied or single node on which only a single boundary condition is applied. The

double node technique is not stable numerically as different type of boundary conditions (Dirichlet condition for free surface and Neumann condition for body surface) are applied to this confluence point (Yan, 2010).

In conjunction with the proposed isolated source point distribution on the free surface, a single node scheme is applied to treat the weak singularity arising from the intersection points, each of which is regarded as a body end point and only the body boundary condition is satisfied. The first source points are placed away from the intersection points and their positions relate to the size of the top body surface panel, the body motion frequency and are selected depending on the required accuracy of the numerical scheme of study. Figure 3.5 presents this points arrangement for the wave-body intersection.

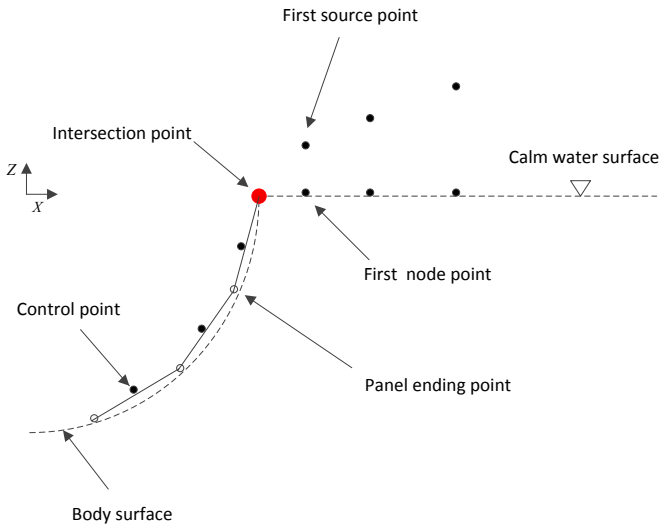

Figure 3.5: Points arrangement for wave-body intersection.

3.5 Instability and smoothing

In the present numerical simulations, sawtooth phenomenon is observed for the fully nonlinear wave-body problem. The source point moves with the updated free surface profile at every time step. The sawtooth instability occurs first at source points near the wave-body intersection, disturbing the wave profile seriously, leading to the numerical simulation failing quickly at next time step.

3.5.1 Model function

A least squares principle based smoothing method is newly developed in this work. This technique is widely used for curve fitting in numerical computation and it aims to minimise the sum of squared residuals between pre-smoothed values and model function (post-smoothed) values (Bevington and Robinson, 1992). Linear, quadratic, exponential and trigonometric functions are examined as model functions to check their effectiveness. Table 3.1 shows these functions $f(x)$ for different model types.

Table 3.1: Model functions $f(x)$.

Type	Linear	Quadratic	Trigonometric	Exponential
$f(x)$	$\alpha_0 x + \beta_0$	$\alpha_0 x^2 + \beta_0 x + \gamma_0$	$\alpha_0 \sin\lambda x + \beta_0 \sin 2\lambda x + \gamma_0 \sin 3\lambda x$	$\alpha_0 e^{-\lambda x} + \beta_0 e^{-2\lambda x} + \gamma_0 e^{-3\lambda x}$

Here the unknown coefficients (α_0, β_0 and γ_0) should satisfy a local minimum point for least square optimal principle. For every model function, two, three and five points methods are applied for the linear model function while three and five points are tested for the other model functions. The three point points quadratic method was most efficient to smooth the wave curve and can effectively eliminate numerical divergency. Therefore this model function is used for fully nonlinear numerical simulations.

3.5.2 Least square optimisation

Given $x_i = x_i^f$ and $y_i = \eta(x_i(t), t)$ for $i = 1, 2, 3$, the least square optimal problem for a quadratic function can be formulated as:

$$\sum_{i=1}^{3} |y_i - f(x_i)|^2 = \min_{|(\alpha,\beta,\gamma)-(\alpha_0,\beta_0,\gamma_0)|\leq\epsilon} \sum_{i=1}^{3} |y_i - (\alpha x^2 + \beta x + \gamma)|^2 \tag{3.20}$$

for a small constant $\epsilon > 0$. Therefore, zero gradient of the quadratic function can be expressed as:

$$\prod(\alpha, \beta, \gamma) = \sum_{i=1}^{3} |y_i - (\alpha x^2 + \beta x + \gamma)|^2 \tag{3.21}$$

with respect to the variable (α, β, γ) at the point $(\alpha, \beta, \gamma) = (\alpha_0, \beta_0, \gamma_0)$. That is,

$$\left.\frac{\partial \prod}{\partial \gamma}\right|_{(\alpha,\beta,\gamma)=(\alpha_0,\beta_0,\gamma_0)} = -2\sum_{i=1}^{3}[y_i - (\alpha_0 x^2 + \beta_0 x + \gamma_0)] = 0, \tag{3.22a}$$

$$\left.\frac{\partial \prod}{\partial \beta}\right|_{(\alpha,\beta,\gamma)=(\alpha_0,\beta_0,\gamma_0)} = -2\sum_{i=1}^{3} x_i[y_i - (\alpha_0 x^2 + \beta_0 x + \gamma_0)] = 0, \tag{3.22b}$$

$$\left.\frac{\partial \prod}{\partial \alpha}\right|_{(\alpha,\beta,\gamma)=(\alpha_0,\beta_0,\gamma_0)} = -2\sum_{i=1}^{3} x_i^2[y_i - (\alpha_0 x^2 + \beta_0 x + \gamma_0)] = 0. \tag{3.22c}$$

Hence coefficients α_0, β_0 and γ_0 are determined by solving the previous set of equations. The new wave elevation at the three points, therefore, can be evaluated by

$$\eta'(x_i(t), t) = f(x_i) = \alpha_0 x^2 + \beta_0 x + \gamma_0, \;\; i = 1, 2, 3. \tag{3.23}$$

For convenience of notation, the superscript primes of $\eta'(x_i(t), t)$ are omitted and the smoothed rather than the original wave elevation and node points are employed in the following sections.

The sawtooth instability might occur again for subsequent points after they are suppressed nearby the intersection. Correspondingly, this smoothing technique is applied subsequently until all the disturbed points smoothed from the source points close to floating body outwards to those in a far field.

3.6 Numerical process

In this work all the numerical simulation is executed using Fortran 90 source code. The numerical process described here is generally for both two-dimensional and three-dimensional problems as they have the same process. Before the start of time-stepping simulation, the number of body panel is selected by considering a body moving with a constant translational velocity in unbounded fluid domain. The numerical simulation starts from an initial time $t = 0$ when the body is located at equilibrium position and free surface coincides with the calm water surface. The body surface and free surface are discretised first and then free surface source points are distributed based on the proposed space ever increasing source distribution method. Influence coefficient matrices are then evaluated according to the position of source point and control point in the last two steps.

The boundary integral formulation will be applied as the main part of the numerical process. The detailed formulation and process are described in Section 2.2.4 and 2.4.3. After the wave elevation is obtained by free surface updating, the free surface regridding and smoothing techniques will be applied to relocate the position of source points on the free surface. As for the body surface, the position of control points can be decided by re-panellization. Once the new position of source point and control point is known at this time step, the simulation can move forward in the same way as previous time step and repeat again until the end of the numerical simulation.

In order to show a complete numerical process, a flowchart is presented in Figure 3.6. However free surface regridding and smoothing techniques are not involved for linear problem and nonlinear body boundary condition problem. Specific flowcharts for different problems will be delivered in corresponding chapters

3.7 Nondimensionalization

The fundamental variables, ρ, g, ω, a together with floating body sectional area A, breadth B and draught T are applied to nondimensionalize other variables. The heave/sway added mass coefficients a_{22}/a_{33} and damping coefficients b_{22}/b_{33} are nondimensional coefficients of heave/sway added mass A_{22}/A_{33} and damping B_{22}/B_{33} respec-

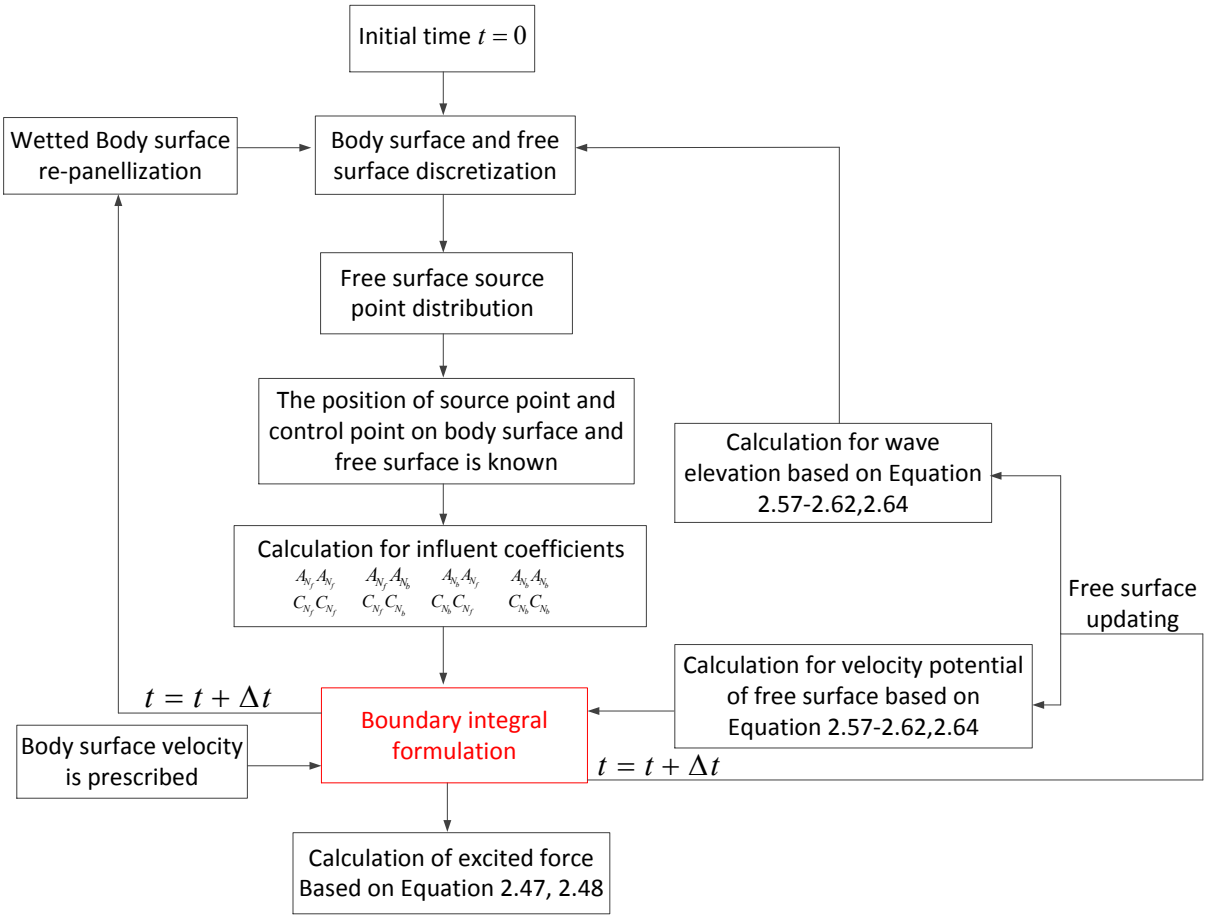

Figure 3.6: Flowchart of numerical process.

tively, therefore for two-dimensional problem:

$$a_{22} = \frac{A_{22}}{\rho A}, \qquad a_{33} = \frac{A_{33}}{\rho A}, \tag{3.24}$$

$$b_{22} = \frac{B_{22}}{\rho A(B/2g)^{1/2}}, \qquad b_{33} = \frac{B_{33}}{\rho A(B/2g)^{1/2}}. \tag{3.25}$$

Second order mean force $F^0(\omega)$, first, second and third order harmonic forces ($F^1(\omega)$, $F^2(\omega), F^3(\omega)$) for two-dimensional problem are nondimensionalized as:

$$F^0(\omega) = \frac{|f^0(0)|}{2\rho g a^2}, \tag{3.26}$$

$$F^1(\omega) = \frac{|f^1(\omega)|}{2\rho g T a}, \tag{3.27}$$

$$F^2(\omega) = \frac{|f^2(2\omega)|}{2\rho g a^2}, \tag{3.28}$$

$$F^3(\omega) = \frac{|f^3(3\omega)|}{2\rho g T^2}, \tag{3.29}$$

where $|f^i(n\omega)|(i = 0, 1, 2, 3)$ is the amplitude of the Fourier component of the force $F_b(t)$ calculated from Equation 2.12. From Fourier Transform view, the time record force $F_b(t)$ can decompose into Fourier Series as:

$$F_b(t) = \sum_{n=0}^{\infty} f^i(n\omega) e^{-in\omega t}. \tag{3.30}$$

By Fourier transform, the first four Fourier components can be obtained as:

$$f^0(0) = \frac{1}{2T_0} \int_0^{2T_0} F_b(t) dt, \tag{3.31}$$

$$f^1(\omega) = \frac{1}{2T_0} \int_0^{2T_0} F_b(t) e^{-i\omega t} dt, \tag{3.32}$$

$$f^2(2\omega) = \frac{1}{2T_0} \int_0^{2T_0} F_b(t) e^{-2i\omega t} dt. \tag{3.33}$$

$$f^3(3\omega) = \frac{1}{2T_0} \int_0^{2T_0} F_b(t) e^{-3i\omega t} dt. \tag{3.34}$$

The time record for the inertia component force $F^1(t)$ and quadratic component force $F^2(t)$ are nondimensionlized similarly using:

$$F^1(t) = \frac{f^1(t)}{\rho g B a}, \tag{3.35}$$

$$F^2(t) = \frac{f^2(t)}{\rho g B a}. \tag{3.36}$$

For completeness the nondimensional form for three-dimensional variables are presented here. In this case the length scale used is the floating body radius R. The added mass and damping coefficients a_{33} and b_{33} are in the format of:

$$a_{33} = \frac{A_{33}}{(2/3)\pi\rho R^3}, \tag{3.37}$$

$$b_{33} = \frac{B_{33}}{(2/3)\pi\rho\omega R^3}. \tag{3.38}$$

The nondimensionalized first and second order harmonic forces $F^1(\omega)$ and $F^2(\omega)$ are respectively expressed as:

$$F^1(\omega) = \frac{|f^1(\omega)|}{\rho g \pi R^2 a}, \tag{3.39}$$

$$F^2(\omega) = \frac{|f^2(2\omega)|}{\rho g \pi R a^2}. \tag{3.40}$$

The time record for the inertia component force $F^1(t)$ and quadratic component force $F^2(t)$ are made nondimensional in a same manner as:

$$F^1(t) = \frac{f^1(t)}{\rho g \pi R^2 a}, \tag{3.41}$$

$$F^2(t) = \frac{f^2(t)}{\rho g \pi R^2 a}. \tag{3.42}$$

3.8 Chapter summary

This chapter concludes the numerical techniques for two-dimensional wave-body problem using Rankine source and MEL method. Numerical algorithms include body surface and free surface discretisation at initial time and regridding in the following time iteration process, and resulted influent coefficient calculation. In addition numerical techniques newly developed to cope with intersection points and numerical divergency is also

elaborated. Process for the numerical simulation is mainly described by a flowchart and nondimensionalization for different variables is present in the last part of this chapter. The remainder of this thesis is dedicated to reporting results and presenting the future work.

Chapter 4

Two-dimensional linear numerical simulation for forced body oscillation motion

In this chapter, two-dimensional forced body motions with small harmonic oscillatory motion amplitudes are numerically solved to demonstrate the accuracy and efficiency of the proposed methods. As only a linear problem is under consideration, the mixed Euler-Lagrange algorithm is not involved in this simulation.

The forced body starts from an initial displacement from the equilibrium position and the wetted body surface remains constant during the body oscillation process under the linear assumption. Physically the free surface wave, excited by this forced body motion, starts from the first node point in the inner domain and travels outwards to the far field domain along a calm water surface level. Due to the assumed small variation of free surface profile for this linear problem, the free surface boundary conditions are satisfied on the calm water surface in this case.

The flowchart for this linear problem is presented in Figure 4.1. Body surface panel number is selected as the preparation for the start of boundary integral formulation. This process is demonstrated in Section 4.1 in detail. Once the position of source points and control points is allocated by discretization. They will stay at the same position during the whole numerical simulation and influent coefficients are calculated only once and applied at every time step.

Figure 4.1: Flowchart of numerical process for two-dimensional linear problem.

This chapter examines body surface panels number selection for a circular cylinder and the optimised values are applied through the numerical simulation for two-dimensional

problems in this chapter and the following two chapters. In Section 4.2, the hydrodynamic coefficients of added mass and damping coefficients are produced from the present simulation for a circular cylinder, a box and a wedge. These computed results are compared with Vugts (1968) experimental data and numerical prediction of Zhang (2007), who based his calculation on even source points distribution. An error analysis is presented in Section 4.3 to explain possible error sources for discrepancy in the comparison. Concluding remarks are provided in Section 4.4.

4.1 Selection of body surface panel number

Circular sections widely exist in the marine industry. The columns of semi-submersible and main body of spar platforms are both circular sections. In academic study for wave-body problem, circular cylinder is widely adopted as numerical model due to its simple, smooth and symmetrical shape.

For forced body motion problem, the fluid flow motion is caused by the body kinematic energy across the wetted body surface. In numerical simulation, the body surface is discretised into a set of panels. Numerical simulation with more panel numbers gives better numerical results, but requires higher computational effort. In the following examination the numerical accuracy and computational effort will be considered and the best compromise identified.

A circular cylinder with radius R moving in an unbounded fluid domain is examined. The analytical form of velocity potential ϕ_a around the cylinder surface is given by Lamb (1993) as:

$$\phi_a = -UR\sin\psi, \tag{4.1}$$

where U is the translational velocity of the cylinder and ψ is angular variation starting from the positive x-axis. Let $U = 1m/s$, $R = 1m$. The circular cylinder panel number N_b is selected to be 10, 20, 30, 40, 50 and 60 respectively. An error coefficient C_e is introduced to exam the agreement between ϕ_a and the numerical solution ϕ_n for different values of the panel number N_b. This coefficient C_e is defined as:

$$C_e = \sqrt{\sum_{i=1}^{N_b} \frac{(\phi_n(i) - \phi_a(i))^2}{\phi_a(i)^2}} \tag{4.2}$$

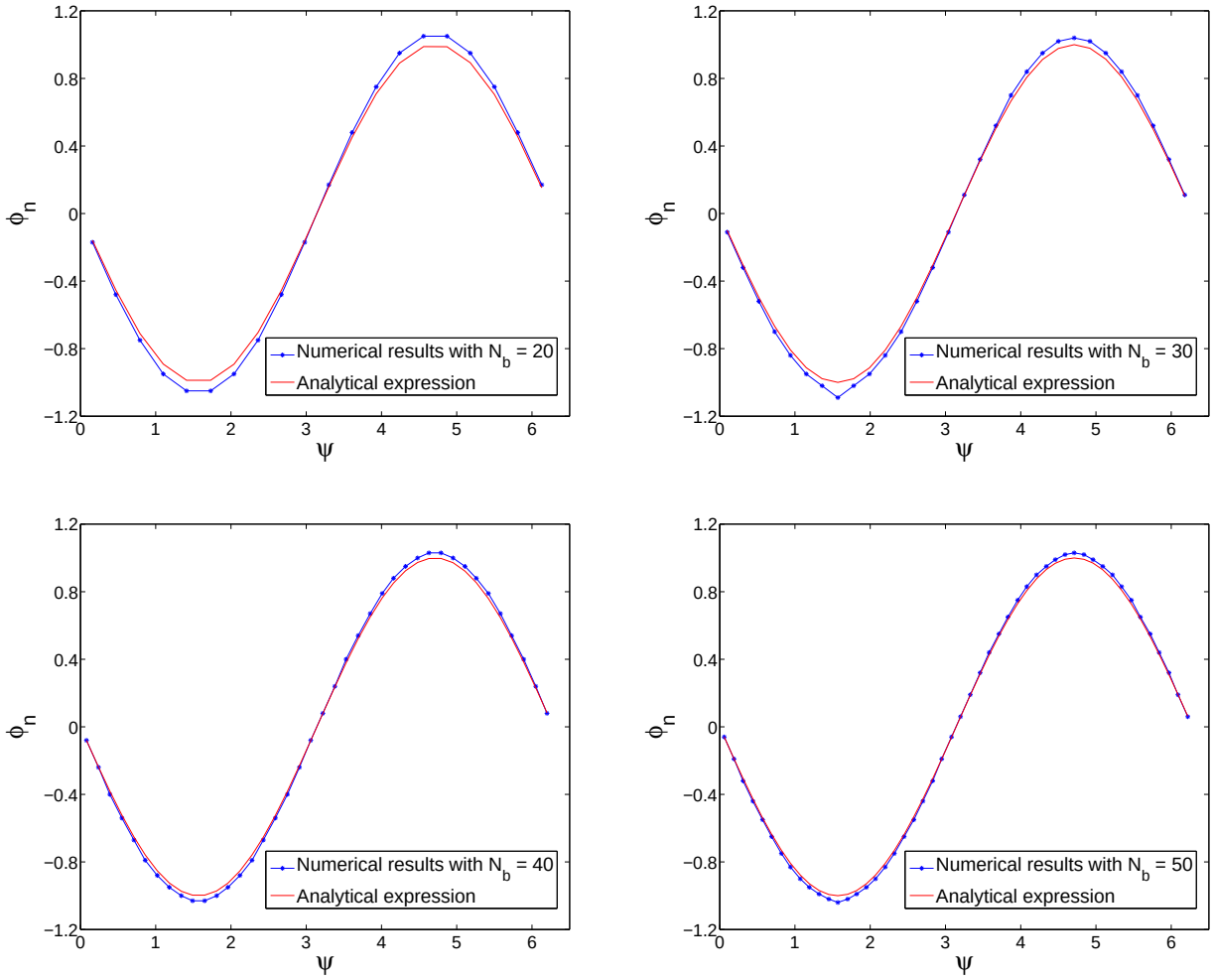

Figure 4.2: Comparisons of analytical solution (4.1) and numerical results for different panel numbers N_b.

The comparisons of numerical results with different body panels N_b and the analytical solution are presented in Figure 4.2 with the error coefficient C_e is shown in Figure 4.3. As the computational cost is proportional to the N_b^2, N_b is replaced by N_b^2 in Figure 4.3. Both Figures 4.2 and 4.3 show that the numerical predictions keep improving with N_b increasing in value. When $N_b = 40(N_b^2 = 1600)$, the agreement is excellent and C_e is below an error of 3.5% compared to the analytical solution. As shown in Figure 4.3, small improvements need much more computational effort.

The numerical prediction shows favourable agreement with the analytical expression by using an even panel discretisation on the body surface. With panel number $N_b = 40$

around the whole circular cylinder, very small numerical error is introduced for body moving in an unbounded fluid domain problem. For this reason, $N_b = 40$ is selected through out this study. In the following wave-body simulation with different numerical models of body shapes: circular cylinder, box and wedge, all the wetted body surfaces are divided evenly into 40 panels without extra investigations. This is reasonable because the whole circular has the largest perimeter compared to other shapes with same characteristics length R.

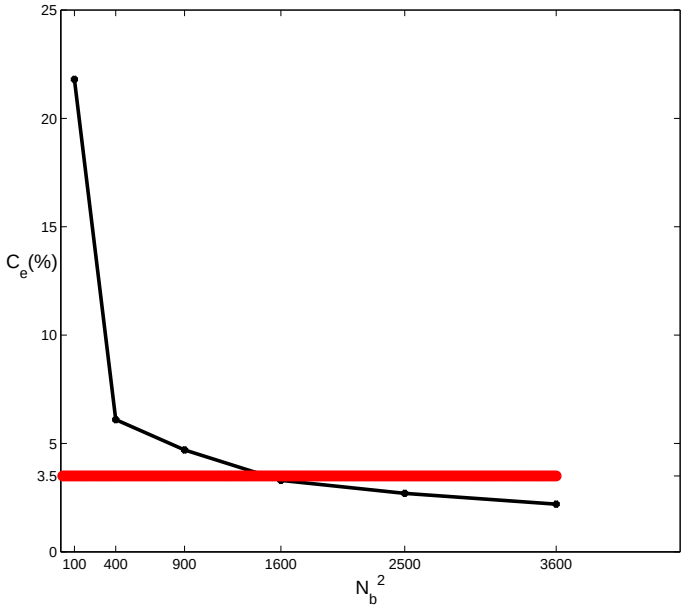

Figure 4.3: The variation of error coefficient C_e with different panel numbers N_b(or N_b^2).

4.2 Numerical simulation for forced body oscillation motion

A forced circular cylinder with small harmonic body motion around free surface is a typical example to investigate fundamental principle of wave-body problem under potential flow frame. Physically added mass and damping are caused by the hydrodynamic reaction as a result of the cylinder motion with respect to the fluid flow. Added mass is

an in-phase part while damping is out-of phase component of the reactive force during an oscillation body motion (Newman, 1977). This pair of coefficients are frequency-based and can be obtained by Fourier transform from the time record of force excited on floating body surface.

Vugts (1968) carried out an exhaustive experimental study on the hydrodynamic coefficients of various cylindrical sections harmonically oscillated around free surface and reported very little scatter. His results offer validation and verification of numerical accuracy for the proposed method in this work.

4.2.1 Free surface source points distribution

As described in Chapter 4, a new source point distribution scheme is proposed for this linear wave-body problem. The free surface distribution is divided into inner and outer domains. Starting from the intersection point $P_{f,0}$, 50 source points are distributed on the right hand side of free surface S_f in the form of:

$$|P_{f,i} - P_{f,i-1}| = \frac{L_b \alpha_j}{\omega^2} \qquad i = 1, 2, ..., N_{in}, \tag{4.3}$$

where α_j are separation factors which decide the separation distances between two neighbouring source points. The inner domain is divided into $11(j = 1, ..., 11)$ regions with a single point in the first region and multi source points in the other regions. Extensive numerical simulations were performed for various values of α_j to derive their most suitable values. Selected results are displayed in Table 4.1.

Table 4.1: The values of separation factors α_j in the inner domain for linear problem.

i	1	2-5	6-8	9-10	11-12	13-14	15-16	17-18	19-20	21-50
j	1	2	3	4	5	6	7	8	9	10
α_j	0.4	1.3	1.6	3.9	5.1	6.4	7.6	10.2	12.7	15.3

Another 20 points in outer domain are distributed in the exponential form as :

$$|P_{f,i} - P_{f,i-1}| = |P_{f,N_{in}} - P_{f,N_{in-1}}| \times 1.05^{\frac{i(i-1)}{2}}, \qquad i = 1, 2, ..., 20. \tag{4.4}$$

The desingularized source point Q_i is placed vertically above the node point $P_{f,i}$. The desingularized distance $D_{d,i}$ between them is given by the recommended equation (Cao, 1991):

$$D_{d,i} = |Q_i - P_{f,i}| = \sqrt{|P_{f,i-1} - P_{f,i}|} \tag{4.5}$$

The wave-body problem is treated symmetrical for the assumed oscillatory body movement and the left hand side source points are arranged in a mirror image manner. This proposed distribution method in the inner domain connects the body panel size with source arrangement and gives a special treatment for the first source point as this point is critical for the numerical convergence and accuracy. Apart from body panel size, this distribution method also connects the source separations with generated wave frequencies and therefore wavelengths, so it is suitable for deep-water waves of any wave length. This distribution scheme can produce surface waves covering nearly five wave lengths in the inner domain and over 100 wavelengths in the outer range, so wave reflection is largely delayed and desired results can be obtained before wave reflection. The distances between source points present a nearly linear increment which is fundamentally different from the constant distance in the even distribution method.

4.2.2 Numerical results for forced body oscillation motion

In numerical tests, the floating body is respectively selected to be a circular cylinder with a radius (R) to draught (T) ratio $R/T = 1.0$, a box with the beam (B) to draught (T) ratio $B/T = 2.0$, and a 30 degree wedge.

The body oscillatory amplitude a is 10% of the draught T for all cases. The gravity equals buoyancy at initial place. The floating body is disturbed by a vertical upward velocity for heave motion and horizontal velocity for sway motion. The produced added mass and damping coefficients are compared with the experimental data (Vugts, 1968) and numerical prediction based on even Rankine source method (Zhang, 2007).

Figures 4.4-4.15 show that results produced from current proposed method are in good agreement with experimental data and the other numerical results prediction.

Furthermore, the local response is examined for the floating circular cylinder with the radius $R = 10m$. Figure 4.16 presents the predicted pressure P_b distributed around the

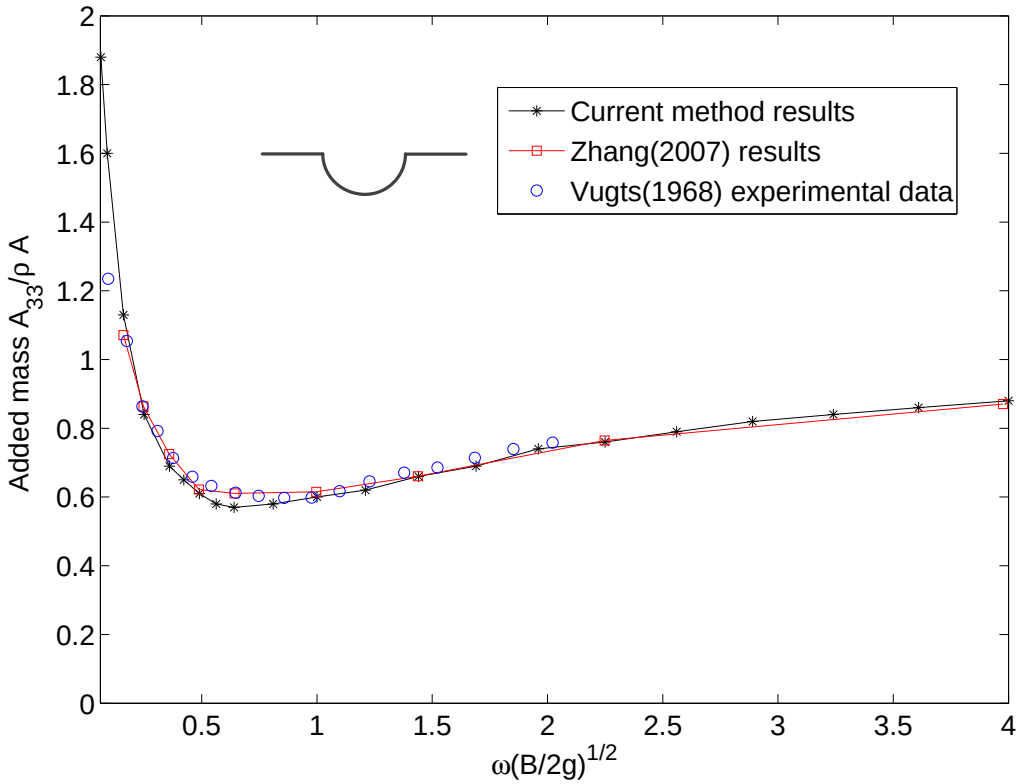

Figure 4.4: Comparison of heave added mass coefficient A_{33} between Zhang (2007) numerical results, Vugts (1968) experimental data and current method prediction for a circular cylinder in oscillatory heave motion with amplitude $a = 0.1T$.

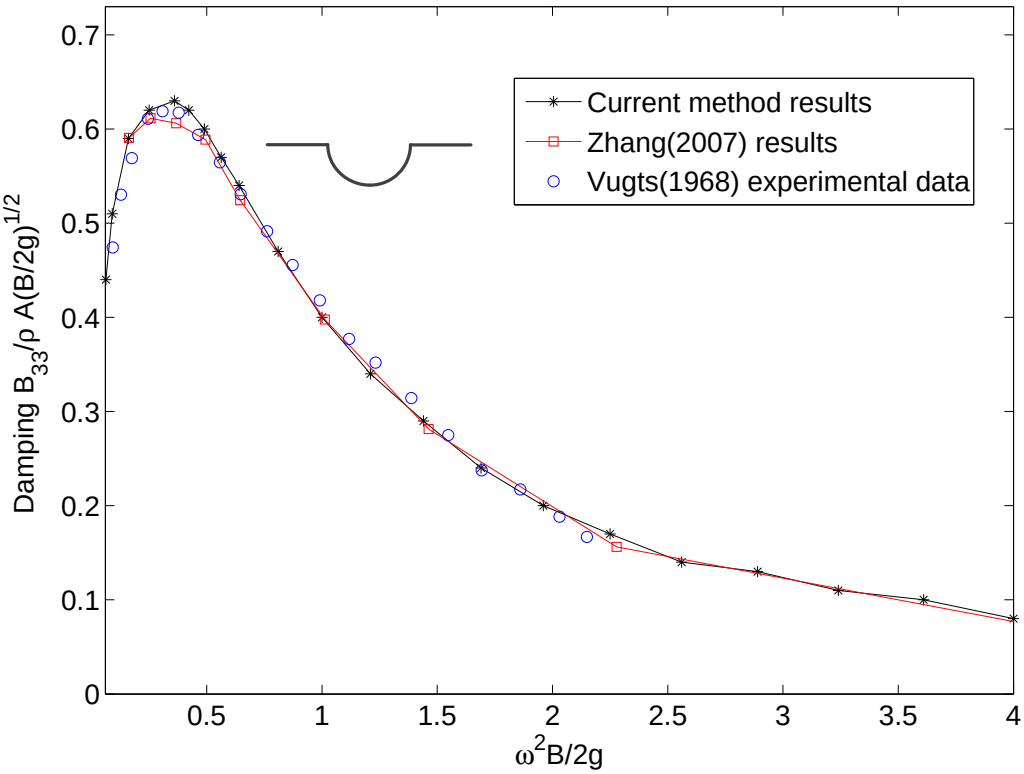

Figure 4.5: Comparison of heave damping coefficient B_{33} between Zhang (2007) numerical results, Vugts (1968) experimental data and current method prediction for a circular cylinder in oscillatory heave motion with amplitude $a = 0.1T$.

cylinder at times $t = 10$, $t = 11$ and $t = 12$ when oscillatory frequency $\omega(B/2g)^{1/2} = 1.0$. The pressure is symmetrical around the body and smoothly varies between the two intersection points. This indicates good efficiency of the intersection points treatment in the present investigation.

Figures 4.17 and 4.18 show the time records for vertical force response $F(t)$ and wave elevation $\eta(t)$ of this circular cylinder in oscillatory heave motion with amplitude $a = 0.1T$ and frequency $\omega^2 R/g = 1.0$, $\Delta t = T_o/60$. The numerical results converge quickly after the simulation starts and no reflection disturbances are evident after 10 periods of simulation. The new source distribution method not only successfully keeps the accuracy of numerical method but also efficiently delays wave reflection.

The proposed space increment source distribution scheme coupled with a single point intersection treatment for the indicated two-dimensional linear oscillatory motion problem

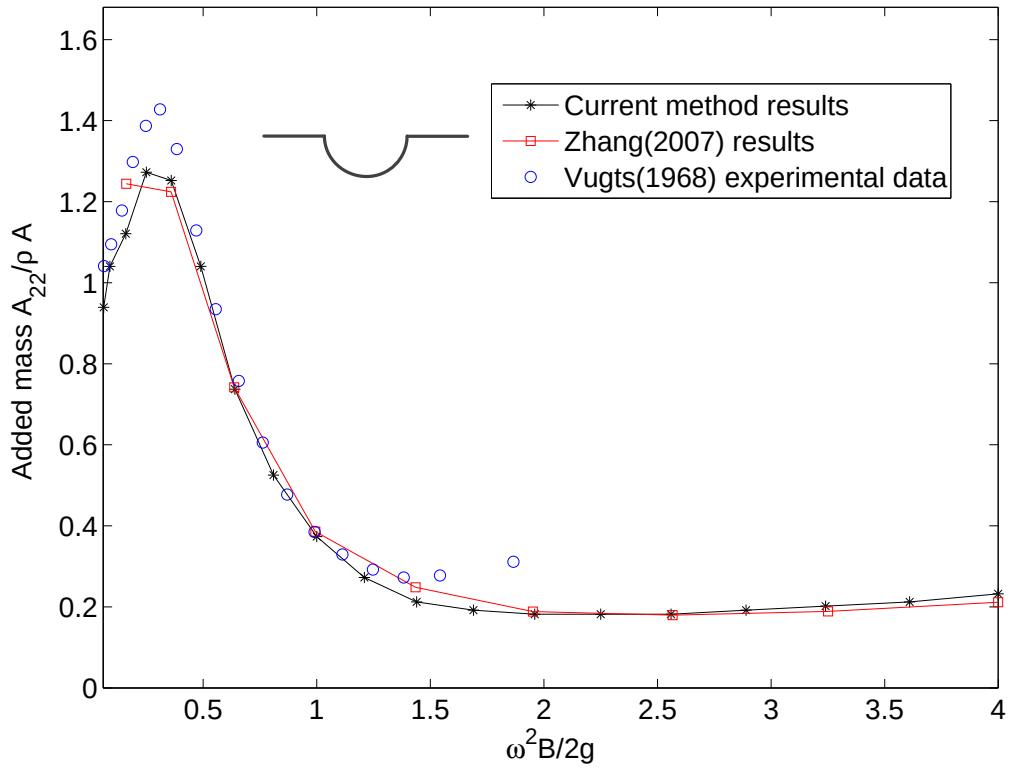

Figure 4.6: Comparison of sway added mass coefficient A_{22} between Zhang (2007) numerical results, Vugts (1968) experimental data and current method prediction for a circular cylinder in oscillatory sway motion with amplitude $a = 0.1T$.

is numerically investigated and the accuracy and efficiency are validated by comparing with available experimental data and numerical results.

160 source points are required to cover the free surface which is a significant reduction compared to the 280 points in traditional method. The computational cost mainly lies in the storage and solution for the $N(N = N_F + N_B) \times N$ influence matrix and computational cost is $O(N^{2\sim3})$, therefore the proposed method can significantly reduce computational memory and time. For this reason computational efficiency is largely improved.

4.2.3 Source strength decaying

The continues free surface is replaced by isolated source points. From the intersection point outwards, the importance of the source points decreases as the distance increases.

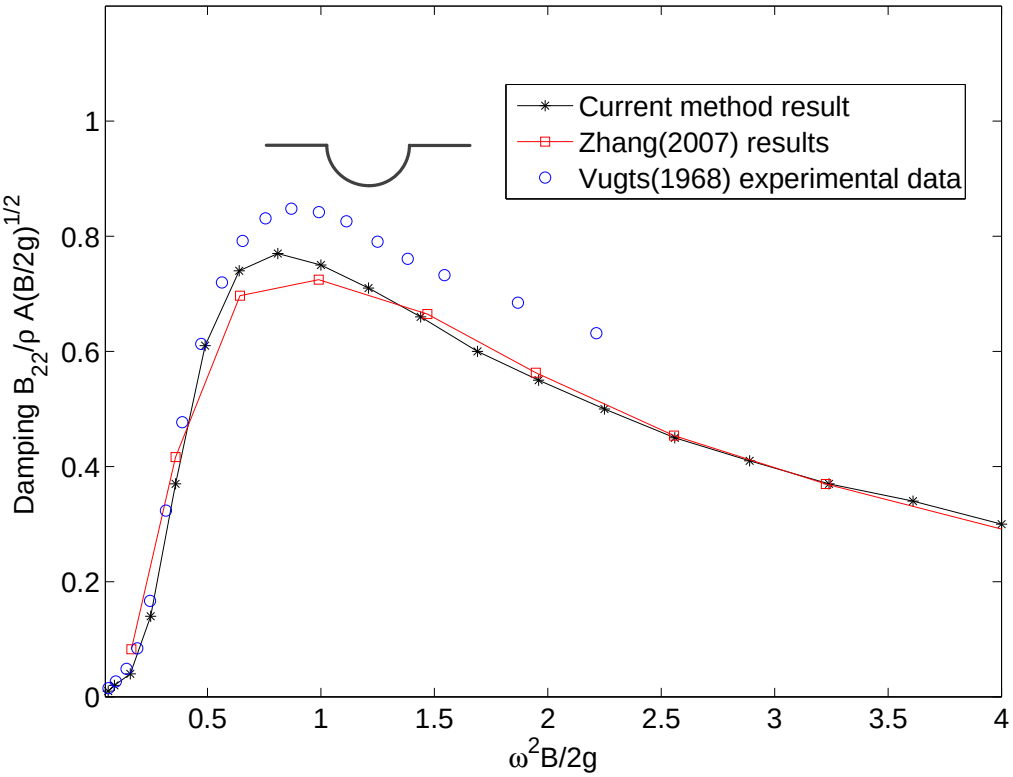

Figure 4.7: Comparison of sway damping coefficient B_{22} between Zhang (2007) numerical results, Vugts (1968) experimental data and current method prediction for a circular cylinder in oscillatory sway motion with amplitude $a = 0.1T$.

Figures 4.19 and 4.20 present the source strength σ_f of the first 20 source points for the circular cylinder in oscillatory heave and sway motions with amplitude $a = 0.1T$ and frequency $\omega^2 R/g = 1.0$. The first source point bears a relatively large value and source strengths decay quickly from the first source point and trends to zero around 20th point. Therefore their importance rapidly decreases as their position is located further from the intersection point. The proposed space increment method conforms with the source strength characteristics. Therefore it is superior to the even distribution pattern.

4.3 Error analysis

Vugts (1968) experimental data offers a validation for the hydrodynamic coefficients of two-dimensional forced body oscillation. The produced results from proposed method

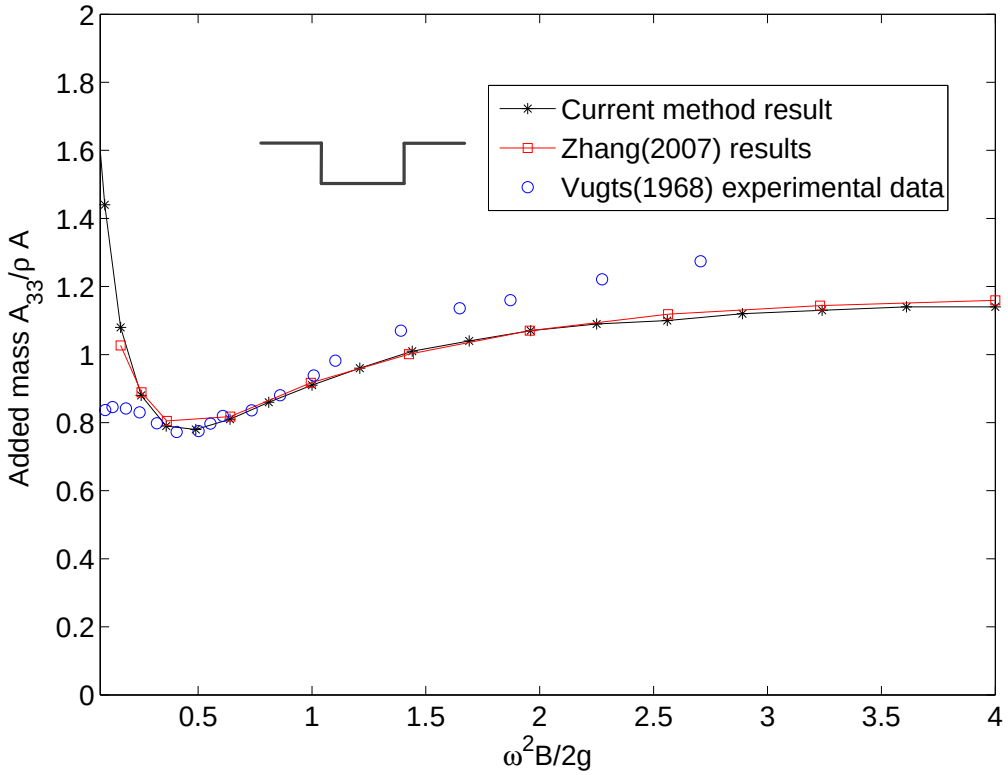

Figure 4.8: Comparison of heave added mass coefficient A_{33} between Zhang (2007) numerical results, Vugts (1968) experimental data and current method prediction for a box in oscillatory heave motion with amplitude $a = 0.1T$.

present good agreement with Vugts experimental data and numerical prediction of Zhang (2007), although discrepancy is observed at some frequency ranges.

The agreement for added mass coefficient A_{33} and damping coefficient B_{33} are excellent for circular cylinder except at very low frequency where a distinct discrepancy occurs for added mass A_{33}. The present prediction overestimates the A_{33} at low frequency range ($\omega^2 B/2g < 0.2$). The discrepancies are bigger for box and wedge than circular as they are not smooth shapes. Vugts (1968) also observed this behaviour arose from two main error sources:

- Force and moment sensors inaccuracy: at low frequencies of oscillation the measured forces and moments are low and a small absolute error in the measure causes large deviations in the coefficients in this range,

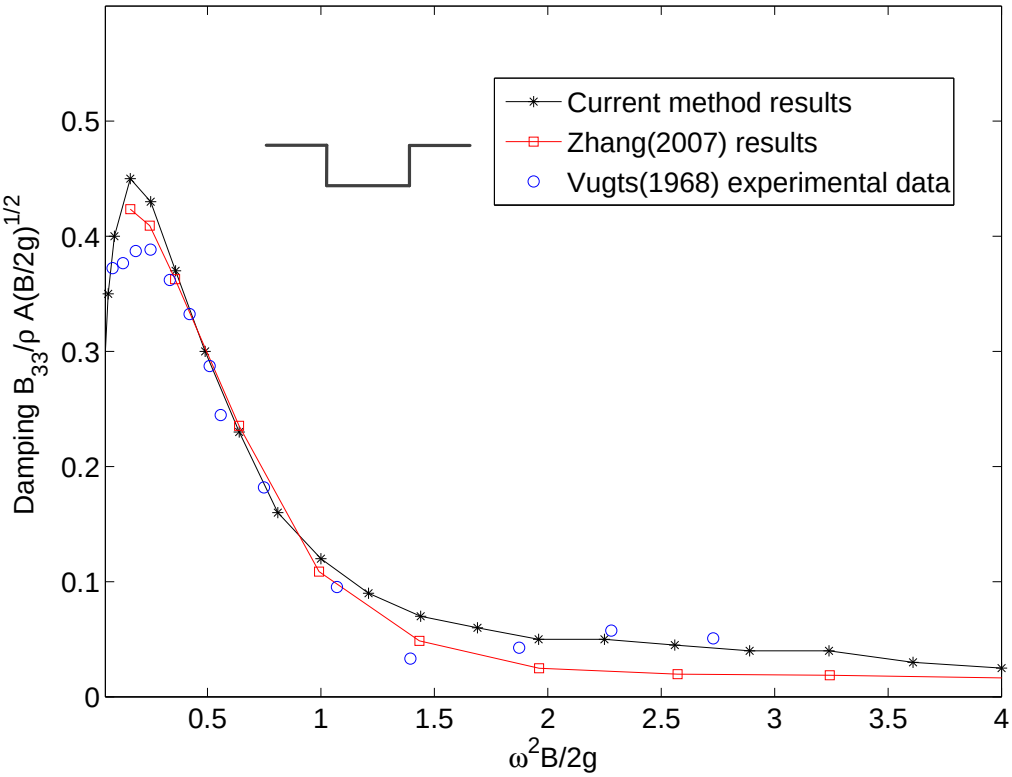

Figure 4.9: Comparison of heave damping coefficient B_{33} between Zhang (2007) numerical results, Vugts (1968) experimental data and current method prediction for a box in oscillatory heave motion with amplitude $a = 0.1T$.

- Wave tank dimension limitation: due to the size of wave tank, generated waves with long wavelengths will reflect and disturb the measured force signal.

At high frequency, the experimental values are higher than the numerical prediction for box and wedge. Vugts attributes these deviations to experiment setup:

- Lack of structural stiffness: the lack of structural stiffness for the experimental instrument can disturb the measurements at high frequencies when high demands are imposed on the rig.

For oscillatory sway motion, the hydrodynamic coefficients obtained from current proposed conform to the experimental data better than those produced from the traditional method. Little discrepancy is observed in the low frequency range except at peak range

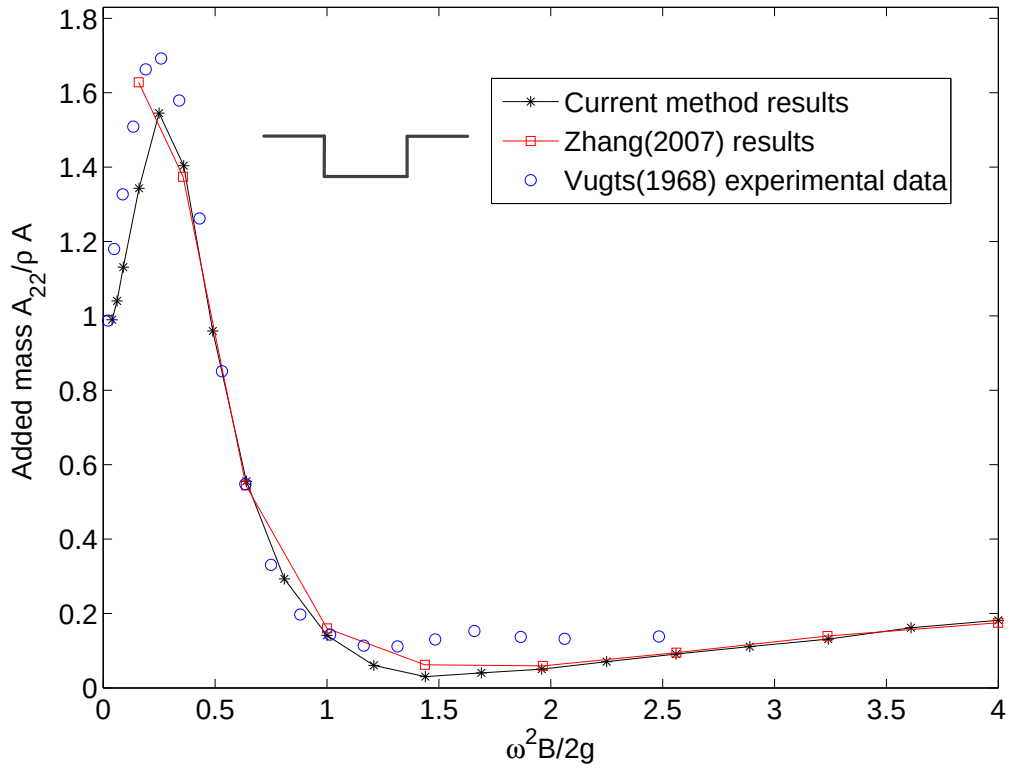

Figure 4.10: Comparison of sway added mass coefficient A_{22} between Zhang (2007) numerical results, Vugts (1968) experimental data and current method prediction for a box in oscillatory sway motion with amplitude $a = 0.1T$.

($\omega^2 B/2g = 0.25$) for added mass A_{22}. Vugts contributes such errors to lack of structural stiffness within the instrument and a slight disturbances can cause a large discrepancy in this range. These reasons also cause deviation at high frequency for both added mass coefficient A_{22} and damping coefficient B_{22}.

Generally larger discrepancy is observed for wedge than circular cylinder and box. This is mainly due to the viscous flow separation and vortex shedding affecting the loads on wedge surface (Yeung and Anathakrishnan, 1992; Sun, 2007). Vugts (1968) admitted that it is impossible to analyse the separate sources of possible errors and to estimate their magnitude. These error sources added together may magnify the total errors and cause a relatively large discrepancy with numerical results. Apart from some systemic discrepancy with experimental data, the current predicted results show a reasonable agreement with both experimental and other numerical results. These validate the accuracy of pro-

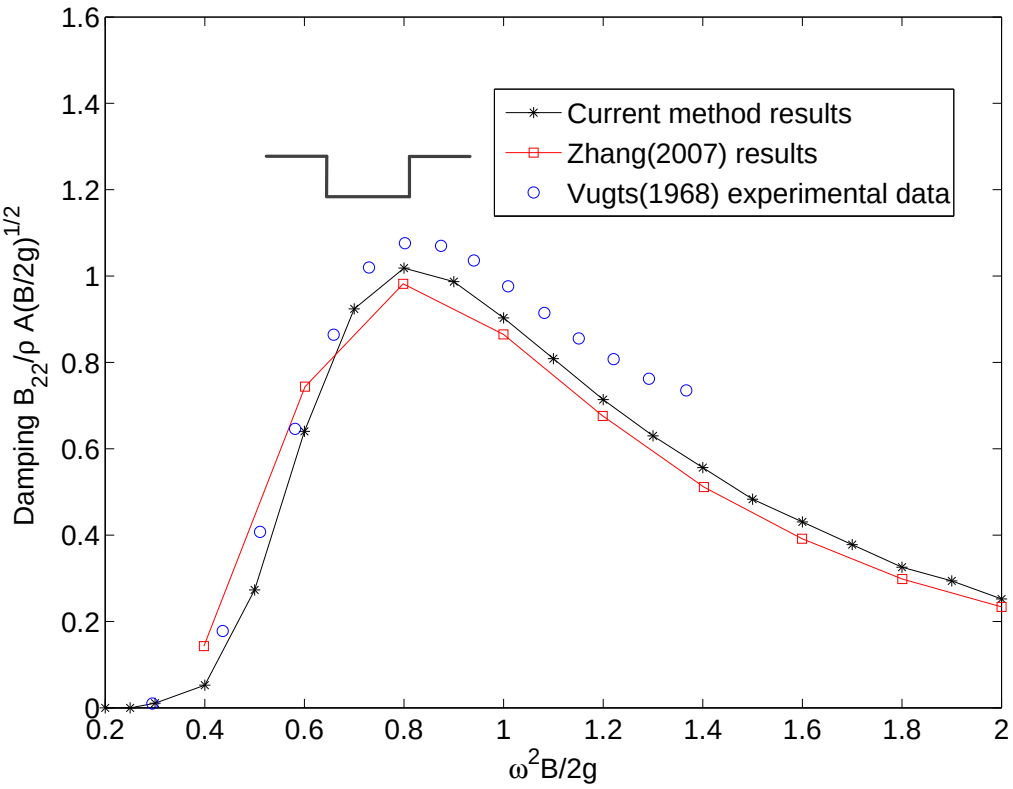

Figure 4.11: Comparison of sway damping coefficient B_{22} between Zhang (2007) numerical results, Vugts (1968) experimental data and current method prediction for a box in oscillatory sway motion with amplitude $a = 0.1T$.

posed numerical techniques in terms of source points distribution and intersection points treatment.

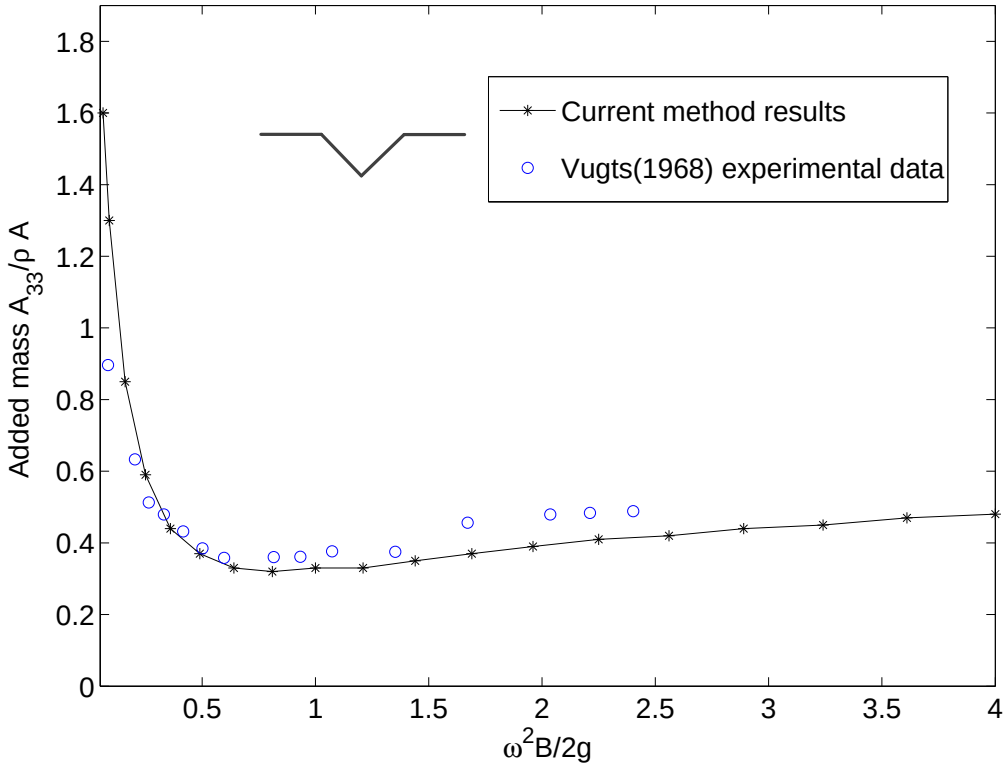

Figure 4.12: Comparison of heave added mass coefficient A_{33} between Vugts (1968) experimental data and current method prediction for a wedge in oscillatory heave motion with amplitude $a = 0.1T$.

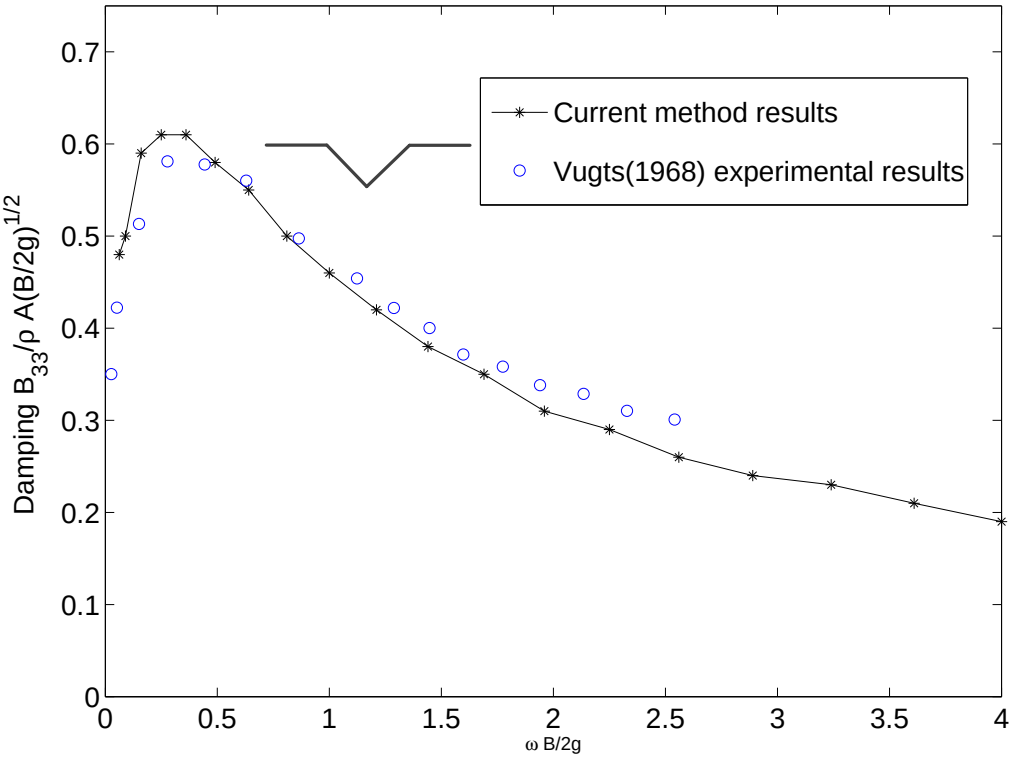

Figure 4.13: Comparison of heave damping coefficient B_{33} between Vugts (1968) experimental data and current method prediction for a wedge in oscillatory heave motion with amplitude $a = 0.1T$.

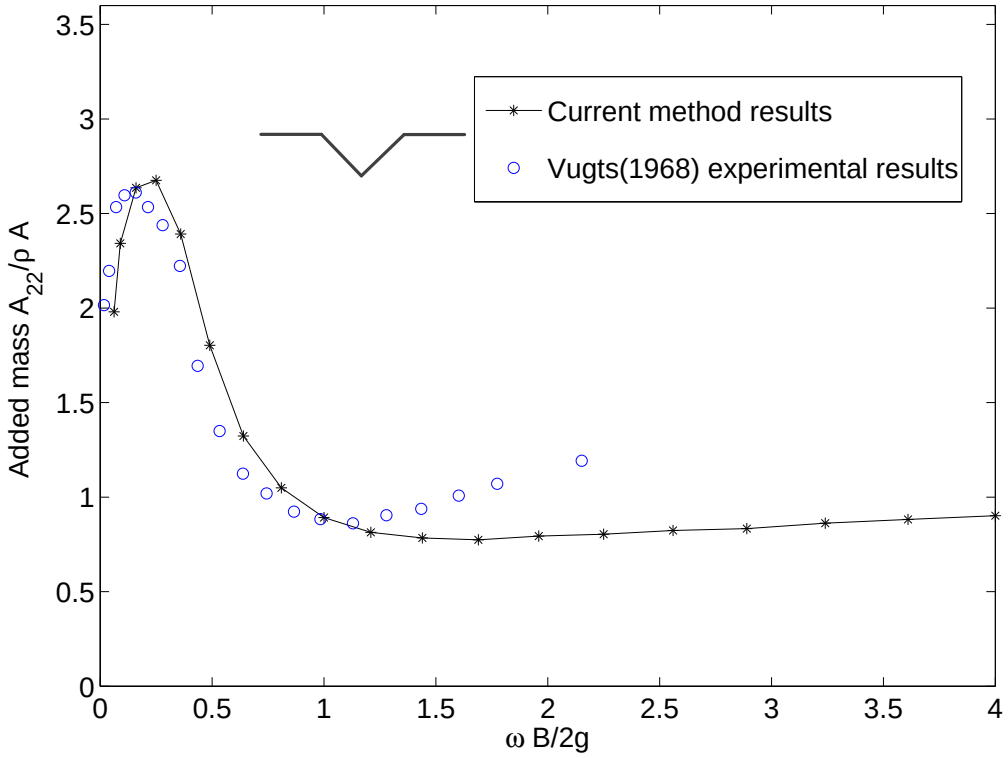

Figure 4.14: Comparison of sway added mass coefficient A_{22} between Vugts (1968) experimental data and current method prediction for a wedge in oscillatory sway motion with amplitude $a = 0.1T$.

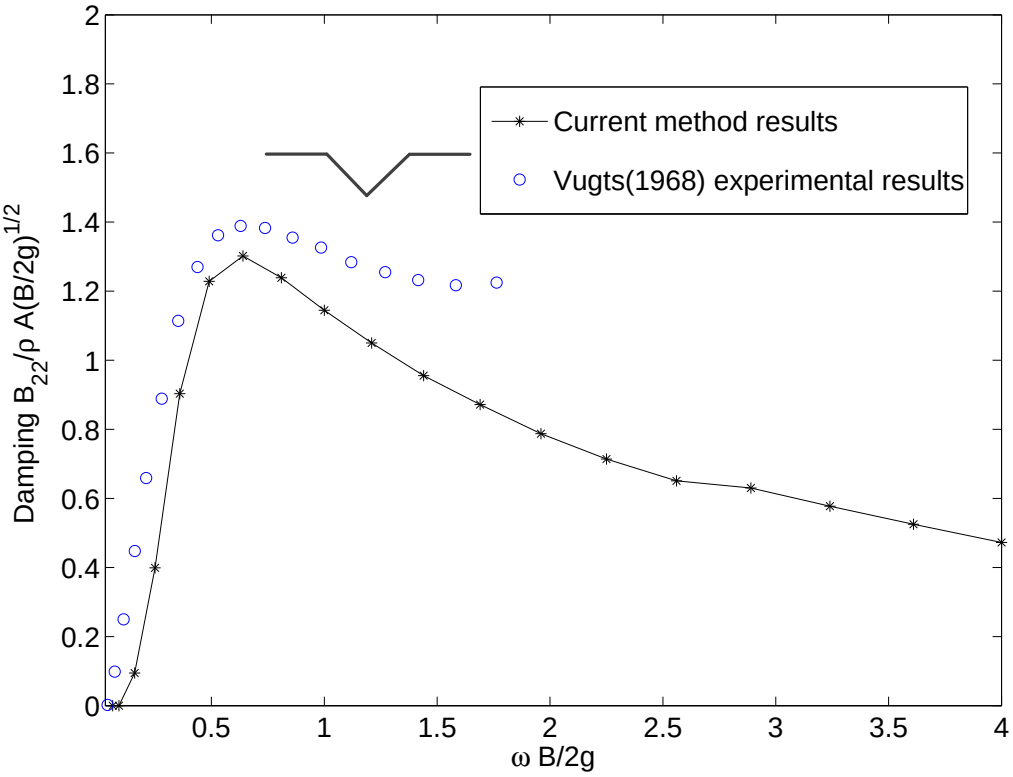

Figure 4.15: Comparison of sway damping coefficient B_{22} between Vugts (1968) experimental data and current method prediction for a wedge in oscillatory sway motion with amplitude $a = 0.1T$.

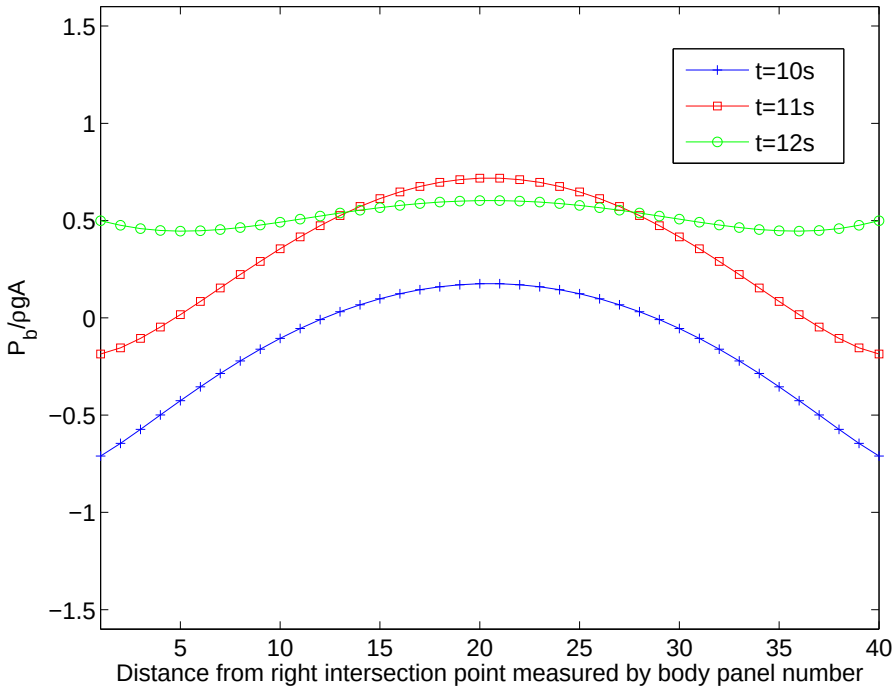

Figure 4.16: Predicted pressure distributions P_b at different times around circular cylinder in oscillatory heave motion with amplitude $a = 0.1T$ and frequency $\omega^2 R/g = 1.0$.

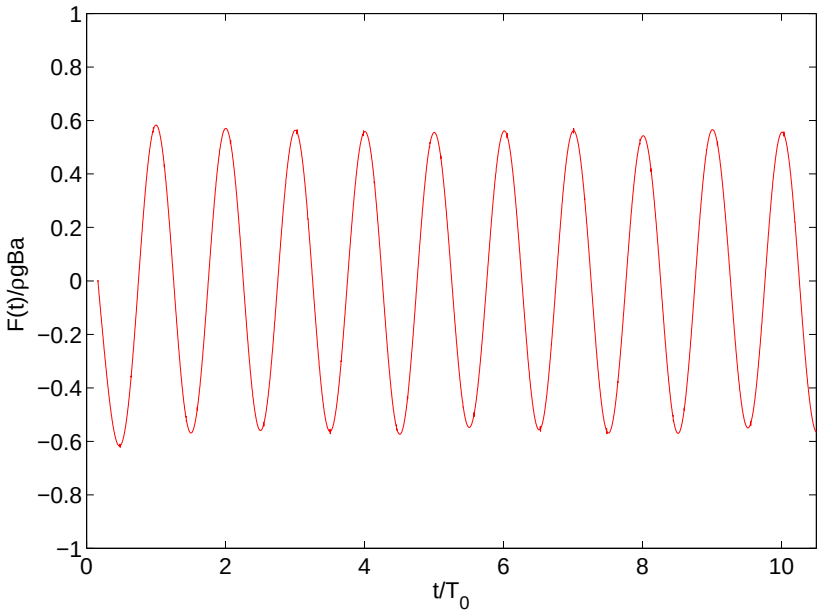

Figure 4.17: Time records for vertical force $F(t)$ of circular cylinder in oscillatory heave motion with amplitude $a = 0.1T$ and frequency $\omega^2 R/g = 1.0$.

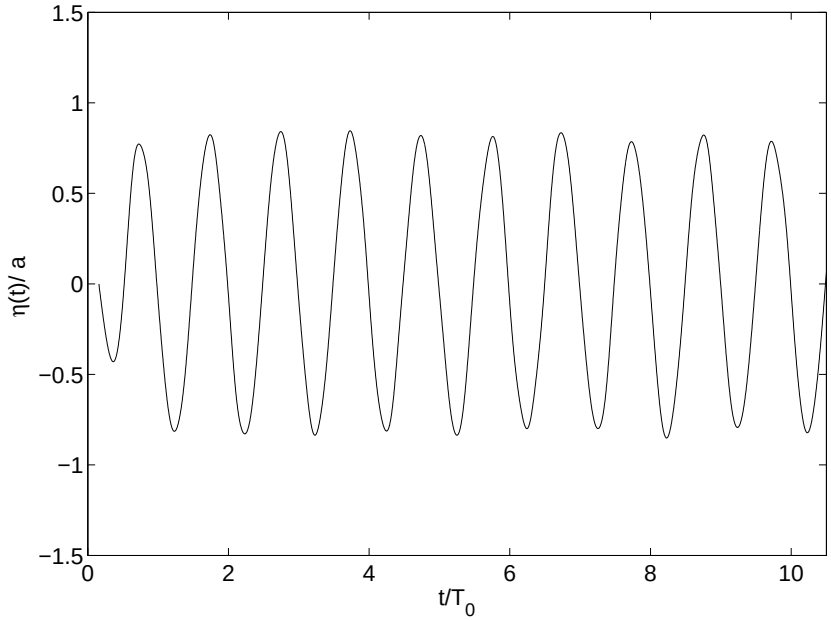

Figure 4.18: Time records for wave elevation $\eta(t)$ of circular cylinder in oscillatory heave motion with amplitude $a = 0.1T$ and frequency $\omega^2 R/g = 1.0$.

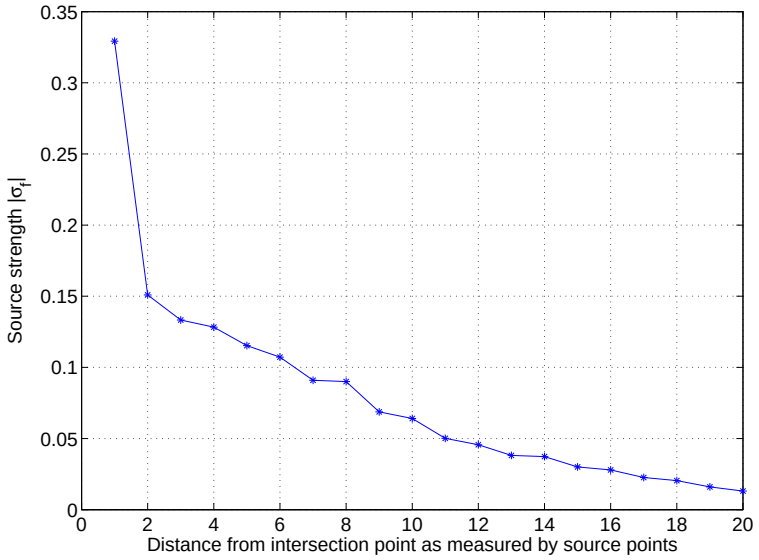

Figure 4.19: Source strength for the first 20 source point distribution for a circular cylinder in oscillatory heave motion with amplitude $a = 0.1T$ and frequency $\omega^2 R/g = 1.0$.

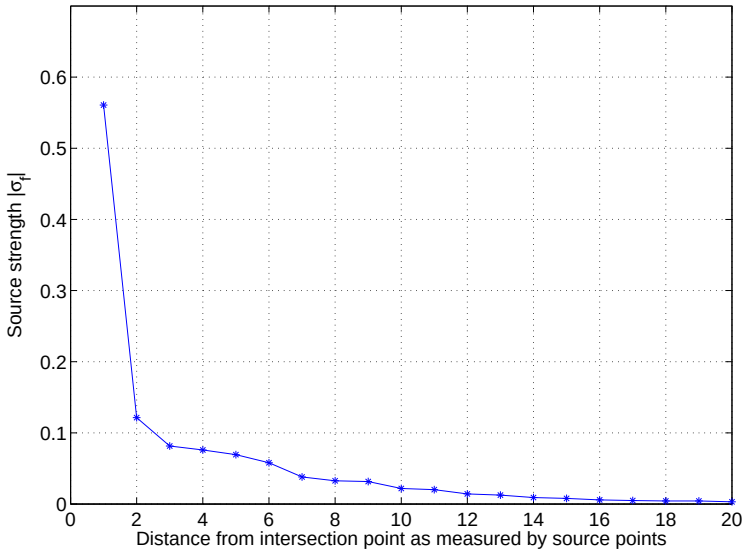

Figure 4.20: Source strength for the first 20 source point distribution for a circular cylinder in oscillatory sway motion with amplitude $a = 0.1T$ and frequency $\omega^2 R/g = 1.0$.

4.4 Concluding remarks

In this chapter, two-dimensional linear forced body motions are numerically solved by Rankine source method to demonstrate the accuracy and efficiency of the proposed method. Both linear body boundary and free surface boundary conditions are satisfied for these small oscillatory motions.

Instead of an even distribution of sources over the free surface an incrementally increasing source space distribution method is developed coupled with a single point intersection treatment. This distribution conforms with the characteristics of source strength decaying and therefore is superior to the traditional even distribution patten. Fewer source points are required to cover a greater free surface range and therefore computational effort is reduced.

The numerical accuracy has been validated by comparing prediction of added mass and damping coefficient with published experimental data and other numerical results for circular cylinder, box and wedge in forced harmonic heave and sway motion. The agreement for heave motion is reasonably good with better conformation to experimental results being obtained for the sway motion than that observed based on Zhang's even distribution method.

The success of numerical simulation for linear problem lays the foundation for further nonlinear analysis with either nonlinear body boundary condition or fully nonlinear boundary conditions applied. The Mixed Euler-Lagrange algorithm will be introduced to capture the nonlinear effects arising from the nonlinear boundary conditions in the following two chapters.

Chapter 5

Two-dimensional nonlinear body boundary problem simulation for forced body oscillation motion

Chapter 4 dealt with wave-body interaction under linear boundary condition assumptions. This mathematical model is suitable only for small amplitude oscillations as it assumes the absence of body surface movement and hence fails to capture high order hydrodynamic responses. If the amplitude is not small, the wetted body surface contour changes significantly over the course of the body motion and therefore nonlinear effects become significant.

In this chapter a nonlinear body boundary or exact body boundary condition is assumed within the wave-body mathematical model. Next the mixed Euler-Lagrange algorithm is introduced to capture the nonlinearity. The nonlinear body boundary problem is difficult to solve analytically (Oakley, 1972). Chapman (1979) examined this problem numerically using time domain free surface Green function and found the nonlinearity is largely influenced by the body shape.

Due to changes of body surface, the intersection points move horizontally with velocity of Equation 2.64, and accordingly, the free surface node points on the calm water surface and the corresponding free surface source points move horizontally. Therefore nonlinear free surface conditions(Equation 2.64) apply in the horizontal direction and linear free

surface conditions(Equations 2.6 and 2.7) in the vertical direction are satisfied for the free surface nodes on the calm water surface. From the Lagrangian frame point, the free surface source point only has horizontal movement and the velocity is evaluated by Equation 2.64.

In the time-dependent numerical simulation of the problem, the wetted body surface needs to be repanelled and the free surface nodes require regridding at every time step. To do this efficiently, a MEL method is employed by solving the field equation in the Eulerian frame and then applying nonlinear boundary conditions to track individual control points in the Lagrangian frame to update their positions. In the course of the time iteration, wetted body panel number and free surface node number are fixed. A flowchart for this nonlinear body boundary problem is presented in Figure 5.1. Different from linear problem, The influence coefficients need to evaluate at every time step and therefore much more computational effort is required for this problem.

This chapter starts from the statement for intersection points treatment in Section 5.1 and then delivers the process for free surface source points distribution in Section 5.2. These two numerical techniques are novel contributions for the nonlinear body boundary condition problems. Numerical predictions are presented in Section 5.3, where numerical simulations are executed for large amplitude forced body oscillation motions. In order to show the availability of proposed methods, both smooth contour body: circular cylinder and sharp contour body : wedge are selected as forced body cross sections. The predicted numerical results are compared with published experimental and other numerical results to validate the numerical accuracy and efficiency of proposed numerical techniques. Concluding remarks are given in Section 5.4.

5.1 Intersection points treatment

The free surface wave is propagated initially from the intersection points. To stabilise the iteration scheme, it is crucial to deal with these intersection points properly. For each intersection point, one traditional technique (Beck, 1994) uses two points to avoid wave breaking around the intersection point. One is the node point located at the intersection point, whereas the other is a source point placed vertically above the node point. The newly developed single point method only allows the intersection points to satisfy body

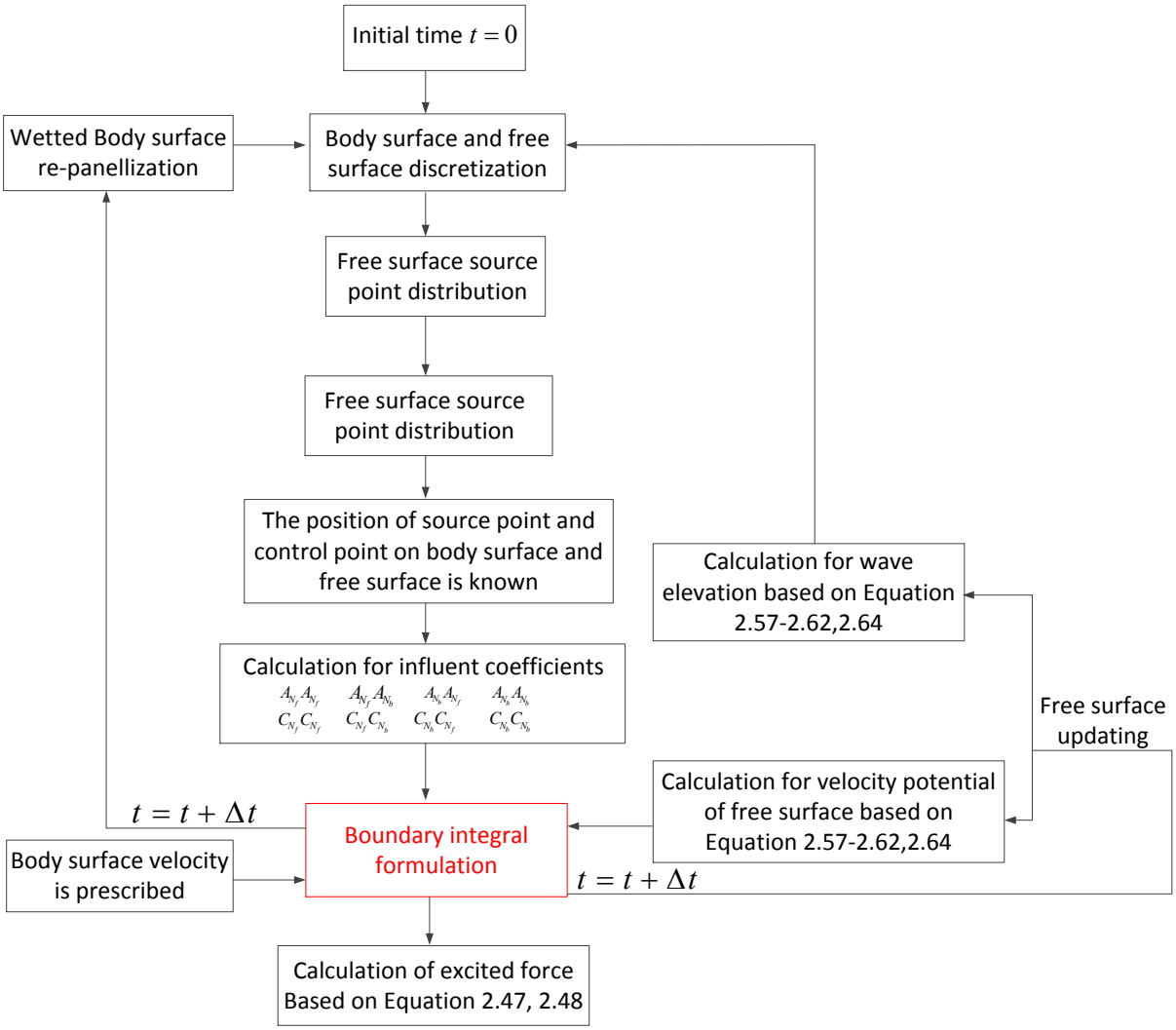

Figure 5.1: Flowchart of numerical process for two-dimensional nonlinear body boundary condition problem.

boundary condition. The movement of the body oscillation causes the intersection points to displace the free surface nodes and source points in the horizontal direction back and forth during the iteration process. This arrangement at different time steps is illustrated

in Figure 5.2.

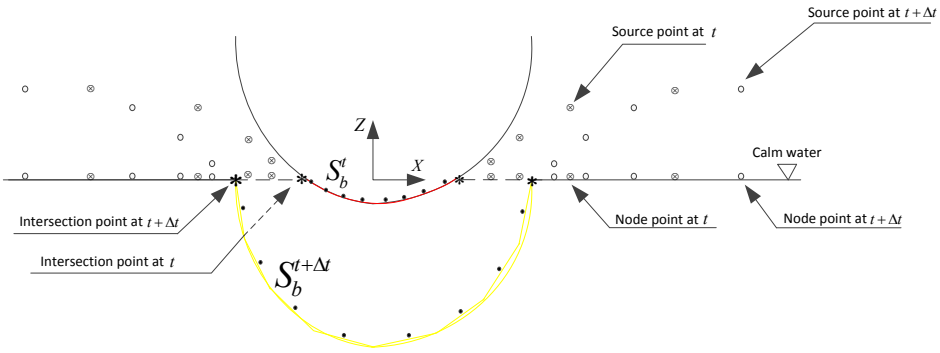

Figure 5.2: Profile of sources, nodes and intersection points at different time steps.

The node points on the free surface are required to be carefully selected. In particular, the chosen distance between the intersection point and the first node point is important (Zhang and Beck, 2007) and is used to locate the first source point vertically above the first node point.

5.2 Free surface source point distribution

In Rankine source method, the continuous free surface profile is replaced by source points in isolation and therefore the free surface boundary condition is satisfied on these isolated source points. The position and numbers of source points are no doubt vitally important for the numerical accuracy and efficiency. The newly adopted space increment source distribution method is further developed in this section to cope with nonlinear body boundary problem.

5.2.1 Source point distribution pattern

The calm water surface on the right hand side of S_f is divided into inner and outer domains distributed with nodes $P_{f,i}$. In the inner domain the neighbouring node distances starting from the intersection point $P_{f,0}$ is expressed in the form:

$$|P_{f,i} - P_{f,i-1}| = \frac{L_b \alpha_j}{\omega^2}, \;\; i = 1, ..., N_{in}. \tag{5.1}$$

The node point number N_{in} (see Section 5.2.2) is discussed later whereas in the outer domain, 20 points are distributed in the exponential form:

$$|P_{f,i} - P_{f,i-1}| = |P_{f,N_{in}} - P_{f,N_{in}-1}| \times 1.05^{i(i-1)/2}, \; i = 1, ..., 20, \tag{5.2}$$

The desingularized source Q_i is placed vertically above the node point $P_{f,i}$. The desingularized distance $D_{d,i}$ between them is given by the recommended equation (Cao, 1991):

$$D_{d,i} = |Q_i - P_{f,i}| = \sqrt{|P_{f,i-1} - P_{f,i}|} \tag{5.3}$$

for the right hand side sources. The wave problem is treated symmetrical for the oscillatory body movement and the left hand side sources are arranged in a mirror image.

In the present method, the nodes distribution in the inner domain is proportional to L_b, the size of the top body surface panel, since this top panel essentially defines the wave motion problem and thus effects the source distribution above the calm water surface. In addition, this method keeps the free surface panel matching to the top body panel during the whole iteration process, greatly benefitting the regridding process as no extra nodes are required. Zhang and Beck (2007) added extra nodes to match these panels and numerical errors might be introduced into the simulation.

5.2.2 Source points number selection

The calm water surface node points in the inner domain are also dependent on the frequency ω and separation factors $\alpha_j (j = 1, ..., 8)$. The chosen number depends on the value of the separation factor α_j in each region $(j = 1, ..., 8)$ as shown in Table 5.1. The approach adopted is discussed here. Firstly 10 node point distribution is associated with

the first three factors α_1, α_2, α_3. From the fourth factor $\alpha_j = 1.1$ until the eighth factor $\alpha_j = 4.0$, the same number of node points are assumed under each α_j. $4, 8, 12$ and 14 node points are chosen respectively in a four distribution approaches, such that the total number of free surface node point is $N_f = 100, 140, 180$ and 220. The number N_f accounts for all free surface node points on the right and the left hand sides without use of the symmetry assumption.

Table 5.1: The values of separation factors α_j in the inner domain for nonlinear body boundary problem.

i	1	2	3-10	—	—	—	—	—
j	1	2	3	4	5	6	7	8
α_j	0.5	0.7	0.9	1.1	1.5	2.0	2.8	4.0

A circular cylinder of a radius-to-draught ratio $R/T = 1$ is adopted as numerical model to illustrate this distribution approach. The cylinder undergoes a forced heave oscillation of amplitude $a = 0.1T$ and given frequency ω in the free surface. Figures 5.3 and 5.4 show comparisons of the added mass and damping coefficients between the experimental data of Vugts (1968) and predictions using different free surface node point values N_f.

Both Figures 5.3 and 5.4 indicate that the closest agreement occurs when $N_f = 180$. Therefore, $N_f = 180$ is selected throughout the present study. In order to further validate this selection. Numerical simulation is executed for this cylinder experiencing forced sway motion with amplitude $a = 0.1T$.

Figures 5.5 and 5.6 present comparisons of sway added mass A_{22} and damping coefficients B_{22} between Zhang (2007) numerical results, Vugts (1968) numerical results, Vugts (1968) experimental data and current method prediction. Zhang (2007) utilise an isolated Rankine source method with even source distribution pattern while Vugts (1968)'s simulation is based on free surface Green function theory. Both figures show a fairly well agreement between current predicted results with the selected source points and other published data. In present proposed method, 90 (20 in the outer domain and 70 in the inner domain) node points are distributed on one side of the floating body. In the method of Zhang and Beck (2007, 2006), 120 node points are evenly placed over four wave lengths on one side of the floating body in the inner domain. Figure 5.7 shows the comparison of

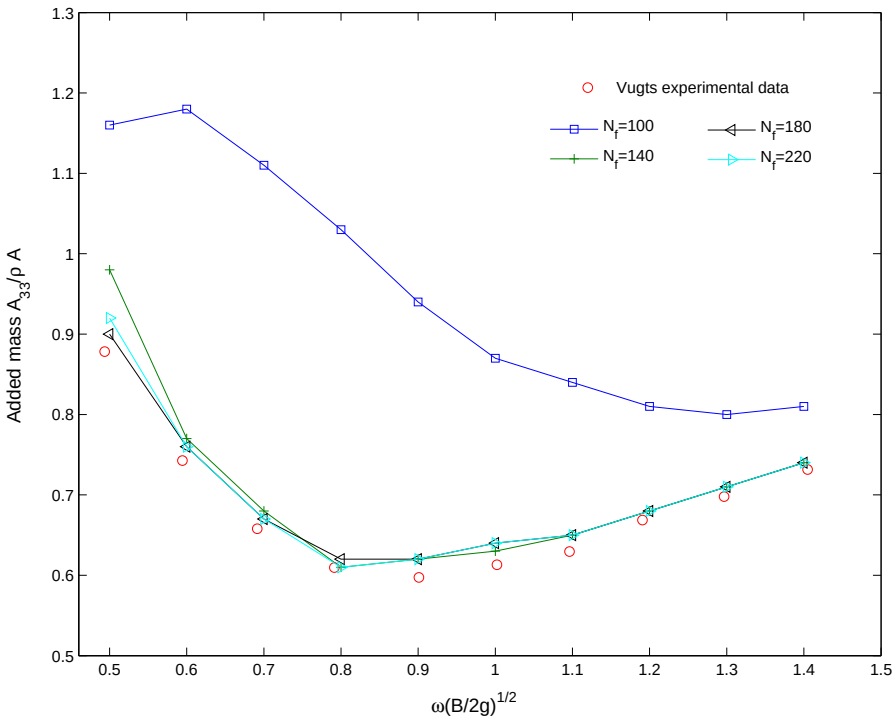

Figure 5.3: Comparisons for added mass coefficient between Vugts experiment data and current methods with different free surface node points N_f when $a = 0.1T$.

the present node point distributions with the even distributed method proposed by Zhang and Beck (2006, 2007) in the inner domain. As seen, more points are distributed in the first wave length than in the method of Zhang and Beck (2006, 2007) and significantly decreasing number in the second and much less in third and fourth wave lengths.

As computational cost mainly lies in the storage of the influent coefficient matrices and their solutions, the computational cost is roughly proportional to N_f^2. The proposed approach reduces computational memory and time roughly to half of the even distribution method and therefore computational efficiency is largely improved.

In the course of the time iteration, wetted body panel number and free surface node number are kept constant. This allows the size of influent coefficient matrix to remain the same with no extra work for unit normal vector updating and also avoids the "spray root phenomenon " (Beck, 1994; Zhang and Beck, 2006, 2007), that is the intersection points move without bound and the simulation must be stopped since the control of the

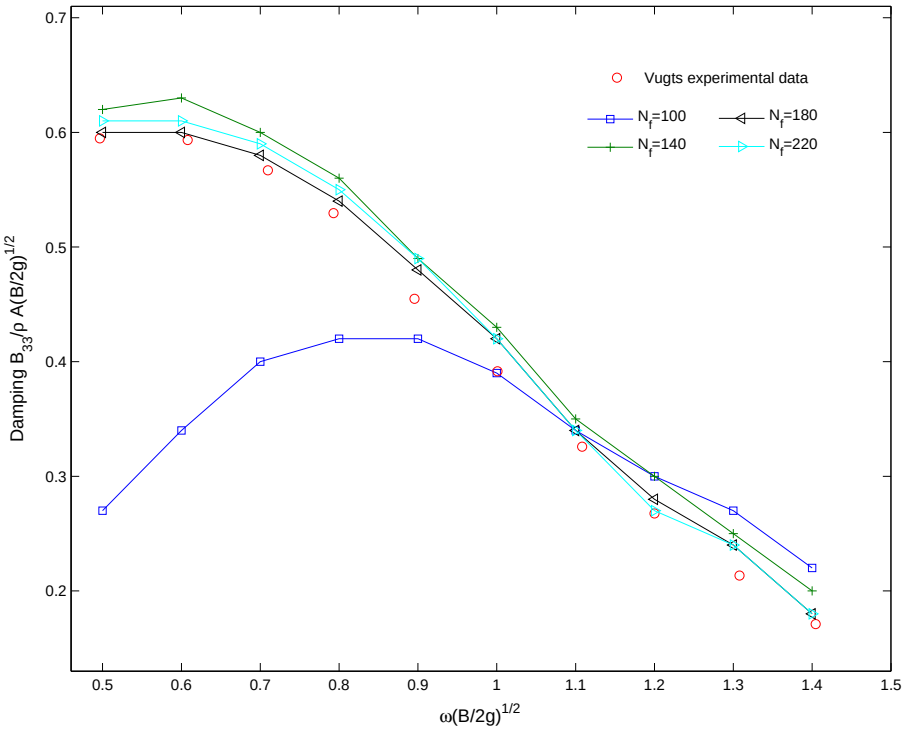

Figure 5.4: Comparisons for damping coefficient between Vugts experiment data and current methods with different free surface node points N_f when $a = 0.1T$.

intersection point is lost.

5.2.3 Source strength decaying

From the intersection point outwards, the importance of the source points decreases as the distance increases. Figures 5.8 and 5.9 present the source strength $|\sigma_f|$ of the first 20 source points for the circular cylinder in oscillatory heave and sway motion with amplitude $a = 0.1T$ and frequency $\omega^2 R/g = 1.0$. Both figures show that source strengths decay quickly from the first point and trends to zero around 20th point and therefore their importance rapidly decreases as their positions located more far from the intersection point. This account for the space increment distribution method proposed in present simulation.

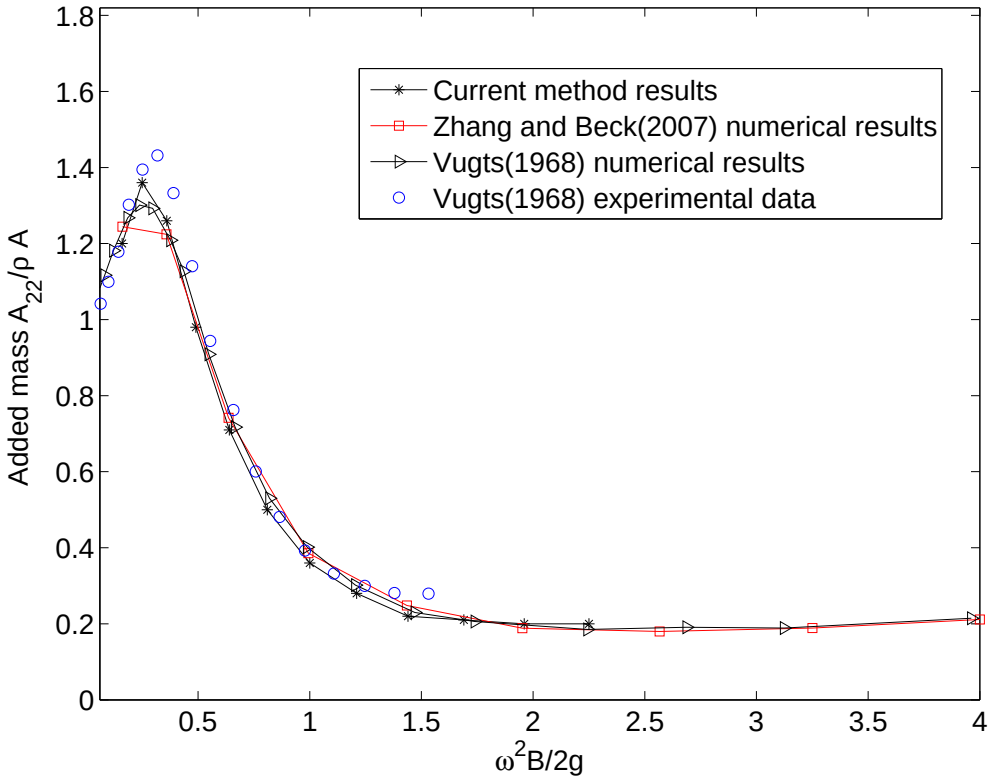

Figure 5.5: Comparison of sway added mass coefficient A_{22} between Zhang (2007) numerical results, Vugts (1968) numerical results, Vugts (1968) experimental data and current method prediction for a circular cylinder in oscillatory sway motion with amplitude $a = 0.1T$.

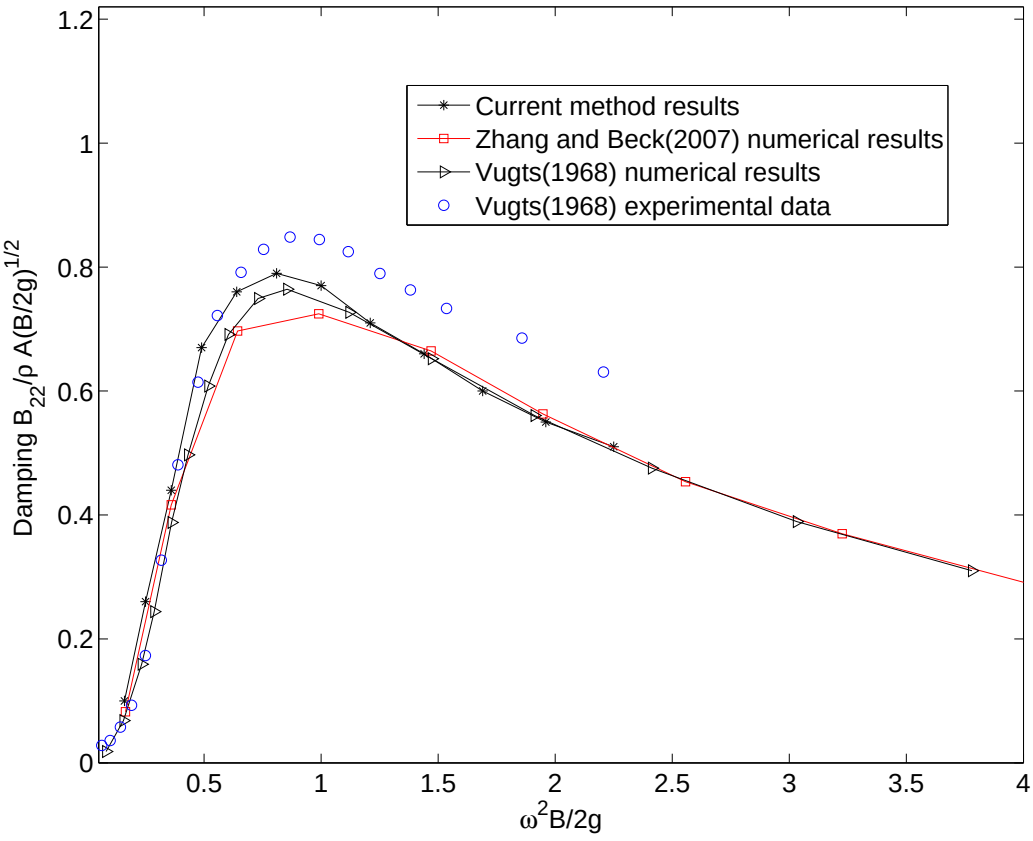

Figure 5.6: Comparison of sway added mass coefficient B_{22} between Zhang (2007) numerical results, Vugts (1968) numerical results, Vugts (1968) experimental data and current method prediction for a circular cylinder in oscillatory sway motion with amplitude $a = 0.1T$.

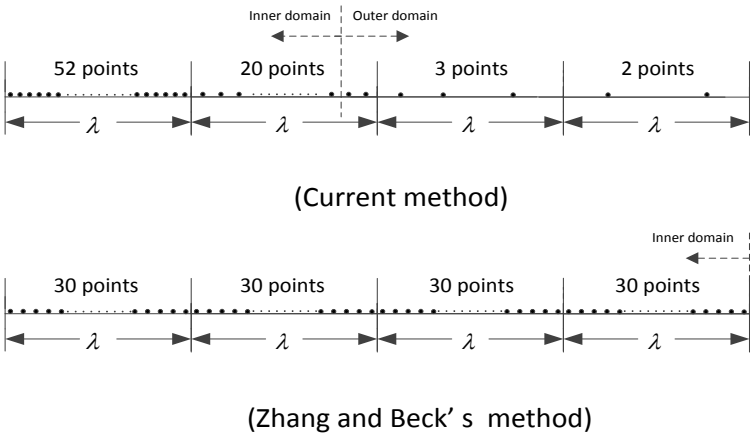

Figure 5.7: Comparisons for node points distribution in inner domain between current method and Zhang and Beck (2006, 2007) method.

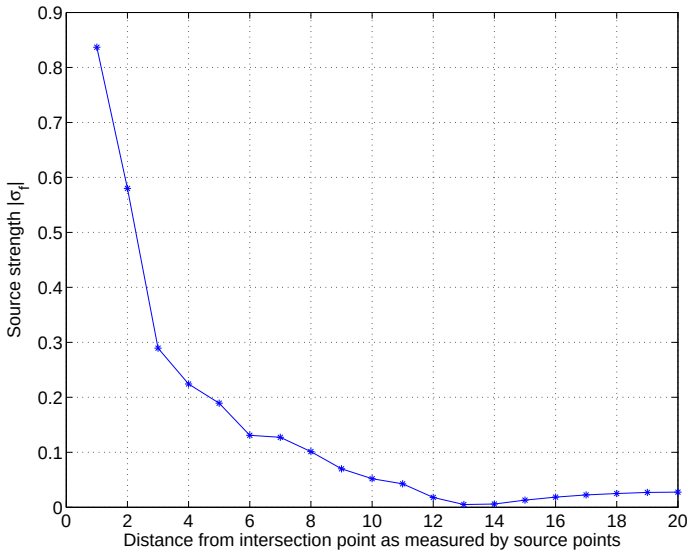

Figure 5.8: Source strength for the first 20 source point distribution for a circular cylinder in oscillatory heave motion with amplitude $a = 0.1T$ and frequency $\omega^2 R/g = 1.0$.

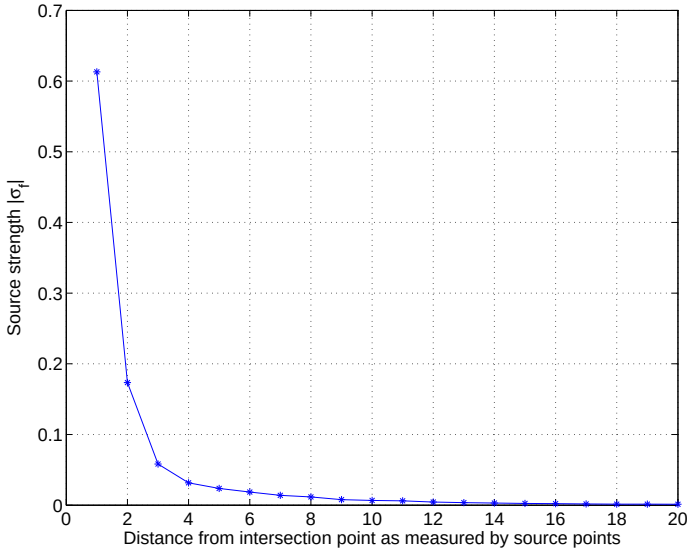

Figure 5.9: Source strength for the first 20 source point distribution for a circular cylinder in oscillatory sway motion with amplitude $a = 0.1T$ and frequency $\omega^2 R/g = 1.0$.

5.3 Numerical results for large body motion amplitude

Following the intersection points treatment and free surface source points distribution in the last two subsections, numerical simulations based on these new techniques are executed and predicted results are compared with published data to validate the proposed methods in this section.

When the floating body oscillates with large amplitude, the nonlinear effects from variation of wetted body surface become important. Here, the floating body is chosen as circular cylinder with radius to draught radio $R/T = 1.0$ and wedge with $B/T = 2\sqrt{3}/3$. For body oscillating with amplitude $a = 0.2T$, hydrodynamic coefficients and force coefficients are obtained and compared with published experimental and other numerical results when possible. Time records of wave elevation $\eta(t)$ and vertical force $F(t)$ at various motion amplitude are presented to show the nonlinear effects from variation of wetted body surface.

5.3.1 Numerical results for circular cylinder with large motion amplitude

The circular cylinder stays at a equilibrium position with its mass centre lying on the calm water surface at initial time $t = 0$. This cylinder is excited by a vertical upward displacement and experiences a harmonic forced oscillatory heave motion during the whole time iteration from time $t > 0$.

Table 5.2 presents information on nondimensional heave added mass coefficient a_{33}, heave damping coefficient b_{33}, second order mean force $F^0(\omega)$ and second order harmonic force $F^2(\omega)$ for three nondimensional frequencies ($\omega^2 B/g = 0.5, 1.0, 1.5$). These values are compared with the experimental data of Yamashita (1977), numerical linear results of Vugts (1968), numerical results of Kent (2005) and (Zhang and Beck, 2007). The last two apply a nonlinear body boundary condition and linear free surface condition.

The agreement of results derived from the proposed method with experimental data shows a reduction in the error compared with the other three numerical approaches at each

Table 5.2: Comparisons of frequency components of circular cylinder in heave motion when amplitude $a = 0.2T$.

Type	$\frac{\omega^2 B}{2g}$	a_{33}	Error	b_{33}	Error	$F^0(\omega)$	Error	$F^2(\omega)$	Error
Yamashita	0.5	0.66	0	0.52	0	-0.01	0	0.228	0
Vugts	0.5	0.6	9.1%	0.58	11.5%	/	/	/	/
Kent	0.5	0.6	9.1%	0.796	53.1%	-0.01	0	0.194	14.9%
Zhang	0.5	0.63	4.5%	0.82	57.7%	-0.013	30%	0.163	28.5%
Current method	0.5	0.67	1.5%	0.56	7.7%	-0.01	0	0.254	11.4%
Yamashita	1.0	0.62	0	0.39	0	-0.08	0	0.498	0
Vugts	1.0	0.6	3.3%	0.41	5.1%	/	/	/	/
Kent	1.0	0.58	6.6%	0.375	3.8%	-0.086	7.5%	0.491	1.4%
Zhang	1.0	0.6	3.3%	0.41	5.1%	-0.086	7.5%	0.428	14.0%
Current method	1.0	0.62	0	0.41	5.1%	-0.081	1.3%	0.508	2.0%
Yamashita	1.5	0.69	0	0.27	0	-0.13	0	0.76	0
Vugts	1.5	0.78	13%	0.25	13.0%	/	/	/	/
Kent	1.5	0.62	1.0%	0.209	22.6%	-0.16	23.1%	0.796	4.7%
Zhang	1.5	0.67	0.3%	0.23	14.8%	-0.19	46.2%	0.62	18.4%
Current method	1.5	0.69	0	0.28	3.7%	-0.1	23.1%	0.759	0.13%

frequency. For added mass coefficient a_{33} at frequency of $\omega^2 B/g = 0.5$, the discrepancy of current method compared with Yamashita is 1.5%; this discrepancy is one third of the next smallest discrepancy of Zhang. The prediction of current method for a_{33} at frequencies $\omega^2 B/g = 1.0\&1.5$ is exactly the same as the experimental data. The other three numerical predictions have obvious discrepancies compared with the Yamashita experimental test. The discrepancy for damping coefficient b_{33} is generally larger than that associated with the added mass coefficient a_{33} but the proposed method shows a reduction in error and this is especially true at frequencies $\omega^2 B/g = 0.5\&1.5$. For mean and harmonic second order forces, $F^0(\omega)$ and $F^2(\omega)$, the results derived from proposed method generally have the smallest discrepancy at each frequency and the largest reduction occurs for second order harmonic force $F^2(\omega)$ at a frequency of $\omega^2 B/g = 0.5$.

Figures 5.10 and 5.11 show prediction from the proposed method compared to the experimental data of Yamashita (1977), and the numerical results of Lee (1968) for heave added mass and damping coefficients from $\omega^2 B/g = 0.2$ to $\omega^2 B/g = 2.0$. The method used by Lee adopts a nonlinear free surface condition coupled to a mean body surface condition. The current method results show favourable agreement with the experimental

data.

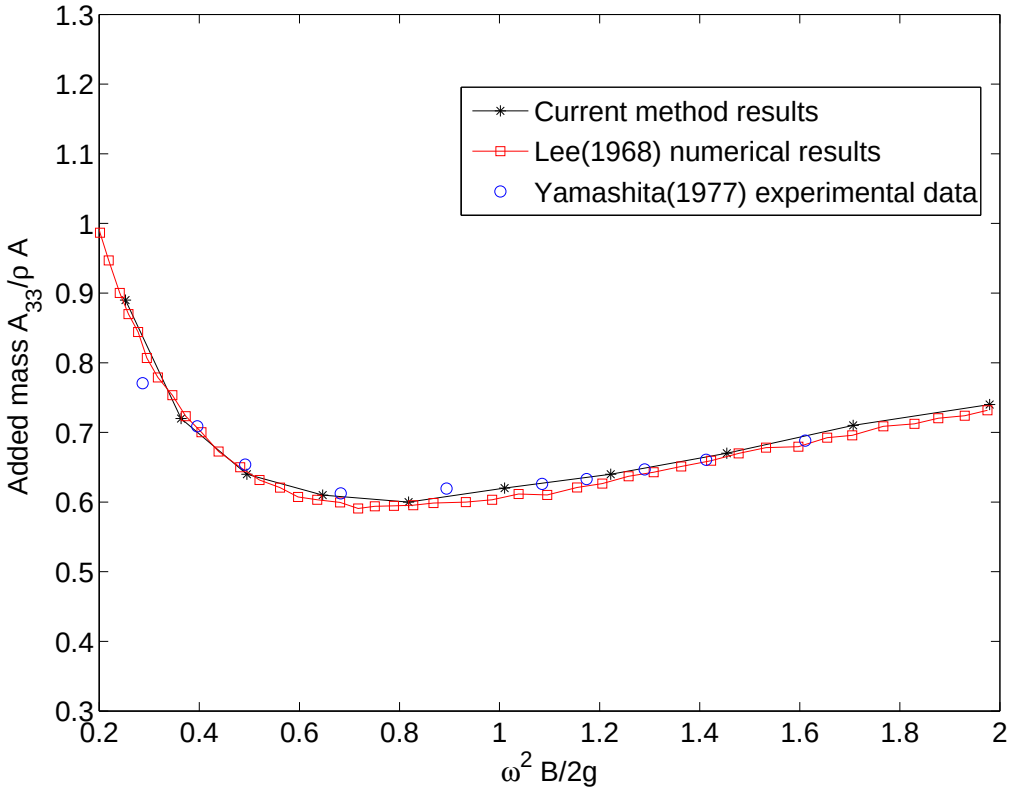

Figure 5.10: Comparisons of heave added mass coefficient A_{33} between Lee (1968) numerical results, Yamashita (1977) experimental data and current method prediction for a circular cylinder in oscillatory heave motion with amplitude $a = 0.2T$.

The proposed method is further validated by comparing first and second order harmonic force response in the frequency domain. Figure 5.12 shows the comparison of first order force from current method with Tasai and Koterayama (1976) experimental result and numerical results of Kent (2005) and Zhang and Beck (2007). Figure 5.13 compares second order force from current method with Yamashita (1977) experimental results, numerical results of Zhang and Beck (2006), Potash (1971) and Parissis (1966). For the last two methods a nonlinear free surface boundary condition and a mean body boundary condition are applied. Figures 5.12 and 5.13 indicate that current method results agree well with experiment data and better results are obtain for second order force than the other three numerical methods.

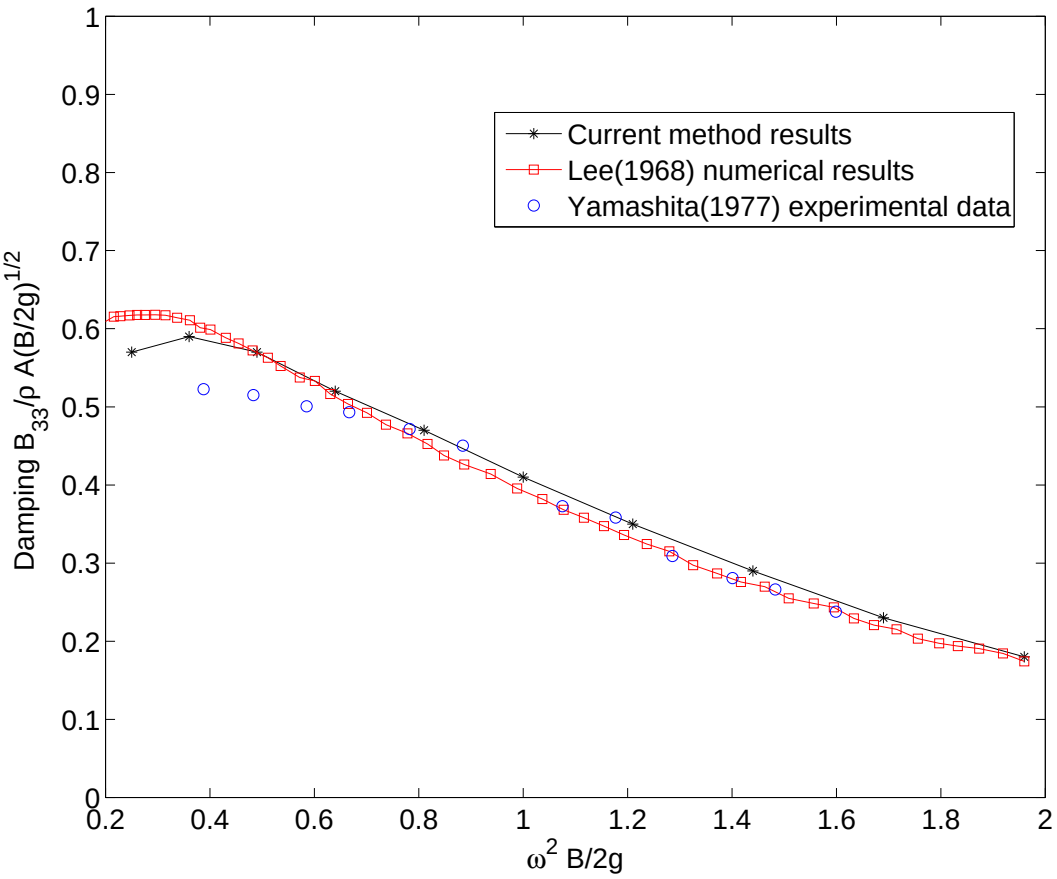

Figure 5.11: Comparisons of heave damping coefficient B_{33} between Lee (1968) numerical results, Yamashita (1977) experimental data and current method prediction for a circular cylinder in oscillatory heave motion with amplitude $a = 0.2T$.

Figures 5.10, 5.11 and 5.13 demonstrate that the nonlinear body boundary condition dominates the nonlinear response and, therefore, satisfactory results can be obtained even ignoring the nonlinear free surface effect for motion amplitude $a = 0.2T$.

In further investigations, the time records of nondimensional wave elevation and vertical force, generated by the circular cylinder experiencing different oscillating heave motion amplitudes of $a = 0.1T$, $0.2T$, $0.4T$ at frequency $\omega^2 B/(2g) = 1.0$ with $\Delta t = T_0/60$, are presented in Figures 5.14 and 5.15. The profile for wave elevation and vertical force is no longer harmonic. The nonlinear response increases as the motion amplitude a increases. The wave elevation and force profile becomes sharper at peak range whereas it is flatter

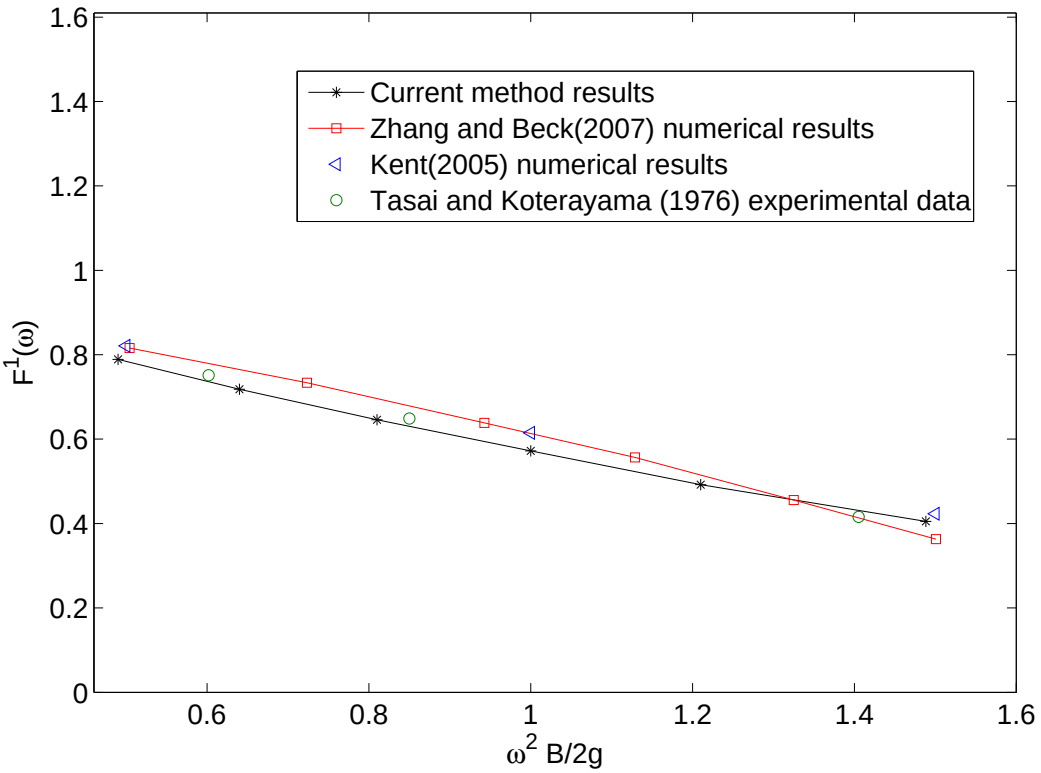

Figure 5.12: Comparisons of first order force $F1(\omega)$ between Zhang and Beck (2007) numerical results, Kent (2005) numerical results, Tasai and Koterayama (1976) experimental data and current method predictions for a circular cylinder in oscillatory heave motion with amplitude $a = 0.2T$.

at trough range. The peak values are larger in magnitude than the trough values and these differences increase as amplitude a increases.

To examine the numerical treatment given to the intersection points, the local response around the floating circular cylinder is investigated. The radius of the cylinder is chosen as $R = 10m$. The panels are numbered starting from the right intersection point towards the left intersection point. Figure 5.16 presents the body surface pressure distributions at different times when $\omega(B/(2g))^{1/2} = 1.0$ and amplitude $a = 0.2T$. The pressure distribution is perfectly symmetrical around the body and varies smoothly between the right and the left intersection points. These results further indicate the efficiency and accuracy of the derived treatment for the intersection points.

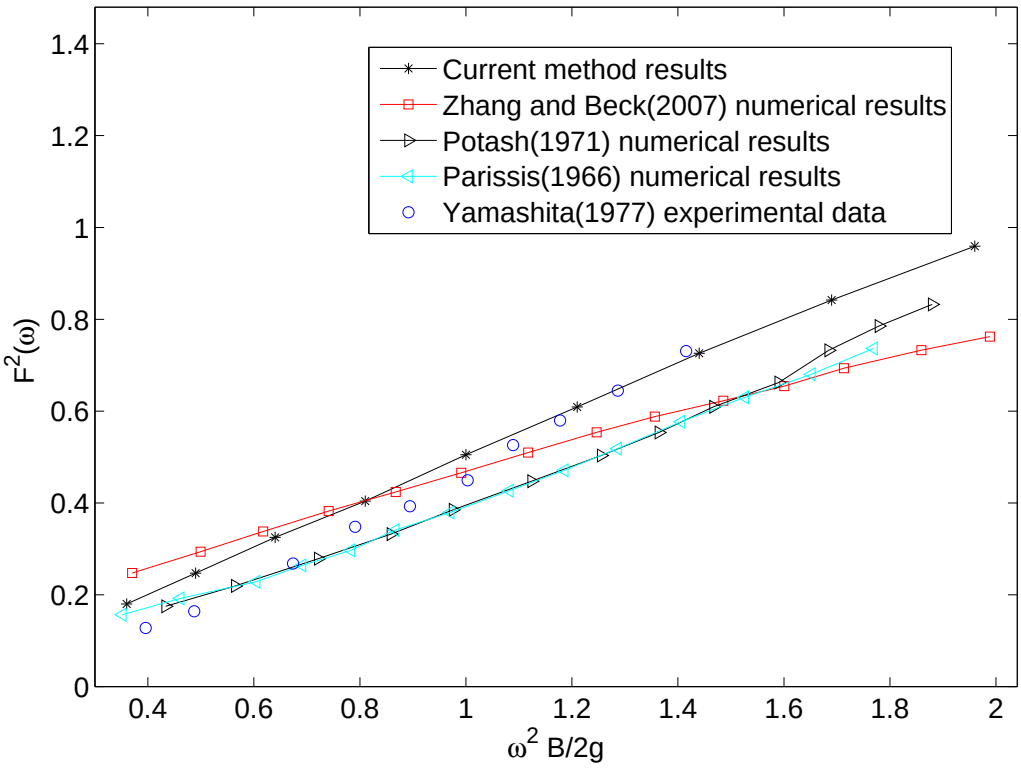

Figure 5.13: Comparisons of first order force $F1(\omega)$ between Zhang and Beck (2007) numerical results, Potash (1971) numerical results, Parissis (1966) numerical results, Yamashita (1977) experimental data and current method predictions for a circular cylinder in oscillatory heave motion with amplitude $a = 0.2T$.

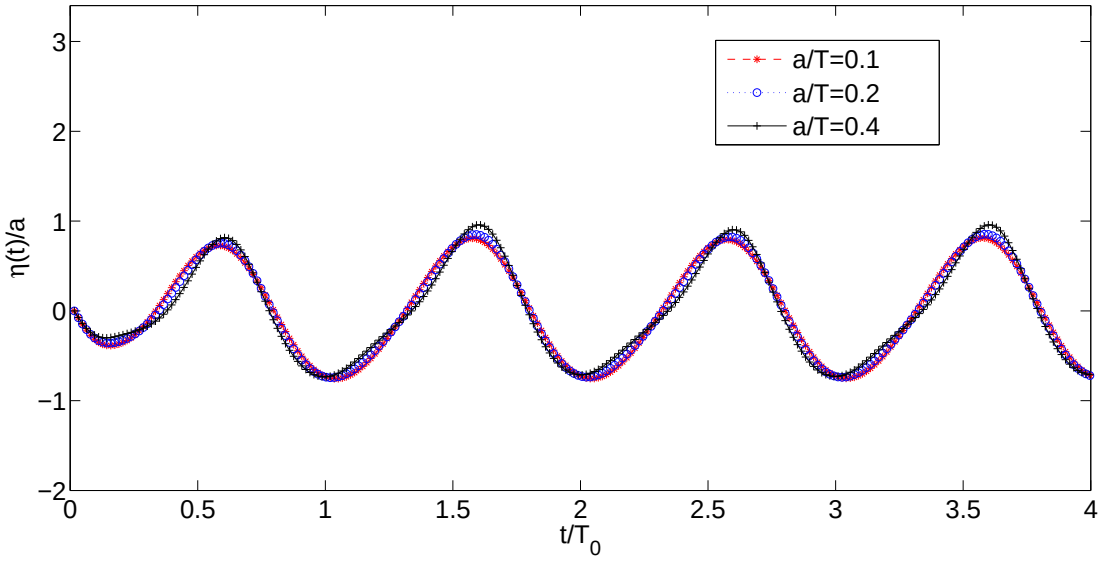

Figure 5.14: Predicted wave elevation time records at various amplitudes of heave oscillatory motion when $\omega^2 B/2g = 1.0$.

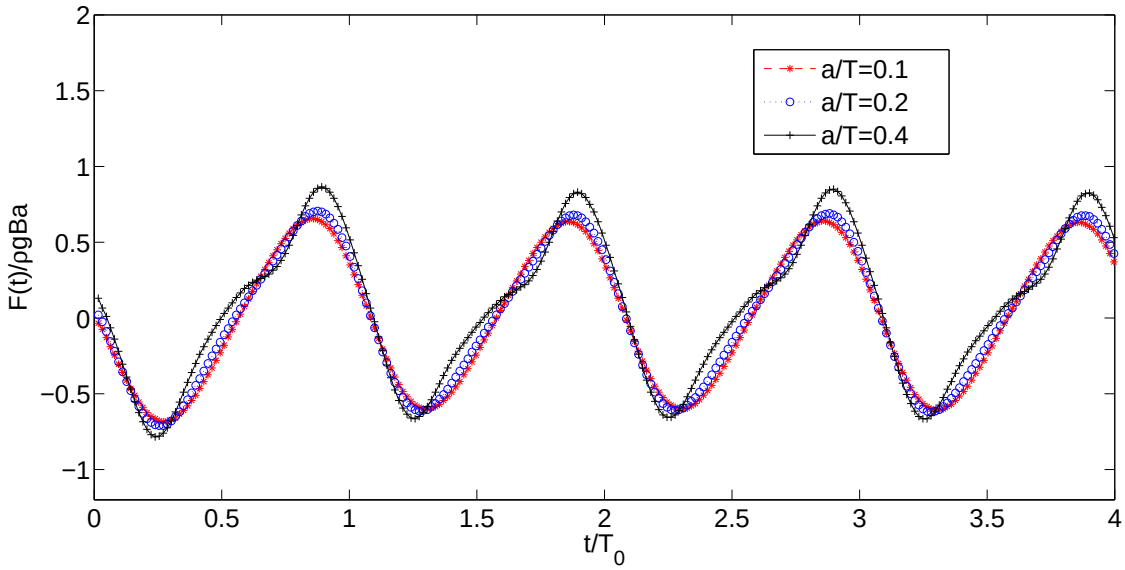

Figure 5.15: Predicted vertical force time records at various amplitudes of heave oscillatory motion when $\omega^2 B/2g = 1.0$.

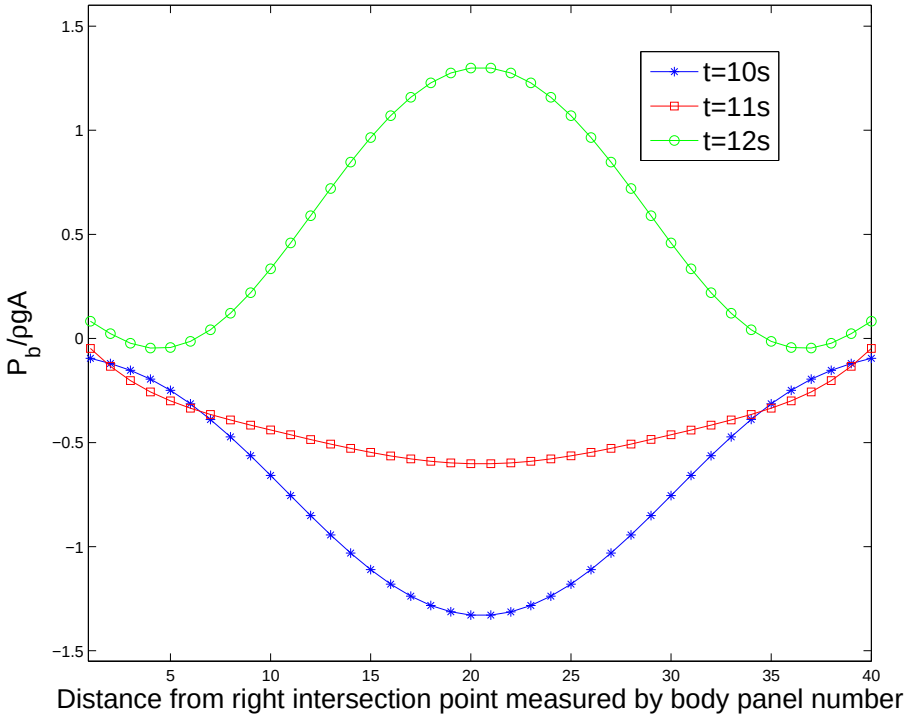

Figure 5.16: Predicted pressure distributions P_b at different times around circular cylinder in oscillatory heave motion with amplitude $a = 0.2T$ and frequency $\omega^2 R/g = 1.0$.

5.3.2 Numerical results for wedge with large motion amplitude

In addition to the wave-body motion around a cylinder, numerical simulations with respect to a wedge floating body are now briefly presented to illustrate the breadth of application of the proposed numerical model. Similar to the cylinder problem, the nonlinear hydrodynamic effect of the body-wave problem with respect to the wedge is reasonably captured when the nonlinear wetted body surface condition is applied for motion amplitude $a = 0.2T$.

Comparisons of the hydrodynamics coefficients A_{33} and B_{33} are presented in Figures 5.17 and 5.18. The Tasai and Koterayama (1976) numerical method utilises a nonlinear free surface body condition and a mean body surface condition. The present method's results agree well with existing results for the wedge body, especially the experimental data of Tasai and Koterayama (1976).

In a manner similar to the one used by Zhang and Beck (2007), the nonlinear hydrodynamic effect of the body-wave problem has been almost captured when the nonlinear wetted body surface condition is applied for motion amplitude $a = 0.2T$.

To examine the single point treatment given to the intersection point, the local response around the floating wedge is assessed. Similar to the cylinder case, panels are numbered starting from the right intersection point and then move towards left intersection point. Figure 5.19 presents body surface pressure distribution at different times when $\omega(B/2g)^{1/2} = 1.0$ and $a = 0.2T$. The pressure distribution is perfectly symmetrical around the body and varies smoothly between the right and the left intersection points. These result further indicates the efficiency and accuracy of the single treatment for the intersection point.

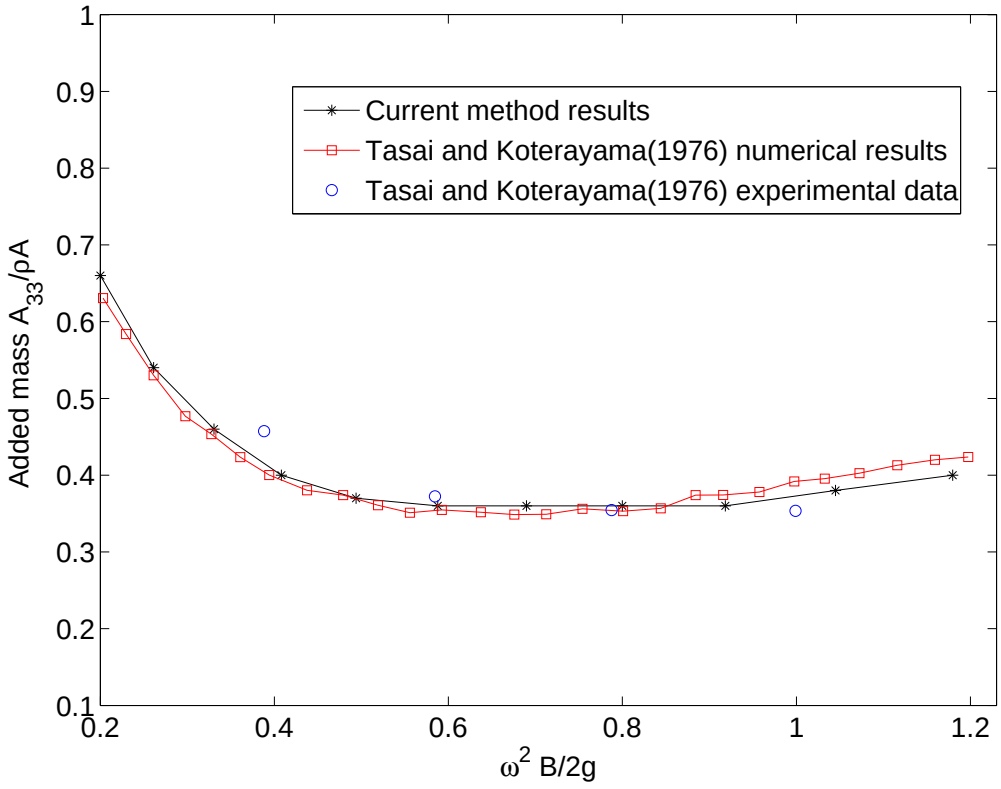

Figure 5.17: Comparison of heave added mass coefficient A_{33} Between Tasai and Koterayama (1976) numerical results, Tasai and Koterayama (1976) experimental data and current method prediction for a wedge of the beam-to-draught ratio $B/T = 2\sqrt{3}/3$ experiencing an oscillatory heave motion of amplitude $a = 0.2T$.

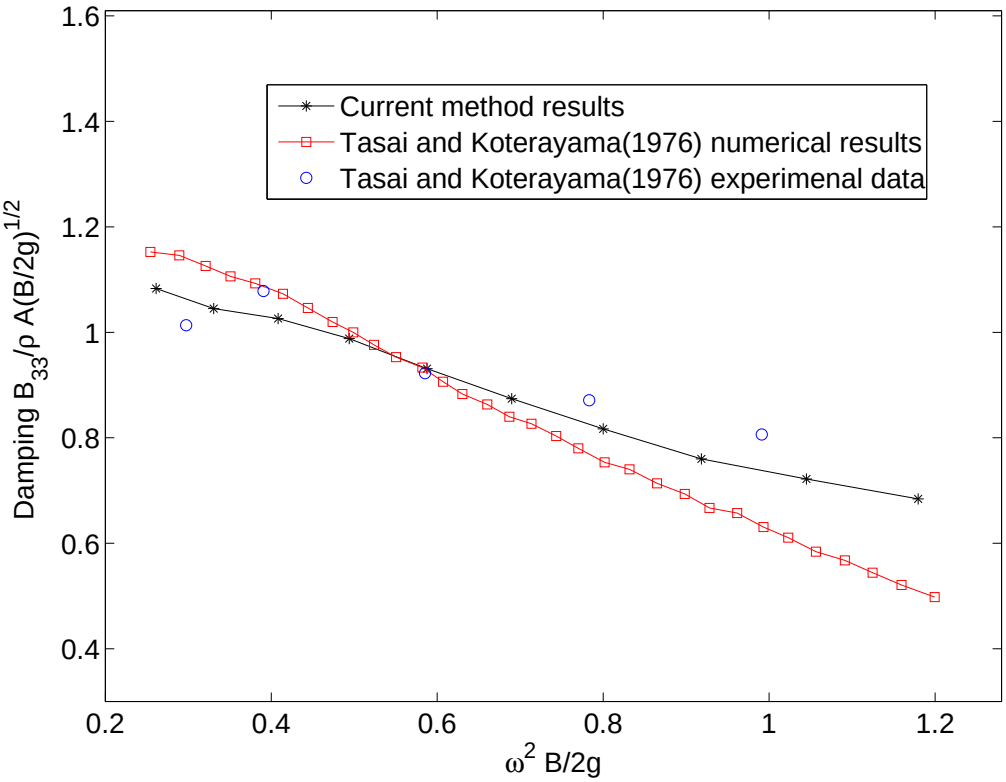

Figure 5.18: Comparison of heave damping coefficient B_{33} between Tasai and Koterayama (1976) numerical results, Tasai and Koterayama (1976) experimental data and current method prediction for a wedge of the beam-to-draught ratio $B/T = 2\sqrt{3}/3$ experiencing an oscillatory heave motion of amplitude $a = 0.2T$.

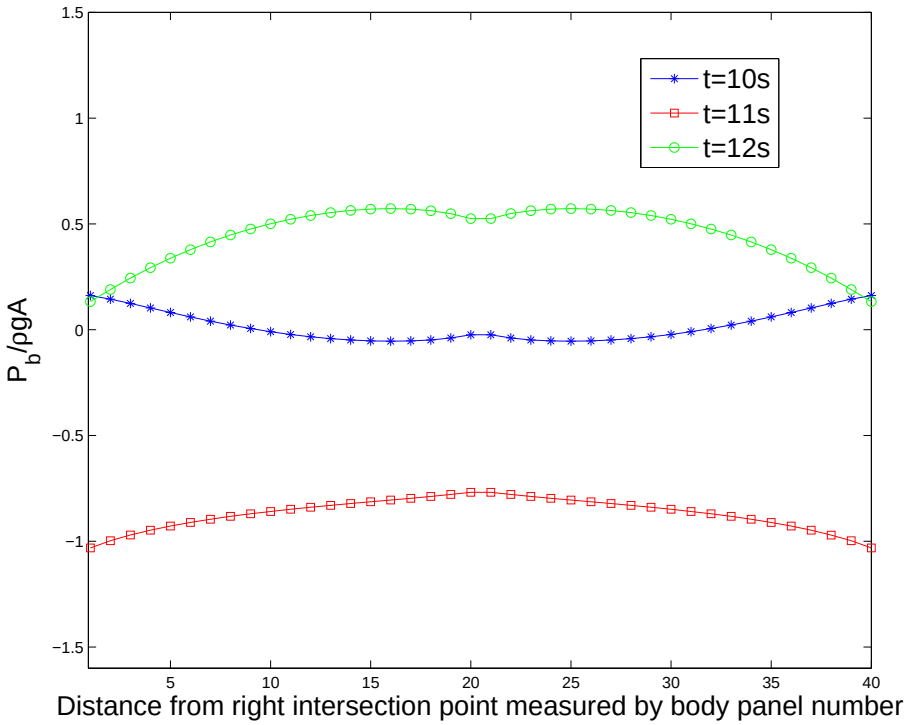

Figure 5.19: Predicted pressure distributions P_b at different times around wedge in oscillatory heave motion with amplitude $a = 0.2T$ and frequency $\omega^2 R/g = 1.0$.

5.4 Concluding remarks

The desingularized Rankine source boundary integral method coupled with MEL algorithm is used to study the two-dimensional nonlinear body-wave problem in this chapter. The source distribution is crucial for the numerical accuracy and efficiency. In order to reduce computation cost and improve accuracy, a new space increasing source point distribution method is developed with a single point treatment for the intersection points. In the form of increasing separation, the proposed distribution method places more nodes points in the first wave length but less in the followings compared to the even distribution method. This distribution pattern is in the line with the source strength decaying characteristics and therefore superior to the traditional even distribution scheme.

The total source point number is much less and therefore computational effort is significantly reduced. In addition, this distribution method connects the grids on the free surface with the body panels, so no extra node points are required to treat intersection points during the regrid process and therefore no numerical errors are introduced. Hence, the numerical results are improved.

Because of the time-dependence of the wetted body surface S_b and the calm water free surface S_f, both these surfaces S_b and S_f are regridded at every time step. The body panel number N_b and the free surface grid number N_f are independent of time. Thus the panel size of the wetted body surface varies in the time iteration process and the calm water surface regridding is only made in the horizontal direction. The present method is based on a Lagrangian specification applied on the nonlinear free surface dynamic and kinematic boundary conditions applied on the calm water surface. An extensive comparison validates the efficiency and robustness of the proposed method.

It is noticed that the present method applies to a medium body motion amplitude $a = 0.2T$ (say). The nonlinear body surface condition dominates the nonlinear response at this motion amplitude and therefore reasonable agreements are obtained even under the assumption that free surface conditions are only satisfied on the calm water surface. This mathematical model is limited in dealing with large motion amplitude problem, say $a = 0.4T$, when the nonlinearity of the free surface becomes more important. The free surface boundary conditions evaluated on the calm water surface inherently ignore the nonlinear effects of the free surface movement in the vertical direction and therefore

limit application when dealing with very large amplitude body-wave problems. The fully nonlinear problem involving the nonlinear free surface boundary conditions evaluated on the real free surface boundary for large motion amplitude is presented in following chapter.

Chapter 6

Two-dimensional fully nonlinear problem simulation for forced body oscillation motion

In the last two chapters, two-dimensional wave-body problems are investigated based on the proposed numerical techniques within the context of Rankine source and mixed Euler-Lagrange algorithms. The assumption that free surface boundary conditions are satisfied on the calm water surface is suitable for small and medium body motion amplitudes simulation and therefore satisfactory results were obtained for linear and nonlinear body boundary condition based wave-body problems in previous two chapters. However, under this assumption, the resulting numerical model is limited for a larger body motion amplitude problem because the excited free surface profile physically varies with the calm water surface during the time iteration process. In this chapter, a fully nonlinear numerical model is formulated to cope with a large body motion problem. Both nonlinear body boundary and free surface boundary conditions are satisfied on their instantaneous surface in this model.

6.1 Overview

Many phenomena occur involving with fully nonlinear wave-body problem, such as water entry and exit, slamming, green water on desk, wave overtopping, et cetera. The

investigations for these extreme nonlinear problems require many other complicated numerical techniques. For example, for water entry and exit problem, jet and spray cutting off, air cavity tracking, non-viscous flow separation control techniques are all crucial for numerical efficiency (Zhao and Faltinsen, 1993; Sun and Faltinsen, 2006; Yan et al., 2009). The research for these problem is out of the scope of this thesis. In order to understand the fundamental mechanism and basic characteristics for a fully nonlinear wave-body problem and check the efficiency of proposed numerical algorithms, the reported numerical simulation is confined to a representative nonlinear wave-body problem: forced body harmonic oscillatory motion around free surface with large motion amplitude.

Previous research adopting even source distribution method either takes account of the nonlinear free surface condition but ignores the nonlinear body surface condition (Cao et al., 1991b, 1992, 1993, 1994; Beck et al., 1994; Beck and Scorpio, 1995; Scorpio, 1997; Subramani et al., 1999; Finn, 2003; Lee, 2003) or otherwise applies the nonlinear body boundary condition whilst keeping the linear free surface boundary condition (Zhang and Beck, 2006, 2007; Zhang et al., 2010; Bandyk, 2009; Bandyk and Beck, 2011). Each of these methods neglects components of the nonlinearity for very large body motions. The even source distribution method is no longer adequate and frequently cause numerical divergency for fully nonlinear problem. In this chapter, the adopted space increment distribution scheme coupled with single point treatment for intersection points in the previous two chapters will be further developed to deal with large body motion problem.

The sawtooth instability occurs in the fully nonlinear wave-body problem in the context of mixed Euler-lagrange algorithm. The remove of this instability must be implemented to succeed time marching simulation. In order to renew the source points position to suppress the numerical divergency, most earlier investigation applied Chebyshev polynomial smoothing scheme which was originally developed by Longuet-Higgins and Cokelet (1976, 1978) with rare exception (Lin et al., 1984; Xue et al., 2001). Some influent investigations of smoothing technique application are presented in Table 6.1.

A least squares principle based smoothing method is newly developed to suppress sawtooth instability. Only three free surface source points in the instability range are used for this smoothing scheme, which is derived in detail in Section 3.5.

Table 6.1: Selected collection of investigations applying smoothing techniques to suppress saw tooth instability.

Author(s)/(year)	Smoothing mthod
Longuet-Higgins/Cokelet	Chebyshev polynomial
(1976,1978)	Chebyshev polynomial
Ferrant(1997)	Chebyshev polynomial
Koo/Kim(2004,2007)	Chebyshev polynomial
Zhang/Khoo/Lou(2006)	Chebyshev polynomial
Sun/Faltinsen(2006)	Chebyshev polynomial
Lin(1984)	smoothing operator
Xue,et.al (2001)	Savitzky Golay type smoothing filter

6.2 Numerical simulation setup

In this section, the numerical model for fully nonlinear problem is formulated and free surface source points distribution is presented in detailed.

6.2.1 Numerical model

For the fully nonlinear problem taking account of both nonlinear effects from body surface and free surface, numerical model should satisfy both nonlinear conditions at instantaneous surfaces. Free surface node(source) points stay along real free surface profile during time iteration. The node(source) points moves both in horizontal and vertical directions. The movement in horizontal direction is caused by the wetted body surface change under nonlinear body boundary condition. The source point moves in vertical direction because of the excited free surface variation based on the application of nonlinear free surface boundary condition. A flowchart in Figure 6.1 presents the numerical process for a fully nonlinear problem. Figure 6.1 is different from the flowchart for a nonlinear body boundary problem, see Figure 5.1, the free surface now needs to be re-discretized and smoothed for the fully nonlinear problem.

A floating body is placed piercing the free surface and is in an equilibrium position at initial time. This floating body is disturbed by a forced harmonic oscillation motion with velocity $V = a\omega\cos(\omega t)$ from time $t > 0$. The node and source points are placed

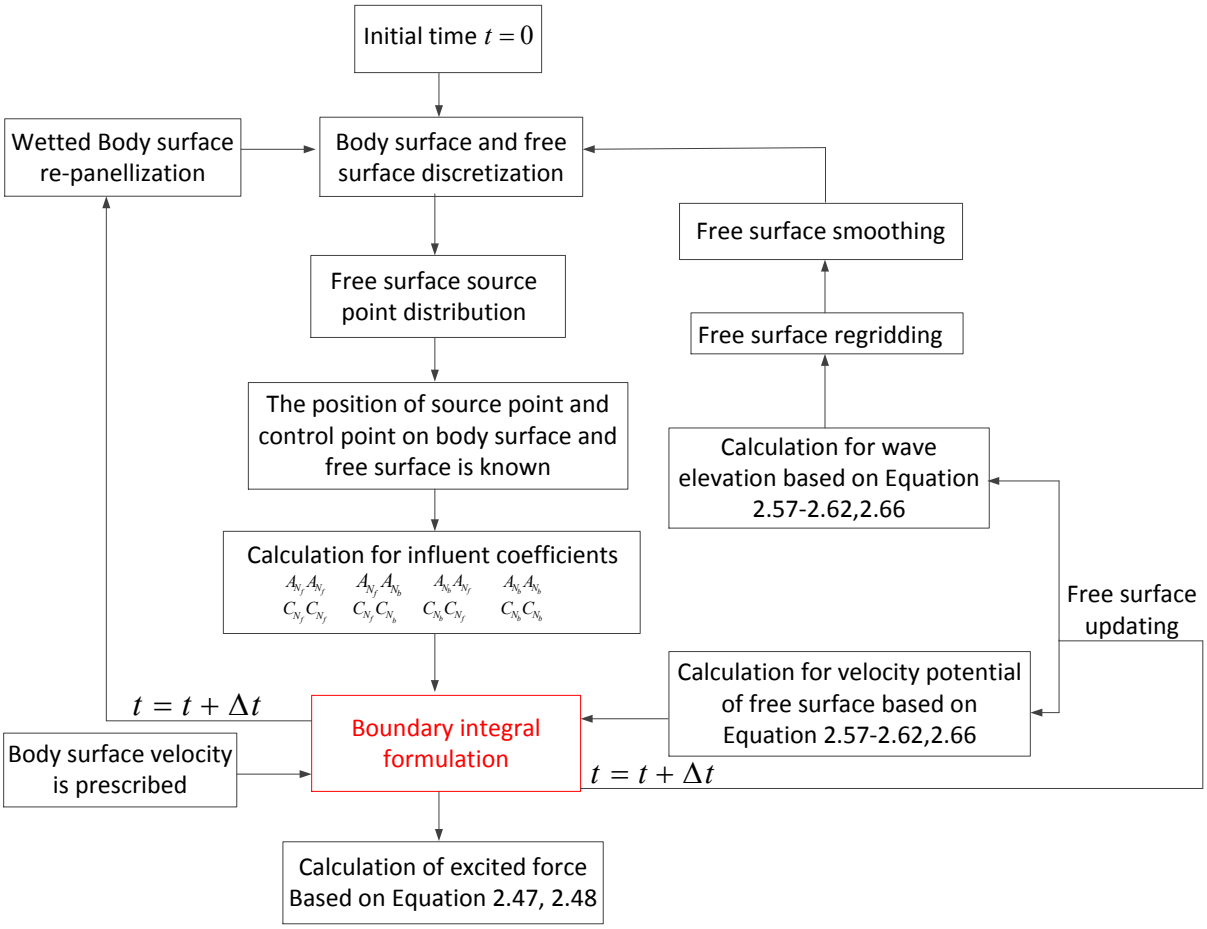

Figure 6.1: Flowchart of numerical process for two-dimensional fully nonlinear problem.

symmetrically around the floating body. Figure 6.2 presents the numerical model for fully nonlinear wave-body problem. A circular cylinder with $R/T = 1$ is adopted as floating body for the numerical setup in this section and numerical test and validation in Section 6.4. A wedge of ratio $B/2T = \tan 21.8°$ is chosen as floating body for further numerical validation.

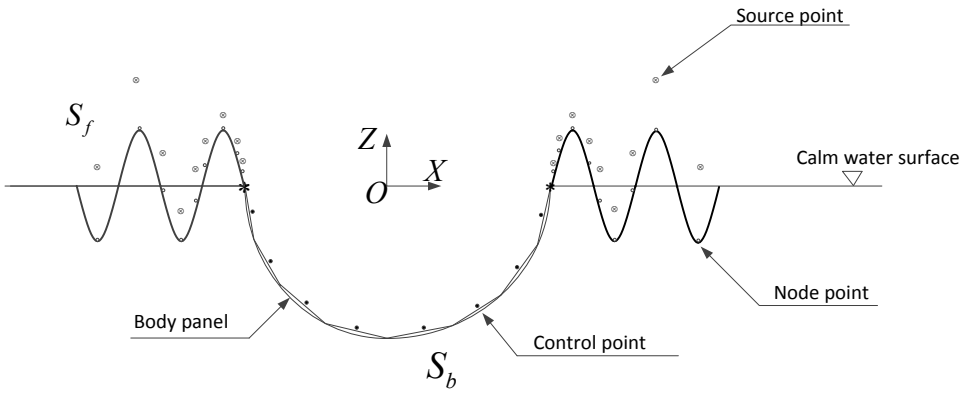

Figure 6.2: Numerical model of node (source) points distribution for fully nonlinear problem.

6.2.2 Free surface source point distribution

The space increment source distribution method is further developed for fully nonlinear problem. The calm water surface on the right hand side of S_f is divided into inner and outer domains distributed with nodes $P_{f,i}$. In the inner domain the neighbouring node distances starting from the intersection point $P_{f,0}$ are expressed in the form:

$$|P_{f,i} - P_{f,i-1}| = \frac{L_b \alpha_j}{\omega^2}, \;\; i = 1, ..., N_{in}. \tag{6.1}$$

20 points are distributed in the exponential form in outer domain:

$$|P_{f,i} - P_{f,i-1}| = |P_{f,N_{in}} - P_{f,N_{in}-1}| \times 1.0378^{i(i-1)/2}, \; i = 1, ..., 20. \tag{6.2}$$

The desingularized source Q_i is placed vertically above the node point $P_{f,i}$. The desingularized distance $D_{d,i}$ between them is given by the recommended equation (Cao, 1991):

$$D_{d,i} = |Q_i - P_{f,i}| = \sqrt{|P_{f,i-1} - P_{f,i}|} \tag{6.3}$$

for the right hand side sources. The wave problem is treated symmetrical for the oscil-

latory body movement and the left hand side sources are therefore arranged in a mirror image.

Table 6.2: Comparison of added mass A_{33} and damping coefficient B_{33} between experimental data (Yamashita, 1977) and numerical data varying with α_1 and α_2 for a cylinder in oscillatory heave motion with amplitude $a = 0.4T$, frequency $\omega^2 B/2g = 1.0$. Symbol $\bigotimes$ indicates numerical divergence with no data derived.

	measured data	numerical data							
α_1		$\frac{10}{2}$	$\frac{10}{4}$	$\frac{10}{6}$	$\frac{10}{8}$	1	$\frac{10}{12}$	$\frac{10}{14}$	$\frac{10}{16}$
α_2		10	$\frac{10}{3}$	$\frac{10}{5}$	$\frac{10}{7}$	$\frac{10}{9}$	$\frac{10}{11}$	$\frac{10}{13}$	$\frac{10}{15}$
A_{33}	0.71	0.84	0.84	0.75	0.74	0.74	0.74	$\bigotimes$	$\bigotimes$
B_{33}	0.36	0.17	0.17	0.23	0.28	0.29	0.36	$\bigotimes$	$\bigotimes$

Separation factors $\alpha_j (j = 1, ..., 9)$ define the distance between neighbouring node points and their selection are crucial for the convergence of the proposed iteration scheme. This is especially true for α_1 and α_2, which determine the location of the first two sources next to the intersection point $P_{f,0}$. If these two distances are too small, numerical divergence will occur and stop the numerical simulation. Extensive numerical simulations were performed for various values of α_j to derive their most suitable values. Selected results are displayed in Table 6.2, which shows the sensitivity of added mass, A_{33}, and damping coefficient, B_{33} to the values of α_1 and α_2. These data further forms the basis of the information for α_j presented in Table 6.3. 135 node points are required in inner domain on right side.

Table 6.3: The values of separation factors α_j for fully nonlinear problem.

i	1	2-10	11-30	31-50	51-70	71-90	91-110	111-130	131-135
j	1	2	3	4	5	6	7	8	9
α_i	$\frac{10}{12}$	$\frac{10}{11}$	1	1.1	1.5	1.9	2.4	3.0	3.6

6.2.3 Source strength decaying

From the intersection point outwards, the importance of the source points decreases as the distance increases. Figure 6.3 present the source strength $|\sigma_f|$ of the first 20 source

points for the circular cylinder in oscillatory heave motion with amplitude $a = 0.4T$ and frequency $\omega^2 R/g = 0.5$. This figure shows that source strengths decay quickly from the first point and trends to zero around the 20th point and therefore their importance rapidly decreases as their position is located further from the intersection point. The proposed method displaces higher source point density near to the intersection point and lower density at the source points located farther away from intersection point. This distribution scheme holds a reasonable conformity with source strength decaying characteristics and therefore can reduce numerical instability for fully nonlinear problem in present simulation.

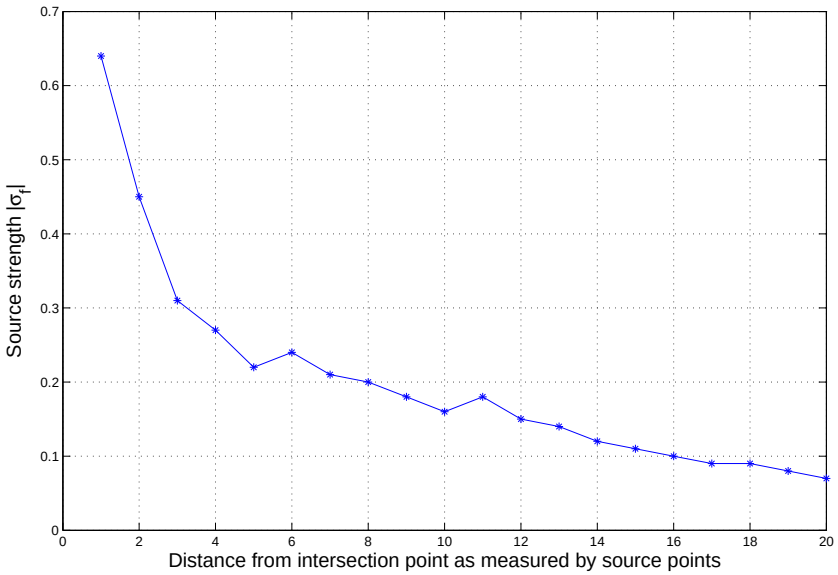

Figure 6.3: Source strength for the first 20 source point distribution for a circular cylinder in oscillatory heave motion with amplitude $a = 0.4T$ and frequency $\omega^2 B/2g = 0.5$.

6.3 Numerical instability and smoothing

Since the flow satisfies the nonlinear conditions on the free surface and wetted body boundaries and the free surface wave is propagated from the intersection points of the nonlinear boundaries, the flow around the intersection points is very vulnerable to di-

vergence in the time iteration scheme for forced body oscillatory motion. Only limited numerical results were derived without the smoothness algorithm applied.

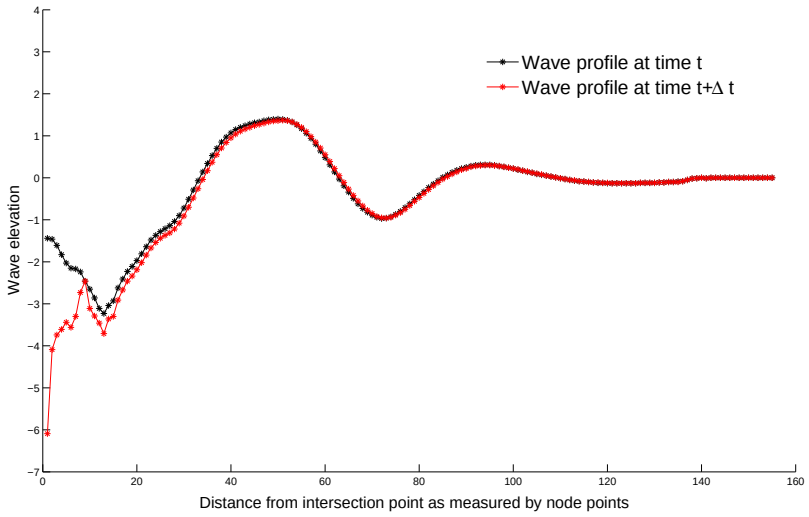

Figure 6.4: Numerical divergence of the wave profile at different time steps.

As described in Chapter 3, the sawtooth phenomenon occurs in the mixed Euler-Lagrange formulation applied in this model for larger body motion amplitude a and (or) frequency ω. This instability leads to numerical failure quickly after it happens as shown in Figure 6.4.

With the use of the three points least square smoothing algorithm, the stability range is enlarged significantly to cover larger amplitude and frequency motions. Figure 6.5 shows comparison of the stability amplitude-frequency ranges for an oscillatory cylinder motion before and after smoothing scheme applied.

6.4 Numerical results for large body motion amplitude

Following the numerical model setup in the last two subsections, numerical simulations based on these new techniques are executed and predicted results are compared with published data to validate the proposed methods in this section.

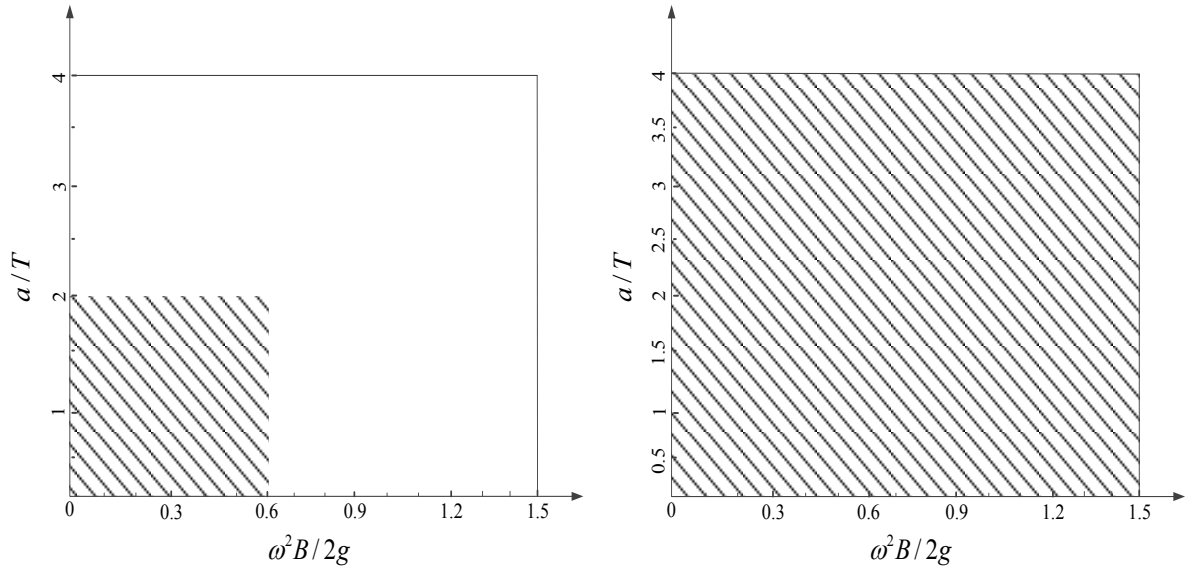

Figure 6.5: The frequency and amplitude that results can be obtained for an oscillatory heave motion before and after smoothing.

When the floating body oscillates with very large amplitude, the nonlinear effects from variation of wetted body surface and free surface become significantly important. The floating body oscillates uniformly with motion amplitude $a = 0.4T$ to show the high nonlinearity in this section. The produced results for added mass coefficient A_{33}, damping coefficient B_{33}, First, second and third order harmonic forces $(F^1(\omega), F^2(\omega), F^3(\omega))$ for circular cylinder are presented as initial validation in Section 6.4.1 and high order force responses for wedge are given as further validation in Section 6.4.2.

6.4.1 Numerical results for circular cylinder with large motion amplitude

Numerical results of added mass coefficient A_{33} and damping coefficient B_{33} are displayed respectively in Figures 6.6 and 6.7 using the current fully nonlinear method and

compared with the experimental data of Yamashita (1977), the linear results based on numerical model in Chapter 4 and the body nonlinear method results based on the numerical model in Chapter 5. In both figures the predicted findings of the described fully nonlinear mathematical model methods show reasonable agreement to the experimental data and illustrate the contributions of the nonlinearities to the total result. For this large amplitude motion, the effect of the free surface nonlinearity exceeds that of the body boundary nonlinearity.

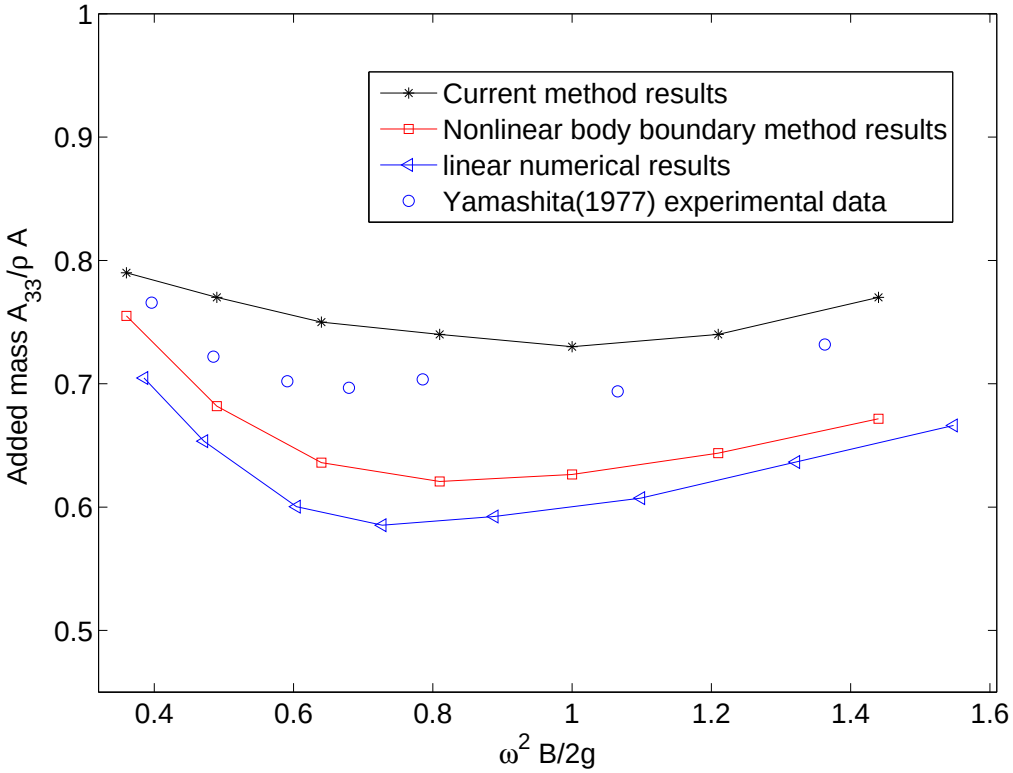

Figure 6.6: Comparison of heave added mass coefficient A_{33} between nonlinear body boundary condition method, linear numerical results, Yamashita (1977) experimental data, and current method prediction for a circular cylinder experiencing an oscillatory heave motion of amplitude $a = 0.4T$.

The proposed method is further validated by comparing first, second, and third order harmonic force responses in the frequency domain. Figure 6.8 shows the comparison of first order force predictions from the current method with the experimental data and linear numerical results of Tasai and Koterayama (1976). Figure 6.9 compares second order force

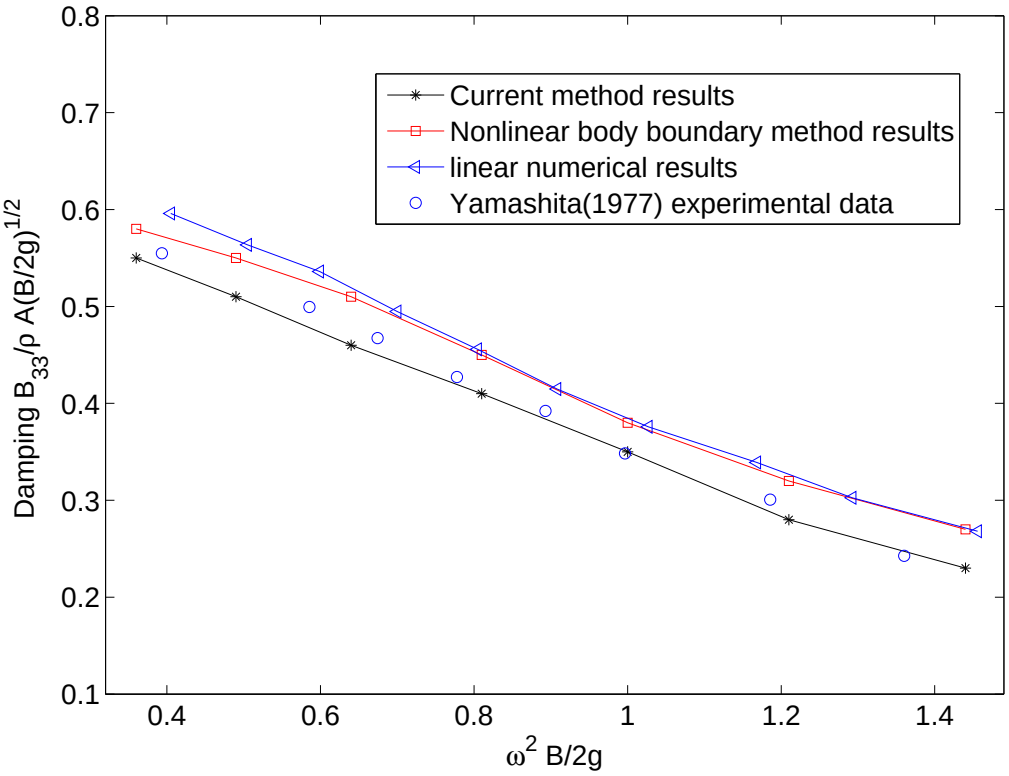

Figure 6.7: Comparison of heave damping coefficient B_{33} between nonlinear body boundary condition method, linear numerical results, Yamashita (1977) experimental data, and current method prediction for a circular cylinder experiencing an oscillatory heave motion of amplitude $a = 0.4T$.

predictions from the proposed method with the experimental data of Yamashita (1977) and numerical results of Zhang and Beck (2007). Figure 6.10 presents comparisons of third order force derived from the current proposed method with the experimental and numerical results of Yamashita (1977). In the experiment test of Tasai and Koterayama (1976); Yamashita (1977), the time-domain force is recorded by sensors around the body surface and then $F^1(\omega)$, $F^2(\omega)$ and $F^3(\omega)$ are obtained by Fourier transform as shown in Equations 3.32, 3.33 and 3.34. All these figures illustrate that the present method results are in reasonable agreement with experimental data. One reason for the deviation is the artificial error introduced by proposed smoothing algorithm. For high order force responses, the predicted $F^2(\omega)$ and $F^3(\omega)$ conform with the experimental better than other numerical simulations.

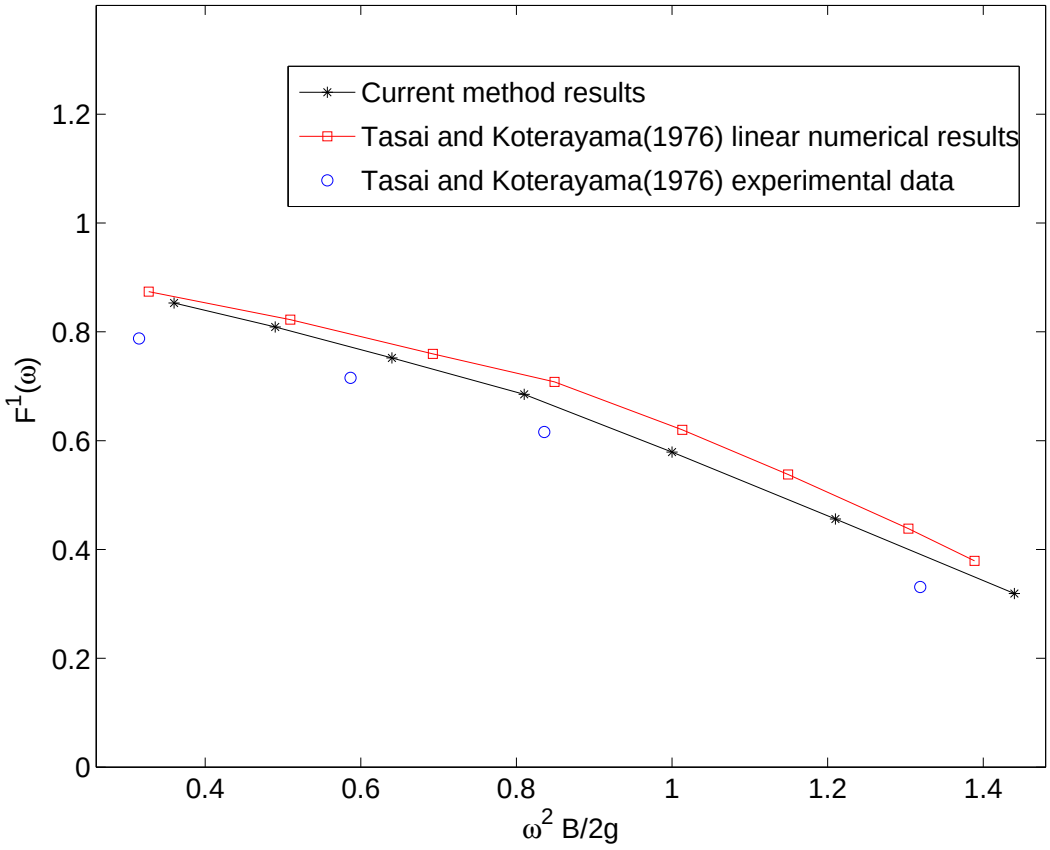

Figure 6.8: Comparison of first order harmonic force $F^1(\omega)$ between Tasai and Koterayama (1976) linear numerical results, Tasai and Koterayama (1976) experimental data, and current method prediction for a circular cylinder experiencing an oscillatory heave motion of amplitude $a = 0.4T$.

The time series of wave elevation $\eta(t)$, inertia component force $F^1(t)$ and quadratic component force $F^2(t)$ for this motion when $\omega^2 B/g = 0.5$ are presented in Figure 6.11, 6.12 and 6.13. Figure 6.11 shows wave peaks become very sharp in this strong nonlinear response. In linear and weak nonlinear problems, the inertia component mainly contains the first order force with the quadratic component dominated by the second order force. In strong nonlinear problem, however, higher order force components become important and are of the same order of magnitude as the low order forces.

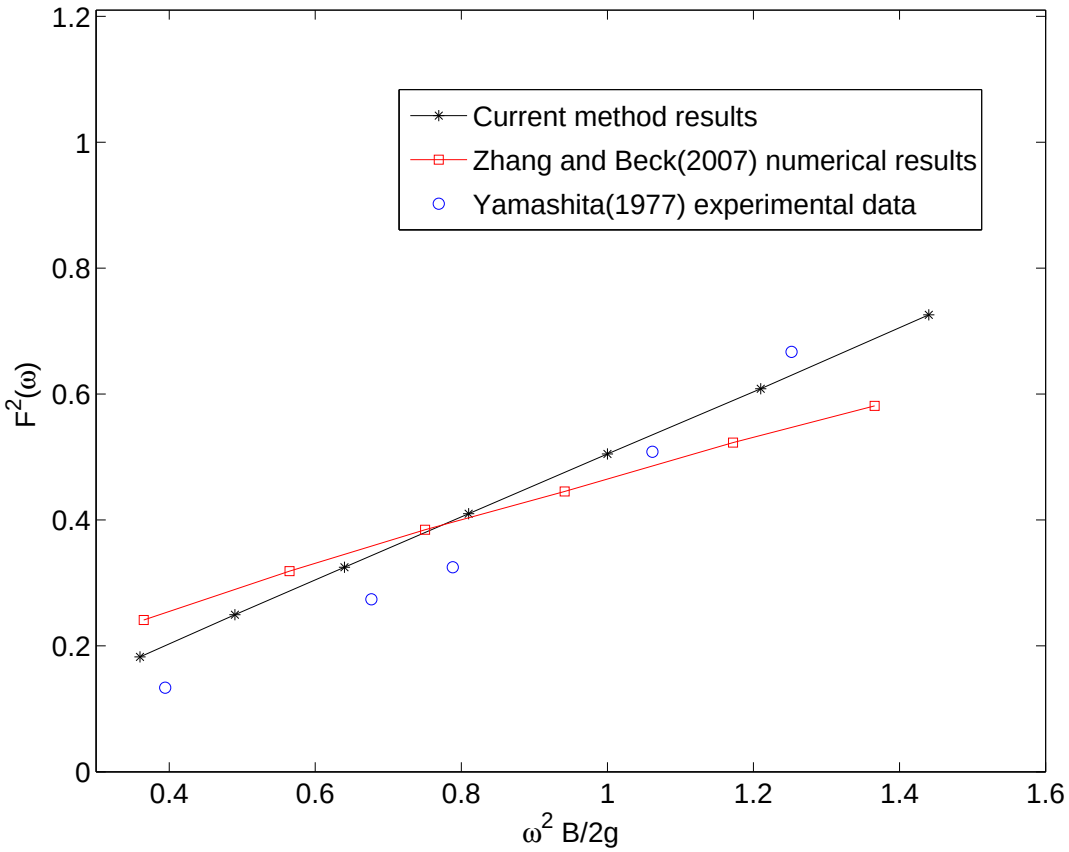

Figure 6.9: Comparison of second order harmonic force $F^2(\omega)$ between Zhang and Beck (2007) numerical results, Yamashita (1977) experimental data, and current method prediction for a circular cylinder experiencing an oscillatory heave motion of amplitude $a = 0.4T$.

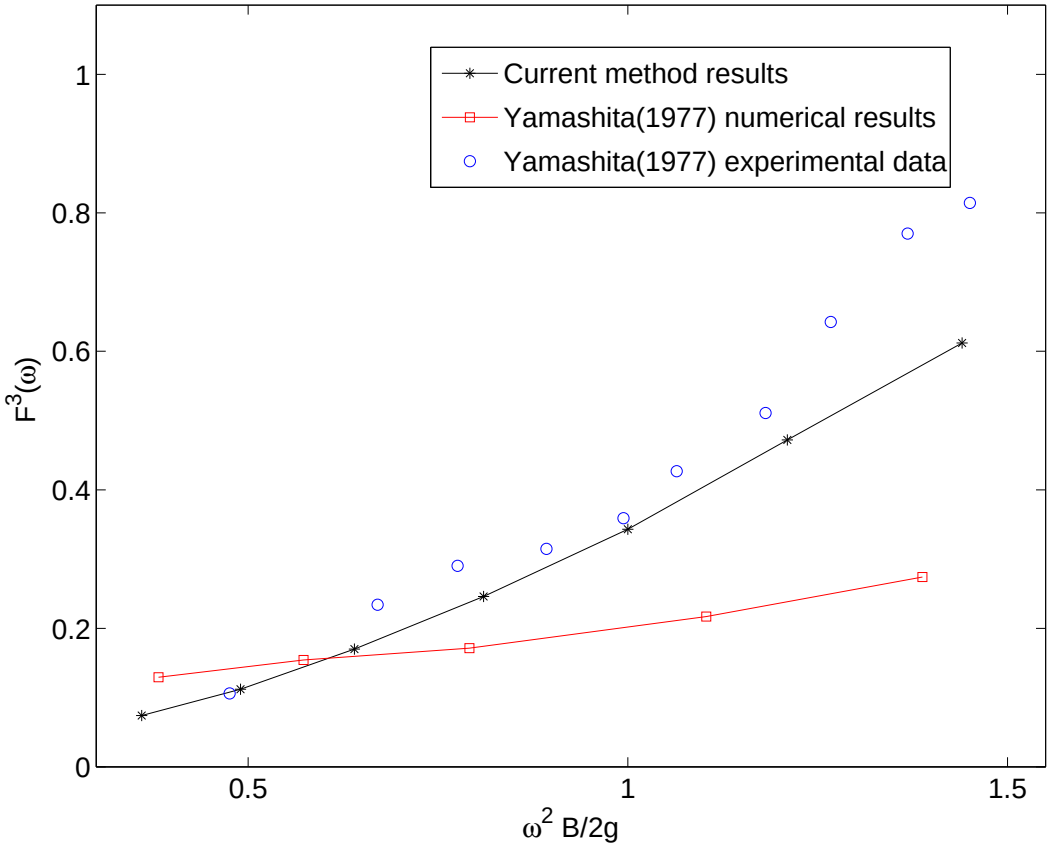

Figure 6.10: Comparison of third order harmonic force $F^3(\omega)$ between Yamashita (1977) numerical results, Yamashita (1977) experimental data, and current method prediction for a circular cylinder experiencing an oscillatory heave motion of amplitude $a = 0.4T$.

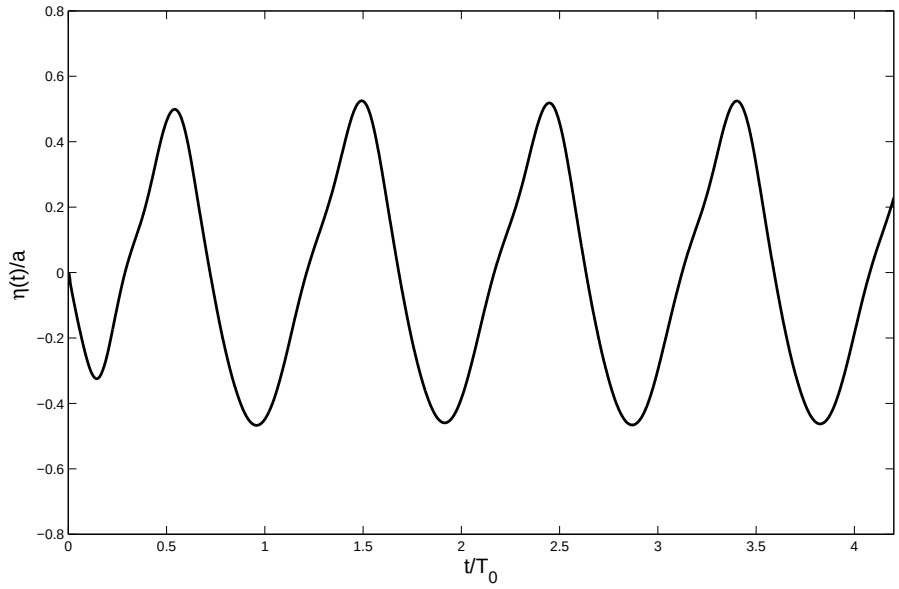

Figure 6.11: Time series of wave elevation $\eta(t)$ for circular cylinder in oscillatory heave motion with amplitude $a = 0.4T$ and frequency $\omega^2 B/g = 0.5$.

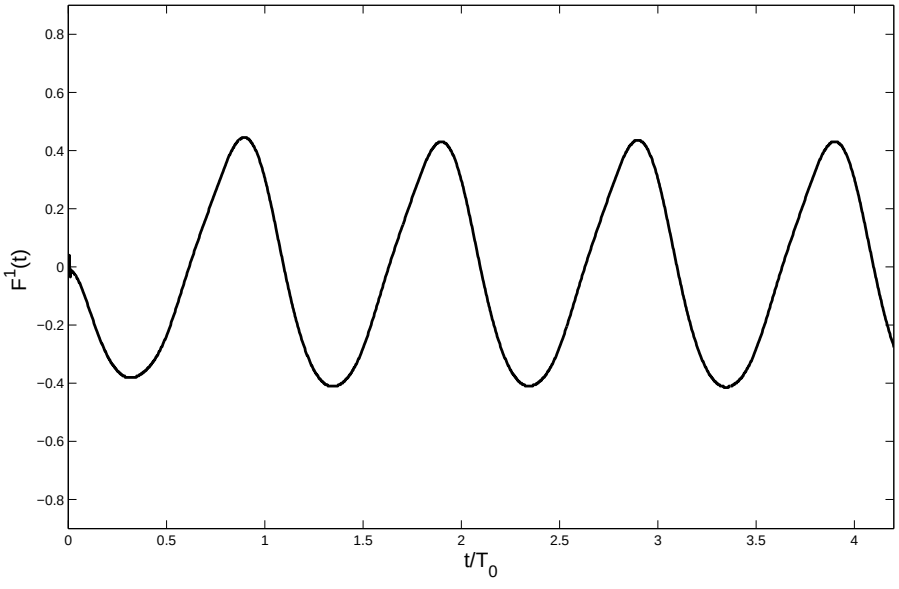

Figure 6.12: Time series of inertia component force $F^1(t)$ for circular cylinder in oscillatory heave motion with amplitude $a = 0.4T$ and frequency $\omega^2 B/2g = 0.5$.

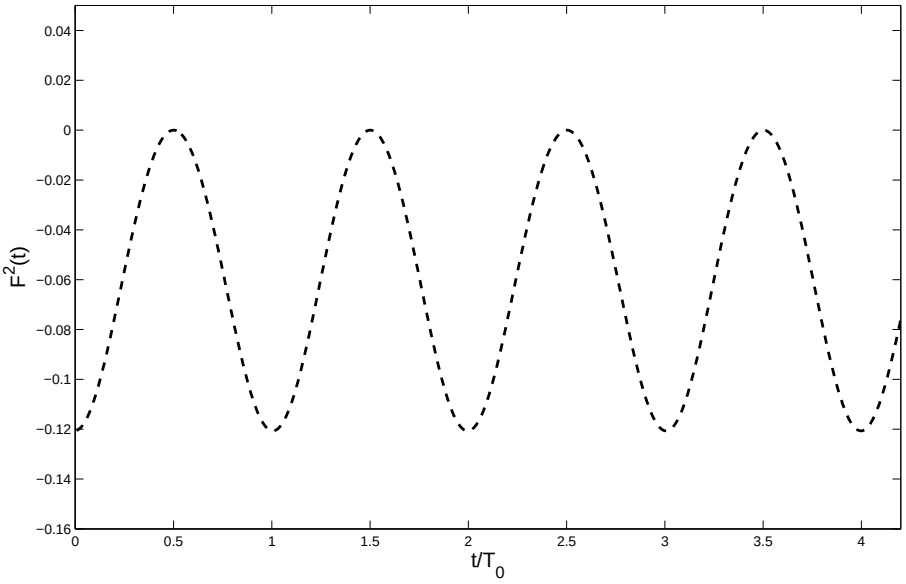

Figure 6.13: Time series of quadratic component force $F^2(t)$ for circular cylinder in oscillatory heave motion with amplitude $a = 0.4T$ and frequency $\omega^2 B/2g = 0.5$.

6.4.2 Numerical results for wedge with large motion amplitude

Numerical simulation for the wedge is further executed for high order response in this section. This wedge has a sharp angle on the bottom which will cause strong nonlinear effects when it undergoes large motion. Figure 6.14 compares second order force $F^2(\omega)$ predictions from the proposed method with the experimental data of Yamashita (1977). Figure 6.10 presents comparisons of third order force $F^3(\omega)$ derived from the current proposed method with the experimental and numerical results of Yamashita (1977).

The difference of second order response is worse than third order simulation, this is because the experimental data is scattered in the test for second order response (Yamashita, 1977). Reasonably good agreement is obtained for both high order responses. The discrepancy is mainly due to the viscous flow separation that occurs and the resulting vortex shedding affects the loads on the wedge surface (Yeung and Anathakrishnan, 1992; Sun, 2007).

In the numerical simulation, the wave elevation near to the intersection points first becomes unstable and leads to the failure of the simulation. Therefore, the first three free surface control points are modified and both wave elevation η and free surface source point velocity are updated by the least square smoothness process. The divergence reduces after these control points are smoothed and the simulation process continues. The smoothing treatment varies for different cases but, generally, when the control points are located closer to the intersection points, less time steps are needed to stop numerical divergence. In all current simulations, the iteration scheme remains stable when the flow around the interaction points are smoothed, though up to three applications of the smoothness procedure are required to derive results at high frequencies.

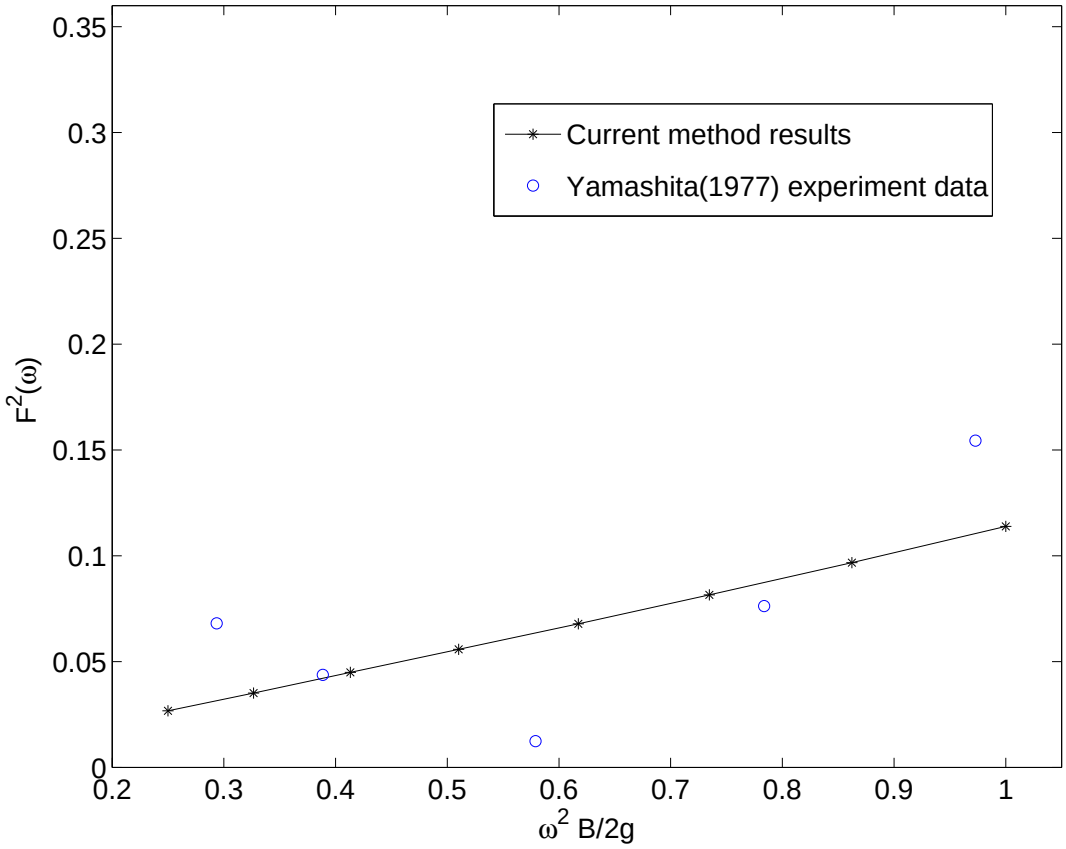

Figure 6.14: Comparison of second order harmonic force $F^2(\omega)$ between Yamashita (1977) experimental data and current method prediction for a wedge experiencing an oscillatory heave motion of amplitude $a = 0.4T$.

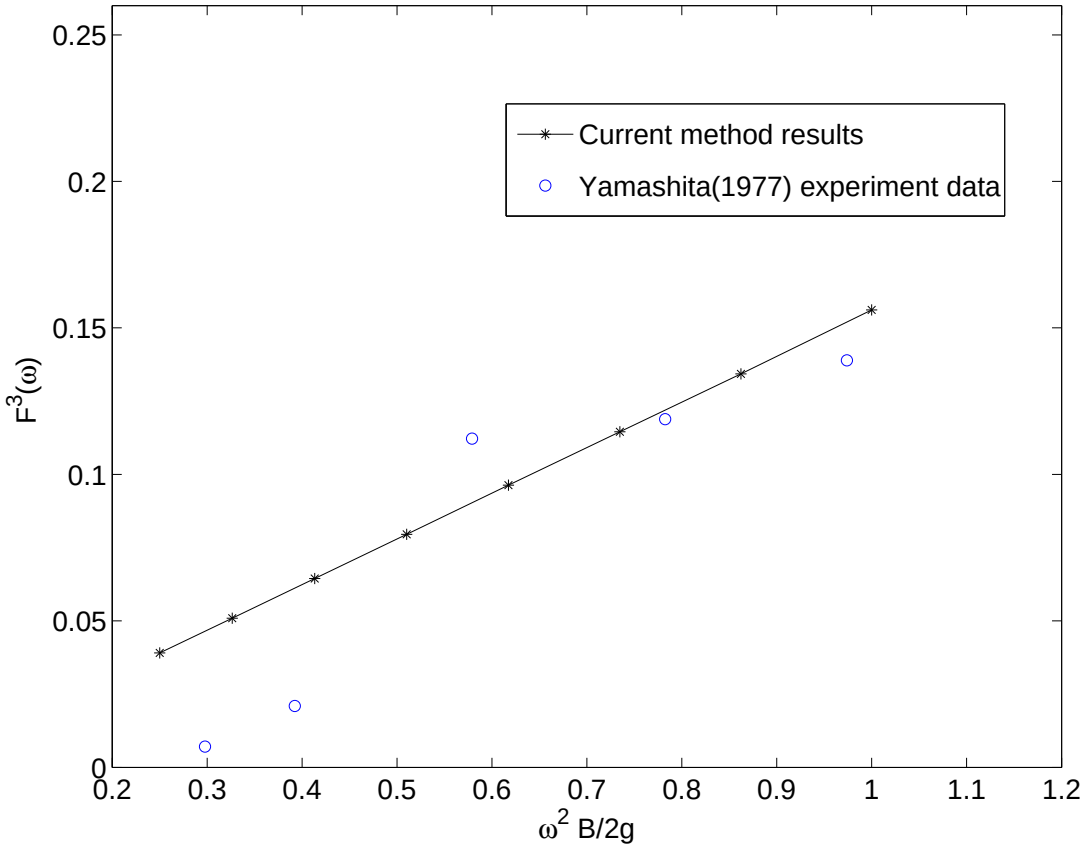

Figure 6.15: Comparison of third order harmonic force $F^3(\omega)$ between Yamashita (1977) experimental data and current method prediction for a wedge experiencing an oscillatory heave motion of amplitude $a = 0.4T$.

6.5 Concluding remarks

Rankine source integral method in combination with a mixed Euler-Lagrange algorithm is further developed to deal with two-dimensional full nonlinear wave-body problem in this chapter. The source distribution on free surface is significantly important for numerical convergence and accuracy. Improper distribution leads to a divergent numerical simulation which starts quickly from the beginning of the time iteration process. The newly adopted space increment distribution pattern in the last two chapters is further applied here. The exact positions for source points are selected according to numerical accuracy for a circular cylinder with forced oscillatory heave motion around free surface.

Compared to linear and body boundary nonlinear problems, the described method requires more source points and those closest to the intersection points need to be more finely distributed. A careful selection of these points distribution is extremely important. However, this divergence phenomenon does not appear in linear and partial nonlinear problems.

For each intersection point, a single point method is proposed treating the intersection point as a body surface point, rather than the double point method of earlier investigations by adding an additional desingularized free surface source vertically above the intersection point. The position of first free surface source point is selected using the same method as for other free surface source points. A least square based smoothing method is implemented to suppress the possible sawtooth phenomenon, reported previously in mixed Euler-Lagrange formulations.

The described numerical techniques are combined together to produce a robust solver for the two-dimensional fully nonlinear wave-body problem under examination. The accuracy and efficiency of the proposed mathematical model are validated in numerical tests for a cylinder and wedge undergoing large amplitude heave motion by comparison with published data. Up to third order responses are compared with published data and good agreement is achieved for both the smooth body (cylinder) and sharp shape body (wedge).

The finish of this chapter marks the end for two-dimensional problem investigation and in the next chapter the numerical simulation will move forward to three-dimensional problem range.

Chapter 7

Numerical algorithm for three-dimensional wave-body problems

In this chapter, the numerical algorithm used for three-dimensional wave-body problems will be described in detail. This includes body surface and free surface discretisation, free surface source point distribution, intersection points treatment, and desingularized distance selection.

The numerical process for a three-dimensional wave-body problem is essentially the same as for a two-dimensional case. The simulation starts from an initial time $t = 0$, when the floating body is in a state of hydrostatic equilibrium and the free surface coincides with the undisturbed calm water surface. The body surface and free surface are then discretised as described in Section 7.1. Once the position of wetted surface control points and the position of free surface source point and control point are assigned after discretisation, the influence coefficient matrices can be evaluated as described in Section 7.2 and Appendix *A*. The influence coefficient matrix together with boundary conditions construct the boundary integral equations. The detailed formulation of the integral equations and the solution process are described in Section 2.4.3.

For a linear wave-body problem, the source points and control points remain fixed during the whole numerical simulation and therefore the influence coefficients are calculated

only once and applied at every time step. In contrast the nonlinear problem requires both body surface and free surface discretisations and reevaluation of influence coefficients at every time step. The numerical process for three-dimensional linear and nonlinear body boundary condition problems is presented in Figures 7.1 and 7.2. To avoid repetition, other applied numerical techniques for three-dimensional problems which are similar to the two-dimensional cases will be not derived again.

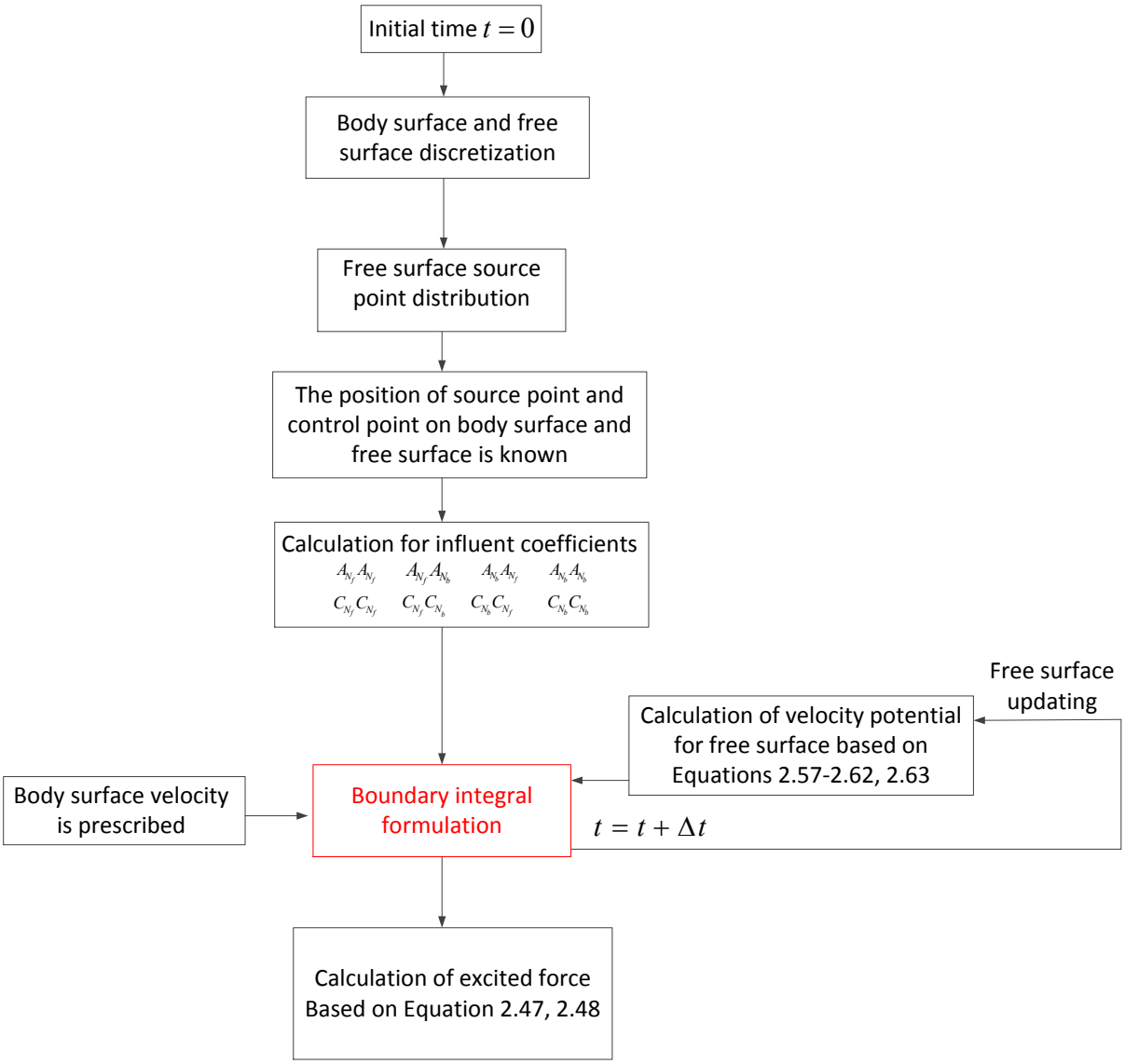

Figure 7.1: Flowchart of numerical process for three-dimensional linear problem.

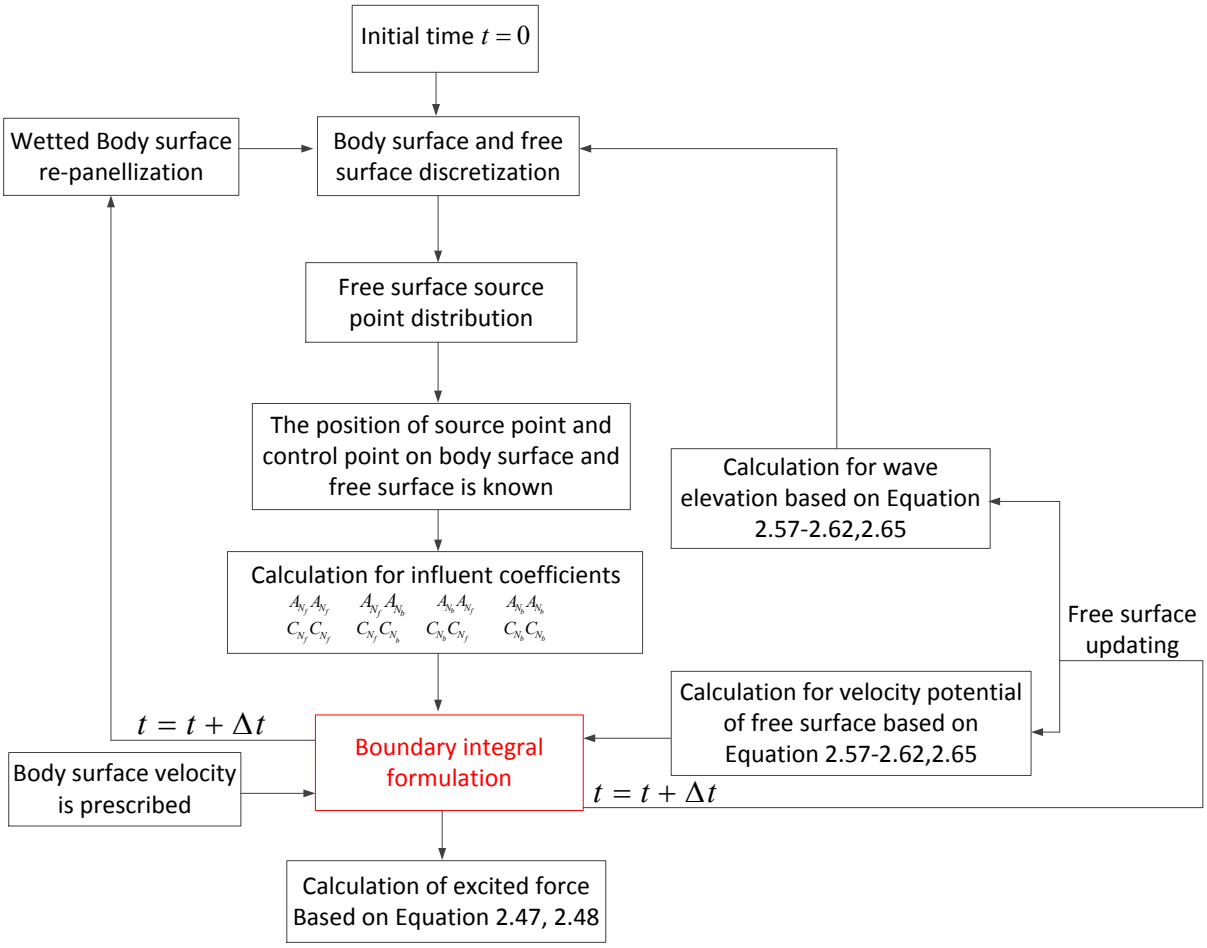

Figure 7.2: Flowchart of numerical process for three-dimensional nonlinear body boundary condition problem.

7.1 Discretisation of free surface and body surface

A three-dimensional body floating on a free surface with forced oscillatory motion is considered here. The continuous calm water surface is replaced by node points in isolation and N_f source points $Q_i(i = 1, ..., N_f)$ with source strengths $\sigma_i^f(Q_i, t)(i = 1, ..., N_b)$ displaced vertically above each node point. The body surface S_b is divided into N_b panels with source points $Q_j(j = 1, ..., N_b)$ of constant strength $\sigma_j^f(Q_j, b)(j = 1, ..., N_b)$ on each panel. Figure 7.3 shows the numerical model schematic for this three-dimensional wave-body problem. This discretisation of both free surface S_f and body surface S_b means that instead of solving Equation 2.41, a free surface time iteration is applied to the following desingularized formulations

$$\phi_{S_f}(P_f, t) = \sum_{i=1}^{N_f} \sigma_i^f(Q_i, t) \frac{1}{r_{P_f Q_i}} + \sum_{j=1}^{N_b} \sigma_j^b(Q_j, t) \int_{S_{b,j}} \frac{1}{r_{P_f Q_j}} ds, \tag{7.1a}$$

$$\frac{\partial \phi_{S_b}(P_b, t)}{\partial n_b} = \sum_{i=1}^{N_f} \sigma_i^f(Q_i, t) \frac{\partial \frac{1}{r_{P_b Q_i}}}{\partial n_b} + \sum_{j=1}^{N_b} \sigma_j^b(Q_j, t) \int_{S_{b,j}} \frac{\partial \frac{1}{r_{P_b Q_j}}}{\partial n_b} ds. \tag{7.1b}$$

Similarly Equations 2.33 and 2.39 can be formulated as:

$$\frac{\partial \phi_{S_f}(P_f, t)}{\partial z} = \sum_{i=1}^{N_f} \sigma_i^f(Q_i, t) \frac{\partial \frac{1}{r_{P_f Q_i}}}{\partial z} + \sum_{j=1}^{N_b} \sigma_j^b(Q_j, t) \int_{S_{b,j}} \frac{\partial \frac{1}{r_{P_b Q_j}}}{\partial z} ds, \tag{7.2a}$$

$$\phi_{S_b}(P_b, t) = \sum_{i=1}^{N_f} \sigma_i^f(Q_i, t) \frac{1}{r_{P_b Q_i}} + \sum_{j=1}^{N_b} \sigma_j^b(Q_j, t) \int_{S_{b,j}} \frac{1}{r_{P_b Q_j}} ds, \tag{7.2b}$$

The body surface is formulated by a spherical coordinate system, thus

$$\begin{aligned} x &= R\cos\theta\sin\phi \quad (0 \le \theta \le 2\pi, \quad 0 \le \phi \le \pi) \\ y &= R\sin\theta\sin\phi \quad (0 \le \theta \le 2\pi, \quad 0 \le \phi \le \pi) \\ z &= R\cos\phi \quad (0 \le \phi \le \pi) \end{aligned} \tag{7.3}$$

Here θ and φ are polar and azimuth angles respectively. The wetted body surface

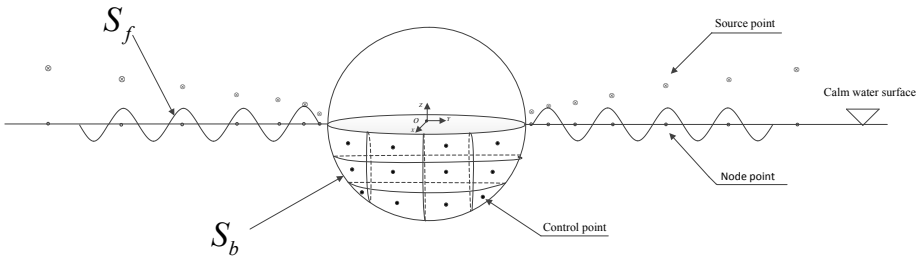

Figure 7.3: Three-dimensional wave-body numerical model sketch.

is divided evenly in θ and φ and in both latitude and longitude directions. The panel central point is taken as control point for each panel of the body surface.

The wetted body surface is divided evenly in both latitude and longitude directions. For example with 10 portions, the spherical wetted surface is modeled by a total of $10X10 = 100$ panels, as recommended by Zhang and Beck (2008).

7.2 Calculation for induced influence coefficient

Similar to the two-dimensional problem in Chapter 3, $\partial\phi_{S_b}(P_b,t)/\partial n_b$ and $\partial\phi_{S_f}(P_f,t)/\partial z$ are replaced with $v_{bn}(P_b,t)$ and $v_{fz}(P_f,t)$ respectively in the left sides of Equation 7.1 and Equation 7.2. These two equations can be formulated in a compact format as:

$$\begin{bmatrix} A_{N_fN_f} & A_{N_fN_b} \\ A_{N_bN_f} & A_{N_bN_b} \end{bmatrix} \begin{bmatrix} \sigma^f \\ \sigma^b \end{bmatrix} = \begin{bmatrix} \phi_{S_f} \\ v_{bn} \end{bmatrix}, \tag{7.4}$$

and

$$\begin{bmatrix} C_{N_fN_f} & C_{N_fN_b} \\ C_{N_bN_f} & C_{N_bN_b} \end{bmatrix} \begin{bmatrix} \sigma^f \\ \sigma^b \end{bmatrix} = \begin{bmatrix} v_{fz} \\ \phi_{S_b} \end{bmatrix}, \tag{7.5}$$

where $A/C_{N_fN_f}$, $A/C_{N_fN_b}$, $A/C_{N_bN_f}$ and $A/C_{N_bN_b}$ are influence coefficients which must be evaluated respectively.

Coefficients $A_{N_fN_f}$ and $C_{N_fN_f}$ reflect the influence of the free surface source points on free surface node points, and are given by:

$$A_{N_fN_f} = \frac{1}{r_{P_fQ_f}}, \tag{7.6}$$

and

$$C_{N_fN_f} = \frac{\partial \frac{1}{r_{P_fQ_f}}}{\partial z}. \tag{7.7}$$

Coefficients $A_{N_bN_f}$ and $C_{N_bN_f}$ reflect the influence of free surface source points on the body panels control points, and are given by:

$$A_{N_bN_f} = \frac{\partial \frac{1}{r_{P_bQ_f}}}{\partial n_b}, \tag{7.8}$$

and

$$C_{N_bN_f} = \frac{1}{r_{P_bQ_f}}. \tag{7.9}$$

In addition, $A_{N_fN_b}$ and $C_{N_fN_b}$ reflect the influence of body panel control points on free surface node points whereas $A_{N_bN_b}$ and $C_{N_bN_b}$ reflect the influence of body panel control points on body panel control points. The calculation of these coefficients requires the transformation of curved panels into flat quadrilateral panels based on the method of Hess and Smith (Hess and Smith, 1964, 1967; Newman, 1986). The process is presented in Appendix A.

7.3 Space increment source point distribution

For desingularized Rankine source method, the continuous free surface profile is replaced by source points in isolation and free surface boundary conditions are satisfied on these insolated source points. The method of distribution for these source points is a key technique for the Rankine source method. The position and number of source points decide the numerical accuracy and efficiency. In this section, the adopted space increment distribution method for source point arrangement in horizontal direction will be further developed for three-dimensional wave-body problem. In addition, a new vertical desingularized distance scheme is proposed to cope with the new space increment method.

Numerical model of sphere experiencing forced oscillatory heave motion is selected to aid the application of the proposed method.

7.3.1 Free surface inner domain distribution

In each horizontal direction, the free surface is divided into inner and outer domains. The neighbouring source points starting from the intersection point $P_{f,0}$ is expressed as:

$$|P_{f,i} - P_{f,i-1}| = \frac{2\pi g S_{b,0} \alpha_j}{\omega^2}, i = 1, ..., N_{in} \tag{7.10}$$

where $S_{b,0}$ is the surface size of the body panel attached to the intersection point. ω is the body oscillation frequency, and α_j are separation factors which decide the separation distances between two neighbouring source points in the radiation direction. The inner domain is divided into 4 ($j = 1, ..., 4$) regions with the same number of source points located in each region. Figure 7.4 presents the profile of domains distribution on the free surface.

Apart from the body panel size, this distribution method also connects the source separations with generated wave frequencies and therefore wave lengths, so it is suitable for deep-water waves of any wave length. In studying the effect of the number of source points utilised upon the solution generated the analysis was repeated with 6, 8, 10, 12 and then 14 source points in each region in turn. An error coefficient C_e is introduced to exam the agreement between predicted hydrodynamics coefficients and analytical linear theory results of Hulme (1982). C_e is defined as:

$$C_e = \frac{\sqrt{(\frac{A_{33} - A'_{33}}{A'_{33}})^2 + (\frac{B_{33} - B'_{33}}{B'_{33}})^2}}{2}, \tag{7.11}$$

where A_{33}, A'_{33} and B_{33}, B'_{33} are added mass coefficients and damping coefficients obtained from current method and Hulme (1982) analytical formulation respectively.

The implementation of the method should be robust enough to apply to all frequencies equally well. Hence we must decide on the number of sources per interval in the free surface, the size of the intervals α_j and the vertical location of the actual sources above the free surface as affected by the distance parameter introduced β_j. Rather than have β_j

constant, as in early reported research (Cao et al., 1991a), a modified method is introduced in the next section.

Ideally the number of the sources per interval will be fixed and the same for each interval, and the values of the parameters (α_j, β_j) for the jth free surface interval will remain fixed for all frequencies.

Following a systematic search of all three sets of parameters for the four free surface intervals used in this fluid structure interaction, the variation of each particular parameter for different frequencies is now presented to provide an indication of the level of error variation in a small region close to the best parameter values identified.

Having identified the most beneficial parameters, Table 7.1 shows how the same number of source point in each interval affects the error coefficient for preferred α_j and β_j values explicitly identified in subsequent tables. Here the range of error displayed is for the specific frequency $\omega^2 R/g = 1.0$ and an $a/R = 0.1$.

Table 7.1: Error coefficient C_e of the analytical results of Hulme (1982) and the proposed distribution method with respect to the different number of source points when amplitude $a/R = 0.1$ and $\omega^2 R/g = 1.0$.

Source points no.	6	8	10	12	14
Ce	2.14%	0.44%	0.15%	0.37%	0.71%

Error coefficient C_e has the least value when 10 points are distributed in each region and therefore this number is selected for the following simulation. Hence 40 source points are required in the inner domain and in the outer domain 20 points are exponentially distributed as suggested by Lee (1992).

7.3.2 Matching interval separation and vertical desingularized distance distribution

The desingularized distance D_d is the distance between the source point and corresponding node point on the free surface. Cao et al. (1991a) determined the desingularized

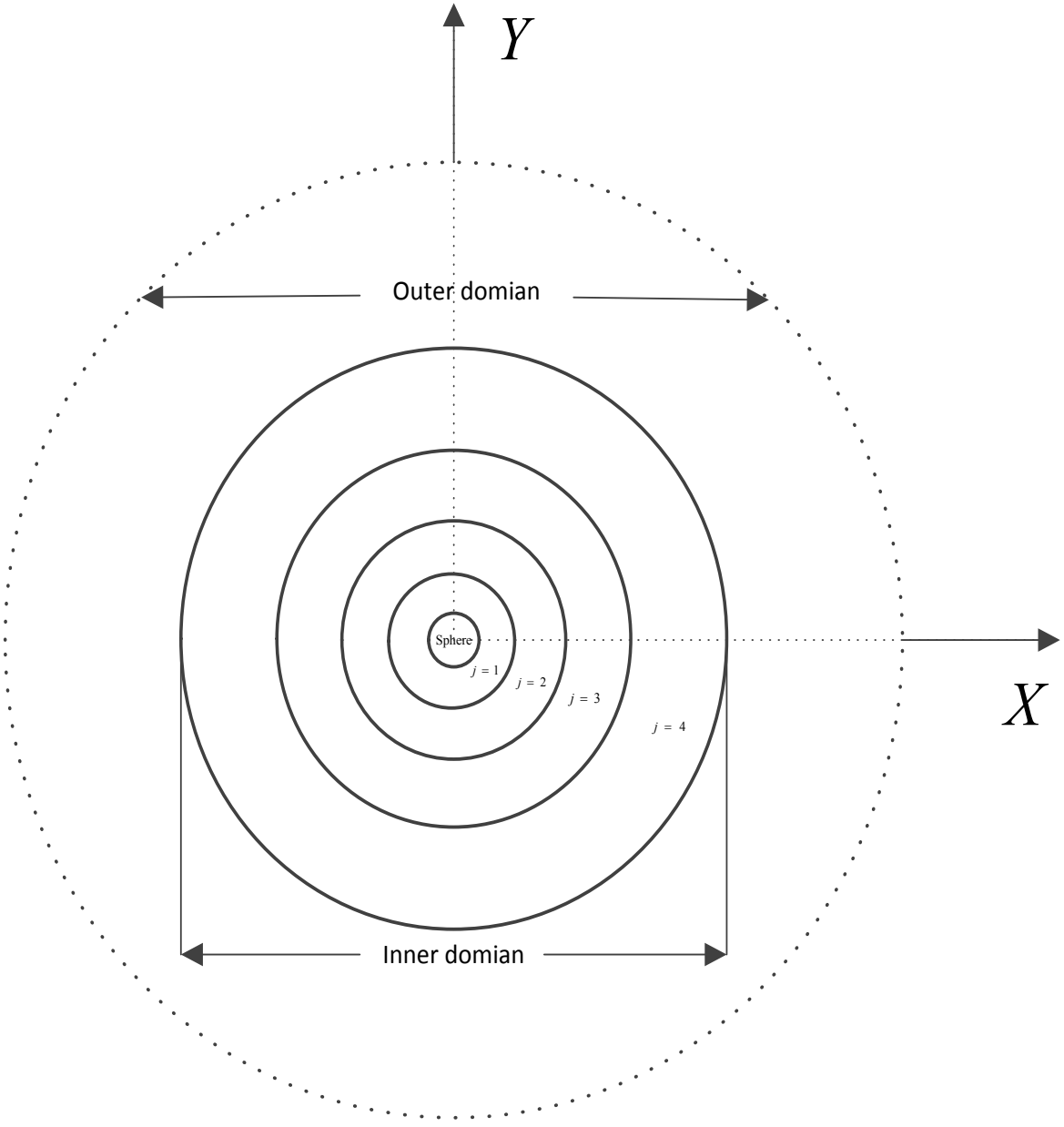

Figure 7.4: Profile of free surface domains distribution.

distance D_d as the square root of the local mesh surface area. A new desingularized distance method is proposed as:

$$D_d = \beta_j \sqrt{S_{b,0}}, \tag{7.12}$$

where β_j $(j = 1, ..., 4)$ are desingularized distance separation factors corresponding to the four inner regions. Therefore this method connects D_d with body panel size attached to the intersection point. These factors β_j $(j = 1, ..., 4)$ are selected by comparing error coefficient C_e.

The separation coefficient α_j $(j = 1, ..., 4)$ decides the space between two neighbouring points. With number of sources totalling 10 in each of the 4 intervals Table 7.2 indicates the spread of error for different α_j values and fixed preferred β_j values yet to be disclosed. In this case we have the same a/R ratio but a slightly lower frequency to demonstrate range of variability of error coefficient.

Table 7.2: Error coefficient C_e of the analytical results of Hulme (1982) and the proposed distribution method with respect to different $\alpha_j (j = 1, ..., 4)$ when amplitude $a/R = 0.1$ and frequency $\omega^2 R/g = 0.9$.

C_e	α_1	α_2	α_3	α_4
2.50%	1.4	1.6	1.9	2.2
2.17%	1.5	1.7	2.0	2.3
1.83%	1.6	1.8	2.1	2.4
1.39%	1.7	1.9	2.2	2.5
1.42%	1.8	2.0	2.3	2.6
1.48%	1.9	2.1	2.4	2.7
1.73%	2.0	2.2	2.5	2.8

Table 7.3 shows the error coefficient C_e of the analytical results of Hulme (1982) and the proposed distribution method with respect to different β_j $(j = 1, ..., 4)$ when $\omega^2 R/g = 1.6$ and amplitude $a/R = 0.1$. Associated α_j values are those of minimum error in Table 7.2.

The $\beta_j : j = 1...4$ corresponding to $1.3, 1.7, 2.0, 2.5$, lead to C_e with the lowest value and therefore they are selected as the desingularized distance factors in this application.

Table 7.3: Error coefficient C_e of the analytical results of Hulme (1982) and the proposed distribution method with respect to different $\beta_j (j = 1, ..., 4)$ when amplitude $a/R = 0.1$ and frequency $\omega^2 R/g = 1.6$.

C_e	β_1	β_2	β_3	β_4
6.24%	1.0	1.4	1.7	2.2
5.35%	1.1	1.5	1.8	2.3
5.15%	1.2	1.6	1.9	2.4
2.20%	1.3	1.7	2.0	2.5
3.11%	1.4	1.8	2.1	2.6
3.63%	1.5	1.9	2.2	2.7
4.13%	1.6	2.0	2.3	2.8

7.4 Intersection points treatment and source strength decaying

Single point treatment is applied in current three-dimensional simulation, i.e the intersection points are taken as the body panel ending points and only the body boundary condition is satisfied at these points. Under this assumption, the generated wave is started from the first source point which is placed away from the intersection point. The position of this point is crucial for the numerical accuracy and the choice of separation coefficient α_j for this point is different from another 9 points in region $j = 1$. Table 7.4 presents the error coefficient C_e of the analytical results of Hulme (1982) and the proposed distribution method with respect to different α_1 for the first source point when $\omega^2 R/g = 0.8$ and amplitude $a/R = 0.1$ for 10 source points and preferred β_j identified.

Table 7.4: Error coefficient C_e of the analytical results of Hulme (1982) and the proposed distribution method with respect to different α_1 for the first source point in region 1 when amplitude $a/R = 0.1$ and frequency $\omega^2 R/g = 0.8$.

α_1	1.1	1.2	1.3	1.4	1.5	1.6	1.7	1.8	1.9
C_e	3.08%	2.91%	2.76%	2.63%	2.37%	2.44%	2.46%	2.54%	2.68%

When $\alpha_1 = 1.5$, error coefficient C_e is least and therefore 1.5 is selected as the separation coefficient for the following simulation.

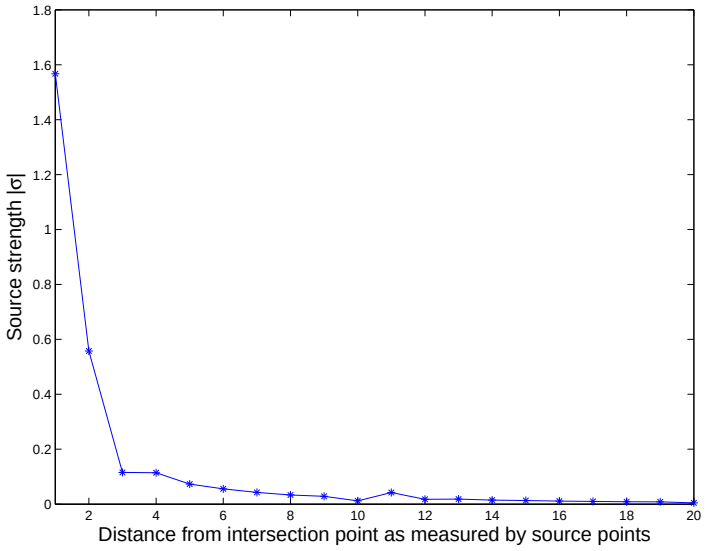

Figure 7.5: Source strength for the first 20 source point distribution when $\omega^2 R/g = 1.0$ and amplitude $a/R = 0.1$.

From the intersection point outwards, the importance of the source points decreases as the distance increases. Figure 7.5 shows the source strength $|\sigma|$ for the first 20 source points when $\omega^2 R/g = 1.0$ and amplitude $a/R = 0.1$. The first source point bears a relatively large value and source strengths decay quickly from the first and trends to zero around 20th point and therefore their importance rapidly decreases as their position located far away the intersection point. The characteristics of source point strength for three-dimensional problems are the same as for the two-dimensional analysis. The proposed space increment distribution method essentially conforms with these characteristics and therefore outperforms the traditional even distribution scheme.

7.5 Chapter summary

Numerical techniques for three-dimensional wave-body problems in context with Rankine source method are derived in this Chapter. Similar numerical algorithms as two-dimensional problems are implicit to avoid repetition. These numerical techniques involve with flow domain discretisation and resulted influence coefficient calculations.

A new source distribution algorithm incorporating vertical desingularized distance and horizontal free surface source arrangements is developed and the method connects body panel size to free surface panel size. Separation factors α_j and β_j decide the positions of source points. They are selected according to numerical accuracy by comparing with analytical results of a forced harmonic oscillatory sphere around free surface. Much less points are required for this new distribution scheme. The reason of superiority for space increment source distribution is due to the conformation with the characteristics of source point strength decaying.

The proposed method can significantly decrease computational cost and reduce the dependence of high computing facilities for three-dimensional wave-body simulation. The numerical accuracy and efficiency of proposed method will be validated for linear and nonlinear body boundary condition problems in next chapter by comparing with published data.

Chapter 8

Three-dimensional numerical simulation for forced body oscillation motion

In this chapter, a spherical structure experiencing forced harmonic oscillatory motion is numerically investigated to demonstrate the accuracy and efficiency of the proposed methods. Spherical structure is a typical offshore structure and widely used as numerical model to validate newly developed method. When the spherical structure oscillates with small amplitude $a = 0.1R$ (say), the nonlinear effects due to body surface and free surface variation is negligibly important and therefore linear boundary conditions are satisfied for this problem. The results for validation for this problem is presented in Section 8.2. The numerical process is similar as two-dimensional counterpart problem and presented in Figure 7.1.

For floating body with larger oscillatory motion amplitude $a \geq 0.2R$ (say), the nonlinear effects from wetted body surface become important and hence nonlinear body boundary condition is applied for this numerical model. The predicted results are compared with published data in Section 8.3. The numerical process is similar as two-dimensional counterpart problem and presented in Figure 7.2. In general, the analysis is performed on personal desktop computer with occasionally use of the University of Southampton Supercomputing facility Iridis 4 to speed up the simulation.

8.1 Introduction

A floating sphere oscillating around free surface is a classic wave-body problem. A floating sphere is placed piercing the free surface in its equilibrium position at initial time $t = 0$. This floating body is disturbed by a forced harmonic oscillation motion with velocity $v_b = a\omega\cos(\omega t)$ from time $t > 0$. The excited wave is generated from wave-body intersection line and propagate along free surface towards far field range.

Under linear assumption, the added mass and damping coefficients for this floating sphere can be analytically investigated by multipole expansions of Hulme (1982). These results are believed to have high accuracy and are compared with other predicted results to check their numerical accuracy. This problem is also examined by a hybrid boundary element method of Matsui et al. (1987). For this hybrid boundary element method, simple fundamental solution is satisfied in the inner region in conjunction with analytical solution employed in outer region. A Fourier-series expansion of fundamental solution based formulation matches the continuity requirements on matching surface. By even distributed Rankine source method, Zhang and Beck (2008) investigate both linear and nonlinear body boundary condition problems. Apart from frequency domain hydrodynamic coefficients, time-domain force response are also obtained to show the periodic characteristic of force response for this problem.

For the body-exact problem, similar to the two-dimensional cylinder problem, first the initial-boundary value problem is solved assuming linearity within an Euler frame of reference. During the body motion process the wetted surface varies and therefore a repanelling of the instantaneous wetted body surface is required. In this process, the position of a control point varies at every time step and the variation of the wetted body surface causes the intersection points to move horizontally resulting in the free surface nodes on the calm water surface and the corresponding free surface sources to also move horizontally. The movement of these points requires evaluation under a Lagrange specification and therefore both Euler and Lagrange frames of references are applied at every time step.

From the viewpoint of numerical computation, in the linear problem the influence coefficient matrices need to be evaluated once only at initial time and these matrices remain constant during time iteration. In addition, these matrices can be used for all

wave frequencies. For nonlinear body boundary problem, the influence coefficient matrices must be computed at every time step due to the position variations for node points and source points and these matrices vary with wave frequencies. The re-evaluation of these matrices leads to a significant computational memory and time increase for the nonlinear problem compared with the linear case.

8.2 Numerical results for linear problem

Figures 8.1 and 8.2 present comparisons of added mass coefficient A_{33} and damping coefficient B_{33} between Hulme's analytical results (Hulme, 1982), linear Rankine source numerical results (Zhang and Beck, 2008), a linear Hybrid boundary element method (Matsui et al., 1987) and the current method results based on the proposed numerical techniques. The current method shows reasonable agreement with the other three results.

The added mass coefficient A_{33} and damping coefficient B_{33} for the sphere shown in Figures 8.1 and 8.2 exhibit less spread than that for the two-dimensional circular cylinder as presented in Figures 4.4 and 4.5. The reason can be explained as: two-dimensional circular cylinder can be regarded as three-dimensional cylinder with unlimited length in three-dimensional domain. The oscillation of this cylinder with radius R around free surface excites stronger hydrodynamic response than the sphere with same radius R and therefore the hydrodynamic coefficients of two-dimensional cylinder is more spread.

Figures 8.3 to 8.8 illustrate comparison of the time dependent nondimensional vertical force F experienced by the sphere at oscillatory frequency $\omega^2 R/g = 0.6, 0.8, 1.0, 1.2, 1.4$ and 1.6 determined from the proposed method, Hulme analytical expression (Hulme, 1982) and the formulation of Lin and Yue (1990). In the last, a Green function method is used and both linear approaches show similar magnitudes and trends with time proceeds.

It should be pointed that the proposed method produces good agreement in time domain simulation in a large frequency range as that in frequency domain range. Time domain results are explicitly presented here at frequency $\omega^2 R/g = 0.6, 0.8, 1.0, 1.2, 1.4, 1.6$ as these frequencies cover a relatively large frequency range and have same frequency interval. The optimized values for the four factors obtained at limited frequency in frequency domain produce a good agreement with published data in a large frequency range for both

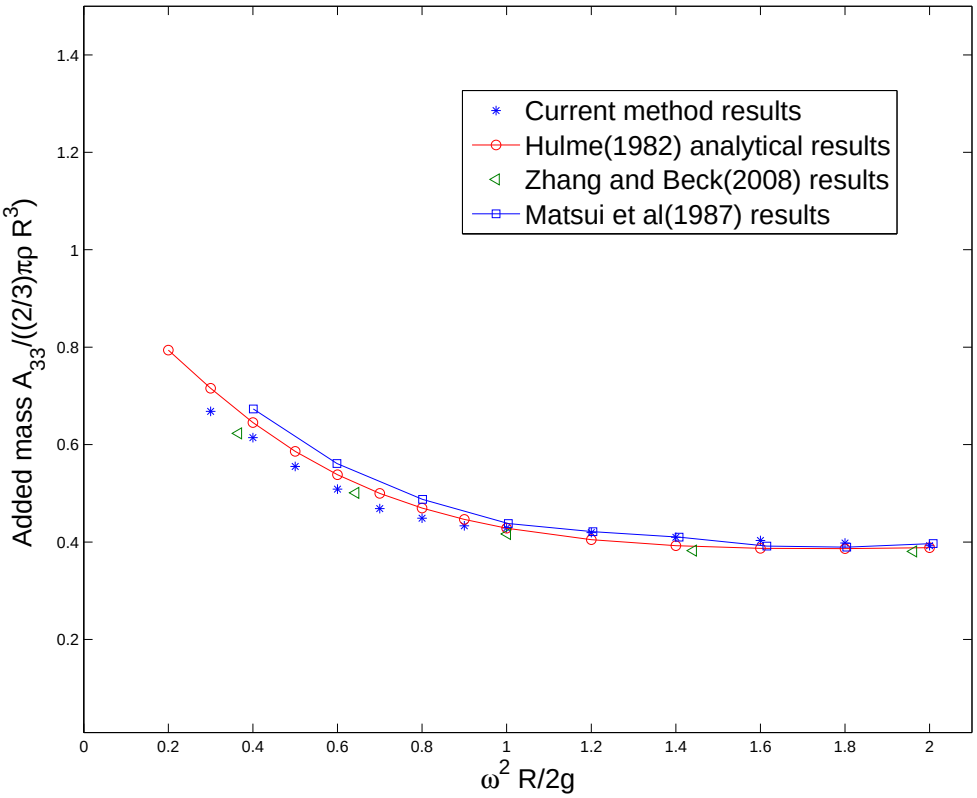

Figure 8.1: Comparison of added mass coefficient A_{33} between Hulme's analytical results, other numerical results and current method prediction.

frequency domain and time domain problem. This demonstrates the wide availability of proposed method and optimized values for the four factors.

It should be noted that the analytical result of Hulme (1982), based on a free-surface Green function without using the infinite domain integration over the free surface, provides results over the complete frequency range. However, the Rankine source method for the computation of source strength over the infinite free surface domain leads to a deviation of the result in the low frequency domain. Small errors arise from the truncation of the infinite free surface domain into a finite free surface domain and this can magnify numerical errors significantly over a large time scale in the low frequency domain prediction. Similarly, in laboratory experiments (Vugts, 1968), a small error in measurement of force resulted from wave reflection and accuracy of sensors may cause large deviation in the production of force coefficients especially in low frequency domain (See Section 4.3).

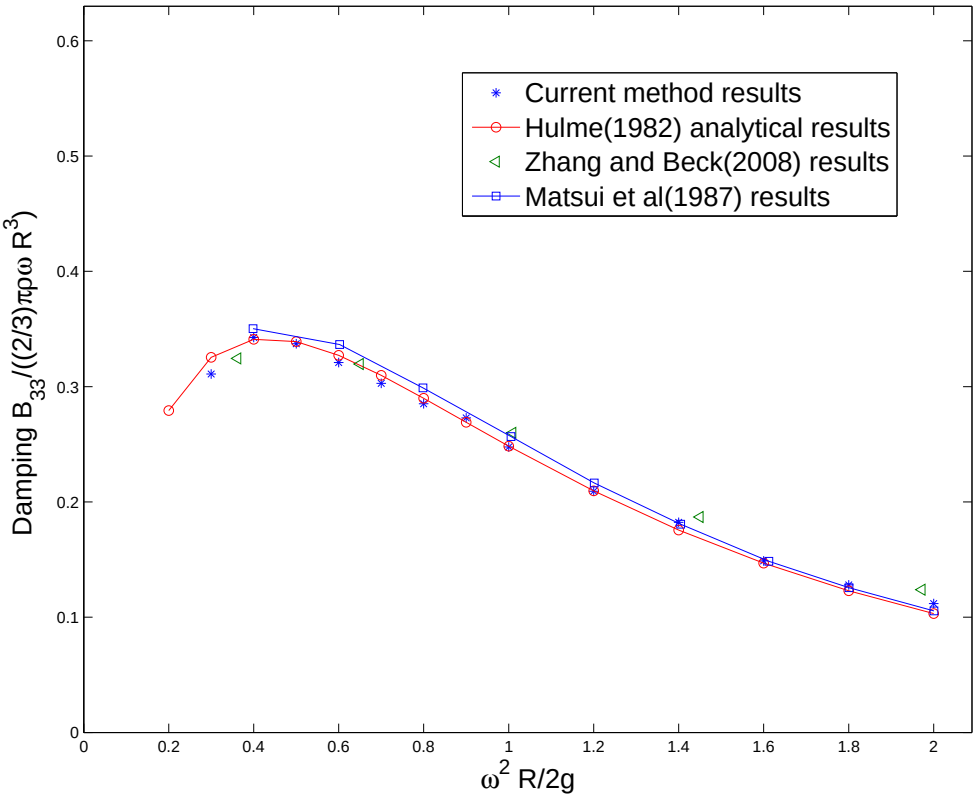

Figure 8.2: Comparison of damping coefficient B_{33} between Hulme's analytical results, other numerical results and current method prediction.

The Rankine source method using the desingularized algorithm has been well studied. However, a rigorous mathematical analysis (in contrast to application) of the way that the desingularized sources are distributed over the free surface is very sparse in the literature, although it is significant in the computation efficiency of the three-dimensional fluid motion problem. As indicated in Table 7.1, the increment of source distribution density does not increase the accuracy of the numerical results. The best agreement occurs when 10 source points are distributed rather than 12 and 14. This phenomenon in the evenly distributed source scheme was also observed by Lee (1992). This contradicts the theoretical understanding of the boundary element method for which more boundary elements are expected to generate better results. It is due to the fact that the source points are displaced above the free surface rather than exactly on the free surface.

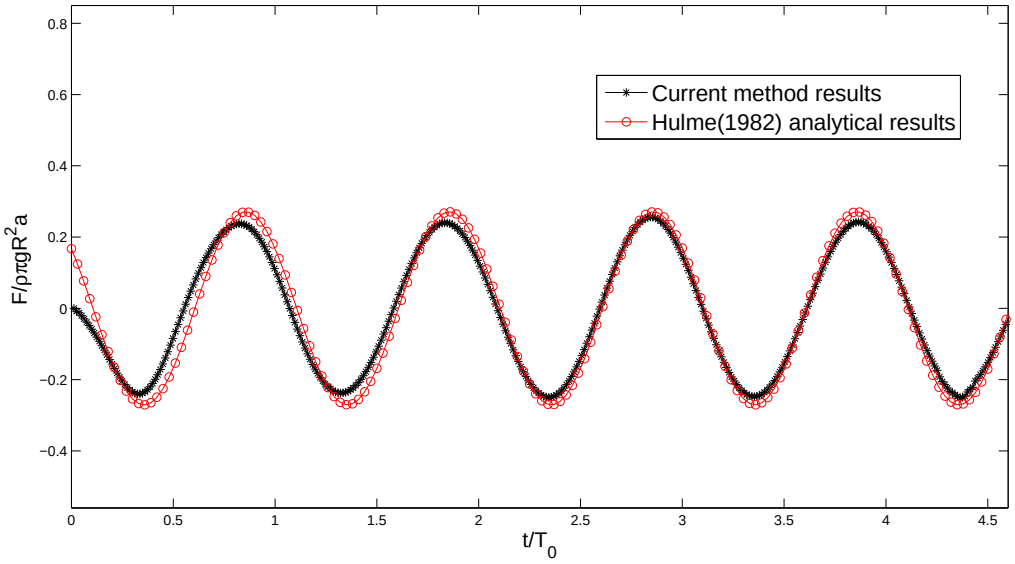

Figure 8.3: Comparison of the time dependent nondimensional vertical force experienced by the sphere at oscillatory frequency $\omega^2 R/g = 0.6$ determined from the proposed method and the expression of Hulme (1982).

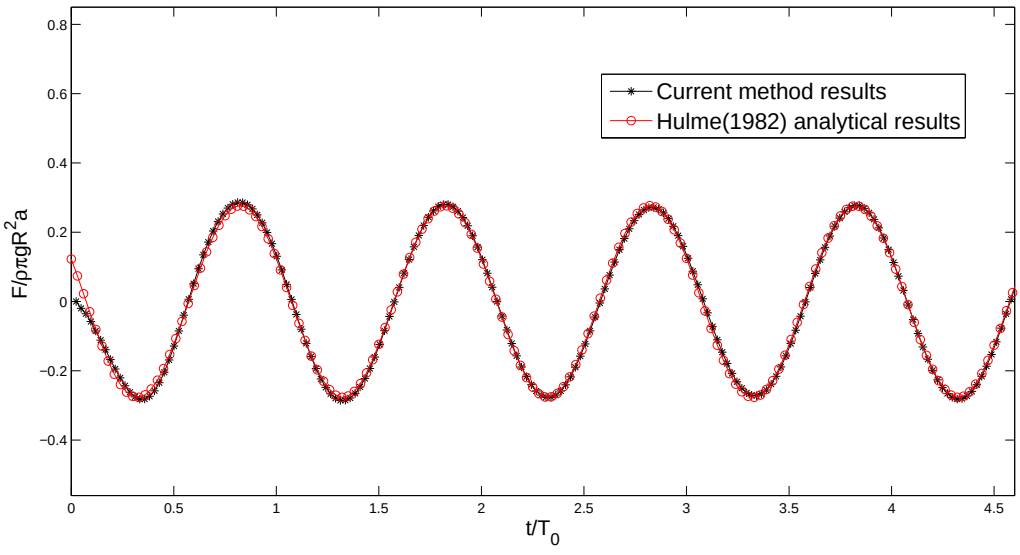

Figure 8.4: Comparison of the time dependent nondimensional vertical force experienced by the sphere at oscillatory frequency $\omega^2 R/g = 0.8$ determined from the proposed method and the expression of Hulme (1982).

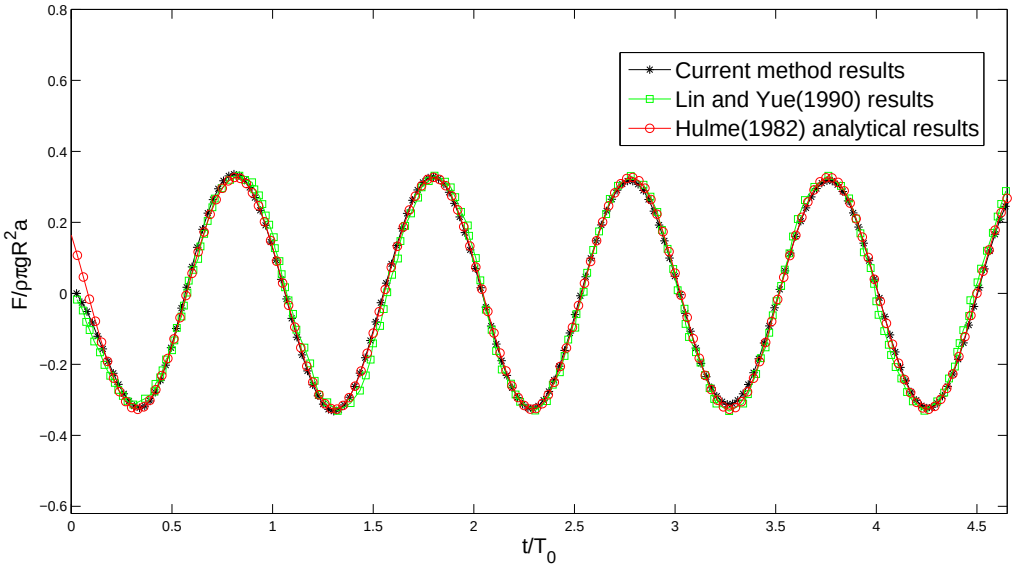

Figure 8.5: Comparison of the time dependent nondimensional vertical force experienced by the sphere at oscillatory frequency $\omega^2 R/g = 1.0$ determined from the proposed method, the expression of Hulme (1982) and the formulation of Lin and Yue (1990); this is the only frequency for which Lin and Yue (1990) comparison can be made.

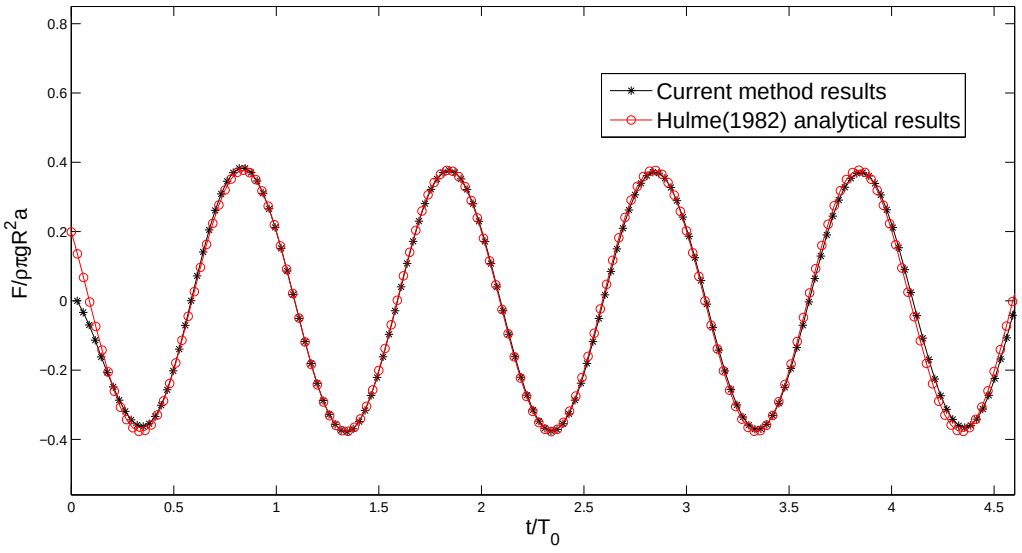

Figure 8.6: Comparison of the time dependent nondimensional vertical force experienced by the sphere at oscillatory frequency $\omega^2 R/g = 1.2$ determined from the proposed method and the expression of Hulme (1982).

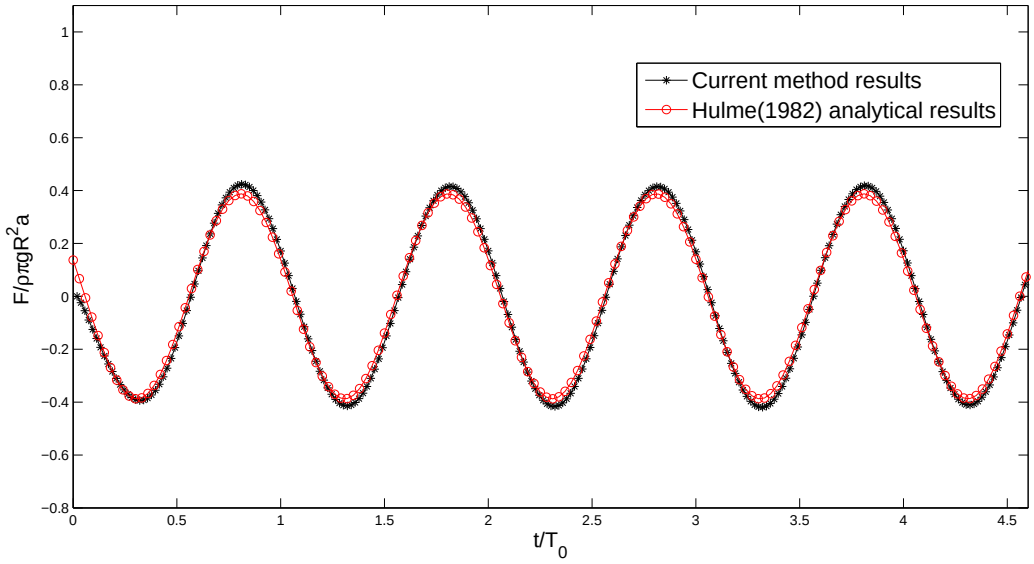

Figure 8.7: Comparison of the time dependent nondimensional vertical force experienced by the sphere at oscillatory frequency $\omega^2 R/g = 1.4$ determined from the proposed method and the expression of Hulme (1982).

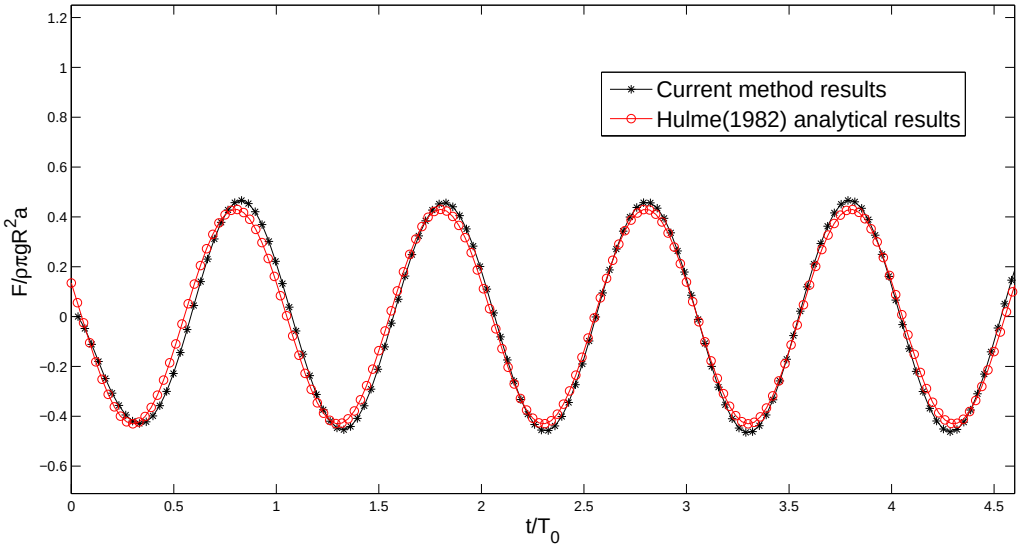

Figure 8.8: Comparison of the time dependent nondimensional vertical force experienced by the sphere at oscillatory frequency $\omega^2 R/g = 1.6$ determined from the proposed method and the expression of Hulme (1982).

8.3 Numerical results for nonlinear body boundary problem

When the body undergoes harmonic oscillatory heave motion with motion amplitude a great than $0.2R$, the wetted body surface changes significantly over the course of the body motion and therefore nonlinear effects are of increasing influence. The assumption of a linear body boundary condition is no longer valid and will cause erroneous numerical predictions so a body-exact or nonlinear body boundary condition is required. At every time step, the body boundary condition is satisfied on the instantaneous wetted body surface and therefore the body surface needs regridding to address the variation of wetted body surface.

From Bernoulli's equation the inertial force $F^1(t) = -\partial\phi/\partial t$ exhibits a harmonic component whereas the quadratic part $F^2 = 1/2|\nabla\phi|^2$ is primarily a second order harmonic. Figure 8.9 illustrates a comparison of time records for inertial force $F^1(t)$ at oscillatory frequency $\omega^2 R/g = 1.0$ and amplitude $a/R = 0.2$ between the proposed method and the method of Zhang and Beck (2008) . A reasonable agreement is obtained between these two methods. The nonlinear effects appear in the force profile of $F^1(t)$ in which the wave peak becomes sharper and of higher value (~ 0.4) whereas the wave trough tends to flatten and of lower value (~ 0.3) and the force slope becomes steeper. The nonlinear effect grows continuously as motion amplitude increases and it become observable when a/R is slightly greater than 0.15 as shown in Figure 8.11.

These nonlinear effects become more noticeable as the body motion amplitude increases. When this sphere oscillates at amplitude $a/R = 0.5$, the wetted body surface S_w varies from 24% of S_b to 72% of S_b. Serious nonlinear effects are assumed to occur. Figure 8.10 presents the time records for $F^1(t)$ and corresponding nondimensional wetted surface area $S_w(t)$ with the oscillation frequency $\omega^2 R/g = 1.0$ and the amplitude $a/R = 0.5$. Figure 8.10 shows the force peaks are sharper and of higher whereas the force troughs are flatter and of smaller value and the force slope becomes much steeper. The force peak appears around $S_w(t) = 0$, that is the sphere surface is half immersed in the fluid and the force trough occurs when $S_w(t)$ is least. It is interesting to note that in these calculations, two turning points occur. The first one is when $S_w(t) = 0$ and the second shortly afterwards. The reason for this is unsolved.

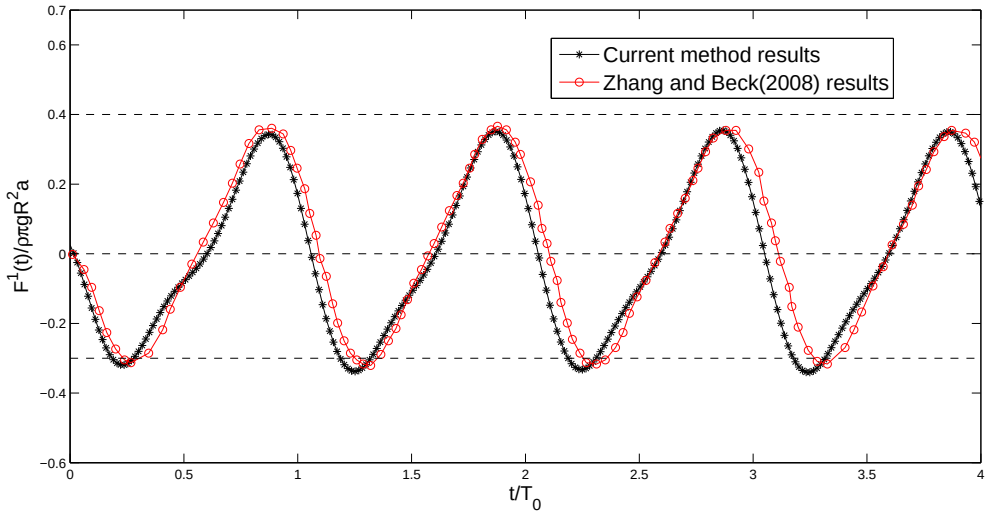

Figure 8.9: Comparisons of time records for nondimensional inertial force $F^1(t)$ with oscillatory frequency $\omega^2 R/g = 1.0$ and amplitude $a/R = 0.2$ between the proposed method and Zhang and Beck (2008) method.

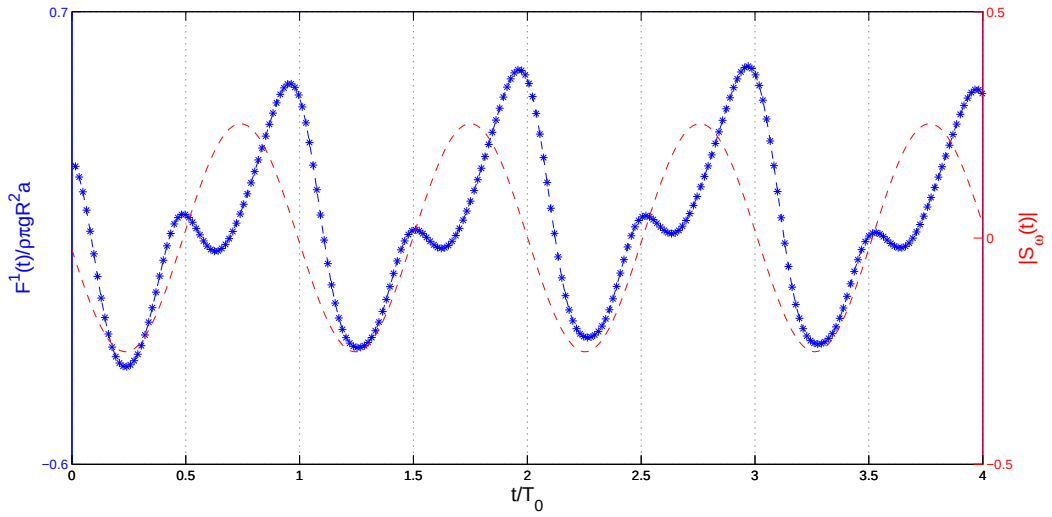

Figure 8.10: Time records for nondimensional inertial force $F^1(t)(--*--)$ and corresponding nondimensional wetted surface area $S_w(t)(- - - -)$ with oscillatory frequency $\omega^2 R/g = 1.0$ and amplitude $a/R = 0.5$.

Figure 8.11 presents the nonlinear force peak and trough amplitudes for both linear and nonlinear problems with oscillatory amplitude a increasing for frequency $\omega^2 R/g = 1.0$. The scales are different as the force peak amplitudes increase whereas trough amplitudes

decrease with oscillatory amplitude a increasing for the body-exact problem.

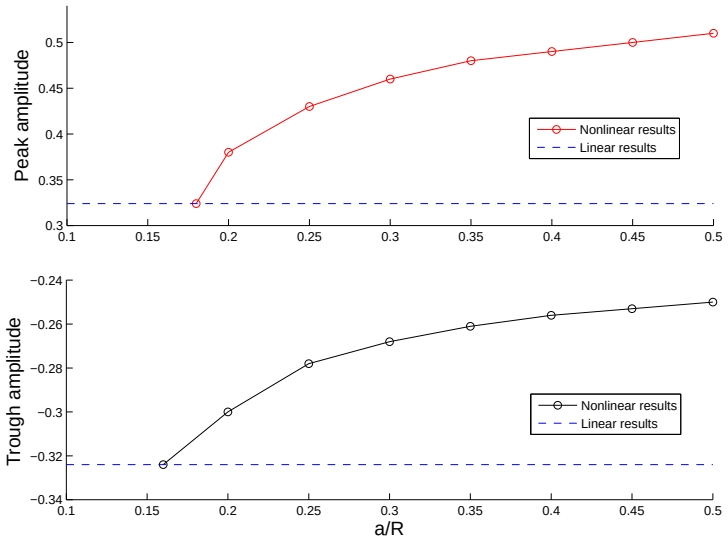

Figure 8.11: Nonlinear force peak amplitudes and trough amplitudes for both linear and nonlinear problems with oscillatory amplitude a increasing for frequency $\omega^2 R/g = 1.0$.

Figure 8.12 shows comparison of the time dependent quadratic force $F^2(t)$ when amplitude $a/R = 0.2$ and $a/R = 0.5$ with oscillatory frequency $\omega^2 R/g = 1.0$. The amplitude of the quadratic force $F^2(t)$ significantly increases as the body motion amplitude a increases. The nonlinear effects arising from nonlinear body boundary condition increase in importance and the nondimensional value of $F^2(t)$ is of the same order of magnitude as $F^1(t)$ when $a/R = 0.5$. However the quadratic force $F^2(t)$ is smaller than the inertial force and therefore no nonlinear effect is observed for $F^2(t)$.

The proposed method is further validated by comparing hydrodynamic coefficients A_{33}, B_{33}, first order force $F^1(\omega)$ and second order force $F^2(\omega)$ responses with variation of oscillatory amplitude a. The predicted results are compared with the numerical results of Zhang and Beck (2008) and Lin and Yue (1990) for oscillatory frequency $\omega^2 R/g = 1.0$. In the simulation of Lin and Yue (1990) , a Green function method coupled to a perturbation expansion approach are adopted to derive first-order and higher order responses. Zhang and Beck (2008) utilised a simple Green function model with a traditional source distribution method and a desingularized distance scheme. The predictions from the proposed method show similar trends to the other two results fairly well. Figures 8.13, 8.14 and

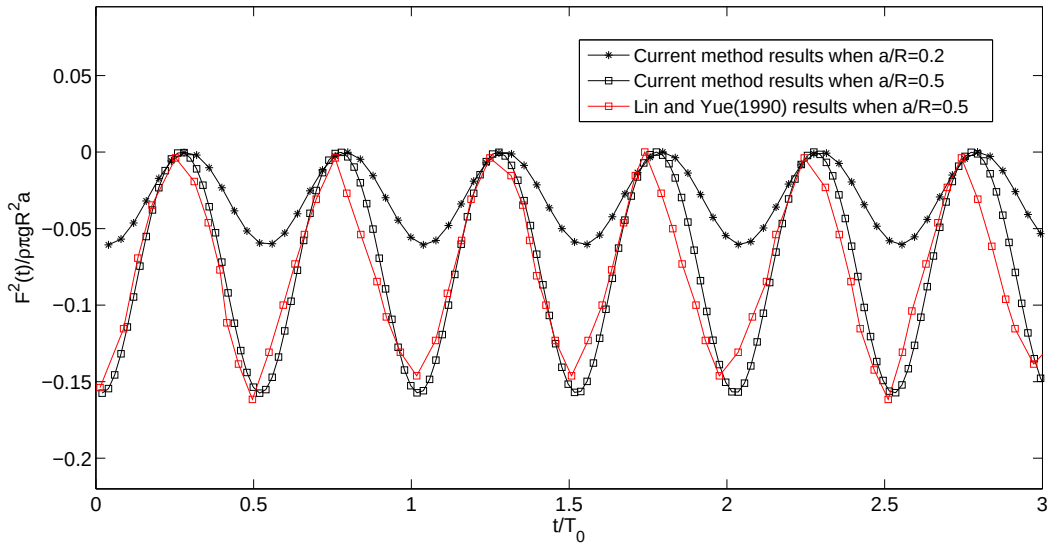

Figure 8.12: Comparisons of time records for quadratic force $F^2(t)$ when oscillatory amplitude $a/R = 0.2$ and $a/R = 0.5$ with frequency $\omega^2 R/g = 1.0$.

8.15 show the hydrodynamic coefficients and first order force responses decrease slightly as oscillation amplitude a increases while second order force responses roughly keep constant as presented in Figure 8.16. In linear wave-body simulation, A_{33}, B_{33} and $F^1(\omega)$ are constant regardless of the motion amplitude. The evaluation of these values in the linear model ignores the nonlinear body boundary condition and will overestimate these values.

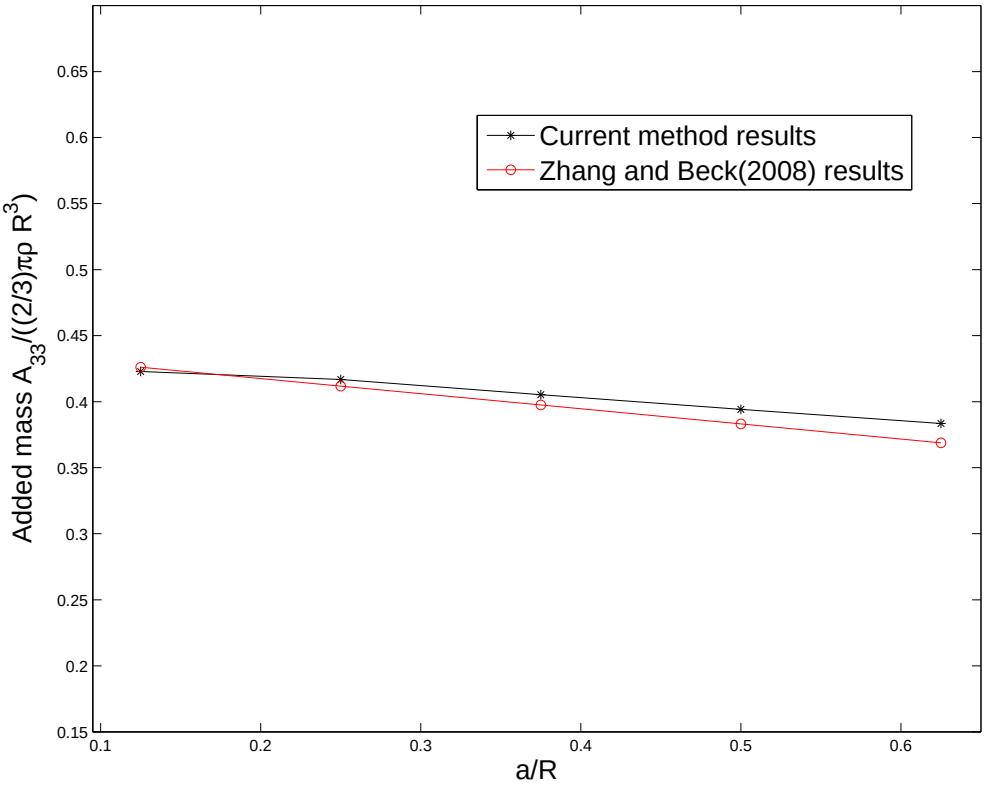

Figure 8.13: Comparisons of added mass coefficient A_{33} with increasing oscillatory amplitude a for frequency $\omega^2 R/g = 1.0$.

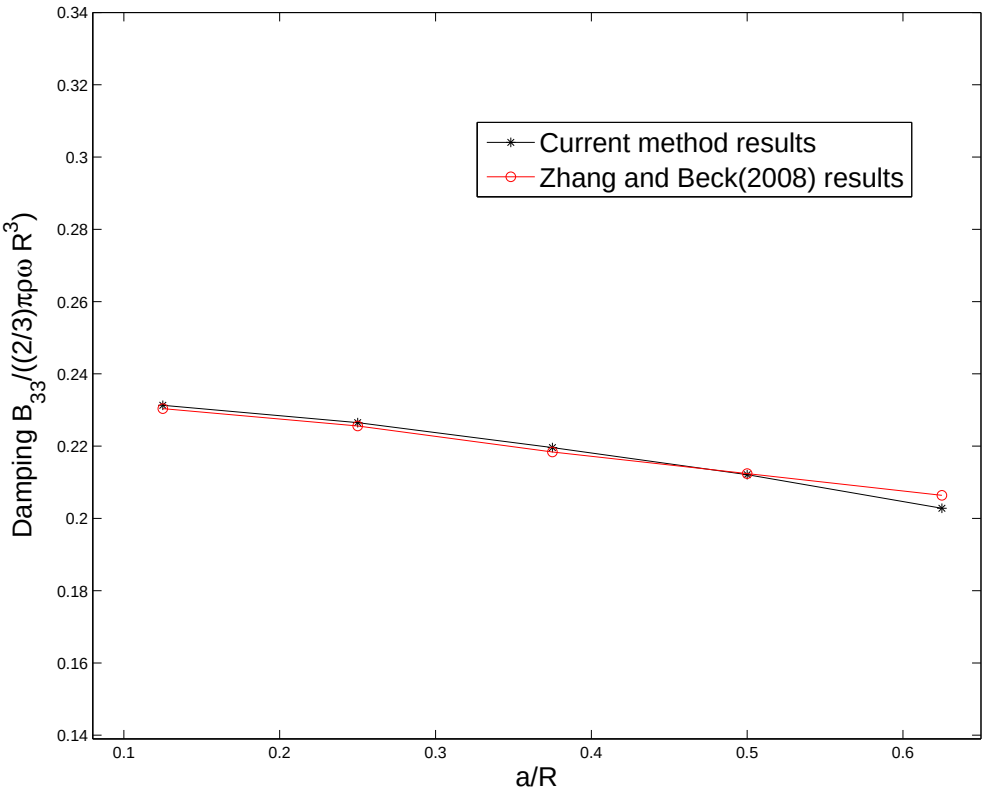

Figure 8.14: Comparisons of damping coefficient B_{33} with increasing oscillatory amplitude a for frequency $\omega^2 R/g = 1.0$.

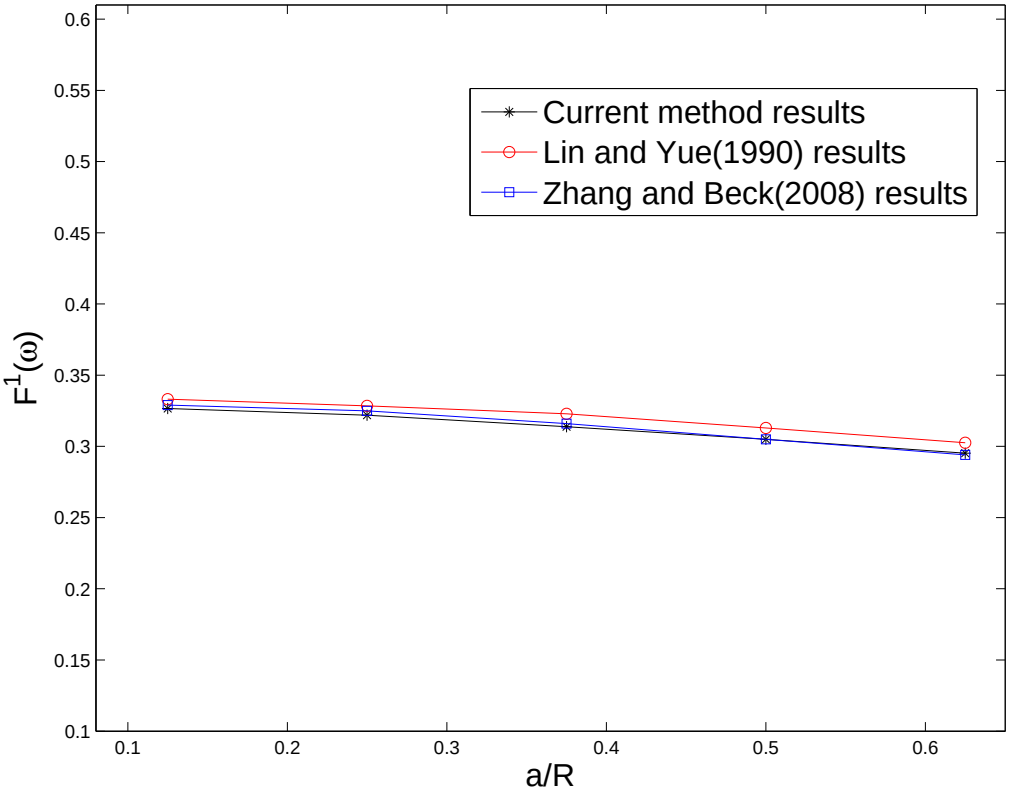

Figure 8.15: Comparisons of $F^1(\omega)$ with increasing oscillatory amplitude a for frequency $\omega^2 R/g = 1.0$.

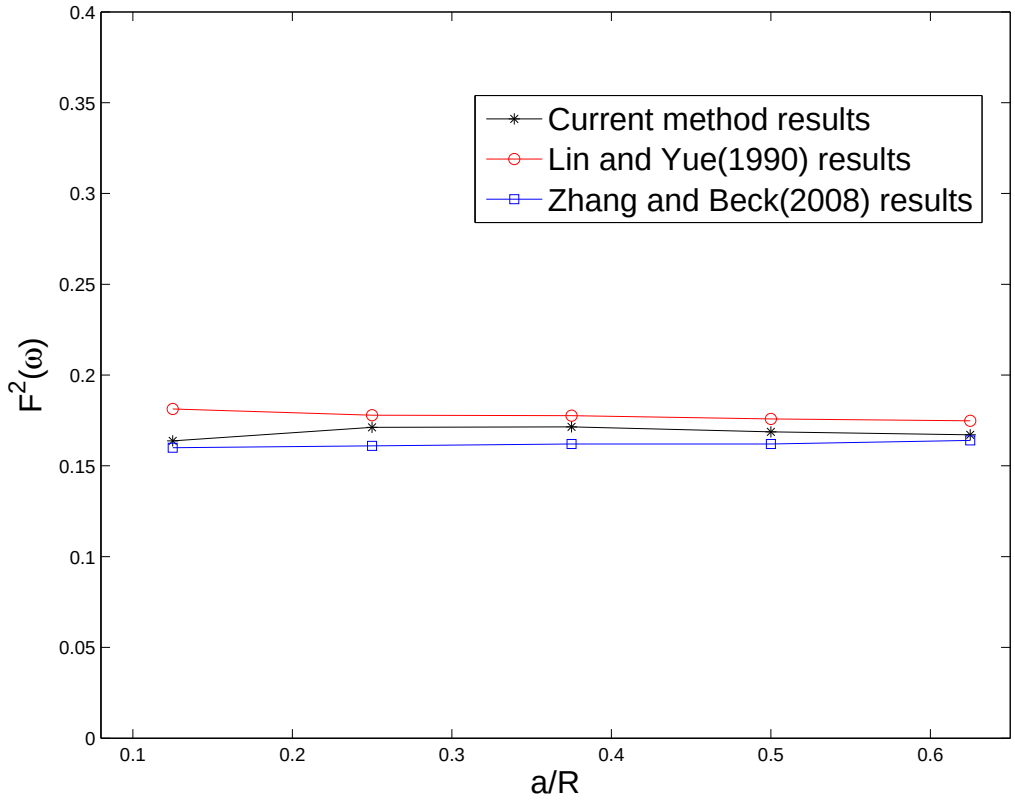

Figure 8.16: Comparisons of $F^2(\omega)$ with increasing oscillatory amplitude a for frequency $\omega^2 R/g = 1.0$.

8.4 Computational effort comparison

In the last two sections, numerical accuracy of the proposed method is well validated by comparing with published data for both linear and nonlinear wave-body numerical models. For boundary integral formulation applied in present simulation, most computational efforts are made for formation of the influence coefficient matrices and evaluation of linear algebra equations constructed by the matrices. The computational cost is roughly $O(N^{2\sim3})$ for boundary element method. Generally three-dimensional problems require approximately one order of magnitude elements more magnitude of elements than two-dimensional case. But this will lead to $2 \sim 3$ orders of magnitude computational effort difference.

In the proposed source distribution method, 10×10 panels are distributed around the sphere surface. In every radiation direction 60 node points are arranged in the free surface and therefore 100 panels and 600 source points are adopted for this method. In traditional even distribution (Bandyk, 2009; Beck et al., 1994; Finn, 2003; Kring, 1994; Lee, 2003; Scorpio, 1997; Zhang and Beck, 2008), totally 2240 source points plus 100 body panels are required. For the body-exact problem with $500-600$ time steps, the traditional method requires $5 \sim 6$ hours CPU time with respect to a processor of 3.0 GHz (Zhang and Beck, 2008) and the code based on current method only needs $1 \sim 2$ hours CPU time for a processor of 2.67 GHz. In practical computation, this reduction makes the nonlinear three-dimensional wave-body simulation feasible on personal workstation and deduces the dependence of supercomputing facility.

8.5 Concluding remarks

Numerical simulations are executed for both linear and nonlinear three-dimensional models of a forced floating sphere experiencing heave motion within a free surface. The analysis is based on the modified methods. For a linear problem, the body boundary condition is satisfied on the mean wetted body surface and the linear free surface boundary condition is applied on the calm water surface. No regridding process is required for this problem.

For a nonlinear body boundary condition problem, because of the time-dependence of the wetted body surface and the calm water free surface, both these surfaces are regridded at every time step. The number of body panel and the number of isolated source points are kept constant. Thus the panel size of the wetted body surface varies in the time iteration process and the calm water surface regridding is only made in the horizontal direction. The acceleration potential caused by fluid point motion is evaluated utilising a Lagrange frame of reference and a mixed Euler-Lagrangian technique is applied to update the free surface at every time step using a 3rd-order Adams-Bashforth scheme. The predicted results show a fairly well agreement with published data. This validates the accuracy of newly adopted method.

The evaluated force time record is no longer harmonic in the body-exact problem and the maximum and minimum values of the records are more skewed with increasing amplitude a. The force peak becomes sharper whereas the force trough displays a flatter shape and two "turning points" appear for body oscillation amplitude $a/R = 0.5$. Higher order responses become important as body amplitude increases and they are of the same order of magnitude as the first order force for the body-exact problem.

Instead of an even distribution of sources over the free surface an incrementally increasing source space distribution method is developed coupled with a single point intersection treatment. This distribution method connects body panel size with source point arrangement and conforms with the characteristics of source strength decaying and therefore is superior to the traditional even distribution patten. Fewer source points are required to cover free surface range and therefore computational effort is largely reduced for three-dimensional wave-body problem. By selecting optimized values for source point number, separation coefficients α_j, β_j and α_1, the source point position is well fixed. Good agreement with published data over a large frequency range for both frequency domain and time domain problem demonstrates the high accuracy and wide availability of the proposed method and optimized values.

The proposed source distribution and single point treatment essentially improves the source distribution on the free surface and no special requirement and assumption for regular three-dimensional body shape. An arbitrary regular three-dimensional body shape can be discretized into continuous panels with control points located in the centre of panels in spherical coordinate system or Cartesian coordinate system. Free surface is discretized

into isolated source points following the proposed method. Influence coefficient can be evaluated according to the position of source points and control points and then numerical simulation moves forward as applied in this chapter.

The traditional even source distribution method has been successfully applied for various regular three-dimensional body shape and the proposed method has been successfully applied for different two-dimensional body shapes. Considering the improvement of proposed method for three-dimensional case this newly proposed method is expected to have a high accuracy and efficiency for the problem of arbitrary regular three-dimensional body shape experiencing forced harmonic motion in the free surface. The diffraction problem requires investigation.

Chapter 9

Conclusions and recommendations for future work

9.1 Conclusions

Desingularized Rankine source method coupled with mixed Euler Lagrangian algorithm has been developed to solve both two-dimensional and three-dimensional wave-body problems in present work. Free surface boundary condition is not satisfied by Rankine source in this mathematical model. By distributing source points in isolation above the free surface, the boundary conditions are satisfied at isolated source points on the free surface. Source points are placed above node points and therefore this avoids the evaluation of a singular kernel for the Rankine source.

One key technique involved is the free surface source points distribution. Numerical accuracy and efficiency largely depend on the source distribution pattern and source number. Improper distribution leads to poor numerical prediction and even numerical divergence for fully nonlinear problems.

In this thesis, a space increment source point distribution scheme is developed which also connects body panel size with free surface grid. Separation factors in these distribution schemes were selected according to numerical accuracy by comparing with published data. This method is essentially in close proximity to the source strength decay characteristics from the first source points to the source points in far field. For this reason, the

proposed distribution scheme is superior to the traditional even distribution method. Less source points are required for the proposed method and therefore numerical efficiency is significantly improved.

Single point technique is developed to treat the weak singular intersection points. The intersection points are regarded as body panel ending points and only the body boundary condition is applied at these points. Numerically, this treatment allows waves generate from first source point rather than intersection point itself and makes this source point unique from other source points. The position of the first source point is selected by comparing numerical accuracy and efficiency for different wave-body problems.

For linear problem, the linear field equation can be only solved under Euler specification. When the nonlinear effects from wetted body surface and free surface variation are considered, the movements of individual source points due to the regridding process needs to be tracked under Lagrange frame. Therefore an Euler-lagrange algorithm was introduced to formulate the nonlinear wave-body simulation.

During surface regridding process, the panel numbers remain constant while panel size varies to accommodate the variation of body surface and free surface. This technique simplifies the evaluation of induced influence coefficient and benefits for the body surface and free surface time iteration process.

Sawtooth instability occurs in two-dimensional fully nonlinear problem. A three point least squared smoothing algorithm is newly introduced to remove this instability. By applying up to three times smoothing schemes, numerical divergency is avoided and all the numerical simulations can proceed smoothly.

All these numerical techniques combined together supply a robust numerical tool to predict two-dimensional and three-dimensional wave-body responses. The produced results are extensively compared with published experimental and numerical data for various numerical models. High numerical accuracy is achieved and better prediction for high order force response are obtained than other numerical methods

From a computational effort point of view, for two-dimensional linear and nonlinear boundary condition wave-body problems, 160 and 180 source points are respectively required but for the even distribution method 280 points are needed. Computational memory and cost are nearly reduced by half. For three-dimensional linear and nonlinear

body boundary problem 160 source points are required. Compared with 280 points applied in even distribution scheme, this scheme reduces computational memory and cost to a quarter of other distribution method for the same numerical model.

Having presented the advantages of proposed method, the limitations of current method can be generally summarized as:

- Exact free surface boundary condition is not satisfied at the desingularized source points.

The desingularized Rankine source method successfully avoids the calculation of singular integral by placing sources above the free surface, but the free surface boundary condition is only satisfied on the exact free surface rather than on the desingularized source points. This deviation can cause numerical error and lead to contradictory conclusion regarding our theoretical understanding of the boundary element method. For example, the increment of source distribution density can't increase indefinitely as too high a source density may reduce the accuracy of numerical simulation for both two-dimensional and three-dimensional problems.

- Low accuracy in the low frequency range

This is the inherent limitation for Rankine source method. Rankine source can only cover limited surface area. Small errors arise from the truncation of infinite free surface and this error can be magnified significantly over a large scale in the low frequency domain predictions.

- Separation coefficient needs to be selected in numerical test rather than by strict mathematical derivation.

Only two coefficients require optimized selection in traditional method, but four coefficients need to be selected in numerical test for three-dimensional problems in current proposed method. Ideally all the setup coefficients should be derived by mathematical analysis and are uniformly applied irrespective of the complexity available of the formulation addressed.

- The proposed space increasing distribution on the free surface coupled with the single point treatment method requires the uppermost wetted body surface to match the near body free surface spacing.

For most marine engineering structures, regular body shapes satisfy this requirement but irregular structures need other numerical techniques to discretize the body surface in order to use the proposed method. If some body surfaces can't be approximated into panels with same surface size for the uppermost part, the proposed coefficients (α_j, β_j) may not be readily identified as near optimized values for this kind of problem.

- The proposed free surface smoothing algorithm introduces an artificial error.

Like most smoothing algorithms, the proposed least square based method will introduce artificial numerical errors and these errors can accumulate with the number of times the smoothing algorithm must be applied.

Although three-dimensional fully nonlinear problem for a forced floating sphere experiencing large oscillatory motion amplitude is not considered in this work due to time constraints, the newly developed numerical tool is supposed to be promoted directly to this problem without inherent limitation considering numerical principals and computational cost.

The achievements so far are summarised briefly as:

- a space increment source points distribution method has been developed to reduce computational time and improve accuracy for both two- and three-dimensional wave-body problems;

- a single point treatment is specified for intersection points;

- a panel number constant re-griding algorithm is presented for horizontal and vertical re-meshing process;

- a least square based smoothing technology is developed to eliminate numerical instabilities in two-dimensional fully nonlinear problem.

9.2 Recommendations for future work

A desingularized Rankine source method incorporating with mixed Euler Lagrangian algorithm offers a robust numerical tool for various wave-body problems. In the work of this thesis, only body with prescribed motions have been investigated. The applications of this numerical tool based on the proposed numerical techniques can be extended to following wave-body simulation problems without much effort:

- Transient motion of floating body around free surface:

A body floating on the free surface of water is given a small vertical displacement from its equilibrium position and released. No extra force is applied on the body. The resulted damped motion is a straightforward task. The main effort lie in the extra evaluation of acceleration potential and application of Newton's second law.

- Diffraction body motion problem:

Only radiation problems have been examined in this thesis. For real seakeeping computation, the incoming waves generate a large response on the body surface. The effects from incident wave must be considered. Compared to radiation problems, no numerical instability occurs but the body boundary condition needs to be modified.

- Body motion with non-zero speed:

For ship moving with a constant non-zero speed, wave-making resistance plays an important role for ship seakeeping performance. Velocity is explicit in the field equation. A major issue is the computation of free surface slope at body and free surface intersection line.

Extreme wave and wave-body problems, such as wave overturning, wave breaking, water entry and exit, slamming, can be formulated by further developing this numerical model. The evaluation for body entry and exit problem requires other numerical algorithms, like jet and spray cutting off, air cavity tracking, et al. The spaces between source points are fixed in present simulation. For the extreme free surface profile variation, the

spaces are variable during free surface updating at every time step, therefore new regridding techniques must be further developed. However the idea of space increasing pattern can be applied in formulation of these problems and the reduction of computational time makes the numerical test feasible and economic on personal computing workstation even without the dependence on expensive supercomputing facilities.

Appendix A

Three-dimensional influence coefficient calculation

In this Appendix, the evaluations for influence coefficient $A_{N_f N_b}$ and $C_{N_f N_b}$, $A_{N_b N_b}$ and $C_{N_b N_b}$ are derived based on the panel method of Hess and Smith (1964, 1967); Newman (1986) . By omitting the subscript, $A_{N_f N_b}$ and $C_{N_b N_b}$ uniformly becomes $\int \frac{1}{r} ds$. These terms are essentially the integral of Rankine source over body panel surface. Similarly $A_{N_b N_b}$ and $C_{N_f N_b}$ are the integrals of Rankine source induced velocity in normal direction on body panel and z direction on free surface.

The source strength σ is assumed constant on the body panel and the source point is located in the centre of the planar element. The calculation for these coefficients require the transformation of curved panels in global coordinate system $O - XYZ$ into quadrilateral in local element coordinate system in $o-xyz$ first and inverse transformation back to global coordinate system at last.

A.1 Transformation from three-dimensional element to two-dimensional quadrilateral element

For every panel on the wetted body surface, generally four corner points are not on the same plane. In order to calculate the integral over the panel surface, the three-

dimensional body panel needs to transformed to two-dimensional quadrilateral element in local coordinate systems.

A three-dimensional body surface panel is located in global coordinate system $O-XYZ$ with four corner points numbered in clockwise direction consecutively as 1, 2, 3, 4. These four points have coordinates as follows:

$$\begin{array}{lccc} 1: & (x_1^i & y_1^i & z_1^i) \\ 2: & (x_2^i & y_2^i & z_2^i) \\ 3: & (x_3^i & y_3^i & z_3^i) \\ 4: & (x_4^i & y_4^i & z_4^i) \end{array}$$

where the superscript i stands for the coordinates as input data. Two "diagonal" vectors are named as $\mathbf{T}_1$ and $\mathbf{T}_2$. The vector $\mathbf{T}_1$ is from point 1 to point 3 and $\mathbf{T}_2$ is from point 2 to point 4. In general these vectors are not orthogonal. Figure A.1 shows the profile of the corner points and vectors. The components of $\mathbf{T}_1$ vectors can be expressed as:

$$\begin{aligned} T_{1x} &= x_3^i - x_1^i, \\ T_{1y} &= y_3^i - y_1^i, \\ T_{1z} &= z_3^i - z_1^i, \end{aligned} \tag{A.1}$$

and for $\mathbf{T}_2$

$$\begin{aligned} T_{2x} &= x_4^i - x_2^i, \\ T_{2y} &= y_4^i - y_2^i, \\ T_{2z} &= z_4^i - z_2^i. \end{aligned} \tag{A.2}$$

Vector $\mathbf{N}$ is defined as the cross product of $\mathbf{T}_1$ and $\mathbf{T}_2$. Its component are:

$$\begin{aligned} N_x &= T_{2y}T_{1z} - T_{1y}T_{2z}, \\ N_y &= T_{1x}T_{2z} - T_{2x}T_{1z}, \\ N_z &= T_{2x}T_{1y} - T_{1x}T_{2y}. \end{aligned} \tag{A.3}$$

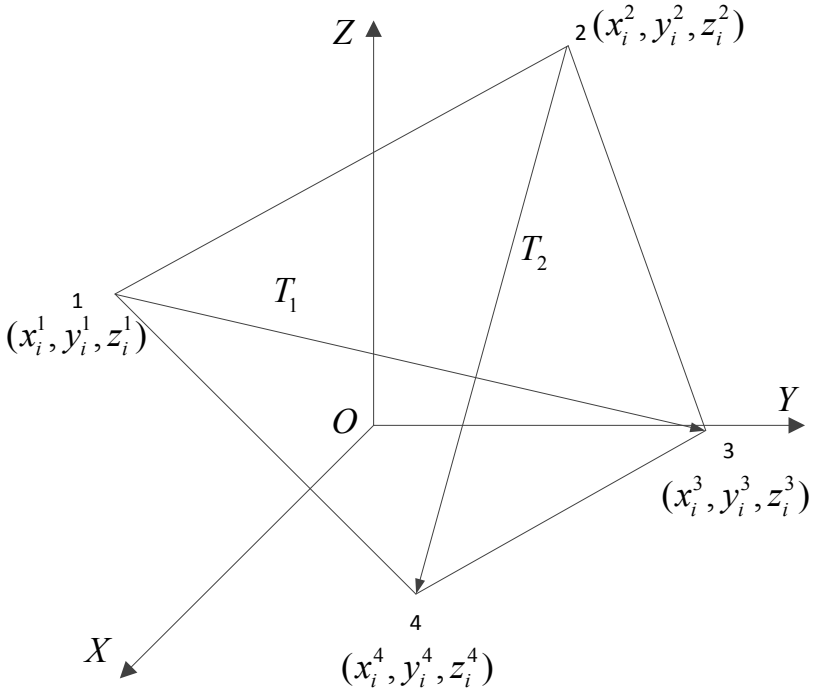

Figure A.1: Profile of corner points and vectors for a body panel in global coordinate system

As $\mathbf{T}_1$ and $\mathbf{T}_2$ are not in general orthogonal, another vector $\mathbf{T}_2^{'}$ is introduced as:

$$\mathbf{T}_2^{'} = \mathbf{T}_1 \times \mathbf{T}_2, \tag{A.4}$$

and therefore its component can be expressed as:

$$\begin{aligned} T_{2x}^{'} &= N_y T_{1z} - N_z T_{1y}, \\ T_{2y}^{'} &= N_z T_{1x} - N_x T_{1z}, \\ T_{2z}^{'} &= N_x T_{1y} - N_y T_{1x}. \end{aligned} \tag{A.5}$$

For the convenience of notation, $\mathbf{T}_2^{'}$ is replaced by $\mathbf{T}_2$. The unit vector $\mathbf{t}_1$, $\mathbf{t}_2$ and $\mathbf{n}$ for

are taken as $\mathbf{T}_1$, $\mathbf{T}_2$, and $\mathbf{N}$ divided by its own length. That is:

$$\begin{aligned} \mathbf{t}_1 &= \frac{\mathbf{T}_1}{T_1}, \\ \mathbf{t}_2 &= \frac{\mathbf{T}_2}{T_2}, \\ \mathbf{n} &= \frac{\mathbf{N}}{N}, \end{aligned} \tag{A.6}$$

where

$$\begin{aligned} T_1 &= \sqrt{T_{1x}^2 + T_{1y}^2 + T_{1z}^2}, \\ T_2 &= \sqrt{T_{2x}^2 + T_{2y}^2 + T_{2z}^2}, \\ N &= \sqrt{N_x^2 + N_y^2 + N_z^2}, \end{aligned} \tag{A.7}$$

are the length for $\mathbf{T}_1$, $\mathbf{T}_2$, and $\mathbf{N}$ respectively.

Unit vectors $\mathbf{t}_1$, $\mathbf{t}_2$ and $\mathbf{n}$ are orthogonal with each other and they construct the local coordinate system $O - xyz$ for quadrilateral element. For the uniform of notation, these vectors are re-denoted as:

$$\begin{aligned} a_{11} = t_{1x}, \qquad a_{12} = t_{1y}, \qquad a_{13} = t_{1z}, \\ a_{21} = t_{2x}, \qquad a_{22} = t_{2y}, \qquad a_{23} = t_{2z}, \\ a_{31} = n_x, \qquad a_{32} = n_y, \qquad a_{13} = n_z. \end{aligned} \tag{A.8}$$

The transformation matrix is therefore in the format of array:

$$\begin{bmatrix} a_{11} & a_{12} & a_{13} \\ a_{21} & a_{22} & a_{23} \\ a_{31} & a_{32} & a_{33} \end{bmatrix}. \tag{A.9}$$

The origin coordinates of this element coordinate system are required for coordinate system transform. They are designed as x_o, y_o and z_o and taken as average point of the panel:

$$x_o = \frac{1}{4}(x_1^i + x_2^i + x_3^i + x_4^i),$$

$$y_o = \frac{1}{4}(y_1^i + y_2^i + y_3^i + y_4^i),$$
$$z_o = \frac{1}{4}(z_1^i + z_2^i + z_3^i + z_4^i). \tag{A.10}$$

For a point with coordinates x^i, y^i, and z^i in global coordinate system and coordinates x^o, y^o, and z^o in local element coordinate system, the transformation from the global to element coordinate system can be formulated as:

$$\begin{bmatrix} x^0 \\ y^0 \\ z^0 \end{bmatrix} = \begin{bmatrix} a_{11} & a_{12} & a_{13} \\ a_{21} & a_{22} & a_{23} \\ a_{31} & a_{32} & a_{33} \end{bmatrix} \begin{bmatrix} x^i - x_o \\ y^i - y_o \\ z^i - z_o \end{bmatrix}, \tag{A.11}$$

while the transform from the element to global reference can be formulated as:

$$\begin{bmatrix} x^i \\ y^i \\ z^i \end{bmatrix} = \begin{bmatrix} a_{11} & a_{12} & a_{13} \\ a_{21} & a_{22} & a_{23} \\ a_{31} & a_{32} & a_{33} \end{bmatrix}^{-1} \begin{bmatrix} x^o \\ y^o \\ z^o \end{bmatrix} + \begin{bmatrix} x_o \\ y_o \\ z_o \end{bmatrix}. \tag{A.12}$$

For point with x_o, y_o and z_o in local coordinate system o_xyz, actually $z_0 = 0$ as this point lies in the plane of the element. For the convenience of notation, the coordinates of point 1, 2, 3 and 4, transformed from global to local coordinate system are denoted as:

1: $(\xi_1 \quad \eta_1 \quad 0)$
2: $(\xi_2 \quad \eta_2 \quad 0)$
3: $(\xi_3 \quad \eta_3 \quad 0)$
4: $(\xi_4 \quad \eta_4 \quad 0)$

These 4 points construct a quadrilateral element in local coordinate systems $o - xyz$.

A.2 Construction of the fundamental potential for one side of the quadrilateral element

Considering a quadrilateral element with 4 corner points 1, 2, 3 and 4 lying in the xy plane in local coordinate systems. The value of source strength σ on this element is

assumed constant. The velocity potential at field point $P(x, y, z)$ is:

$$\Phi = \int\int_{A_q} \frac{1}{r} ds = \int\int_{A_q} \frac{d\xi d\eta}{\sqrt{(x-\xi)^2 + (y-\eta)^2 + z^2}}, \tag{A.13}$$

where r is the distance from field point P to point on the quadrilateral element with coordinates $(\xi, \eta, 0)$ and A_q is the area of quadrilateral element. Figure A.2 show the plane quadrilateral element and field point P in local coordinate system. The velocity

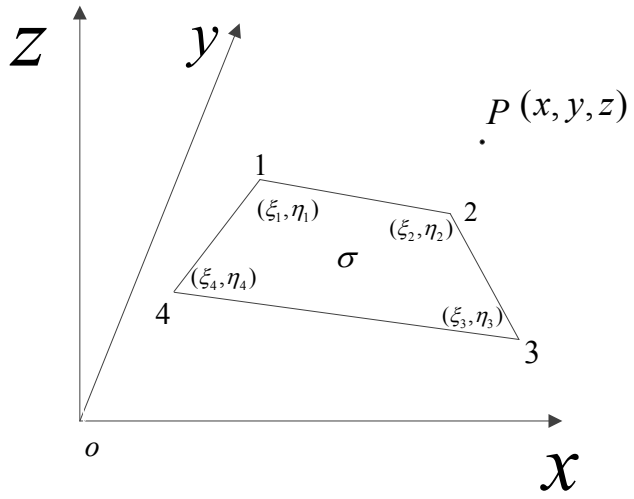

Figure A.2: Profile of plane quadrilateral element and field point P in local coordinate system

$\mathbf{V}(V_x, V_y, V_z)$ at point P are therefore given by:

$$V_x = -\frac{\partial \phi}{\partial x} = \int\int_{A_q} \frac{(x-\xi) d\xi d\eta}{r^3}, \tag{A.14}$$

$$V_y = -\frac{\partial \phi}{\partial y} = \int\int_{A_q} \frac{(y-\xi) d\xi d\eta}{r^3}, \tag{A.15}$$

$$V_z = -\frac{\partial \phi}{\partial z} = \int\int_{A_q} \frac{(z-\xi) d\xi d\eta}{r^3}. \tag{A.16}$$

The integral over quadrilateral element A_q with source strength σ can be discretized into four sides integration with source strength $\frac{1}{2}\sigma$ as shown in figure A.3 and this gives:

$$V_x = V_{x_{12}} + V_{x_{23}} + V_{x_{34}} + V_{x_{41}}, \tag{A.17}$$

$$V_y = V_{y_{12}} + V_{y_{23}} + V_{y_{34}} + V_{y_{41}}, \tag{A.18}$$

$$V_z = V_{z_{12}} + V_{z_{23}} + V_{z_{34}} + V_{z_{41}}, \tag{A.19}$$

where

$$\begin{aligned} V_{x_{12}} &= \int_{\eta_1}^{\eta_2} \frac{d\eta}{r}, \qquad & V_{x_{23}} &= \int_{\eta_2}^{\eta_3} \frac{d\eta}{r}, \\ V_{x_{34}} &= \int_{\eta_3}^{\eta_4} \frac{d\eta}{r}, \qquad & V_{x_{41}} &= \int_{\eta_4}^{\eta_1} \frac{d\eta}{r}, \end{aligned} \tag{A.20}$$

$$\begin{aligned} V_{y_{12}} &= \int_{\xi_1}^{\xi_2} \frac{d\xi}{r}, \qquad & V_{y_{23}} &= \int_{\xi_2}^{\xi_3} \frac{d\xi}{r}, \\ V_{y_{34}} &= \int_{\xi_3}^{\xi_4} \frac{d\xi}{r}, \qquad & V_{y_{41}} &= \int_{\xi_4}^{\xi_1} \frac{d\xi}{r}. \end{aligned} \tag{A.21}$$

and

$$\begin{aligned} V_{z_{12}} &= \frac{-z}{[(x-\xi)^2+z^2]} \int_{\xi_1}^{\xi_2} \frac{(y-\eta_{12})d\xi}{\sqrt{(x-\xi)^2+(x-\eta_{12})^2+z^2}}, \\ V_{z_{23}} &= \frac{-z}{[(x-\xi)^2+z^2]} \int_{\xi_2}^{\xi_3} \frac{(y-\eta_{23})d\xi}{\sqrt{(x-\xi)^2+(x-\eta_{23})^2+z^2}}, \\ V_{z_{34}} &= \frac{-z}{[(x-\xi)^2+z^2]} \int_{\xi_3}^{\xi_4} \frac{(y-\eta_{34})d\xi}{\sqrt{(x-\xi)^2+(x-\eta_{34})^2+z^2}}, \\ V_{z_{41}} &= \frac{-z}{[(x-\xi)^2+z^2]} \int_{\xi_4}^{\xi_1} \frac{(y-\eta_{41})d\xi}{\sqrt{(x-\xi)^2+(x-\eta_{41})^2+z^2}}. \end{aligned} \tag{A.22}$$

For $V_{z_{12}}$, η_{12} stands for a variable point on the line between point 1 and 2. It be expressed as function of ξ in the following form:

$$\eta_{12} = m_{12}\xi + b_{12}, \tag{A.23}$$

where

$$m_{12} = \frac{\eta_2 - \eta_1}{\xi_2 - \xi_1}, \tag{A.24}$$

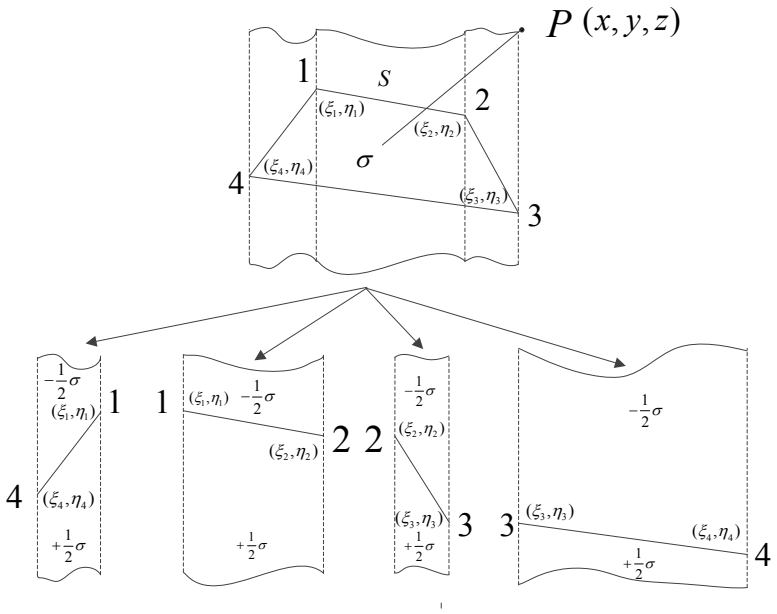

Figure A.3: Discretization of integral over quadrilateral element into four sides

is the slope of the side 12 and

$$b_{12} = \frac{\xi_2\eta_1 - \xi_1\eta_2}{\xi_2 - \xi_1}. \tag{A.25}$$

For the convenience of notation in the following derivation, symbols q_{12} and u are introduced as:

$$q_{12} = y - b_{12} - m_{12}x, \tag{A.26}$$

$$u = x - \xi, \tag{A.27}$$

and therefore

$$du = -d\xi. \tag{A.28}$$

In terms of these new symbols, $V_{z_{12}}$ becomes:

$$\begin{aligned}
V_{z_{12}} &= z\int_{x-\xi_1}^{x-\xi_2}\frac{(m_{12}u+q_{12})du}{(u^2+z^2)u^2+(m_{12}u+q_{12})^2+z^2} \\
&= -\frac{1}{z}\tan^{-1}\{\frac{q_{12}\sqrt{q_{12}^2+m_{12}^2z^2[m_{12}^2z^2-m_{12}q_{12}u]}}{z\sqrt{q_{12}^2[m_{12}^2z^2-m_{12}q_{12}u]^2+[q_{12}^2+m_{12}q_{12}u]^2[(1+m_{12}^2)z^2+q_{12}^2]m_{12}^2}}\}|_{x-\xi_1}^{x-\xi_2} \\
&= -\frac{1}{z}\tan^{-1}\{\frac{m_{12}z^2-q_{12}u}{z\sqrt{u^2+z^2+[q_{12}+m_{12}u]^2}}\}|_{x-\xi_1}^{x-\xi_2} \\
&= -\frac{1}{z}\tan^{-1}\{\frac{m_{12}(u^2+z^2)-(y-\eta_{12})u}{z\sqrt{u^2+(y-\eta_{12})^2+z^2)}}\}|_{x-\xi_1}^{x-\xi_2} \\
&= \tan^{-1}(\frac{m_{12}e_1-h_1}{zr_1})-\tan^{-1}(\frac{m_{12}e_2-h_2}{zr_2}), \qquad \text{(A.29)}
\end{aligned}$$

where

$$e_1=z^2+(x-\xi_1)^2, \qquad e_2=z^2+(x-\xi_2)^2, \qquad \text{(A.30)}$$

$$h_1=(y-\eta_1)(x-\xi_1), \qquad h_2=(y-\eta_2)(x-\xi_2), \qquad \text{(A.31)}$$

$$r_1=\sqrt{(x-\xi_1)^2+(y-\eta_1)^2+z^2}, \qquad r_2=\sqrt{(x-\xi_2)^2+(y-\eta_2)^2+z^2}. \qquad \text{(A.32)}$$

A.3 Summary of velocity components and fundamental potential

Similar as $V_{z_{12}}$, the induced velocity $V_{z_{23}}$, $V_{z_{34}}$ and $V_{z_{41}}$ can be obtained and therefore V_z can be calculated according to Equation A.19. By similar manner, the induced velocity V_x and V_y by the quadrilateral element can be accompanied. Here the expression for these velocity components are summarized as:

$$\begin{aligned}
V_x &= \frac{\eta_2-\eta_1}{d_{12}}\ln(\frac{r_1+r_2-d_{12}}{r_1+r_2+d_{12}})+\frac{\eta_3-\eta_2}{d_{23}}\ln(\frac{r_2+r_3-d_{23}}{r_2+r_3+d_{23}}) \\
&+ \frac{\eta_4-\eta_3}{d_{34}}\ln(\frac{r_3+r_4-d_{34}}{r_3+r_4+d_{34}})+\frac{\eta_1-\eta_4}{d_{41}}\ln(\frac{r_4+r_1-d_{41}}{r_4+r_1+d_{41}}), \qquad \text{(A.33)}
\end{aligned}$$

$$\begin{aligned} V_y &= \frac{\xi_1-\xi_2}{d_{12}}\ln(\frac{r_1+r_2-d_{12}}{r_1+r_2+d_{12}}) + \frac{\xi_2-\xi_3}{d_{23}}\ln(\frac{r_2+r_3-d_{23}}{r_2+r_3+d_{23}}) \\ &+ \frac{\xi_3-\eta_4}{d_{34}}\ln(\frac{r_3+r_4-d_{34}}{r_3+r_4+d_{34}}) + \frac{\xi_4-\eta_1}{d_{41}}\ln(\frac{r_4+r_1-d_{41}}{r_4+r_1+d_{41}}), \end{aligned} \tag{A.34}$$

$$\begin{aligned} V_z &= \tan^{-1}(\frac{m_{12}e_1-h_1}{zr_1}) - \tan^{-1}(\frac{m_{12}e_2-h_2}{zr_2}) \\ &+ \tan^{-1}(\frac{m_{23}e_2-h_2}{zr_2}) - \tan^{-1}(\frac{m_{23}e_3-h_3}{zr_3}) \\ &+ \tan^{-1}(\frac{m_{34}e_3-h_3}{zr_3}) - \tan^{-1}(\frac{m_{34}e_3-h_4}{zr_4}) \\ &+ \tan^{-1}(\frac{m_{41}e_4-h_4}{zr_4}) - \tan^{-1}(\frac{m_{41}e_1-h_1}{zr_1}), \end{aligned} \tag{A.35}$$

where

$$\begin{aligned} d_{12} &= \sqrt{(\xi_2-\xi_1)^2+(\eta_2-\eta_1)^2}, \\ d_{23} &= \sqrt{(\xi_3-\xi_2)^2+(\eta_3-\eta_2)^2}, \\ d_{34} &= \sqrt{(\xi_4-\xi_3)^2+(\eta_4-\eta_3)^2}, \\ d_{41} &= \sqrt{(\xi_1-\xi_4)^2+(\eta_1-\eta_4)^2}, \end{aligned} \tag{A.36}$$

and

$$\begin{aligned} m_{12} &= \frac{\eta_2-\eta_1}{\xi_2-\xi_1}, \qquad m_{23} = \frac{\eta_3-\eta_2}{\xi_3-\xi_2}, \\ m_{34} &= \frac{\eta_4-\eta_3}{\xi_4-\xi_3}, \qquad m_{41} = \frac{\eta_1-\eta_4}{\xi_1-\xi_4}, \end{aligned} \tag{A.37}$$

and

$$r_k = \sqrt{(x-\xi_k)^2+(y-\eta_k)^2+z^2}, \qquad k=1,2,3,4 \tag{A.38}$$

$$e_k = z^2+(x-\xi_k)^2, \qquad k=1,2,3,4 \tag{A.39}$$

$$h_k = (y-\eta_k)(x-\xi_k), \qquad k=1,2,3,4 \tag{A.40}$$

The velocity potential induced by the quadrilateral element can be formulated as:

$$\begin{aligned}\Phi &= [\frac{(x-\xi_1)(\eta_2-\eta_1)-(y-\eta_1)(\xi_2-\xi_1)}{d_{12}}(\frac{r_1+r_2+d_{12}}{r_1+r_2-d_{12}}) \\ &+ \frac{(x-\xi_2)(\eta_3-\eta_2)-(y-\eta_2)(\xi_3-\xi_2)}{d_{23}}(\frac{r_2+r_3+d_{23}}{r_2+r_3-d_{23}}) \\ &+ \frac{(x-\xi_3)(\eta_4-\eta_3)-(y-\eta_3)(\xi_4-\xi_3)}{d_{34}}(\frac{r_3+r_4+d_{34}}{r_3+r_4-d_{34}}) \\ &+ \frac{(x-\xi_4)(\eta_1-\eta_4)-(y-\eta_4)(\xi_1-\xi_4)}{d_{41}}(\frac{r_4+r_1+d_{41}}{r_4+r_1-d_{41}})] \\ &- zV_z \end{aligned} \tag{A.41}$$

There is no trouble to evaluate V_x and V_y. They becomes infinity on the edge of the quadrilateral element, but only the influence of the element on itself is desired in practice. The evaluation for V_z requires special handle for some cases. when point p approaches a point in the element plane outside the boundary of this quadrilateral, then

$$V_z = 0, \tag{A.42}$$

and when point p approaches a point in the element plane within the boundary of this quadrilateral, then

$$V_z = 2\pi. \tag{A.43}$$

It should be noticed that once the velocity components and velocity potential are obtained. They must be transformed from local element coordinate system $o-xyz$ back to global coordinated system $O-XYZ$ according to Equation A.12.

A.4 Formulation for influence coefficients

Once the velocity $\mathbf{V}(V_x, V_y, V_z)$ and velocity potential Φ are readily available from last section. Influence coefficient $A_{N_fN_b}$ and $C_{N_fN_b}$ can be formulated by the induced velocity potential Φ as:

$$A_{N_fN_b} = \Phi_{P_fQ_b}, \tag{A.44}$$

$$C_{N_bN_b} = \Phi_{P_bQ_b}, \tag{A.45}$$

where P_f and P_b indicate the field point P is the node point on free surface and control point on body panel respectively while Q_b stands for the body panel. $A_{N_f N_b}$ and $C_{N_f N_b}$ can be formulated by the induced velocity $\mathbf{V}(V_x, V_y, V_z)$ as:

$$C_{N_f N_b} = V_z, \tag{A.46}$$

$$A_{N_b N_b} = \mathbf{V} \cdot \mathbf{n_b} \tag{A.47}$$

where $\mathbf{n_b}$ is the unit normal vector of body panel.

References

Andersen, P. and He, W. (1985). On the calculation of two-dimensional added mass and damping coefficients by simple green's function technique, *Ocean Engineering* **12**(5): 425–451.

Bai, K. (1977). The added mass of two-dimensional cylinders heaving in water of finite depth, *Journal of Fluid Mechanics* **81**(01): 85–105.

Bai, K., Kim, J. and Lee, H. (1994). A localized finite-element method for nonlinear free-surface wave problems, *Proceedings of the 19th Symposium on Naval Hydrodynamics*, pp. 113–139.

Bai, K. and Yeung, R. (1974). Numerical solutions to free-surface flow problems, *Proceedings of the 10th Symposium on Naval Hydrodynamics*, pp. 609–641.

Bandyk, P. (2009). *A body-exact strip theory approach to ship motion computations*, PhD thesis, University of Michigan.

Bandyk, P. and Beck, R. (2011). The acceleration potential in fluid–body interaction problems, *Journal of Engineering Mathematics* **70**(1): 147–163.

Beck, R. (1994). Time-domain computations for floating bodies, *Applied Ocean Research* **16**(5): 267–282.

Beck, R., Cao, Y. and Lee, T. (1994). Fully nonlinear water wave computations using the desingularized method, *Proceedings of the 6th International Conference on Numerical Ship Hydrodynamics*, pp. 3–20.

Beck, R. and Liapis, S. (1987). Transient motions of floating bodies at zero forward speed, *Journal of Ship Research* **31**(3): 164–176.

Beck, R. and Reed, A. (2000). Modern seakeeping computations for ships, *Proceedings of the 23rd Naval Hydrodynamics Conference*, pp. 1–43.

Beck, R. and Scorpio, S. (1995). A desingularized boundary integral method for fully nonlinear water wave problems, *Proceedings of the 12th Australasian Fluid Mechanics Conference*, pp. 255–258.

Bevington, P. and Robinson, D. (1992). *Data reduction and error analysis for the physical sciences*, McGraw-Hill, Boston.

Bishop, R. and Price, W. (1979). *Hydroelasticity of ships*, Cambridge University Press, Cambridge.

Butcher, J. (2008). *Numerical methods for ordinary differential equations*, Wiley, New York.

Cao, Y. (1991). *Computation of nonlinear gravity waves by a desingularized boundary integral method*, PhD thesis, University of Michigan.

Cao, Y., Beck, R. and Schultz, W. (1993). Numerical computations of two-dimensional solitary waves generated by moving disturbances, *International Journal for Numerical Methods in Fluids* **17**(10): 905–920.

Cao, Y., Beck, R. and Schultz, W. (1994). Nonlinear computation of wave loads and motions of floating bodies in incident waves, *Proceedings of the 9th International Workshop on Water Waves and Floating Bodies*, pp. 33–37.

Cao, Y., Lee, T. and Beck, R. (1992). Computation of nonlinear waves generated by floating bodies, *Proceedings of the 7th International Workshop on Water Waves and Floating Bodies*, pp. 47–50.

Cao, Y., Schultz, W. and Beck, R. (1990). Three-dimensional, unsteady computations of nonlinear waves caused by underwater disturbances, *Proceedings of the 18th Symposium on Naval Hydrodynamics*, Vol. 1, pp. 417–425.

Cao, Y., Schultz, W. and Beck, R. (1991a). Three-dimensional desingularized boundary integral methods for potential problems, *International Journal for Numerical Methods in Fluids* **12**(8): 785–803.

Cao, Y., Schultz, W. and Beck, R. (1991b). Two-dimensional solitary waves generated by a moving disturbance, *Proceedings of the 6th International Workshop on Water Waves and Floating Bodies*, pp. 25–28.

Chakrabarti, S. (1978). Comments on second-order wave effects on large-diameter vertical cylinder, *Journal of Ship Research* **22**(4): 266–268.

Chapman, R. (1979). Large-amplitude transient motion of two-dimensional floating bodies, *Journal of Ship Research* **23**(1): 20–31.

Cummins, W. (1962). The impulse response function and ship motions, *Schiffstechnik* **9**: 101–109.

Davis, A. (1971). Short surface waves due to an oscillating half-immersed sphere, *Mathematika* **18**(01): 20–39.

Dawson, C. (1977). A practical computer method for solving ship-wave problems, *Proceedings of the 2nd International Conference on Numerical Ship Hydrodynamics*, pp. 30–38.

Dean, W. (1948). On the reflexion of surface waves by a submerged circular cylinder, *Mathematical Proceedings of the Cambridge Philosophical Society*, Vol. 44, pp. 483–491.

DNV (2013). Sesam user manual@version 6.5, *Norway: Det Norske Veritas.* .

Dold, J. (1992). An efficient surface-integral algorithm applied to unsteady gravity waves, *Journal of Computational Physics* **103**(1): 90–115.

Dommermuth, D. and Yue, D. (1987). Numerical simulations of nonlinear axisymmetric flows with a free surface, *Journal of Fluid Mechanics* **178**: 195–219.

Eatock Taylor, R. and Hung, S. (1987). Second order diffraction forces on a vertical cylinder in regular waves, *Applied Ocean Research* **9**(1): 19–30.

Eatock Taylor, R., Hung, S. and Chau, F. (1989). On the distribution of second order pressure on a vertical circular cylinder, *Applied Ocean Research* **11**(4): 183–193.

Faltinsen, O. (1972). Wave forces on a restrained ship in head-sea waves, *Proceedings of the 9th Symposium on Naval Hydrodynamics*, pp. 1763–1843.

Faltinsen, O. (1974). Motions of large structures in waves at zero froude number, *Proceedings of International Symposium on the Dynamics of Marine Vehicles and Structures In Waves*, pp. 99–114.

Faltinsen, O. and Loken, A. (1979). Slow drift oscillations of a ship in irregular waves, *Applied Ocean Research* **1**(1): 21–31.

Ferrant, P. (1997). Simulation of strongly nonlinear wave generation and wave-body interactions using a 3-D MEL model, *Proceedings of the 21st Symposium On Naval Hydrodynamics*, pp. 93–109.

Finkelstein, A. (1957). The initial value problem for transient water waves, *Communications on Pure and Applied Mathematics* **10**(4): 511–522.

Finn, P. (2003). *Large amplitude nonlinear seakeeping using a desingularized method*, PhD thesis, University of Michigan.

Frank, W. (1967). Oscillation of cylinders in or below the free surface of deep fluids, *Technical report*, David W. Taylor Naval Ship Research Development Center.

Garrison, C. (1978). Hydrodynamic loading of large offshore structures: three-dimensional source distribution methods, *Numerical Methods in Offshore Engineering* pp. 97–140.

Greenhow, M., Vinje, T., Brevig, P. and Taylor, J. (1982). A theoretical and experimental study of the capsize of salter's duck in extreme waves, *Journal of Fluid Mechanics* **118**(1): 221–239.

Grilli, S. T., Guyenne, P. and Dias, F. (2001). A fully non-linear model for three-dimensional overturning waves over an arbitrary bottom, *International Journal for Numerical Methods in Fluids* **35**(7): 829–867.

Guerber, E., Benoit, M., Grilli, S. and Buvat, C. (2010). Modeling of fully nonlinear wave interactions with moving submerged structures, *Proceedings of the 20th International Offshore and Polar Engineering Conference*, pp. 529–536.

Haskind, M. (1944). The oscillation of a body immersed in heavy fluid, *Philosophical Magazine* **8**: 287–300.

Haskind, M. (1952). Translational motion of bodies under the free surface of a heavy fluid of finite depth, *Technical report*, National Advisory Commitee for Aeronautics.

Haskind, M. (1954). On wave motions of a heavy fluid, *Philosophical Magazine* **18**: 15–26.

Havelock, T. (1955). Waves due to a floating sphere making periodic heaving oscillations, *Proceedings of the Royal Society of London. Series A. Mathematical and Physical Sciences* **231**(1184): 1–7.

Hess, J. L. and Smith, A. (1967). Calculation of potential flow about arbitrary bodies, *Progress in Aerospace Sciences* **8**: 1–138.

Hess, J. and Smith, A. (1964). Calculation of non-lifting potential flow about arbitrary three dimensional bodies, *Journal of Ship Research* **8**(2): 22–44.

Hulme, A. (1982). Wave forces acting on a floating hemisphere undergoing forced periodic oscillations, *Journal of Fluid Mechanics* **121**(1): 443.

Jensen, G., Soding, H. and Mi, Z. (1986). Rankine source methods for numerical solutions of the steady wave resistance problem, *Proceedings of the 16th Symposium on Naval Hydrodynamics*, pp. 593–606.

John, F. (1950). On the motion of floating bodies ii. simple harmonic motions, *Communications on Pure and Applied mathematics* **3**(1): 45–101.

Kang, C. (1988). *Bow flare slamming and nonlinear free surface-body intersection in the time domain.*, PhD thesis, University of Michigan.

Kent, C. (2005). *A pseudo-spectral method for calculating wave-body interaction using an explicit free-surface formulation*, PhD thesis, University of Michigan.

Kim, C. (1969). Calculation of hydrodynamic forces for cylinders oscillating in shallow water, *Journal of Ship Research* **13**: 137–164.

Kim, M. and Yue, D. (1989). The complete second-order diffraction solution for an axisymmetric body, Part 1. Monochromatic incident waves, *Journal of Fluid Mechanics* **200**(1): 235–264.

Kim, M. and Yue, D. (1990). The complete second-order diffraction solution for an axisymmetric body, Part 2. Bichromatic incident waves and body motions, *Journal of Fluid Mechanics* **211**(1): 557–593.

King, B. (1987). *Time-domain analysis of wave exciting forces on ships and bodies*, PhD thesis, University of Michigan.

Kleinman, R. (1982). On the mathematical theory of the motion of floating bodies-an update., *Technical report*, David W. Taylor Naval Ship Research and Development Center.

Koo, W. and Kim, M. (2004). Freely floating-body simulation by a 2D fully nonlinear numerical wave tank, *Ocean Engineering* **31**(16): 2011–2046.

Koo, W. and Kim, M. (2007). Fully nonlinear wave-body interactions with surface-piercing bodies, *Ocean Engineering* **34**(7): 1000–1012.

Korvin-Kroukovsky, B. and Jacobs, W. (1957). Pitching and heaving motions of a ship in regular waves, *Society of Naval Architects and Marine Engineers Transactions* **65**: 590–632.

Kring, D. C. (1994). *Time domain ship motions by a three-dimensional Rankine panel method*, PhD thesis, Massachusetts Institute of Technology.

Lamb, H. (1993). *Hydrodynamics*, Cambridge University Press, Cambridge.

Lee, C. (1968). The second-order theory of heaving cylinders in a free surface, *Journal of Ship Research* **12**(4): 313–327.

Lee, C. and Newman, J. (2005). Computation of wave effects using the panel method, *Numerical Models in Fluid Structure Interaction* **42**: 211–251.

Lee, C., Newman, J. and Zhu, X. (1996). An extended boundary integral equation method for the removal of irregular frequency effects, *International Journal for Numerical Methods in Fluids* **23**(7): 637–660.

Lee, C. and Sclavounos, P. (1989). Removing the irregular frequencies from integral equations in wave-body interactions, *Journal of Fluid Mechanics* **207**(1): 393–418.

Lee, T. (1992). *Nonlinear radiation problems for a surface-piercing body*, PhD thesis, University of Michigan.

Lee, T. (2003). Fully nonlinear wave computations for arbitrary floating bodies using the delta method, *Journal of Hydrodynamics* **15**(002): 24–31.

Liapis, S. (1993). A method for suppressing the irregular frequencies from integral equations in water wave-structure interaction problems, *Computational Mechanics* **12**(1): 59–68.

Lin, W., Newman, J. and Yue, D. (1984). Nonlinear forced motions of floating bodies, *Proceedings of the 15th Symposium on Naval Hydrodynamics*, pp. 33–49.

Lin, W. and Yue, D. (1990). Numerical solutions for large-amplitude ship motions in the time domain, *Proceedings of the 18th Symposium on Naval Hydrodynamics*, pp. 41–65.

Liu, Y., Xue, M. and Yue, D. (2001). Computations of fully nonlinear three-dimensional wave–wave and wave–body interactions, Part 2. Nonlinear waves and forces on a body, *Journal of Fluid Mechanics* **438**(1): 41–66.

Longuet-Higgins, M. and Cokelet, E. (1976). The deformation of steep surface waves on water: I. A numerical method of computation, *Proceedings of the Royal Society of London. A. Mathematical and Physical Sciences* **350**(1660): 1–26.

Longuet-Higgins, M. and Cokelet, E. (1978). The deformation of steep surface waves on water: II. Growth of normal-mode instabilities, *Proceedings of the Royal Society of London. A. Mathematical and Physical Sciences* **364**(1716): 1–28.

Matsui, T., Kato, K. and Shirai, T. (1987). A hybrid integral equation method for diffraction and radiation of water waves by three-dimensional bodies, *Computational Mechanics* **2**(2): 119–135.

Matsui, T., Suzuki, T. and Sakoh, Y. (1992). Second-order diffraction forces on floating three-dimensional bodies in regular waves, *International Journal of Offshore and Polar Engineering* **2**(3): 175–185.

Molin, B. (1979). Second-order diffraction loads upon three-dimensional bodies, *Applied Ocean Research* **1**(4): 197–202.

Molin, B. and Marion, A. (1986). Second-order loads and motions for floating bodies in regular waves., *Proceedings of the 5th International Offshore Mechanics Arctic Eengineering Symposium*, Vol. 1, pp. 353–360.

Moore, D. (1983). Resonances introduced by discretization, *IMA Journal of Applied Mathematics* **31**(1): 1–11.

Munk, M. (1924). The aerodynamic forces on airship hulls, *Technical report*, National Advisory Committee for Aeronautics.

Nakos, D. and Sclavounos, P. (1990). On steady and unsteady ship wave patterns, *Journal of Fluid Mechanics* **215**(1): 263–288.

Nestegard, A. and Sclavounos, P. (1984). A numerical solution of two-dimensional deep water wave-body problems, *Journal of Ship Research* **28**(1): 48–54.

Newman, J. (1964). A slender-body theory for ship oscillations in waves, *Journal of Fluid Mechanics* **18**(04): 602–618.

Newman, J. (1967). The drift force and moment on ships in waves, *Journal of Ship Research* **11**(1): 51–60.

Newman, J. (1977). *Marine hydrodynamics*, The MIT press, Cambridge, Massachusetts.

Newman, J. (1979). The theory of ship motions, *Advances in Applied Mechanics* **18**: 221–283.

Newman, J. (1986). Distributions of sources and normal dipoles over a quadrilateral panel, *Journal of Engineering Mathematics* **20**(2): 113–126.

Newman, J. (1990). The evaluation of free-surface Green functions, *Proceedings of the 4th International Conference on Numerical Ship Hydrodynamics*, pp. 4–23.

Newman, J. (1992). *The approximation of free-surface Green functions*, Cambridge University Press.

Newman, J. and Sclavounos, P. (1980). The unified theory of ship motions, *Proceedings of the 13th Symposium on Naval Hydrodynamics*, pp. 373–394.

Newman, J. and Tuck, E. (1964). Current progress in the slender body theory for ship motions, *Proceedings of the 5th Symposium on Naval Hydrodynamics*, pp. 129–166.

Noblesse, F. (1981). Alternative integral representations for the green function of the theory of ship wave resistance, *Journal of Engineering Mathematics* **15**(4): 241–265.

Oakley, O. (1972). *Large amplitude oscillations of floationg cylinders at low frequencies*, PhD thesis, Massachusetts Institute of Technology.

Ogilvie, T. and Shin, Y. (1978). Integral-equation solutions for time-dependent free-surface problem, *Journal of the Society of Naval Archiotects of Japan* **143**: 43–53.

Ogilvie, T. and Tuck, E. (1969). A rational strip theory of ship motions: Part I, *Technical report*, University of Michigan.

Parissis, G. (1966). *Second Order Potentials and Forces for Oscillating Cylinders on a Free Surface*, PhD thesis, Massachusetts Institute of Technology.

Paulling, J. and Porter, W. (1962). Analysis and measurement of pressure and force on heaving cylinders in a free surface, *Proceedings of the 4th US National Congress of Applied Mechanics*, pp. 1369–1381.

Porter, W. (1960). *Pressure distribution, added mass, and damping coefficients for cylinders oscillating in a free surface*, PhD thesis, University of California, Berkeley.

Potash, R. (1971). Second-order theory of oscillating cylinders, *Journal of Ship Research* **15**(4): 295–324.

Rahman, M. (1984). Wave diffraction by large offshore structures: an exact second-order theory, *Applied Ocean Research* **6**(2): 90–100.

Salvesen, N., Tuck, E. and Faltinsen, O. (1970). Ship motions and sea loads, *Society of Naval Architects and Marine Engineers Transactions* **78**: 250–287.

Schultz, W., Cao, Y. and Beck, R. (1990). Three-dimensional nonlinear wave computation by desingularized boundary integral method, *Proceedings of the 5th International Workshop on Water Waves and Floating Bodies*, pp. 169–172.

Schultz, W. and Hong, S. (1989). Solution of potential problems using an overdetermined complex boundary integral method, *Journal of Computational Physics* **84**(2): 414–440.

Sclavounos, P. (1985). The unified slender-body theory: Ship motion in waves, *Proceedings of the 15th Symposium on Naval Hydrodynamics*, pp. 177–192.

Sclavounos, P. (1988). Radiation and diffraction of second-order surface waves by floating bodies, *Journal of Fluid Mechanics* **196**(1): 65–91.

Scorpio, S. (1997). *Fully nonlinear ship-wave computations using a multipole accelerated, desingularized method*, PhD thesis, University of Michigan.

Subramani, A., Beck, R. and Scorpio, S. (1999). Fully nonlinear free-surface computations for arbitrary and complex hull forms, *Proceedings of the 22nd Symposium on Naval Hydrodynamics*, pp. 390–402.

Sun, H. (2007). *A boundary element method applied to strongly nonlinear wave-body interaction problems*, PhD thesis, Norwegian University of Science and Technology.

Sun, H. and Faltinsen, O. M. (2006). Water impact of horizontal circular cylinders and cylindrical shells, *Applied Ocean Research* **28**(5): 299–311.

Sun, H. and Faltinsen, O. M. (2007). The influence of gravity on the performance of planing vessels in calm water, *Journal of Engineering Mathematics* **58**(1-4): 91–107.

Tanizawa, K. (1996). Long time fully nonlinear simulation of floating body motions with artificial damping zone, *Journal of the Society of Naval Architects of Japan* **180**: 311–319.

Tasai, F. and Koterayama, W. (1976). Nonlinear hydrodynamic forces acting on cylinders heaving on the surface of a fluid, *Technical Report 77*, Reports of Research Institute for Applied Mechanics.

Teng, B. and Li, Y. (1996). A unique solvable higher order bem for wave diffraction and radiation, *China Ocean Engineering* **10**(3): 333–342.

Thorne, R. (1953). Multipole expansions in the theory of surface waves, *Mathematical Proceedings of the Cambridge Philosophical Society*, Vol. 49, pp. 701–716.

Tsai, W. and Yue, D. (1996). Computation of nonlinear free-surface flows, *Annual Review of Fluid Mechanics* **28**(1): 249–278.

Ursell, F. (1950). Surface waves on deep water in the presence of a submerged circular cylinder. I, *Mathematical Proceedings of the Cambridge Philosophical Society*, Vol. 46, pp. 141–152.

Ursell, F. (1962). Slender oscillating ships at zero forward speed, *Journal of Fluid Mechanics* **14**: 496–516.

Ursell, F. (1964). The decay of the free motion of a floating body, *Journal of Fluid Mechanics* **19**(02): 305–319.

Vinje, T. and Brevig, P. (1981). Nonlinear ship motions, *Proceedings of the 3rd International Conference on Numerical Ship Hydrodynamics*, pp. 1–10.

Vugts, J. (1968). The hydrodynamic coefficients for swaying, heaving and rolling cylinders in a free surface, *International Shipbuilding Progress* **15**: 251–275.

Vugts, J. (1971). The hydrodynamic forces and ship motions in oblique waves, *Technical report*, Netherlands Ship Research Centre.

Wamit (2013). Wamit user manual@ version 7.0, *Wamit, Inc.* .

Webster, W. (1975). The flow about arbitrary, three-dimensional smooth bodies, *Journal of Ship Research* **19**(4): 206–218.

Wehausen, J. and Laitone, E. (1960). *Surface Waves*, Springer, Berlin.

Xue, M., H., X., Liu, Y. and Yue, D. (2001). Computations of fully nonlinear three-dimensional wave–wave and wave–body interactions, Part 1. Dynamics of steep three-dimensional waves, *Journal of Fluid Mechanics* **438**(1): 11–39.

Yamashita, S. (1977). Calculation of hydrodynamic forces acting upon thin cylinders oscillating vertically with large amplitude, *Journal of the Society of Naval Architects of Japan* **141**: 61–70.

Yan, H. (2010). *Computations of fully nonlinear three-dimensional wave-body interactions*, PhD thesis, Massachusetts Institute of Technology.

Yan, H. and Liu, Y. (2011). An efficient high-order boundary element method for nonlinear wave–wave and wave-body interactions, *Journal of Computational Physics* **230**(2): 402–424.

Yan, H., Liu, Y., Kominiarczuk, J. and Yue, D. K. (2009). Cavity dynamics in water entry at low froude numbers, *Journal of Fluid Mechanics* **641**: 441.

Yeung, R. (1973). A singularity-distribution method for free-surface flow problems with an oscillating body, *Technical report*, University of Berkeley.

Yeung, R. (1982). The transient heaving motion of floating eylinders, *Journal of Engineering Mathematics* **16**(2): 97–119.

Yeung, R. W. and Anathakrishnan, P. (1992). Oscillation of a floating body in a viscous fluid, *Journal of Engineering Mathematics* **26**(1): 211–230.

Yu, Y. and Ursell, F. (1961). Surface waves generated by an oscillating circular cylinder on water of finite depth: theory and experiment, *Journal of Fluid Mechanics* **11**(04): 529–551.

Zhang, X. (2007). *Large amplitude ship motion computations using a time dependent body geometry*, PhD thesis, University of Michigan.

Zhang, X., Bandyk, P. and Beck, R. (2007). Large amplitude body motion computations in the time-domain, *Proceeding of the 9th International Conference on Numerical Ship Hydrodynamics*.

Zhang, X., Bandyk, P. and Beck, R. (2010). Time-domain simulations of radiation and diffraction forces, *Journal of Ship Research* **54**(2): 79–94.

Zhang, X. and Beck, R. (2006). 2-D body-exact computations in the time domain, *Proceedings of the 21st International Workshop on Water Waves and Floating Bodies*, pp. 197–200.

Zhang, X. and Beck, R. (2007). Computations for large-amplitude two-dimensional body motions, *Journal of Engineering Mathematics* **58**(1): 177–189.

Zhang, X. and Beck, R. (2008). Three-dimensional large amplitude body motions in waves, *Journal of Offshore Mechanics and Arctic Engineering* **130**(4): 16–23.

Zhang, X., Khoo, B. and Lou, J. (2006). Wave propagation in a fully nonlinear numerical wave tank: A desingularized method, *Ocean Engineering* **33**(17): 2310–2331.

Zhao, R. and Faltinsen, O. (1993). Water entry of two-dimensional bodies, *Journal of Fluid Mechanics* **246**(1): 593–612.